Potential of high resolution remote sensing data for Leaf Area Index derivation using statistical and physical models

Inaugural-Dissertation
zur Erlangung des naturwissenschaftlichen Doktorgrades
der Philosophischen Fakultät I
der Julius-Maximilians-Universität Würzburg

vorgelegt von

Sarah Asam

aus Murnau am Staffelsee

Würzburg 2014

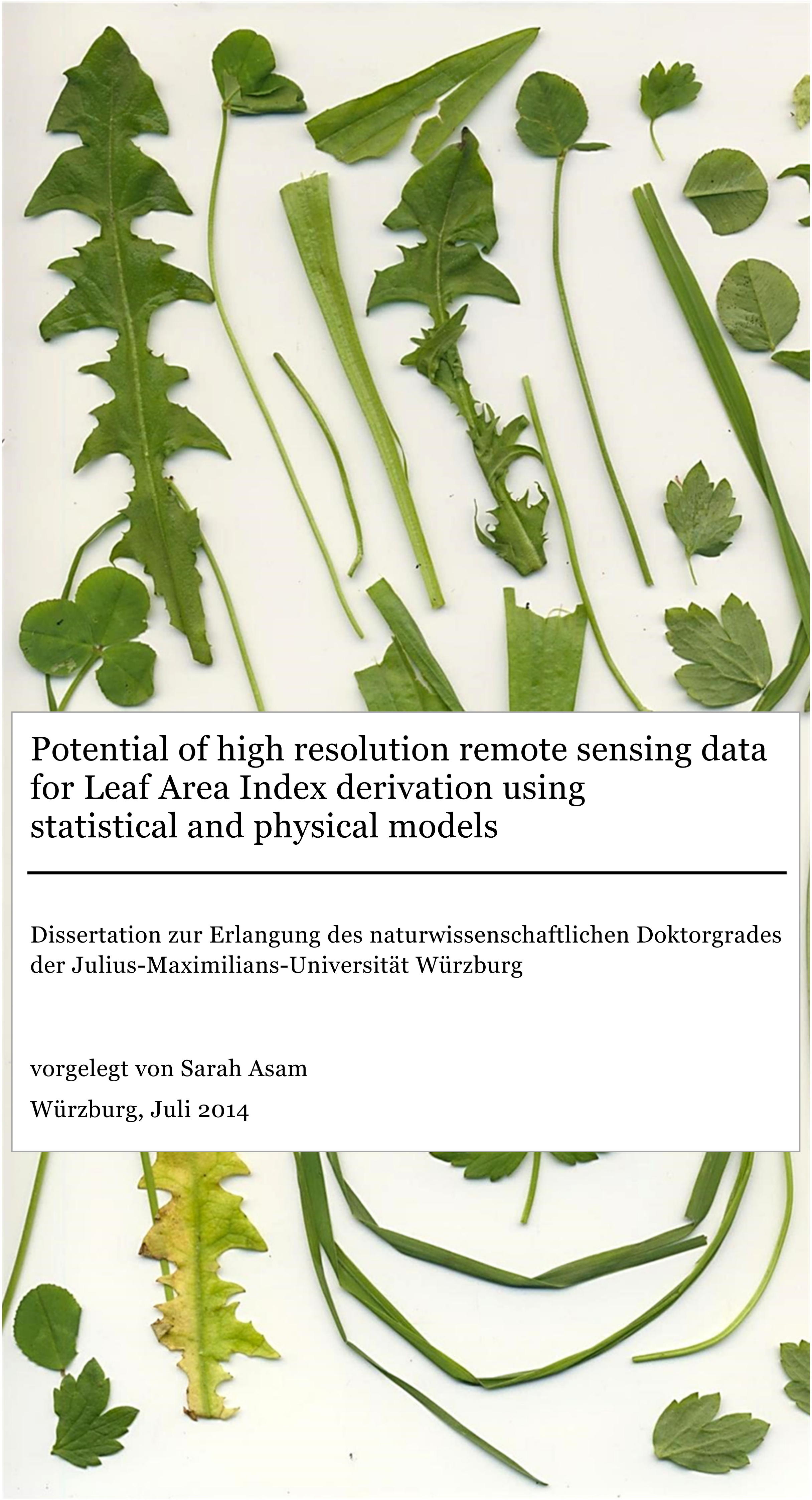

Potential of high resolution remote sensing data for Leaf Area Index derivation using statistical and physical models

Dissertation zur Erlangung des naturwissenschaftlichen Doktorgrades
der Julius-Maximilians-Universität Würzburg

vorgelegt von Sarah Asam

Würzburg, Juli 2014

Eingereicht am: 25.07.2014

1. Gutachter: Prof. Dr. Stefan Dech
2. Gutachter: Prof. Dr. Harald Kunstmann

Mentorin: Dr. Doris Klein

Tag der Disputation: 03.12.2014

Abstract

Information on the state of the terrestrial vegetation cover is important for several ecological, economical, and planning issues. In this regard, vegetation properties such as the type, vitality, or density can be described by means of continuous biophysical parameters. One of these parameters is the leaf area index (LAI), which is defined as half the total leaf area per unit ground surface area. As leaves constitute the interface between the biosphere and the atmosphere, the LAI is used to model exchange processes between plants and their environment. However, to account for the variability of ecosystems, spatially and temporally explicit information on LAI is needed both for monitoring and modeling applications.

Remote sensing aims at providing such information. LAI is commonly derived from remote sensing data by empirical-statistical or physical models. In the first approach, an empirical relationship between LAI measured *in situ* and the corresponding canopy spectral signature is established. Although this method achieves accurate LAI estimates, these relationships are only valid for the place and time at which the field data were sampled, which hampers automated LAI derivation. The physical approach uses a radiation transfer model to simulate canopy reflectance as a function of the scene's geometry and of leaf and canopy parameters, from which LAI is derived through model inversion based on remote sensing data. However, this model inversion is not stable, as it is an under-determined and ill-posed problem.

Until now, LAI research focused either on the use of coarse resolution remote sensing data for global applications, or on LAI modeling over a confined area, mostly in forest and crop ecosystems, using medium to high spatial resolution data. This is why to date no study is available in which high spatial resolution data are used for LAI mapping in a heterogeneous, natural landscape such as alpine grasslands, although a growing amount of high spatial and temporal resolution remote sensing data would allow for an improved environmental monitoring. Therefore, issues related to model parameterization and inversion regularization techniques improving its stability have not yet been investigated for this ecosystem.

This research gap was taken up by this thesis, in which the potential of high spatial resolution remote sensing data for grassland LAI estimation based on statistical and radiation transfer modeling is analyzed, and the achieved accuracy and robustness of the two approaches is compared. The objectives were an ecosystem-adapted radiation transfer model set-up and an optimized LAI derivation in mountainous grassland areas. Multi-temporal LAI *in situ* measurements as well as time series of RapidEye data from 2011 and 2012 over the catchment of the River Ammer in the Bavarian alpine upland were used.

In order to obtain accurate *in situ* data, a comparison of the LAI derivation algorithms implemented in the LAI-2000 PCA instrument with destructively measured LAI was performed first. For optimizing the empirical-statistical approach, it was then analyzed how the selection of vegetation indices and regression models impacts LAI modeling, and how well these models can be transferred to other dates. It was shown that LAI can be derived with a mean accuracy of 80 % using contemporaneous field data, but that the accuracy decreases to on average 51 % when using these models on remote sensing data from other dates. The combined use of several data sets to create a regression which is used for LAI derivation at different points in time increased the LAI estimation accuracy to on average 65 %. Thus, reduced field measurement labor comes at the cost of LAI error rates being increased by 10 - 30 % as long as at least two campaigns are conducted. Further, it was shown that the use of RapidEye's red edge channel improves the LAI derivation by on average 5.4 %.

With regard to physical LAI modeling, special interest lay in assessing the accuracy improvements that can be achieved through model set-up and inversion regularization techniques. First, a global sensitivity analysis was applied to the radiation transfer model in order to identify the most important model parameters and most sensitive spectral features. After model parameterization, several inversion regularizations, namely the use of a multiple sample solution, the additional use of vegetation indices, and the addition of noise, were analyzed. Further, an approach to include the local scene's geometry in the retrieval process was introduced to account for the mountainous topography. LAI modeling accuracies of in average 70 % were achieved using the best combination of regularization techniques, which is in the upper range of accuracies that were achieved in the few existing other grassland studies based on *in situ* or air-borne measured hyperspectral data. Finally, further physically derived vegetation parameters and inversion uncertainty measures were evaluated in detail to identify challenging modeling conditions, which was mostly neglected in other studies. An increased modeling uncertainty for extremely high and low LAI values was observed. This indicates an insufficiently wide model parameterization and a canopy deviation from model assumptions on some fields. Further, the LAI modeling accuracies varied strongly between the different scenes. From this observation it can be deduced that the radiometric quality of the remote sensing data, which might be reduced by atmospheric effects or unexpected surface reflectances, exerts a high influence on the LAI modeling accuracy.

The major findings of the comparison between the empirical-statistical and physical LAI modeling approaches are the higher accuracies achieved by the empirical-statistical approach as long as contemporaneous field data are available, and the computationally efficiency of the statistical approach. However, when no or temporally unfitting *in situ* measurements are available, the physical approach achieves comparable or even higher accuracies. Furthermore, radiation transfer modeling enables the derivation of other leaf and canopy variables useful for ecological monitoring and modeling applications, as well as of pixel-wise uncertainty measures indicating the robustness and reliability of the model inversion and LAI derivation procedure. The established look-up tables can be used for further LAI derivation in Central European grassland also in other years.

The use of high spatial resolution remote sensing data for LAI derivation enables a reliable land cover classification and thus a reduced LAI mapping error due to misclassifications. Furthermore, the RapidEye pixels being smaller than individual fields allow for a radiation transfer model inversion over homogeneous canopies in most cases, as canopy gaps or field parcels can be clearly distinguished. However, in case of unexpected local surface conditions such as blooming, litter, or canopy gaps, high spatial resolution data show corresponding strong deviations in reflectance values and hence LAI estimation, which would be reduced using coarser resolution data through the balancing effect of the surrounding surface reflectances. An optimal pixel size with regard to modeling accuracy hence depends on the canopy and landscape structure. Furthermore, a reduced spatial resolution would enable a considerable acceleration of the LAI map derivation.

This illustration of the potential of RapidEye data and of the challenges associated to LAI derivation in heterogeneous grassland areas contributes to the development of robust LAI estimation procedures based on new and upcoming, spatially and temporally high resolution remote sensing imagery such as Landsat 8 and Sentinel-2.

Zusammenfassung

Informationen zum Zustand der Vegetation sind relevant für einige ökologische, ökonomische, und planerische Fragestellungen. Vegetationseigenschaften wie der Typ, die Vitalität oder die Dichte einer Pflanzendecke können dabei anhand von kontinuierlichen biophysikalischen Parametern beschrieben werden. Einer dieser Parameter ist der Blattflächenindex (engl. leaf area index, LAI), der als die halbe gesamte Blattoberfläche pro Bodenoberfläche definiert ist. Da die Blattfläche eine wichtige Schnittstelle zwischen der Biosphäre und der Atmosphäre darstellt, wird der LAI dazu verwendet, Austauschprozesse zwischen Pflanzen und ihrer Umwelt zu modellieren. Um die natürliche Variabilität von Ökosystemen berücksichtigen zu können, benötigt man für solche Monitoring- und Modellierungsanwendungen jedoch räumlich und zeitlich explizite LAI Informationen.

Die Fernerkundung stellt solche Informationen zur Verfügung. Fernerkundungsbasierte LAI-Kartierung basiert auf empirisch-statistischen und physikalischen Modellen. Im ersten Ansatz wird ein empirisches Verhältnis zwischen dem aufgezeichneten Reflexionssignal der Vegetationsdecke und in situ gemessenem LAI erstellt. Obwohl dieses Verfahren meist hohe Genauigkeiten erzielt, gilt das erstellte Verhältnis nur für den Ort und Zeitpunkt der Feldmessungen, was ein automatisiertes Verfahren behindert. Der physikalische Ansatz verwendet ein Strahlungstransfermodell um die spektrale Signatur einer Pflanzendecke in Abhängigkeit von der Szenengeometrie und verschiedenen Blatt- und Pflanzenparametern zu simulieren, von der LAI durch die Inversion des Modells basierend auf Fernerkundungsdaten abgeleitet wird. Die Modellinversion ist jedoch nicht stabil, da sie ein unterdeterminiertes und inkorrekt gestelltes Problem ist.

Bisher fokussierten LAI-Studien entweder auf die Verwendung räumlich grob ausgelöster Fernerkundungsdaten für globale Anwendungen, oder auf LAI-Modellierung für Wälder und Anbaufrüchte innerhalb eines räumlich eingeschränkten Gebiets basierend auf mittel und hoch aufgelösten Daten. Obwohl die Menge an räumlich und zeitlich hoch aufgelösten Fernerkundungsdaten für ein verbessertes Umweltmonitoring kontinuierlich zunimmt, führte dies dazu, dass es keine Studie gibt die sich mit der Ableitung des LAI in heterogenen Landschaften wie beispielsweise alpinem Grünland, basierend auf räumlich hoch aufgelösten Daten, beschäftigen. Dementsprechend wurden damit verbundene Aspekte wie die Modellparametrisierung und Regularisierungsmöglichkeiten der Inversion für dieses Ökosystem noch nicht untersucht.

Diesem Forschungsbedarf wird mit dieser Arbeit, in der das Potenzial räumlich hoch aufgelöster Fernerkundungsdaten für die Ableitung von Grünland-LAI basierend auf statistischen Modellen und Strahlungstransfermodellierung analysiert wird, und in der die Genauigkeiten und Stabilität beider Verfahren verglichen werden, begegnet. Die Ziele der Arbeit sind eine an das Grünlandökosystem angepasste Einrichtung des Strahlungstransfermodells und die Ableitung des LAI für Grünland im Gebirgsraum. Multitemporale *in situ* LAI-Messungen sowie RapidEye-Zeitreihen aus den Jahren 2011 und 2012 aus dem Ammereinzugsgebiet im bayrischen Voralpenland wurden dazu verwendet.

Um verlässliche *in situ* Messwerte zu erhalten, wurde zunächst ein Vergleich der im LAI-2000 PCA Messinstrument implementierten Algorithmen mit destruktiv erhobenen LAI Werten durchgeführt. Zur Optimierung des empirisch-statistischen Ansatzes wurde dann untersucht, in welchem Maße die Verwendung verschiedener Vegetationsindizes und Regressionsmodelle die LAI-Modellierung beeinflussen, und wie gut diese Modelle auf andere Zeitpunkte übertragen werden können. Es wurde gezeigt, dass unter Verwendung von zeitgleich erhobenen Felddaten der LAI mit einer mittleren Genauigkeit von 80 % abgeleitet werden kann, dass sich die Genauigkeit aber auf 51 % verringert, wenn die Modelle auf Fernerkundungsdaten anderer Zeitpunkte angewendet werden. Die gemeinsame Nutzung mehrerer Felddatensätze zur Erstellung einer Regression welche auf andere Zeitpunkte angewendet wird, erhöhte die Genauigkeit der LAI-Ableitung wiederum auf durchschnittlich 65 %. Ein verringerter Arbeitsaufwand für Feldmessungen wird also durch erhöhte Fehlerraten von 10 - 30 % pro Szene ausgewogen, solange mindestens zwei Messkampagnen durchgeführt werden. Außerdem wurde gezeigt, dass die Verwendung des “red edge” Bandes des RapidEye Sensors die LAI-Ableitung um im Mittel 5.4 % verbessert.

Im Hinblick auf die physikalische LAI-Modellierung waren vor allem die Verbesserung der Genauigkeit, die anhand von Modelleinstellungen und Regularisierungstechniken erzielt werden konnten, von Interesse. Zunächst wurde eine globale Sensitivitätsanalyse des Strahlungstransfermodells durchgeführt, um die wichtigsten Modellparameter und die sensitivsten spektralen Bereiche zu identifizieren. Nach der darauf basierenden Modellparametrisierung wurden in den nächsten Schritten mehrere Verfahren zu Stabilisierung der Inversion, nämlich die Verwendung multipler Lösungen, von Vegetationsindizes als Inputdaten, und von simuliertem Datenrauschen, analysiert. Außerdem wurde ein Ansatz eingeführt, der die Berücksichtigung der lokalen Szenengeometrien, und damit der Topographie des Untersuchungsgebietes, erlaubt. Genauigkeiten von im Mittel 70 % konnten für die LAI-Modellierung unter Verwendung der besten Modell- und Inversionseinstellungen erreicht werden. Diese sind mit den Ergebnissen anderer Grünland-Studien, die jedoch auf *in situ* oder flugzeuggetragen gemessenen hyperspektralen Daten beruhen, vergleichbar. Zuletzt wurden weitere physikalisch modellierte Vegetationsparameter sowie Inversionsunsicherheitsmaße evaluiert, um besonders schwierige Modellierungsbedingungen zu identifizieren, was in anderen Studien bisher meist vernachlässigt wurde. Erhöhte Modellierungsunsicherheiten wurden für die Ableitung besonders niedriger und hoher LAI Werte beobachtet, was auf eine ungenügend weit gefasste Modellparametrisierung und stellenweise Abweichungen der Vegetationsdecke von den Modellannahmen hinweist. Außerdem variieren die Genauigkeiten der LAI-Modellierung stark zwischen den einzelnen Szenen woraus abgeleitet werden kann dass die radiometrische Qualität der Fernerkundungsdaten, welche beispielsweise durch atmosphärische Effekte oder unerwartete Oberflächenreflexionen beeinfluss werten kann, einen großen Einfluss auf die Modellierungsgenauigkeit hat.

Im Vergleich der empirisch-statistischen und physikalischen LAI-Modellierung fiel der empirisch-statistische Ansatz mit höheren Genauigkeiten, solange zeitgleich aufgenommene Felddaten vorliegen, sowie mit einer geringeren Berechnungszeit auf. Wenn jedoch keine zeitlich passenden Felddaten vorhanden sind, erreicht die physikalische Modellierung vergleichbare oder sogar höhere Genauigkeiten. Des Weiteren ermöglicht das Strahlungstransfermodel die Ableitung weiterer Blatt- und Pflanzeneigenschaften, welche für ökologische Monitoring- und Modellierungsanwendungen nützlich sind. Außerdem werden pixelgenaue Unsicherheitsmaße generiert, welche die Stabilität und Verlässlichkeit der Modellinversion und des gewonnenen LAI-Wertes charakterisieren. Die erstellten Datenbanken können darüber hinaus für die LAI-Modellierung in anderen Mitteleuropäischen Grünländern auch in anderen Jahren verwendet werden.

Die Verwendung von hochaufgelösten Fernerkundungsdaten ermöglicht eine verlässliche Landbedeckungsklassifikation und verringert damit Fehler in der LAI-Modellierung die durch Fehlklassifikationen verursacht werden. Da die RapidEye-Pixel außerdem kleiner als einzelnen Felder sind, konnte das Strahlungstransfermodell in den meisten Fällen über homogenen Pflanzendecken invertiert werden. Angesichts unerwarteter lokaler Oberflächenreflexionen, hervorgerufen beispielsweise durch Blüten, Streu, oder Lücken, zeigen die hochaufgelösten Daten jedoch auch entsprechend starke Abweichungen, welche in gröber aufgelösten Daten durch die Reflexion der umgebenden Oberflächen verringert sind. Eine optimale Pixelgröße im Hinblick auf die Modellierungsgenauigkeit hängt also von der Struktur der Vegetationsdecke und der Landschaft ab. Eine verringerte Pixelgröße würde darüber hinaus die Ableitung von LAI-Karten deutlich beschleunigen.

Diese Darstellung des Potenzials von RapidEye Daten für LAI-Modellierung und der speziellen Herausforderungen an die genutzten Verfahren in heterogenen Grünländern kann zur Entwicklung von robusten LAI-Ableitungsverfahren beitragen, anhand welcher neue, räumlich und zeitlich hoch aufgelöste, Fernerkundungsdaten wie die der Landsat 8 oder Sentinel-2 Sensoren in Wert gesetzt werden können.

Table of Contents

List of Figures

List of Tables

The lists of figures and tables contain short versions of the headings which are used for the figures and tables in the text.

List of Abbreviations

AFRI	**A**erosol **F**ree **V**egetation **I**ndex
ALA	**A**verage **L**eaf **A**ngle
ANN	**A**rtificial **N**eural **N**etwork
AOD	**A**erosol **O**ptical **D**epth
ARVI	**A**tmospherically **R**esistant **V**egetation **I**ndex
a.s.l.	**A**bove **S**ea **L**evel
AVHRR	**A**dvanced **V**ery **H**igh **R**esolution **R**adiometer
AVIRIS	**A**irborne **V**isible/**I**nfra**R**ed **I**maging **S**pectrometer
bf	**B**rightness **F**actor
BRDF	**B**idirectional **R**eflectance **D**istribution **F**unction
BRF	**B**idirectional **R**eflectance **F**actor
C_{ab}	**C**hlorophyll **a**+**b** content
C_{ar}	**Car**otenoid content
C_{bp}	**B**rown **P**igment **C**ontent
CCA	**C**anonical **C**orrelation **A**nalysis
CEOS	**C**ommittee on **E**arth **O**bservation **S**atellites
CHRIS	**C**ompact **H**igh **R**esolution **I**maging **S**pectrometer
C_m	Dry **M**atter **C**ontent
CORINE	**CO**o**R**dination of **IN**formation on the **E**nvironment
CV	**C**oefficient of **V**ariation
C_w	**W**ater **C**ontent
CYCLOPES	**C**arbon c**Y**cle and **C**hange in **L**and **O**bservational **P**roducts from an **E**nsemble of **S**atellites
DART	**D**iscrete **A**nisotropic **R**adiative **T**ransfer model
DEM	**D**igital **E**levation **M**odel
DHP	**D**igital **H**emispherical **P**hotography
DN	**D**igital **N**umber
DOY	**D**ay **O**f the **Y**ear
DVI	**D**ifference **V**egetation **I**ndex
DWD	**D**eutscher **W**etter**D**ienst
ECV	**E**ssential **C**limate **V**ariable
EFAST	**E**xtended **F**ourier **A**mplitude **S**ensitivity **T**est
ESA	**E**uropean **S**pace **A**gency
ESU	**E**lementary **S**ampling **U**nit
EVI	**E**nhanced **V**egetation **I**ndex
EWT	**E**quivalent **W**ater **T**hickness
fCover	**F**ractional vegetation **Cover**

FLiES	**F**orest **Li**ght **E**nvironmental **S**imulator
FLIM	**F**orest **L**ight **I**nteraction **M**odel
FOV	**F**ield **Of** **V**iew
FPAR	**F**raction of **P**hotosynthetically **A**ctive **R**adiation
GAI	**G**reen **A**rea **I**ndex
GCOS	**G**lobal **C**limate **O**bserving **S**ystem
GCP	**G**round **C**ontrol **P**oints
GORT	**G**eometrical-**O**ptical **R**adiation **T**ransfer
HDRF	**H**emispherical-**D**irectional **R**eflectance **F**actor
HNV	**H**igh **N**ature **V**alue
hs	**H**ot **S**pot
IFOV	**I**nstantaneous **F**ield **Of** **V**iew
INFORM	**IN**vertible **FO**rest **R**eflectance **M**odel
JRC	**J**oint European **R**esearch **C**enter
LAD	**L**eaf **A**ngle **D**istribution
LAI	**L**eaf **A**rea **I**ndex
LIBERTY	**L**eaf **I**ncorporating **B**iochemistry **E**xhibiting **R**eflectance and **T**ransmittance **Y**ields
LIDAR	**LI**ght **D**etection **A**nd **R**anging
LIDF	**L**eaf **I**nclination **A**ngle **F**unction
LMA	**L**eaf **M**ass per **A**rea
LSE	**L**east **S**quares **E**stimate
LUT	**L**ook-**U**p **T**able
MCARI	**M**odified **C**hlorophyll **A**bsorption **R**atio **I**ndex
MERIS	**ME**dium **R**esolution **I**maging **S**pectrometer
MISR	**M**ultiangle **I**maging **S**pectro**R**adiometer
MODIS	**Mod**erate-resolution **I**maging **S**pectroradiometer
MODTRAN	**MOD**erate resolution atmospheric **TRAN**smission
MSARVI	**M**odified **S**oil-adjusted and **A**tmospherically **R**esistant **V**egetation **I**ndex
MSAVI	**M**odified **S**oil **A**djusted **V**egetation **I**ndex
MSR	**M**odified **S**imple **R**atio
MTA	**M**ean **T**ilt **A**ngle
MTVI	**M**odified **T**riangular **V**egetation **I**ndex
N	Leaf structure
NASA	**N**ational **A**eronautics and **S**pace **A**dministration
NDVI	**N**ormalized **D**ifferenced **V**egetation **I**ndex
NIR	**N**ear **I**nfra**R**ed
OAT	**O**ne-**A**t-a-**T**ime
OLS	**O**rdinary **L**east **S**quares

OOB	**O**ut-**O**f-**B**ag
OSAVI	**O**ptimized **S**oil **A**djusted **V**egetation **I**ndex
PAI	**P**lant **A**rea **I**ndex
PAR	**P**hotosynthetic **A**ctive **R**adiation
PCA	**P**lant **C**anopy **A**nalyzer
φ_o	**O**bserver azimuth angle
φ_r	**R**elative azimuth angle
φ_s	**S**un azimuth angle
PLS	**P**artial **L**east **S**quares
POLDER	**POL**arization and **D**irectionality of the **E**arth's **R**eflectances
PVI	**P**erpendicular **V**egetation **I**ndex
RAMI	**RA**diation transfer **M**odel **I**ntercomparison
RDVI	**R**enormalized **D**ifference **V**egetation **I**ndex
REIP	**R**ed **E**dge **I**nflection **P**oint
RF	**R**andom **F**orest
RMA	**R**educed **M**ajor **A**xis
RMSE	**R**oot **M**ean **S**quare **E**rror
RPC	**R**ational **P**olynomial **C**oefficients *or* **R**apid **P**ositioning **C**oordinates
RRI	**R**ed edge **R**atio **I**ndex
RS	**R**emote **S**ensing
RSE	**R**esidual **S**tandard **E**rror
RTM	**R**adiation **T**ransfer **M**odel
RVI	**R**atio **V**egetation **I**ndex
SA	**S**ensitivity **A**nalysis
SAIL	**S**cattering by **A**rbitrarily **I**nclined **L**eaves
SAR	**S**ynthetic **A**perture **R**adar
SARVI	**S**oil and **A**tmosphere **R**esistant **V**egetation **I**ndex
SAVI	**S**oil-**a**djusted **V**egetation **I**ndex
SD	**S**tandard **D**eviation
6S	**S**econd **S**imulation of the **S**atellite **S**ignal in the **S**olar **S**pectrum
skyl	Fraction of diffuse incident radiation
SLA	**S**pecific **L**eaf **A**rea
SLOPE	**S**tochastic model for **L**eaf **O**ptical **P**roperties **E**xtended for fluorescence
SMR	**S**tepwise **M**ultiple **R**egressions
SR	**S**imple **R**atio
SRTM	**S**huttle **R**adar **T**opography **M**ission
SVAT	**S**oil-**V**egetation-**A**tmosphere-**T**ransfer
SVR	**S**upport **V**ector **R**egression
SWIR	**S**hort-**W**avelength **I**nfra**R**ed
TERENO	**TER**restrial **EN**vironmental **O**bservatories
θ_o	**O**bserver zenith angle

θ_s	**S**olar zenith angle
TOA	**T**op-**O**f-**A**tmosphere
TOC	**T**op-**O**f-**C**anopy
TRAC	**T**racing **R**adiation and **A**rchitecture of **C**anopies
TRIM	**T**hree-dimensional **R**adiation **I**nteraction **M**odel
TSAVI	**T**ransformed **S**oil **A**djusted **V**egetation **I**ndex
TVI	**T**ransformed **V**egetation **I**ndex
UTM	**U**niversal **T**ransverse **M**ercator
VALERI	**VA**lidation of **L**and **E**uropean **R**emote sensing **I**nstruments
VI	**V**egetation **I**ndex
VIS	**V**isible **L**ight
WAI	**W**ood **A**rea **I**ndex
WDVI	**W**eighted **D**ifference **V**egetation **I**ndex

1. Introduction

This thesis analyzes and compares the potential of high spatial resolution remote sensing (RS) data for the estimation of grassland leaf area index (LAI) based on statistical relationships and radiation transfer modeling. The overall aim is an ecosystem-adapted radiation transfer model (RTM) set-up and optimized LAI derivation in mountainous grassland areas of the Ammer catchment. In this introduction, the relevance of environmental monitoring based on RS data for various applications is emphasized (chapter 1.1), with special focus on the LAI parameter (chapter 1.2). The common procedures for LAI estimation as well as their limitations in general and with regard to grasslands and mountainous landscapes are briefly outlined (chapter 1.3). Subsequent to that, emerging research issues, the objectives, and innovative analyses of this thesis are presented, followed by a short overview of the structure of the thesis (chapter 1.4).

1.1. Remote sensing for environmental monitoring

Information on the state of the earth's surface is important for several ecological, economical, and planning issues. For instance, in addition to information about land cover and land use, monitoring the phenological stage, vitality, or density of vegetation is of high interest for agricultural applications and environmental protection. Furthermore, these vegetation properties directly influence natural processes in vegetation canopies, which makes their knowledge crucial for understanding terrestrial biosphere processes (Foley et al., 2000; Baret and Buis, 2008). Process-based models, which simulate these interactions between plants and their environment by linking them to driving variables like weather condition and nutrient availability, are increasingly being used to understand ecosystem dynamics. The simulations from these models are highly dependent on the accuracy of vegetation biophysical properties (Running et al., 1989). Hence, sciences such as climatology, hydrology, and ecology, which aim at emulating, quantifying, and ultimately predicting natural processes over a wide range of scales, strongly rely on this knowledge. Vegetation properties can be described by means of continuous physical, chemical, and biological state parameters such as the LAI, chlorophyll and water content, the fraction of photosynthetically active radiation (FPAR), or the fraction of vegetation ground cover. However, spatially and temporally explicit information on these vegetation properties is needed both for scientific monitoring and input for modelling applications (Dorigo, 2007).

RS aims at providing such information. What makes RS interesting for environmental sciences is its ability to deliver spatially continuous and periodical observations of vegetation over large extents and also in remote areas. With the launch of the Landsat satellites in the 1970s, the scientific community recognized RS as a valuable tool. In the subsequent decades, the retrieval of vegetation parameters has been largely addressed by the use of sensors such as Advanced Very High Resolution Radiometer (AVHRR) or Moderate-resolution Imaging Spectroradiometer (MODIS). These sensors can provide almost daily global information, albeit at the expense of coarser[1] observation supports, e.g. 1 km pixel size for AVHRR.

However, due to the increasingly relevant role of RS in environmental monitoring (Baret and Buis, 2008) and other sectors of human activities such as urban planning, disaster management, or civil protection, great efforts have been made to continuously improve RS technologies. During the last two decades, a number of new high spatial resolution satellites such as RapidEye (Tyc et al., 2005) and Landsat 8 (Irons et al., 2012) emerged. Currently, a new generation of high spatial and temporal resolution multi-spectral land monitoring missions is being launched including the upcoming Sentinel mission (Drusch et al., 2012) within the Copernicus[2] program, or the upcoming VENµs mission (Ferrier et al., 2010). Such a growing amount of high temporal and spatial resolution RS data allows for improved environmental monitoring, but also calls for the development of accurate, robust and effective methods for vegetation parameter retrieval. These methods should be capable of deriving vegetation information without requiring field calibration and be applicable to a wide range of landscape types (Liang, 2008; Duveiller et al., 2011b; Verrelst et al., 2014).

1.2. Relevance of LAI for ecological processes

Environmental monitoring based on RS data traditionally relies on the use of vegetation indices (VIs), which trace the relative abundance and health of vegetation. However, VIs should only be used as measures of canopy light absorption, as they have no inherent physical meaning related to structural, chemical, and biological vegetation state properties (Glenn et al., 2008). Biophysical parameters on the other hand are quantifiable measures of mass or area. One such key biophysical parameter and perhaps the most commonly used canopy structure parameter is the LAI, which quantifies the green plant area that constitutes the canopy-atmosphere interface. RS provides the only practical option for mapping LAI continuously over the landscape. The importance of LAI estimates from RS for vegetation monitoring has also been recognized by the Global Climate Observing System (GCOS), which identified LAI as an Essential Climate Variable (ECV) and its operational generation as one of GCOS's main tasks (GCOS, 2006). Therefore, LAI mapping has been a major objective in RS.

The LAI is a dimensionless variable and was first defined by Watson (1947) as the total one-sided leaf area per unit horizontal ground surface area. Although this definition is precise for flat broad leaves, it is ambiguous for cylindrical needles and wrinkled, bent or rolled leaves, as the one-sided leaf area is not clearly defined in these cases. Lang et al. (1991) and Chen and Black (1992) proposed to define LAI as half the total intercepting leaf area per unit ground surface area, because this definition is valid regardless of leaf shape, and because it has an actual physical (e.g. radiation interception) and biological (e.g. gas exchange) meaning. Myneni et al. (1997) suggested the use of the maximum projected leaf area per unit

---

[1] Although no universally accepted definition of spatial resolution categories exists, in this dissertation remote sensing data are defined as very high resolution (≤ 1 m), high resolution (1 - 20 m), medium resolution (20 - 100 m), and coarse resolution (≥ 100 m) systems (see chapter 2.2.1).

[2] Copernicus is a joint initiative of the European Commission (EC) and the European Space Agency (ESA) that aims at the provision and use of operational high resolution monitoring information for environment and security applications. For information see http://www.copernicus.eu/. Last access: April 4, 2014.

ground surface area, which can also be related to total exchange and interception areas. Further definitions have been proposed (e.g. Bolstad and Gower, 1990; Smith, 1991), and it is crucial to note that the application of different LAI definitions can result in large differences in LAI estimates for some biomes. In this thesis and close to Watson's definition, LAI is defined as one half the total leaf area per unit ground surface area (Jonckheere et al., 2004).

Usually, LAI measures between zero for bare soil and ten or higher for dense forests. Values between zero and one mean that there is less leaf area than soil area. Values above one do not necessarily mean that the soil is completely covered, as the leaves can be situated one above the other. In contrast to other biophysical vegetation parameters such as albedo, FPAR, or the mean foliage angle, LAI has no theoretical upper limit. LAI depends on the canopy species composition, development stage and seasonality, site conditions, and – if anthropogenically influenced – management practices. Hence, it is a temporally and spatially (horizontally as well as vertically) highly variable parameter (Jonckheere et al., 2004).

Green leaves constitute the interface between biosphere and atmosphere, and thus play a major role in several biological and ecological energy and matter exchange processes. Firstly, photosynthesis takes place in leaves, which directly drives gas exchange of oxygen and carbon oxide, biogenic emissions, and biomass production. Being a proxy for vegetation biomass, LAI is an important variable for characterizing vegetation abundance and distribution across the landscape. The estimation of biomass is required for carbon stock accounting and monitoring, which is crucial within the framework of several international conventions (Brown, 2002; Rosenqvist et al., 2003). Another important impact of LAI is its effect on the hydrological cycle by quantifying the water exchange through canopy interception and transpiration, thus influencing evapotranspiration, infiltration and runoff generation. Further, changes in foliage density alter the albedo of a surface and thus processes on scales from local micro-meteorological fluxes up to the earth's radiation balance (Bonan, 1997).

Due to these interrelations with gas, water and energy fluxes, the availability of spatially and temporally distributed information on LAI is crucial for spatially explicit ecological, hydrological, and climate modeling over a wide range of grid scales (Bonan, 1993; Dorigo et al., 2007; van Gorsel et al., 2011). LAI is employed in most land surface process models, which are also called ecosystem process models (Running and Coughlan, 1988; Nemani et al., 1993) or Soil-Vegetation-Atmosphere-Transfer (SVAT) models (Flerchinger et al., 1998; Foley et al., 2000). On the large scale (regional to global), SVAT models are linked to hydrological models (Kunstmann, 2008), atmospheric circulation models (Bonan, 1995; Sellers et al., 1996; Sellers, 1997), net primary productivity models (Running et al., 1989; Cayrol et al., 2000; Matsushita and Tamura, 2002), or carbon cycle models (Turner et al., 2004) through the fluxes in terrestrial vegetation described above. Next to LAI, other remotely sensed vegetation properties such as albedo (Lucht et al., 2000), FPAR (Sellers et al., 1996), surface roughness (Lefsky et al., 2002), and phenology (Stöckli et al., 2008) are inputs to SVAT models (Sellers, 1997). Temporal changes in LAI or other state variables are adjusted by means of assimilation techniques (Dorigo et al., 2007; Quaife et al., 2008). Due to limited CPU resources and partly coarse resolution meteorological input data, most of these models use spatial grid resolutions (10 - 50 km) that are coarser than vegetation information provided by RS (0.3 - 1 km). This more accurate sub-grid information is still accounted for through aggregation techniques (Kunstmann, 2008).

LAI is also required on the high and medium resolution scales. For instance, runoff, sediment transport, and soil erosion models rely on LAI information on the catchment scale (Wigmosta et al., 1994; Mueller et al., 2008). The scale invariant FAO Penman-Monteith method for evapotranspiration computation also uses LAI as input data (Allen et al., 2000). The Joint European Research Center (JRC)[3] conducts comprehensive agricultural monitoring activities on the regional scale using medium resolution data. High spatial resolution LAI is relevant for investigations on the field-scale and sub-field scale, e.g. for agricultural applications such as precision farming, fertilizer and pesticide management, or yield modeling (Moulin et al., 1998, Dorigo et al., 2007). Thereby, LAI and other biochemical and structural properties are relevant to accurately representing agricultural units and within-field variabilities (Dorigo et al., 2007). A large number of studies coupling satellite data and canopy state variables within crop production models exist (e.g. Doraiswamy et al., 2004; Faivre et al., 2004; Olioso et al., 2005; Dente et al., 2008; Atzberger, 2013).

1.3. LAI derivation in mountainous grassland

RS observations do not directly sample LAI. Instead, changes in the chemical, physical, and structural characteristics of a vegetation canopy can cause variations in the spectral reflectance signature, which in turn can be measured by RS and quantified with changes in LAI. Two methods for RS based LAI retrieval are commonly used:

1) Empirical-statistical LAI derivation: this radiometric data-driven technique establishes a statistical relationship between the spectral signatures of a surface measured by a RS system and LAI measured *in situ*. This relationship expressed as a regression model is used for mapping LAI based on the RS imagery. Due to its simplicity, accurate results over a confined area and known land cover, and its computational efficiency, this approach has been widely used in the RS community. However, in reality the relationship between canopy reflectance and LAI is not linear, but complex and saturates with high LAI, which limits the approach for dense canopies (Glenn et al., 2008). Further, the method relies on the availability of time consistent field measurements, which are usually time-consuming and expensive. Another drawback is that empirical relationships typically depend on site and sampling conditions and are sensitive to variations in space and time, and thus cannot be automated (Baret and Guyot, 1991; Meroni et al., 2004). Empirical-statistical LAI derivation has therefore mostly been applied to medium to high resolution data covering a small area at one point in time, representing LAI as a single snap-shot (Gobron et al., 1997a; Turner et al., 1999; Chen et al., 2002b; Johnson et al., 2003; Colombo et al., 2003; Dorigo et al., 2009; Rinaldi et al., 2010). Only few studies investigated the seasonal development of LAI using statistical methods and mostly in forested areas (e.g. Cohen et al., 2003a; Wang et al., 2005; Heiskanen et al., 2012; Potithep et al., 2013).

2) Radiation transfer modeling: During the last few decades, physical algorithms for estimating vegetation properties have been increasingly used as an alternative to empirical approaches (Liang, 2008). The physical approach uses a RTM that describes transmittance, absorbance, and reflectance of light within a canopy as a function of canopy characteristics (i.e. structural, chemical and biophysical parameters) and of the illumination and viewing geometries. This simulation of a radiation field reflected by a canopy is called “forward mode” of the RTM. In the so-called “inverse mode”, LAI and other canopy parameters can be derived from the RTM based on matching simulated reflectances to reflectance measurements (see chapter 6). As these models do not rely on *in situ* measurements, they are appealing for automated procedures. LAI derivation studies based on RTMs in the last few

---

[3] http://mars.jrc.ec.europa.eu/mars/About-us/AGRI4CAST/Crop-Monitoring-and-Yield-Forecasting

decades have focused primarily on the improvement of forward modeling of the radiative transfer problem (Liang, 2004). Only recently has inverse modeling come to the fore in RS research. However, model inversion is not straight-forward as, due to the complex character of RTMs, an analytical closed-form solution is mostly not possible. Consequently, numerical schemes have to be used for solving the inverted transport equation. Canopy reflectance is, however, not only influenced by LAI but also by other canopy variables such as leaf orientation or soil reflectance, so that several parameter combinations can lead to similar reflectances, which makes the inversion of a physical model an ill-posed problem. Further, due to the high number of model parameters together with the limited number of independent data dimensions in most RS systems, inversion is also an under-determined problem (Baret and Guyot, 1991; Verstraete et al., 1996; Kimes et al., 2000; Tarantola, 2005). To minimize these problems for RTM inversion and to stabilize the LAI derivation, model parameterization adaptation based on prior information and regularization techniques such as the selection of multiple inversion solutions or the addition of noise to the simulated spectra can be applied (Combal et al., 2002b; Bacour et al., 2006; Baret and Buis, 2008). However, a conclusive solution to these challenges has not yet been found and optimization strategies have not been consolidated yet (Verrelst et al., 2014).

Until now, operational LAI derivation relied on the use of coarse resolution RS data due to their availability for several decades and their high temporal resolution provided, which is needed for various applications such as phenological analysis. No high spatial resolution optical sensor was available that could fulfill this requirement. The use of coarse resolution data fostered research and validation activities in large-scale ecosystems, such as forests or monoculture crops. Regional LAI studies that used medium to high spatial resolution data for LAI derivation over a confined area also focused on these vegetation types because they were either simple to characterize (crops), or led to the development of more complex models (forests) (see chapter 2.2.3 for a review). Although this is a comprehensible approach, it has resulted in the fact that very little research has been conducted in relatively heterogeneous as well as spatial and temporal variable natural ecosystems such as alpine grassland (Darvishzadeh et al., 2008c). Unlike most agricultural crops, which grow in rather homogeneous canopies and mostly exhibit a regular annual life cycle, grasslands are composed of different plant species, all of which have unique morphologic and chemical features, and whose dynamic consists of periods of growth and re-growth (Vohland and Jarmer, 2008). Additionally, grassland occurrence, composition and structure depend on the individual management techniques such as mowing or pasturing, for which the timing is mostly highly irregular. To date, no study is available in which high spatial resolution data are used for the derivation of grassland LAI, and accordingly, issues related to RTM parameterization or inversion regularization techniques have not yet been investigated for this ecosystem. However, especially in heterogeneous landscapes with small-scale land use patterns, monitoring of agricultural areas needs frequent observations throughout the growing season, as well as a high spatial resolution to differentiate between various land uses and management forms, thus observations that will be provided by the use of recent and upcoming RS systems.

In Central Europe, more than one third of the agricultural land is made up of permanent grassland (FAO, 2013). On a global scale, grasslands are among the largest biomes in the world as they cover 40.5% of the earth’s landmass excluding Greenland and Antarctica (Suttie et al., 2005). Grassland is an important land cover with essential functions for regulating ecosystem services, and an agro-ecosystem used for the production of domestic livestock. In this context, the mapping of grasslands for subsidies is relevant in the European rural economy. Besides this economic importance, grassland habitats play an important role for biodiversity conservation, carbon storage, soil protection and slope stability, water purification, and regulating hydrologic and metabolic balances (Reid, 2005; Hopkins and Holz, 2006; Silva, 2008). Furthermore, the cultural and recreational services of grasslands, which are also of great relevance to tourism in rural areas, should be mentioned. Monitoring the ecosystem services of grasslands and the impact of environmental changes in regular inventories is of high interest with regard to ecological, economic, and political issues (Vohland and Jarmer, 2008). LAI is a suitable parameter for such inventories, offering information based on the current state and productivity of grasslands. However, information and data on the spatial distribution and changes in grasslands are scarce even in Central Europe (Smit et al., 2008). Such information is especially seldom available for areas that are hard to access, such as mountain regions.

Mountainous areas are mostly fragmented and vertically structured ecosystems in which grasslands, apart from forests, are the dominant land cover. The monitoring of mountain ecosystems is of interest as they are biologically valuable habitats and especially affected by climate change and anthropogenic influence (Nagy et al., 2003; Pauli et al., 2003b; Dirnböck et al., 2011). Further, alpine grasslands are very suitable for studying climate and global change effects, as a wide range of environmental conditions are set up by topography at relatively small spatial scales (Becker et al., 2007). From a RS perspective, mountains present extreme conditions. Strong topographic and climatic gradients over small distances frequently result in high spatial heterogeneity with a mixture of patchy land cover and continuous transitions between cover types. Topography complicates data preprocessing by the need to correct for shadows, exposition, and atmosphere layers of different thicknesses. Finally, the very limited availability of representative reference samples caused by the difficult access to these regions hampers training and validation activities (Pasolli, 2012). Therefore, the retrieval of alpine grassland LAI from RS imagery has been only marginally investigated up to now (e.g. Vescovo and Gianelle, 2008; Pasolli, 2012) and the above mentioned established methodologies require further investigations to adapt to the complexity of LAI retrieval in this environment.

1.4. Objectives and innovative analyses

As outlined above, the high relevance of LAI for monitoring and modeling applications in conjunction with the future abundance of high spatial resolution RS data call for robust and adapted LAI retrieval techniques. In this regard, the question remains which data and technique to use, especially for fragmented ecosystems. Only few studies have used high spatial resolution time series data in physical LAI derivation methods so far, which is why the knowledge of their potential for robust LAI derivation and possible limitations is still tentative. Indeed, at the time of writing this thesis no LAI estimation from RTMs based on high spatial resolution satellite data has been conducted in alpine grassland ecosystems. To fill this gap, grassland LAI is derived in this thesis using two different LAI estimation methods based on high spatial resolution RS data to assess and compare the accuracy and robustness of the retrieval approaches. In perspective, this thesis can contribute to the development of automated data analysis protocols in challenging landscapes.

The objective of this thesis is the optimization of an RTM for grassland LAI mapping over a heterogeneous mountainous landscape using high resolution RS data, and the evaluation of its performance in comparison to empirical-statistical models. Multi-temporal *in situ* LAI measurements as well as time series of RapidEye data from 2011 and 2012 over the Ammer catchment in southern Germany are used as input. So far, only a few studies have analyzed the potential of RapidEye with regard to mapping biophysical parameters (Vuolo et al., 2010; Ehammer et al., 2010; Eitel et al., 2011; Friese et al., 2011; Lex et al., 2013; Mannschatz and Dietrich, 2013; Tillack et al., 2014), and none have used RapidEye for LAI derivation in grasslands. The following research questions and are hence addressed in this thesis:

1) How does the selection of VIs and regression models impact the statistical modeling of LAI, and how well can these models be transferred to other points in time?

For empirical-statistical LAI derivation, model optimization comprises the testing of a large number of spectral indices and statistical models. Benefits achieved through the use of RapidEye's red edge band, as well as through the combination of data sets from different phenological phases, are quantified for the first time. Overall, the hypothesis is that once a robust statistical transfer function is established, it can be used on other points in time for which no observations are available, as managed grasslands present a similarly wide range of LAI occurrences at all points in time. The focus therefore lies on the accuracy loss caused by temporal transfer of established models, which has not been quantitatively evaluated so far.

2) Which RTM settings are most relevant for establishing an adapted and robust LAI derivation procedure, and which grassland-specific limitations occur during inversion?

The optimization of physical LAI modeling aims at the reduction of its under-determined and ill-posed character. Several inversion regularization techniques are tested which have been suggested in the literature (e.g. Weiss et al., 2000; Combal et al., 2002b; Rivera et al., 2013), but have never been applied to high spatial resolution RS data for grassland LAI derivation. To improve the model parameterization, a comprehensive global sensitivity analysis covering the visible and near infrared spectrum is applied to the used RTM for the first time to identify the relevance of each model parameter and of additional spectral features. Finally, further physically derived vegetation parameters and RTM inversion uncertainty measures are evaluated in detail, which has been mostly neglected in other studies. Based on these analyses, the potential and limitations of RTM inversion in general and specific to grassland LAI derivation are assessed.

3) Which of the empirical-statistical and physical LAI modeling approaches is more appropriate for grassland LAI derivation?

The performances of statistical and physical models are finally evaluated and compared using LAI measured *in situ*. In order to obtain accurate *in situ* data, a comparison of the LAI derivation algorithms implemented in the LAI-2000 PCA instrument with destructively measured LAI was performed first. The aim is to assess the LAI mapping potential of these methods over a heterogeneous grassland landscape. Apart from the LAI estimation accuracy, aspects regarding the reliability and practicability of the approaches are also of interest.

4) Does the use of high spatial resolution remote sensing data for LAI derivation involve specific advantages and limitations?

The use of high spatial resolution RS data for grassland LAI derivation on a landscape scale allows for an assessment of benefits and drawbacks resulting from the increased spatial detail, also with regard to the technical implementation of the approaches.

The conceptual framework as well as the new aspects of this thesis are depicted in Figure 1-1. This thesis is structured as follows: a comprehensive description of the theoretical background and the state of the art technologies for LAI measurement and estimation is given first (chapter 2). The study area is presented, with special focus on the occurring grassland types, in chapter 3. Then the *in situ* and satellite data used in this thesis, the data preprocessing, as well as the applied land cover classification are described (chapter 4). Chapter 5 comprises the first of the two LAI derivation methods, statistical LAI derivation. A range of spectral indices and statistic models is tested to identify the best fitting models for each time step as well as for some combinations of *in situ* samples. The achieved accuracies are investigated and the temporal transferability of the transfer functions is analyzed. The properties of the RTM, its sensitivity analysis, its parameterization, and the optimized inversion strategies are presented in chapter 6. To account for the mountainous topography in the RTM, an approach to include local viewing geometry in the retrieval process is introduced, and the results of the physical LAI derivation procedure are presented and discussed. In chapter 7, the performance of both approaches is compared, conclusions on the potential of high spatial resolution data for LAI derivation are drawn, and an outlook on possible future fields of research is provided.

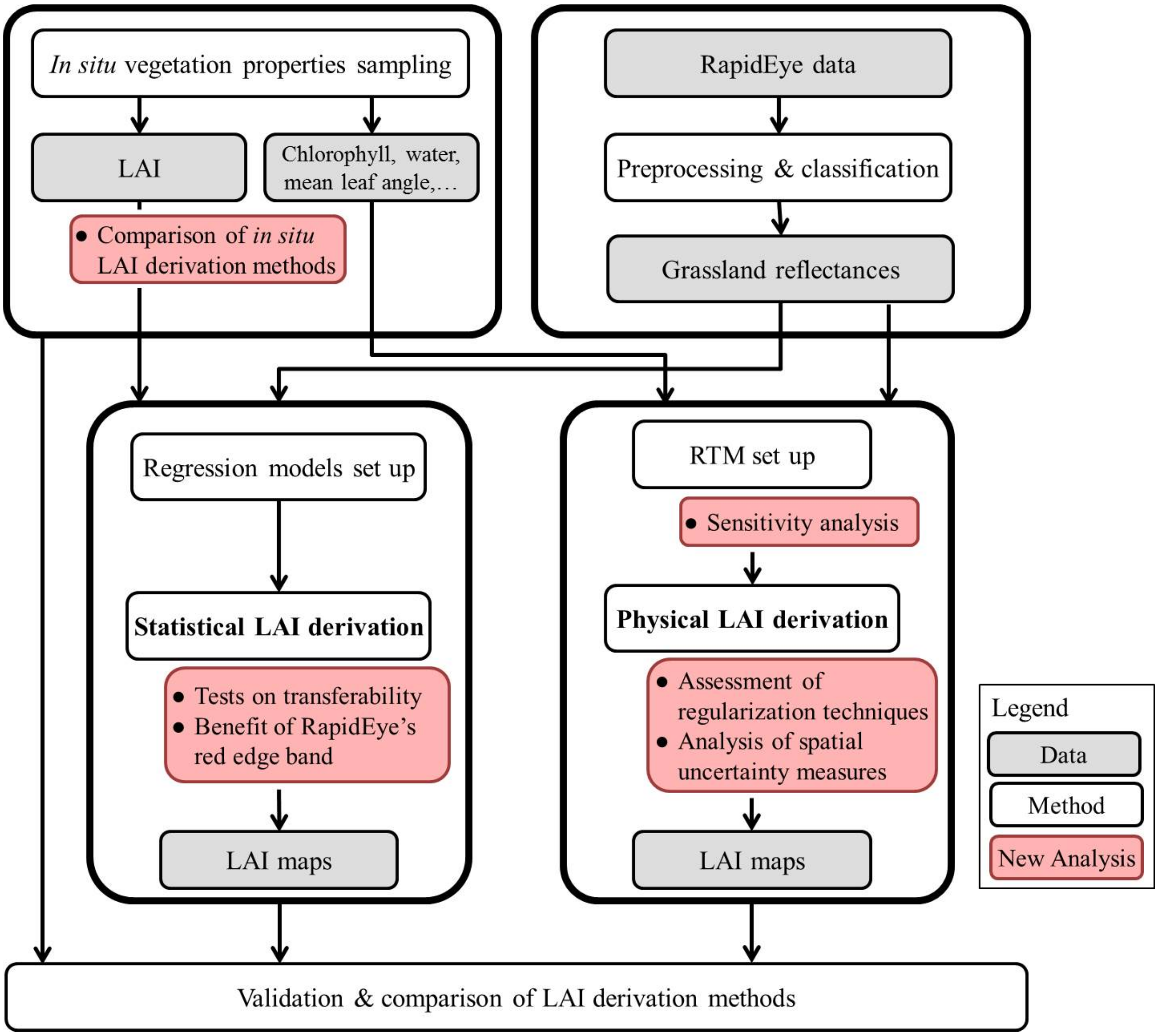

Figure 1-1: Overview of the conceptual framework and objectives of this thesis.

2. State of the art in LAI derivation

LAI is a parameter which has been used in ecology and forestry for decades to characterize vegetation canopies. As it has a high spatial and temporal variability, it is difficult to quantify. Various methods for LAI derivation have been developed since the early 1930s. The suitability of these methods for application in grassland varies. The family of *in situ* measurement techniques and related limitations are described first (chapter 2.1). The second section (chapter 2.2) gives an overview of the theoretical background of vegetation RS relevant for grassland LAI estimation, as well as on empirical-statistical methods and RTMs. Finally, an overview of available LAI products is provided (chapter 2.3), followed by some conclusions on research needs with regard to grassland LAI mapping (chapter 2.4).

2.1. *In situ* measurement methods

Two main categories of *in situ* LAI measurement can be distinguished: direct and indirect methods. The former group consists of direct LAI measurement techniques, while the latter comprises methods in which LAI is derived from parameters which are easier to measure, with both of them being applicable to grassland canopies.

2.1.1. Direct and semi-direct measurements

In this thesis, a direct method is defined as a technique to quantify LAI during which the plants are touched in some manner. The only way to truly determine LAI is by measuring the surface of all the leaves within a certain surface area (Bréda, 2003). In the early stages, this was performed by harvesting the biomass, drawing the outline of each leaf after it had been horizontally fixed to a flat surface, and measuring the shape's area using a planimeter or a reference grid (Ross, 1981). This method is obviously not feasible for small or non-flat leaves and plant parts. Modern leaf area meters measure the LAI by scanning the leaf shape or the leaf surface. In the field, the leaves within an area are measured employing a portable area meter e.g. the LI-3000 (LI-COR, NE, USA, see Figure 2-1) that uses an electronic method of rectangular approximation for area estimation while a leaf is drawn through the scanning head. In the laboratory, detached leaves can be measured using e.g. the LI-3100 area meter (LI-COR, NE, USA, see Figure 2-2), which scans the leaves while they pass by a camera on a transparent conveyor belt. Further alternatives include the portable scanning planimeter CI-202 from CID Inc. (NW Camas, WA, USA), the WinDIAS color image analyzer (Delta-T devices, Cambridge, UK), and the DIAS II Digital Image Analysis System (Decagon Devices Inc., Pullman, USA). The two latter companies also offer video image analysis systems (Jonckheere et al., 2004). A similar approach is to photograph or scan the flattened

Figure 2-1: Usage of the LI-COR LI-3000 leaf area meter (Adapted from LI-COR, 2006).

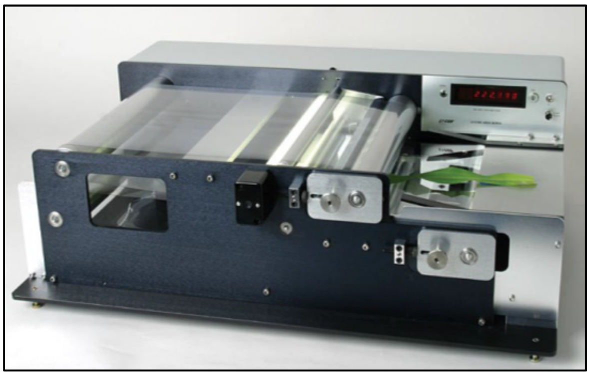

Figure 2-2: Usage of the LI-COR LI-3100C area meter (Adapted from LI-COR, 2004).

harvested plants and to use image analysis to identify the leaves in the picture (see Figure 2-3). For practical considerations, the direct method is most widely used for crops and grasses (Bréda, 2003), as it also is in this thesis. However, it is destructive and hence not feasible for LAI monitoring over time. Furthermore, the approach is too laborious to be applied on large samples.

Thus, to derive the LAI for whole canopies, the specific leaf area (SLA) is used for scaling. The SLA, as well as its reciprocal, leaf mass per area (LMA), is an empirical quantity of leaf area per unit dry biomass (Bréda, 2003). It is established by taking a sub-sample of the harvested foliage, measuring its LAI directly, drying the biomass in an oven at between 75 and 105 °C until constant weight, and weighing it. Simultaneously, the remaining material of the entire sample collected within a known area is dried and the total dry mass of leaves is converted into LAI by multiplying it with the SLA established on the sub-sample. A balanced distribution of different leaves (sun / shade, old / young) in the sub-samples is important in this regard. The SLA is species-specific and also varies between different years and sites, which is why care has to be taken for its establishment, since it otherwise potentially introduces errors in the LAI up-scaling (Bréda, 2003; Jonckheere et al., 2004). SLA is also used for leaf characterization in some RTMs.

These techniques, for the purpose of which all leaves in a defined area need to be harvested or scanned, are useful for herbaceous vegetation but not for monitoring forest stands, as the

Figure 2-3: Leaf area estimation from harvested biomass. The leaves are photographed (left) with a known picture size. The photo is then classified into leaf pixels and background pixels (right), from which the area can be calculated. Source: Own illustration.

leaves are not easily reachable, and a destructive method would strongly affect the integrity of the forest. Therefore, foresters have developed so-called allometric methods that relate LAI to more easily measureable plant parameters such as tree height, crown base height, or diameter at breast height (see e.g. Rogers and Hinckley, 1979; O'Hara and Valappil, 1995; Vertessy et al., 1995; Le Dantec et al., 2000). Another direct method relevant for deciduous forests is leaf litter collection in a number of traps distributed below the canopy during leaf fall. See e.g. Neumann et al. (1989), Dufrêne and Bréda (1995), Eriksson et al. (2005), and Wagner and Hagemeier (2006) for more details.

A method applied to both woody and herbaceous canopies is the inclined point quadrat method. With this method, the number of contacts (‘relative frequency’) of a long needle with vegetation in a certain direction is counted, which equals the LAI (Wilson, 1960). As the variation in relative frequency not only dependents on LAI but also on leaf inclination, the optimal probe angle varies with species. However, as the lowest variability occurs at a point quadrat inclination angle of 32.5°, this angle is mostly chosen for measurements, irrespective of species composition (Wilson, 1960). The method is attractive because it is non-destructive and quick. However, many measurements (typically at least 1000) are required in order to obtain a reliable result (Vanderbilt et al., 1979; Caldwell et al., 1983; Jonckheere et al., 2004). A derivation from this method is the needle technique for sampling litter. A needle of 1 - 2 mm in diameter is stuck vertically into the litter and the number of leaves collected on the needle corresponds to LAI. This method also requires intensive sampling to quantify LAI correctly (Dufrêne and Bréda, 1995; Bréda, 2003).

The disadvantage of all direct methods is that they are mostly destructive as well as extremely expensive. Because of this time-consuming and labor-intensive character, direct LAI determination is not compatible for long-term monitoring of spatial and temporal LAI dynamics (Jonckheere et al., 2004). However, as they can account for leaves which are located above each other, and as they solely relate to foliage but no other vegetation elements such as flowers or stems, they are the only approaches which give access to real LAI. Therefore, direct LAI derivation methods provide the reference for calibration and validation of indirect methods. As in most studies working on crops or grassland, in this thesis the scanning of leaves as well as the derivation of a grassland SLA is used to measure real LAI.

2.1.2. Indirect measurement methods

Indirect methods derive LAI from observations of other variables and are generally faster, feasible to automation, and thus allow for larger areas to be measured (Jonckheere et al., 2004). They are based on radiation transfer theory, which is shortly outlined below due to its relevance for the LAI derivation approaches tested in chapter 4.3.2, and for the functioning of RTMs. Afterwards, the instrument used in this thesis (the LAI-2000), as well as further popular measurement devices are introduced to provide an overview. The inherent limitations of indirect methods are finally explained as they also affected the *in situ* measurements in this thesis.

Radiation transfer theory

As incident light travels through the canopy, it is intercepted by plants. In this regard, the attenuation of downward radiation corresponds to the vertical depth and structure of the canopy (Saeki, 1975). Because radiative transfer and canopy structure are linked in this way, information about one can be used to predict the other. Thus, relatively simple radiation measurements can be used to estimate structural quantities of the canopy (Ross, 1981; Welles, 1990). The basic principle is the simulation of light transmission through the canopy using statistical models that describe the probability of radiation interception. Under the assumptions that leaves are randomly distributed within the canopy, that individual leaf size is small compared to the canopy height, and that radiation is measured at wavelengths where leaves are opaque (i.e. non-reflecting and non-transmitting), transmittance is equivalent to gap fraction (Lang, 1986). Gap fraction is the fraction of view looking up from beneath the canopy at a given zenith angle that is not blocked by foliage (Baret et al., 1995).

A statistical model describing transmittance can eventually be inverted to calculate LAI if gap fraction information for a range of angles is available (Norman and Campbell, 1989). Though several probabilistic models are in use to approximate the distribution of foliage elements, gap fraction probability is most commonly described by a Poisson distribution, as no additional parameters for the description of canopy structure are needed (Monsi and Saeki, 1953). Other theoretical models of vegetation structure are positive and negative binominal models and Markov models (see Nilson, 1971 for more details). The Poisson model assumes that the canopy is divided into n statistically independent layers. If $n \rightarrow \infty$, the probability of gaps decreases and can be described by the Poisson distribution. Gap fraction is therefore the probability $\mathrm{P}(\theta)$ of light transmitting the canopy, i.e. of zero layer overlaps (Lang et al., 1985):

$$\mathrm{P}(\theta) = \mathrm{e}^{-\mathrm{G}(\theta)\mu\mathrm{S}(\theta)} \tag{2.1}$$

with $\mathrm{G}(\theta)$ being the fraction of leaf area projected in the direction of the zenith angle θ, μ being the foliage density and $\mathrm{S}(\theta)$ being the length of the light path in the direction θ. According to Miller (1967), the foliage density μ is

$$\mu = 2 \int_{0}^{\pi/2} -\frac{\ln P(\theta)}{S(\theta)} \sin\theta d\theta \tag{2.2}$$

with $d\theta$ being the angle width in the direction θ. Assuming a homogeneous horizontal canopy, the path length $\mathrm{S}(\theta)$ can be derived by

$$S(\theta) = \frac{h}{\cos\theta}\,. \tag{2.3}$$

As the vegetation height h can be set to one, $\mathrm{S}(\theta)$ becomes a relative path length depending on the angle θ (Welles, 1990). With the foliage density relating to the LAI by

$$LAI = \mu h, \tag{2.4}$$

Equation 2.1 can be written as

$$\mathrm{P}(\theta) = \mathrm{e}^{-\mathrm{G}(\theta)\frac{\mathrm{LAI}}{\cos(\theta)}}. \tag{2.5}$$

Based on the approach by Miller (1967), LAI can be derived from Equation 2.5 without a prior knowledge of $\mathrm{G}(\theta)$ as

$$LAI = 2\int_{0}^{\pi/2} -\ln P(\theta) \cos\theta \sin\theta d\theta\cdot \tag{2.6}$$

Equation 2.6 shows that LAI can be mathematically derived by measuring the gap fraction over several zenith angles θ. Several measurement methods that rely on this approximation are described below. While gap fraction-based methods (e.g. hemispherical images) measure gap fraction directly, transmittance measurement devices (e.g. LAI-2000) make use of the

Beer-Lambert extinction law to estimate gaps (Bréda, 2003; Jonckheere et al., 2004). Measurement inaccuracies and unfulfilled model assumptions that hamper indirect LAI estimation methods are discussed at the end of this chapter.

LAI-2000, DEMON, ceptometers

There are four commercial canopy analyzers available to optically measure the transmittance in canopies. The instruments which are most widely used is the LAI-2000 Plant Canopy Analyzer (PCA) (LI-COR Biosciences, Lincoln, NE, USA, see Figure 2-4) and its successor LAI-2200 PCA. This is a portable sensor system designed to derive transmittance by relating the irradiation of diffuse light measured below the canopy to the diffuse irradiation measured above the canopy (LI-COR, 2009). The field of view of the optical hemispherical sensor head is divided into five concentric light-detecting silicon rings i, thus having five constant θ values. There are several approaches implemented in the LAI-2000 to derive LAI from transmission measured in these rings (see chapter 4.3.2). The LAI-2000 PCA has been successfully used in a number of studies, especially in homogeneous canopies such as crops and grassland (Gower and Norman, 1991; Dufrêne and Bréda, 1995; Levy and Jarvis, 1999; Lee et al., 2004; Gonsamo Gosa et al., 2007; Darvishzadeh et al., 2008b; Garrigues et al., 2008b; Vuolo et al., 2010; Tang et al., 2014), and it is also used in this thesis. It is a popular device as it does not require additional data acquisition and is able to provide LAI instantaneously. Further, the simultaneous measurement of radiation at different angles reduces the workload. A potential weakness of the LAI-2000 is the requirement of above-canopy readings (Kraus, 2008). However, in contrast to tall stands, alternating below- and above-canopy measurements can be easily performed in grassland. Further, LAI-2000 measurements should only be taken under diffuse irradiance, reducing the possible operating time. For more details on the functioning and handling of the LAI-2000, see chapter 4.3.2.

The DEMON instrument (CSIRO, Canberra, Australia) adapts the basic functioning from the above mentioned point quadrat method (Wilson, 1960). It measures direct beam radiation above and below the canopy through a directional narrow angle of view, thereby replacing the needle (Welles, 1990). DEMON measurements have to be conducted under clear conditions and repeated several times over the day to collect data over a range of sun zenith angles (Dufrêne and Bréda, 1995). In tall canopies, the operator moves beneath the canopy along a linear path, directing the instrument to the sun. In crops, the sensor is driven along a track beneath the canopy. The DEMON instrument has been reported to derive similar results as the LAI-2000 (Dufrêne and Bréda, 1995). However, the requirement of repeated measurements over the day reduces its applicability if many plots have to be investigated.

Figure 2-4: The LI-COR LAI-2000 Plant Canopy Analyzer (Source: LICOR, 2005)

The SunSCAN (Delta-T Devices Ltd, Cambridge, UK) as well as the Sunfleck Ceptometer and its successor AccuPAR LP-80 Ceptometer (Decagon Devices Inc., Pullman, WA, USA) are sensitive to incident photosynthetic active radiation (PAR, 400 - 700 nm). They are also known as line quantum sensors, as they are equipped with a linear probe that has several (64 to 80) individual photodiodes (Welles, 1990). Like the other optical devices, they derive the transmitted PAR by relating readings above and below canopy, but recorded at several of the available sensors on the bar at a time. LAI is calculated based on PAR, the sun zenith angle, and an estimate of the leaf angle distribution provided by the user in a simple light scattering model (Wilhelm et al., 2000; Tewolde et al., 2005; Decagon Devices, 2013).

Hemispherical photographs

A straight approach to deriving canopy gap fraction is to visually identify it in a photograph. In doing so, photographs of single directions (see e.g. Macfarlane et al., 2007; Baret et al., 2010b) as well as of the hemisphere can be used. In digital hemispherical photography (DHP), photographs are acquired through a fisheye lens from within the canopy oriented upwards, or placed above the canopy looking downwards (Rich, 1990; Jonckheere et al., 2004). A circular image is produced, with the zenith in the center and the horizon at the edges (see Figure 2-5 a) (Goel and Norman, 1990; Rich, 1990). To represent the canopy structure adequately, several images should be taken within one plot, and under diffuse light and uniform sky conditions, to avoid sun glares, chromatic lens aberration, foliage reflections, and sky luminance heterogeneity (Neumann et al., 1989; Weiss et al., 2004). The selections of exposure time and shutter speed are also critical steps, as they influence the image's brightness and contrast (Zhang et al., 2005b; Macfarlane et al., 2007). In downward-looking images taken e.g. over dense grassland, shaded areas impede the identification of gaps. The use of infrared light measurement (see e.g. Kucharik et al., 1997) can reduce this limitation (Rich, 1990; Welles, 1990). Through the classification of the photographs, the soil/sky and canopy elements are distinguished. Several tools have been developed for this purpose, e.g. the CAN-EYE software (Weiss and Baret, 2010), HemiView PCA (Delta-T Devices, Cambridge, UK), and Gap Light Analyzer (GLA, Frazer et al., 1997). A range of image classification algorithms have been proposed and discussed in the literature, with the most common approach being interactive or automatic thresholding, i.e. the selection of a brightness value which is used to differentiate the classes (Leblanc et al., 2005; Wagner and

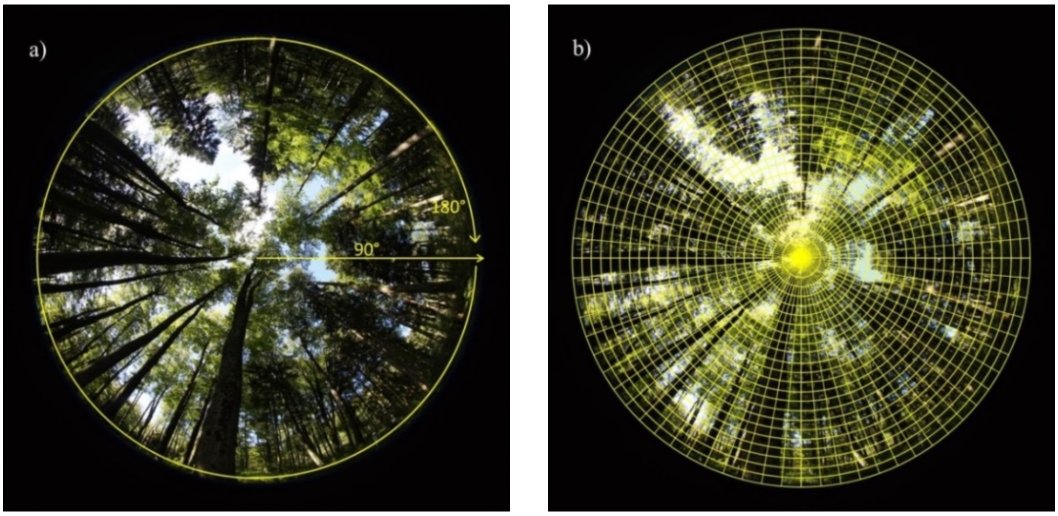

Figure 2-5: Hemispherical photograph taken on September 9, 2011 near the Fendt measurement site. a) Illustration of the angular field of sight. b) Subdivision of hemisphere into regular segments in order to derive gap fraction information for individual viewing directions.

Hagemeier, 2006; Macfarlane et al., 2007; Englund et al., 2000; Jonckheere et al., 2005). After classification, the hemisphere is subdivided into regular segments to exploit different directions concurrently (Figure 2-5 b), and gap fraction is extracted in each segment. Canopy parameters such as LAI, leaf angle, and gap frequency distributions are subsequently derived by inverting Equation 2.6 (Norman and Campbell, 1989; Weiss et al., 2004).

Although there are many steps involved in deriving LAI from DHP, there has been a renewal of interest in this method with the development of high resolution digital cameras and advances in image processing software. Its advantages are low purchase costs and the rapid picture acquisition in the field. One of the most important assets is the high amount of information recorded (gap fraction, size and distribution), which enables the use of different light extinction models. A further advantage is the possibility of detecting green and non-green elements (Jonckheere et al., 2004; Kraus, 2008). Several authors have successfully used DHPs for studies in forests (Neumann et al., 1989; Chen et al., 1997; White et al., 2000; Jonckheere et al., 2004; Leblanc et al., 2005; Macfarlane et al., 2007), while the approach is less often used in crops (e.g. Garrigues et al., 2008b) or grassland due to the above mentioned shadows and an insufficient plant-soil contrast (Demarez et al., 2008).

Limitations of indirect LAI measurement methods

A large number of studies compare the results of direct and indirect measurement techniques for crops (Levy and Jarvis, 1999), shrubs (Brenner et al., 1995), and forest stands (Neumann et al., 1989; Chason et al., 1991; Smith, 1993; Fassnacht et al., 1994; Comeau et al., 1998; Barclay and Trofymow, 2000), with some of them revealing great differences. The main factor causing errors in indirect LAI measurements is the result of most canopies deviating from the assumption behind the Poisson model of random foliage dispersion, i.e. clumping of vegetation elements (Figure 2-6). Clumping results in higher canopy transmittance than predicted for random canopies, and thus in LAI underestimation (Black et al., 1991; Fassnacht et al., 1994; Chen and Cihlar, 1995). Therefore, indirectly derived LAI has been named *effective LAI* (LAI_{eff}) by Chen et al. (1991). LAI_{eff} is defined as the product of LAI and a clumping index Ω (Nilson, 1971; Macfarlane et al., 2007; Ryu et al., 2010).

Several approaches have been suggested to overcome this issue. It would be straight-forward to incorporate the non-random distribution of plant elements in a probabilistic model underlying the inversion process. A canopy consisting of non-randomly distributed leaves could be described more adequately by binomial models or Markov models (Nilson, 1971). However, these models require additional information on leaf angle or gap distribution within the canopy, which is not measured by the devices presented above (Chason et al., 1991). Lang and Xiang (1986) proposed to correct for clumping at plant level by modifying

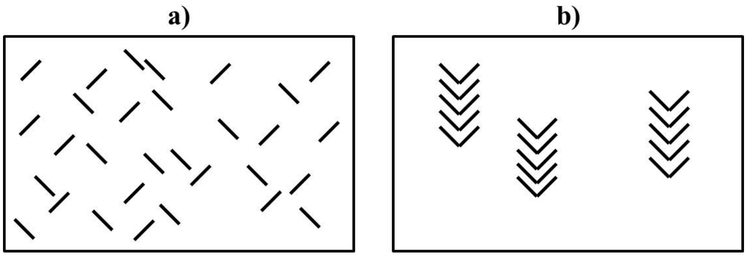

Figure 2-6: Illustration of the clumping effect with leaves being either randomly distributed or arranged to shoots. While the same amount of leaves is present, the gap fraction in b) is bigger than in a), leading to an underestimation of LAI using indirect measurement techniques (adapted from Nilson, 1999).

the use of the Beer-Lambert law. The basic assumption is that the required random distribution of foliage is fulfilled when looking at a small part of the canopy. Lang and Xiang (1986) showed that if multiple transmittance measurements are made in small sectors and combined by averaging the logarithms of the transmittances, an improved LAI can be derived. Instead of using the logarithm of the mean of $P(\theta)$ over all azimuth ranges, the logarithm of $P(\theta)$ for each sector is averaged (Ryu et al., 2010). Equation 2.6 hence becomes

$$LAI = 2\int_0^{\pi/2} -\overline{\ln P(\theta)}\cos\theta\sin\theta d\theta \tag{2.7}$$

The clumping parameter Ω is then provided by the ratio of Equation 2.6 to Equation 2.7. This method is implemented in the LAI-2000 algorithm. Chen and Cihlar (1995) developed another procedure for deriving Ω based on gap fraction, size and distribution using the Tracing Radiation and Architecture of Canopies (TRAC) instrument (3rd Wave Engineering, Ontario, Canada; Kucharik et al., 1997; Chen et al., 1997; Chen et al., 2002b). Further development of this method has been conducted by Leblanc (2002), who normalized Ω, and by Leblanc (2004) in developing a software which connects the TRAC to fisheye photographs. Leblanc et al. (2005) finally combined the gap size distribution theory with Lang's and Xiang's method. The TRAC can also be used in combination with the LAI-2000 (Chen et al., 1997), but care has to been taken not to overcorrect clumping by using TRAC together with the LAI-2000 output, which is already corrected (Ryu et al., 2010). Some authors (Chen et al., 1991; Fournier et al., 1997) indicated that clumping occurs at several scales, i.e. between plants, branches and shoots. For that reason they divide the clumping factor into two components, a between-shoots clumping factor Ω_e and a within-shoot clumping factor γ_e. The γ_e values of Gower et al. (1991) are implemented in the LAI-2000 software.

Apart from the clumping issue, another characteristic of most measurement devices is that they cannot distinguish between leaves and non-photosynthetically active plant parts such as branches, flowers, or fruits. In fact, indirect methods do not measure leaf area, as all canopy elements intercepting radiation are included. Therefore, the terms "Plant Area Index (PAI)" (Neumann et al., 1989), "Vegetation Area Index" (Fassnacht et al., 1994), "Foliage Area Index" (Welles and Norman, 1991), or "Surface Area Index" (Bréda, 2003) are sometimes used. Some studies tried to derive true LAI by measuring the "Wood Area Index" (WAI) in deciduous forests in winter (e.g. Neumann et al., 1989; Cutini et al., 1998; Barclay et al., 2000). However, a simple subtraction of WAI from PAI does not equal LAI, as the contribution of woody material to LAI at its maximum is far less than WAI (Dufrêne and Bréda, 1995; Gower et al., 1999). On the other hand, WAI which is derived during vegetation maximum (e.g. from photographs) cannot simply be subtracted, due to leaves that are obscured by the stems. Macfarlane et al. (2007) suggest that the use of upward-looking photographs would reduce the influence of woody material, because stems contribute little to LAI at the zenith. As a further drawback, most transmittance measurement instruments reach an asymptotic signal saturation level in dense canopies (Gower et al., 1999). Finally, indirect methods do not account for leaves that lie on top each other and essentially act as one leaf.

Due to these issues, most comparisons between direct and indirect methods point to an underestimation of LAI by 25% to 50% in different ecosystems with the latter techniques (Gower and Norman, 1991; Fassnacht et al., 1994; Stenberg et al., 1994; Cutini et al., 1998; Comeau et al., 1998; van Gardingen et al., 1999; Gower et al., 1999; Küßner and Mosandl, 2000; Macfarlane et al., 2000; Wilhelm et al., 2000). A measurement device which overcomes this restriction is still not available. In RS, *in situ* measurements are indispensable for the validation of LAI estimates. It can be thus concluded that a sound measurement technique and sampling design as well as correction for clumping are crucial when measuring LAI, and that a comparison of directly and indirectly measured LAI is advised to assess the accuracy of indirect *in situ* measurements.

2.2. Estimation of LAI from remote sensing data

The spectral signal recorded over vegetation results from radiative processes within canopies, depending on plant parameters and observation configurations. This relationship enables the derivation of LAI from spectral vegetation properties. The two most common approaches to retrieve LAI, the empirical-statistical (subchapter 2.2.2) and the physical approach (subchapter 2.2.3), are presented here. The concepts and some examples of all relevant methods for LAI estimation are presented, while the specific details of the methods applied in this study are discussed in chapters 5 and 6. Beforehand, an overview of basic terms and the theoretical background of solar-reflective RS of vegetation is given (subchapter 2.2.1), as these processes also constitute the basis of RTMs.

2.2.1. Theoretical background of vegetation remote sensing

RS is the science and technology of deriving information about an area of interest without being directly in contact with it. A sensor is used to measure the energy emitted or reflected by a surface. A detailed description of the physical principles of optical RS is given in Richards and Jia (2006) and Asrar (1989). Only the most relevant aspects of RS for radiation transfer in vegetation canopies are explained here.

Basic terms

The physical quantity that is measured by an RS sensor is the electromagnetic *radiant flux* ϕ emitted or reflected by an object. The total amount of radiation incident on a surface, i.e. the flux density per area, is called *irradiance* E, with E_{sun} being used for direct solar irradiance, and E_{sky} for diffuse hemispherical irradiance. When only the irradiance coming from a certain direction is considered, it is called *radiance* dL and expressed as flux density per unit projected area and unit solid angle. By relating radiance measured at the sensor to the irradiance at the surface, *reflectance* ρ_{λ} can be derived, which is commonly used to describe the spectral properties of surfaces. The reflectance factor R_{λ} of each wavelength λ is the ratio of the radiant flux reflected by a surface to that reflected into the same direction by a 100 % reflecting surface (Martonchik et al., 2000; Schaepman-Strub et al., 2006).

Optical RS systems record energy from around 400 to 2500 nm that is emitted from an external illumination source, such as the sun or the target itself. This wavelength range can be subdivided into visible (VIS; 400 - 700 nm), near infrared (NIR; 700 - 1300 nm) and shortwave infrared (SWIR; 1300 - 2500 nm) radiation. The energy measured at the sensor is integrated over wavelength intervals. The number and width of these bands defines the spectral resolution of the system (Richards and Jia, 2006). The spatial resolution of the sensor is defined as the smallest distance between two objects that can be distinguished by the sensor. Although spatial resolution is defined quite differently in the literature (e.g. Franklin and Wulder, 2002; Navulur, 2006) and no standard definition exists, here RS systems are divided into very high resolution (with a resolution $\leq$ 1 m), high resolution (1 < 20 m), medium resolution (20 < 100 m), and coarse resolution ($\geq$ 100 m) systems.

The spectral signal coming from a vegetation surface is a combination of scattering, absorption, and emission processes that take place in the atmosphere and on the surface. According to Goel (1988) and Kimes (2000) the reflectance factor R_λ detected by a sensor is determined by the properties of the atmosphere (a_λ), background (b_λ), the optical and structural plant properties of the canopy (c_λ), the solar source parameters (s_λ) including the angular location (θ_s, φ_s), and the sensor properties (o_λ) including the view angle (θ_o, φ_o)[4]:

$$R_\lambda = f(a_\lambda, b_\lambda, c_\lambda, s_\lambda, o_\lambda) \tag{2.8}$$

In this chapter, soil reflectance is not explicitly discussed. The influence of the soil is wavelength-dependent and largest in the near infrared region (see Figure 2-7). Soil reflectance is dominated by soil composition, roughness and moisture content, although also plant residues, litter, and organic and salt crusts can contribute to it. See Verhoef and Bach (2007), Cierniewski and Verbrugghe (1997), or Farys (2003) for more details. Thus, when looking only at processes within the canopy, R_λ is a result of incident light that interacts with pigments, water, and intercellular air parcels within plant elements. These processes as well as directional and atmospheric effects are discussed in below.

Leaf optical properties

A typical signal of healthy green vegetation is dominated in the VIS by overall low reflectance values but a small peak in the green region (see Figure 2-7). This strong absorption is caused

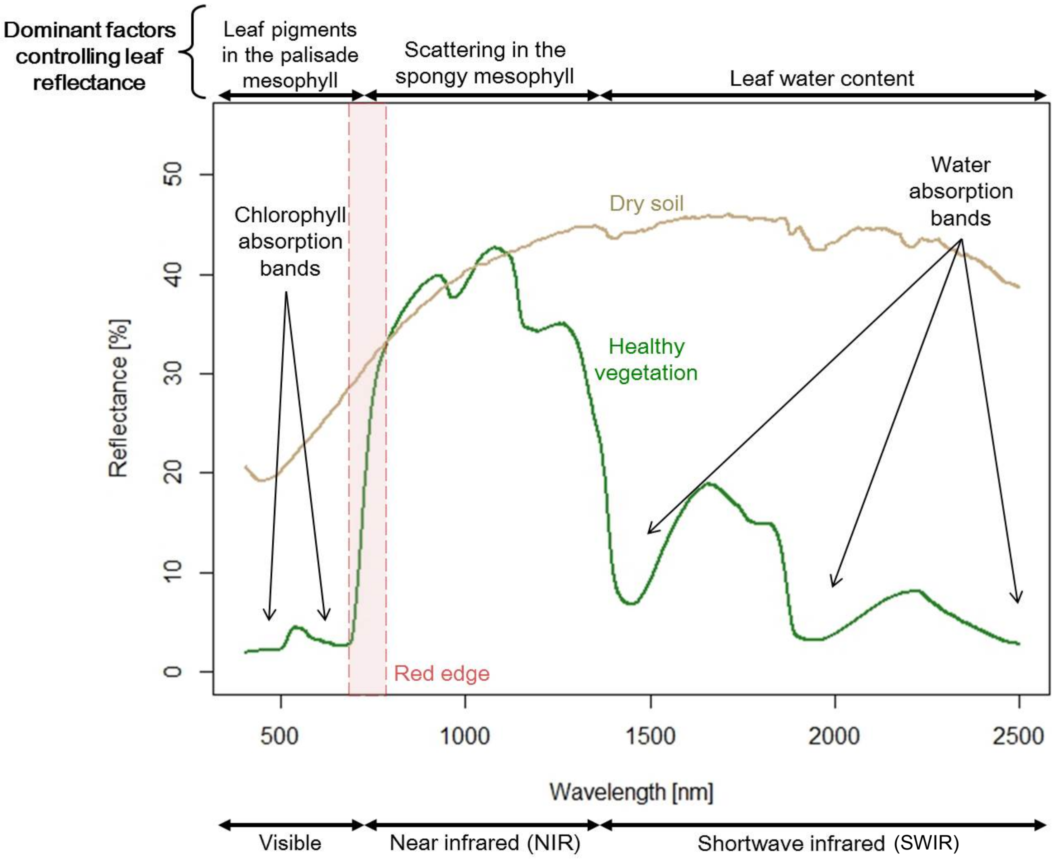

Figure 2-7: Typical spectral signals of soil and healthy green vegetation. Figure adapted from Jensen (2000), data generated using PROSAIL (Verhoef et al., 2007).

---

[4] The zenith angles of the sun (θ_s) and the sensor (θ_o) are measured relative to nadir, i.e., a zenith angle of 0° is equal to nadir, while the horizon has a zenith angle of 90°.

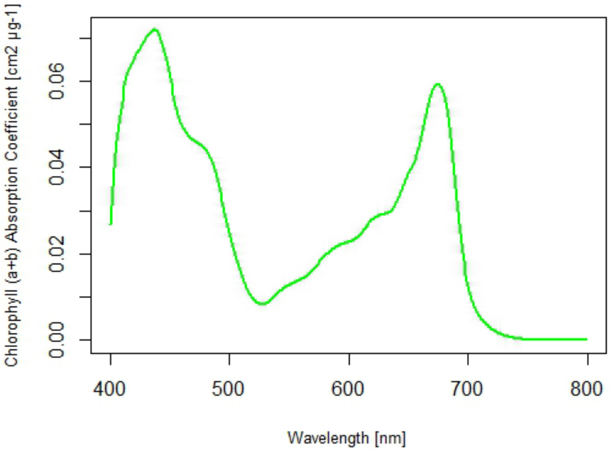

Figure 2-8: Chlorophyll a + b absorption coefficient in the VIS and NIR spectrum as implemented in the PROSAIL model. Adopted from Feret et al. (2008).

by leaf pigments relevant for photosynthesis, namely chlorophyll pigments concentrated within the palisade mesophyll cells (Jones and Vaughan, 2010). Photons are absorbed by chlorophyll a + b molecules, yet only the PAR between approximately 350 and 700 nm is used for photosynthesis. Chlorophyll absorbs mainly blue and red light (see Figure 2-8): chlorophyll a at wavelengths of 430 and 660 nm and chlorophyll b at 450 and 650 nm (Wellburn, 1994). The lack of absorption in between the chlorophyll bands produces a relative maximum around 540 nm, i.e. in the green spectral range, which explains the natural color of plants (Richards and Jia, 2006). There are also other pigments present in mesophyll cells that are masked in healthy vegetation by the abundance of chlorophyll pigments (Jacquemoud and Baret, 1990). The most important are carotenes and xanthophyll pigments with an absorption maximum in the blue wavelength region. As for brown pigment, their concentration increases with the decay of a plant (Jacquemoud and Baret, 1990; Féret et al., 2008).

In contrast to the VIS part of the spectrum, reflectance and transmittance increases strongly in the NIR part. This strong increase between red and NIR canopy reflectance is called the red edge region (Baret et al., 1992). The high amount of reflected NIR energy is caused by high leaf surface reflectance as well as by the cell structure of the spongy mesophyll with its intercellular air spaces causing scattering at the cell wall/air interfaces (Gausman et al., 1969). Another reason for the high NIR reflectance is the fact that energy transmitted through the leaf (about 40 - 60 % of irradiance) can be potentially reflected by leaves below. Thus, NIR reflectance increases with the number of leaf layers. This so-called leaf additive reflectance enables NIR reflectance to distinguish vegetation densities and to provide 3D information about the canopy. This is of high value for optical vegetation monitoring.

In the SWIR, tissue materials (e.g. lignin, protein, cellulose) dominate absorption and lead to a decreased reflectance with respect to the NIR plateau. Especially strong local reflectance reductions are caused by water absorption bands at 1400 nm, 1900 nm and 2700 nm. Based on this, RS in the NIR, SWIR, and thermal infrared can provide information about the plant turgidity. While all these properties describe healthy vegetation, senescence is marked by an overall reflectance increase. As leaf structure decomposes, it gives room to extra intra-leaf scattering in the NIR. At the same time, reduced chlorophyll content increases VIS reflectance and unmasks the characteristics of the other leaf pigments, leading to a flattening of the red edge. Reflectance in the SWIR increases due to reduced water content. Thus, the spectral shape of senescent vegetation gradually approximates that of soil.

Canopy structure

The spatial configuration of plants in a canopy determines the magnitude and the directional variation in reflectance over all wavelengths. Therefore, the most important canopy structure characteristics are briefly presented. Canopy architecture is described at the plant level through LAI and the leaf angle distribution (LAD). LAI represents the quantity of leaves. As scattering and absorption within the canopy increases with LAI, canopy reflectance changes accordingly. However, Haboudane et al. (2004) showed that incoming radiation does not reach lower leaves at LAI values greater than 3 and 5 for the VIS and NIR, respectively. This means that no light reflected from more leaves can contribute to the spectral signal, leading to so-called signal saturation over dense canopies (Baret and Guyot, 1991).

The LAD describes the distribution of leaf inclination and orientation angles and is often also indicated as leaf inclination distribution function (LIDF), average leaf angle (ALA) or mean tilt angle (MTA). While the distribution of leaf azimuth angles is usually assumed to be uniform, zenith angle distributions are often mathematically described by one of six LAD types: planophile, erectophile, plagiophile, extremophile, uniform, or spherical (see Figure 2-9, Wit, 1965). The spherical foliage orientation is popular because the fraction of projected area is always 0.5 (Welles, 1990). Goel and Strebel (1984) showed that all of these ideal distributions are special cases of a “universal” distribution, the “two parameter beta distribution”. Campbell (1986) equated the LAD to the surface of an ellipsoid which can be continuously derived by varying the ratio between its two principle axes. This is a less flexible but more intuitive one-parameter approach. For a detailed description of LAD functions, see Liang (2004) or Wang (2007). The LAD varies among vegetation species, and sometimes also with phenological stages and stress (Wirth et al., 2001; Medhurst and Beadle, 2001). It plays a prominent role in any description of canopy structures and thus in RTMs (Welles, 1990).

The canopy structure is described through the relationship between LAI and LAD, but also leaf size, plant density, canopy height, and canopy heterogeneity (Verhoef, 1984; Widlowski et al., 2004). Examples of a heterogeneous vertical canopy profile are forest canopies with litter, understory vegetation, and several tree layers, or cereal crops with a top layer of fruit, a green leaves layer, and a bottom layer of senescent material. A strong horizontal

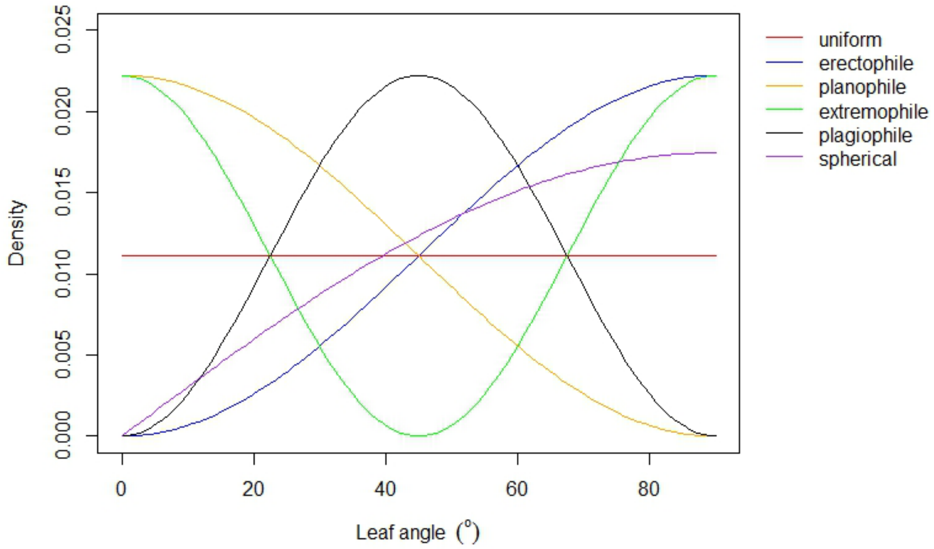

Figure 2-9: Common leaf angle distributions: uniform, erectophile, planophile, extremophile, plagiophile, and spherical distribution functions. Plot generated using the ‘LeafAngle’ R package provided by Duursma (2012).

heterogeneity is found in open forest canopies or row crops. Although such heterogeneities are highly important, they are not further described as this thesis investigates solely grasslands, which show no horizontal or vertical structure profiles.

BRDF effect

The directional behavior of leaf, canopy, and soil reflectance has already been mentioned above. Reflectance of a surface depends on the sun and sensor angles relative to the target as most terrestrial surfaces are not isotropic. Isotropic surfaces, also called “Lambertian”, reflect incoming light equally in all directions. In vegetation canopies, anisotropy is mainly caused by surface roughness, foliage orientation, shading, and gaps (Roujean, 2002). Figure 2-10 illustrates the geometries resulting from the orientation of the sun (θ_s,φ_s) and of the observer (θ_o,φ_o) to the target (Kimes, 1983; Sandmeier and Itten, 1999). Due to this twofold dependency on illumination and viewing angles, anisotropic reflectance is characterized as “bidirectional”. The mathematical description of the hemispheric scattering of incident light over all combinations of illumination and viewing angles is the bidirectional reflectance distribution function (BRDF) (Martonchik et al., 2000; Lillesand and Kiefer, 2000). The BRDF f_r is formally defined as the ratio of the radiance dL (W m^{-2} sr^{-1} nm^{-1}) reflected in one direction (θ_o,φ_o) to the sun’s incident irradiance dE_{sun} (W m^{-2} nm^{-1}) from the direction (θ_s,φ_s) for each wavelength λ (Sandmeier and Itten, 1999):

$$f_r(\theta_s, \varphi_s;\ \theta_o,\ \varphi_o; \lambda) = \frac{dL(\theta_s, \varphi_s;\ \theta_o,\ \varphi_o; \lambda)}{dE_{sun}(\theta_s, \varphi_s; \lambda)} \tag{2.9}$$

Since both dL and dE_{sun} are defined in terms of infinitesimal solid angles, and since natural irradiance does not consist of a single direction, f_r cannot be measured, making it a useful but non-measurable concept (Schaepman-Strub et al., 2006). Instead, the BRDF is assumed to be retrievable from actual bi-conical radiance measurements made over a small solid angle. Thus, if using an ideal Lambertian surface (i.e. a Spectralon panel) as reference dL_{ref}, for which the BRDF is 1/π, a dimensionless bidirectional reflectance factor (BRF) can be derived for each wavelength and angle combination from the radiant flux dL actually

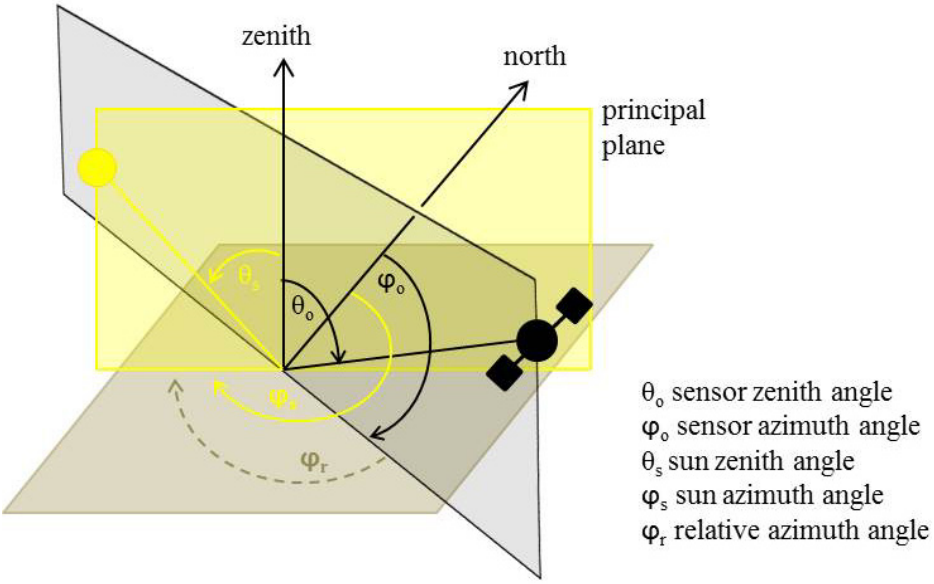

Figure 2-10: The geometry of solar irradiance and observer viewing direction. The amount of reflected radiance depends on the zenith (θ_o) and azimuth (φ_o) angles of the observer and on the zenith (θ_s) and azimuth (φ_s) angles of the sun with respect to the target. For modeling purposes, the relative azimuth angle (φ_r) between the sun and the sensor is often used.

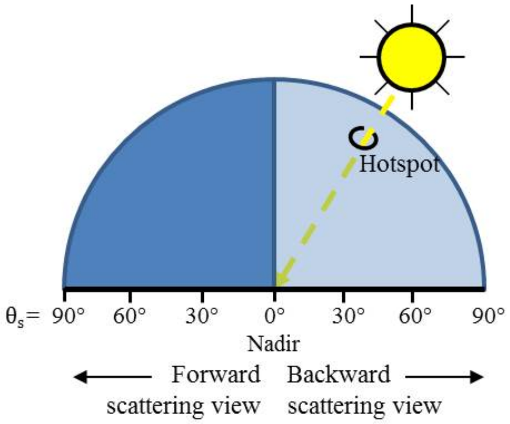

Figure 2-11: Principle of forward and backward scattering.

reflected from a surface in a specific direction (Sandmeier and Itten, 1999):

$$BRF = R(\theta_s, \varphi_s;\ \theta_o,\ \varphi_o; \lambda) = \left[\frac{dL(\theta_s, \varphi_s;\ \theta_o,\ \varphi_o; \lambda)}{dL_{ref}(\theta_s, \varphi_s;\ \lambda)}\right] \times R_{ref}(\theta_s, \varphi_s;\ \theta_o,\ \varphi_o; \lambda) \tag{2.10}$$

The hemispherical-directional reflectance factor (HDRF) is similar to the BRDF, but assumes additional diffuse sky illumination from the hemisphere. HDRF thus depends on atmospheric conditions and reflectance of the surrounding terrain (Martonchik et al., 2000).

Depending on the viewing and illumination geometry, surfaces appear brighter or darker. Broadly, the bidirectional reflectance can be distinguished in backward and forward scattering (Figure 2-11). This distinction is described by the relative azimuth angle φ_r. In backward scattering view, when the surface is seen from the same side at which it is illuminated (i.e. $\varphi_r < 90°$), most of the shadows are hidden and the terrain appears brighter. In forward scattering mode, the sun and the viewer are on opposite sides (i.e. $\varphi_r > 90°$) and surfaces seem darker. The so-called solar principal plane is formed when the sun, the target, and the sensor are in the same plane (i.e. $\varphi_r = [0°, 180°]$). This is where BRDF effects are most pronounced. The overall highest BRF occurs in the viewing direction that is equal to the sun azimuth and zenith angles, due to the fact that the sensor views only sunlit surfaces. This area of increased reflectance is called *hot spot* (Kuusk, 1995a; Lillesand and Kiefer, 2000).

In the nadir view, a maximum of the background can be seen by the sensor, particularly over canopies with a vertical structure such as grasses or conifer forests (Sandmeier et al., 1998; Sandmeier and Deering, 1999). These canopies show a very strong anisotropy effect, due to the quickly changing fraction of soil seen by the sensor with changing view angles, and they have a typical bell shape of the BRF in the principle plane. Canopies having a predominant horizontal structure have a rather bowl-shaped anisotropy (Widlowski et al., 2004; Widlowski et al., 2005; Koetz et al., 2005b). Further, the BRDF varies considerably with wavelength. In the blue and red spectra, BRDF effects are strong, while they are less pronounced in the green and most of the NIR ranges because multiple scattering reduces the contrast between shadowed and illuminated canopy components (Sandmeier et al., 1998).

The BRDF effect is relevant for sensors with a large instantaneous field of view (IFOV[5]) or for sensors that provide off-nadir measurements. Furthermore, the BRDF is crucial for multi-temporal studies with varying illumination angles, as the spectra measured at different points

---

[5] IFOV is the angle over which the detector records radiation. Together with the platform altitude, this controls the pixel size.

in time cannot be directly compared (Jensen, 2000). VIs (see chapter 2.2.2) can also be biased by the BRDF effect. Overall, the incorporation of the BRDF is essential when the detailed comparison of surface reflectance data is concerned.

Atmospheric and topographic influences

As can be seen from Equation 2.8, radiance which reaches the sensor is not only influenced by surface properties, but also by processes occurring during the downward and upward transfer of radiance through the atmosphere. Molecular and aerosol scattering and absorption contribute to the measured radiance, especially at shorter wavelengths (Richter and Schläpfer, 2012). The radiance L that actually reaches the sensor consists of three components:

$$L = L_{path} + L_{pixel} + L_{adj} \tag{2.11}$$

with L_{path} being the photons scattered into the sensor's IFOV without having ground contact, and L_{adj} being radiance originating from the land surface surrounding a pixel but scattered by air into the instantaneous direction ('adjacency effect', see Figure 2-12). The surface information L_{pixel} that is of interest for RS analysis is masked, as it were. In areas of rugged terrain, an additional radiation component is the radiance reflected from the terrain to the detected pixel (L_{ter} in Figure 2-12). Furthermore, the terrain introduces variations to the spectral signals recorded over a certain surface as it changes the local viewing and illumination geometry. In areas with steep slopes, the local solar zenith angle (i.e. the angle between the sun zenith angle and the slope surface normal) may vary over a wide range (0 - 90°) and thus creates areas with maximum solar irradiance as well as with zero direct irradiance, i.e. shadowed areas (Richter and Schläpfer, 2012).

For a meaningful comparison of surface reflectances and RTM outputs, it is therefore indispensable to unmask the object spectral properties and thus to eliminate the influence of atmosphere and topography on the RS signal. Butson and Fernandes (2004) showed that an automated atmospheric correction with a fixed aerosol concentration used on different overlapping satellite images can lead to significant differences in the LAI retrieval, and that abandoning the atmospheric correction even slightly increases the consistency between the LAI maps. The proper correction of atmospheric effects is thus crucial, but at the same time

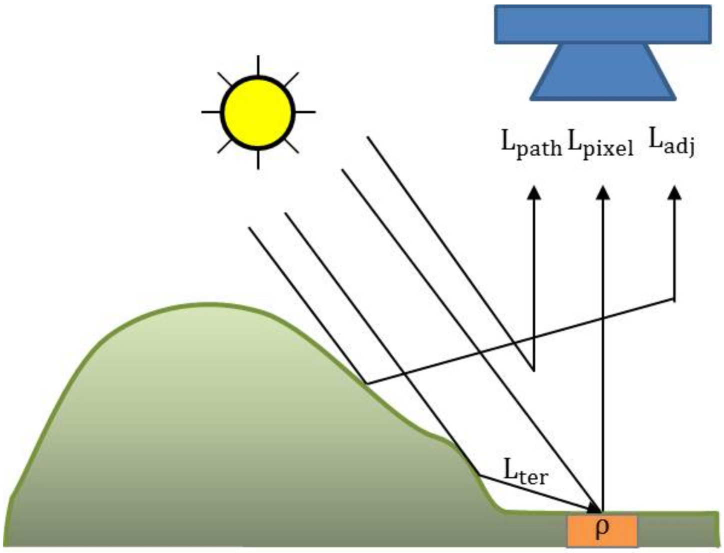

Figure 2-12: Radiation components in rugged terrain. Adapted from Richter and Schläpfer (2012).

runs the risk of introducing new errors to the RS data (see Mannschatz and Dietrich, 2013).

As the overall aim of atmospheric correction is the derivation of top-of-canopy (TOC) reflectances from remotely sensed top-of-atmosphere (TOA) radiances, an integral part is the conversion of radiance values to reflectances (see chapter 4.1.2). This is achieved by relating the radiance L at a certain earth-sun distance d to the extraterrestrial irradiance E from a solar zenith angle θ:

$$\rho_{TOA} = \frac{\pi \, d^2 \, L}{E \, cos\theta} \tag{2.12}$$

To account for the atmosphere influence, absolute or relative atmospheric corrections can be applied (Song et al., 2001). Absolute correction methods employ an atmospheric RTM that explicitly accounts for the optical properties of the atmosphere and models the resulting atmospheric transmittance τ and path radiance L_{path} (Gao et al., 2009). Based on equations 2.11 and 2.12, and disregarding the adjacency component, TOC reflectance can be derived by equation 2.13., which is a key formula of atmospheric correction:

$$\rho_{TOC} = \frac{\pi \, \{d^2 L - L_{path}\}}{\tau \, E} \tag{2.13}$$

To simulate the atmosphere transfer processes sufficiently well, scene acquisition conditions as well as atmosphere conditions need to be known. Information specifying the conditions of the scene (e.g. location coordinates, acquisition date and time, elevation data, viewing geometries) is mostly provided by the scene’s metadata. The atmosphere can be characterized by its aerosol type, water vapor content, or visibility. As the aerosol contribution is the most influential atmospheric component, aerosol optical depth (AOD), rather than visibility, is often used to characterize the atmosphere (Liang et al., 2001; Richter and Schläpfer, 2012). An ideal method of visibility or AOD determination would be to obtain atmospheric measurements at the time of sensor overpass, which is however rarely possible because aerosols are very variable in space and time. Therefore, this value is either estimated by the operator or derived directly from the used RS scene (Kaufman et al., 1997; Liang et al., 1997). The automatic derivation is most frequently performed over dark objects, as these are especially sensitive to AOD estimates because their reflectances become negative if the AOD is estimated too high. An accurate estimate of the main atmospheric parameters is necessary, because these influence the values of path radiance, transmittance, and global irradiance. The adjacency component is calculated in a second step by relating the average reflectance of the surrounding area to the ratio of the diffuse and direct transmissions and adding it to the term in equation 2.13 (Richter and Schläpfer, 2012).

A relative atmospheric correction is a simple and straight-forward statistical method that assumes a linear relationship between image bands across time, but does not account for individual radiance components. Examples are the invariant-object method, histogram matching, or contrast reduction. For empirical methods such as the empirical line approach, reflectance spectra field measurements are required (Liang et al., 2001; Gao et al., 2009).

2.2.2. Empirical-statistical LAI derivation

Empirical-statistical LAI derivation is one of the two approaches pursued in this thesis. It searches for a continuous relationship between the spectral signature of a canopy and LAI. Thereby a statistical model, also referred to as transfer function, relates LAI measured *in situ* to corresponding RS spectral information. The RS reflectance measurements are then

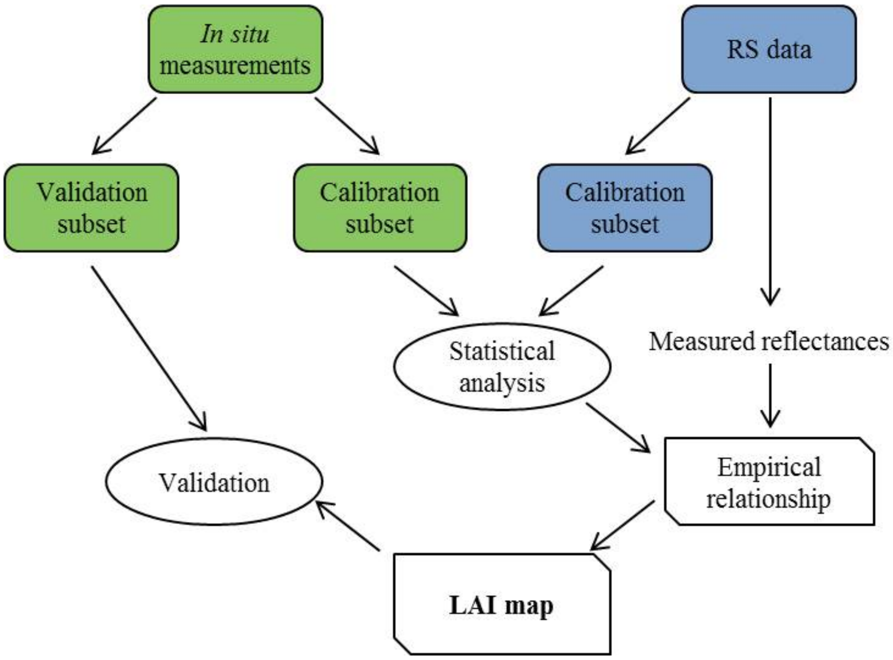

Figure 2-13: Schematic concept of the empirical-statistical approach. Adapted from Dorigo et al. (2007).

converted to LAI by inverting the transfer function (see Figure 2-13, Cohen et al., 2003a; Dorigo et al., 2007). In addition to the selected spectral information and transfer function described below, the accuracy and range of *in situ* measurements sampled for model training determine the validity of the derived map (Turner et al., 1999; Sims and Gamon, 2002).

Empirical-statistical approaches to derive properties of vegetation canopies have been in use since the early exploitation of satellite data in the 1970s (Weiss et al., 2000). Statistical LAI derivation was first used on crop canopies. One of the earliest attempts was carried out by Kanemasu (1974), who derived wheat LAI using Landsat MSS data. Recent studies on crop LAI have been published by Broge and Mortensen (2002), Colombo et al. (2003), Yang et al. (2007), or Ehammer et al. (2010). After investigations on crop LAI yielded promising results, LAI estimation for forests started in the 1980s. Since the first forest LAI mapping by Peterson et al. (1987), a high number of empirical studies have been conducted (see e.g. Chen and Cihlar, 1996; White et al., 1997; Turner et al., 1999; Cohen et al., 2003a; Fernandes et al., 2003; Kalácska et al., 2004; Soudani et al., 2006). With regard to grassland LAI, the number of studies is smaller. Since the BigFoot site in the Konza Prairie has been used for ecological research since 1980, several LAI studies focused on this tallgrass prairie (see e.g. Asrar et al., 1986; Turner et al., 1999; Cohen et al., 2003b; Lee et al., 2004; Cohen et al., 2006). Other studies using empirical relationships to derive grassland LAI are He et al. (2006), Frank and Karn (2003), Mutanga et al. (2004), or Vescovo and Gianelle (2008).

Vegetation indices

For the establishment of empirical relationships, the spectral signature is rarely directly used, as it is influenced by various factors (Equation 2.8). Therefore band reflectance is often transformed to enhance the spectral contribution of green vegetation while minimizing those from soil background, senescent vegetation, atmosphere, and variations in viewing geometry (Huete, 1989). Although several manipulations have been proposed (see Dorigo, 2007), the most common method is to mathematically combine spectral band reflectance to create a VI.

VIs are dimensionless variables that mostly rely on the strong reflectance difference between VIS and NIR described above. VIs are hence basically linked to relative abundance and activity of green vegetation (Baret and Guyot, 1991; Baret et al., 1992; Glenn et al., 2008). Due to this relationship, VIs constitute a convenient tool to monitor spatial and temporal patterns of vegetation canopies and to estimate biophysical vegetation properties (He et al., 2006; Dorigo et al., 2007; Glenn et al., 2008). The number of VIs used in scientific studies is constantly increasing, as each VI tries to reach maximum sensitivity to a specific biochemical or biophysical parameter under different conditions (Haboudane, 2004; Dorigo et al., 2007). Classical broad band VIs based on multispectral sensors are distinguished from VIs based on narrow bands recorded by hyperspectral sensors. A review of the latter group of VIs is given in Dorigo et al. (2007) or Liang (2004). Broadband VIs can be divided into ratio, orthogonal, and hybrid indices (Broge and Mortensen, 2002).

Ratio VIs are based on the ratio between red and NIR reflectance and computed irrespective of soil properties. Their LAI isolines, i.e. lines of equal LAI values from different vegetation structures and soil types, join the origin in the red-NIR feature space (see Figure 2-14). The first VI was the NIR reflectance divided by the reflectance in the red band, named Simple Ratio (SR) or Ratio Vegetation Index (RVI) (Jordan, 1969). Rouse et al. (1974) developed the Normalized Difference Vegetation Index (NDVI), which is the difference between the NIR and red reflectance, related to their sum. The NDVI is adopted in many studies as well as for operational monitoring and is probably the most widely used VI. Further, several variations have been proposed (an overview is given by Huete and Liu, 1994, and Karnieli et al., 2001).

Orthogonal indices have been developed to minimize the influence of soil reflectance. For these VIs, the LAI isolines do not converge at the origin of the Red-NIR space but stay parallel to the soil line (Huete, 1988). The difference between NIR and red reflectance was the first index of this category (DVI, Jordan, 1969), which was modified by Clevers et al. (1989) as Weighted Difference Vegetation Index (WDVI). The Tasseled Cap transformation presented by Kauth and Thomas (1976) is also an orthogonal transformation. Quite similarly, Richardson and Wiegand (1977) used the perpendicular distance to the soil line as an indicator of plant development and created the Perpendicular Vegetation Index (PVI).

Hybrid VIs contain elements of both ratio and orthogonal VIs. The Soil Adjusted Vegetation

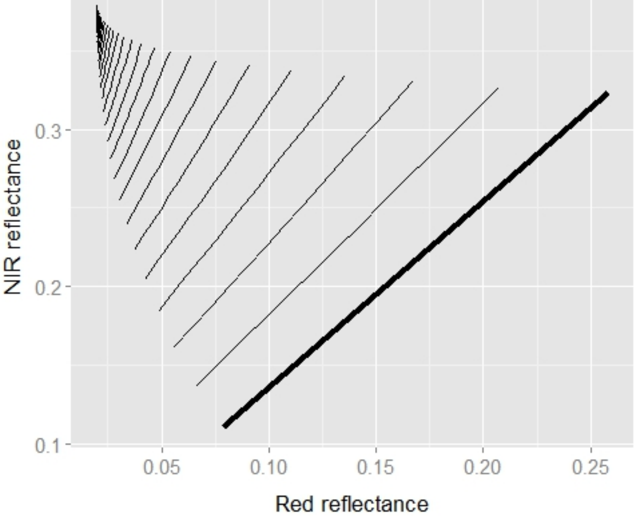

Figure 2-14: Simulated LAI isolines of a planophile canopy (ALA = 30°) in the red-NIR feature space generated using the PROSAIL model. LAI values range from 0 (bare soil, bold line) to 6 by 0.2 steps.

Index (SAVI, Huete, 1988) introduces a soil calibration factor to minimize soil background influences. The SAVI has also been further modified, e.g. in the Transformed Soil Adjusted Vegetation Index (TSAVI, Baret et al., 1989), the Modified Soil Adjusted Vegetation Index (MSAVI, Qi et al., 1994), the Soil adjusted and Atmospherically Resistant Vegetation Index (SARVI), and the modified SARVI (MSARVI, Huete and Liu, 1994). Using SWIR reflectances in VIs enables the monitoring of LAI (Brown et al., 2000), dead plant material (Xu et al., 2014), and of water content (Bowyer and Danson, 2004). However, as no RS data providing SWIR bands are used in this study, the review of those indices would be out of scope.

Overall, soil adjusted indices are reported to be especially suitable for estimating structural canopy parameters such as LAI (Baret et al., 1995; Huete, 1997; Haboudane, 2004). However, the SR being linearly related and the NDVI and TSAVI being exponentially related have also been identified as suitable VIs (Wiegand et al., 1992; Liang, 2004). Thus, a general recommendation on which VI performs best for LAI derivation cannot be given. Systematic comparisons of VI performances have been conducted using synthetic (Broge and Leblanc, 2001; Haboudane, 2004; Féret et al., 2011) and measured data (Jordan, 1969; Broge and Mortensen, 2002; Darvishzadeh et al., 2008a), but even these studies only refer to a limited data set, specific vegetation types, and specific atmospheric conditions.

Transfer functions

The most established way to model the relationship between VIs and the variable of interest is by ordinary least squares (OLS) regressions (see e.g. Fassnacht et al., 1997; Schlerf et al., 2005; Heiskanen, 2006) of the form

$$Y = \beta_0 + \beta_1 X + \varepsilon \tag{2.14}$$

where Y is the response variable (LAI), X is the explanatory variable (VI), β_0 and β_1 are intercept and slope, and ε is the error term. Although it can be argued that the spectral signal is dependent on vegetation state and not vice versa, in most studies the vegetation parameter is modeled as the dependent variable Y (Cohen et al., 2003a). The unknown parameters $\beta_0$and $\beta_1$of the best fit are identified using the OLS method, which minimizes the sum of squared vertical distances between the observed and the predicted variable X values. Due to the fact that the spectral signal reaches a saturation level at higher canopy densities (chapter 2.2.1), the relationships between VIs and LAI are often reported to be non-linear (Weiss et al., 2000; Baret and Buis, 2008). Thus, several studies used transformed predictors in logarithmic, exponential, power, or polynomial regression models (see e.g. Clevers, 1989; Turner et al., 1999; Hansen and Schjoerring, 2003; Kalácska et al., 2004; Ehammer et al., 2010). Cohen et al. (2003a) mention the limitations of traditional linear models for RS applications. Assumptions about the data sets' statistical properties are often violated when using RS data and data measured *in situ*, as there are errors in both measured X and Y variables (Brown, 1979). Larsson (1993) and Heiskanen (2006) therefore used the Reduced Major Axis (RMA) method instead of OLS for the establishment of regressions. For a detailed discussion, see Curran and Hay (1986) and Cohen et al. (2003a).

Integrating multiple data (e.g. several VIs, angle measurements, or dates) into one index or empirical model is another approach to improving the estimate of the variable of interest. In multiple regressions, the regression equation contains two or more predictor variables. In stepwise multiple regressions (SMR) these predictors are added and removed successively to automatically select the most relevant variables. The use of SMR for LAI estimation has e.g.

been tested by Jacquemoud et al. (1995b), De Jong et al. (2003), Mutanga et al. (2004), Atzberger et al. (2010) and Duveiller et al. (2011b). Cohen et al. (2003a), Lee et al. (2004), and Heiskanen (2006) incorporated multiple information by means of canonical correlation analysis (CCA), which permits the use of several weighted explanatory variables in a linear model. The partial least squares (PLS) regression is an extension of the multiple regression approach well suited for dealing with highly multicollinear data. The multidimensional feature space is transformed such that information which correlates with the variable of interest is combined into a few factors, while irrelevant information is grouped into less important factors (Hansen and Schjoerring, 2003; Cho et al., 2007; Darvishzadeh et al., 2008c; Atzberger et al., 2010). Huang et al. (2004) and Curran et al. (2001) further tested the continuum-removal analysis of Kokaly and Clark, an approach that pursues the same strategy of isolating the spectral features of interest by normalizing the reflectances.

Machine learning techniques constitute another group of statistical approaches. In contrast to OLS approaches, machine learning techniques do not assume a linear relationship but can model complex non-linear functions. An advantage thereof is that no assumptions have to be made about the data distribution (Fourty and Baret, 1997; Beale and Jackson, 1998; Huang et al., 2004). For empirical-statistical LAI derivation, artificial neural networks (ANN) are often used. ANNs mimic biological mechanisms used to process information. During a calibration phase, a relation between the predictor variables X (inputs) and a response variable Y (output), that minimizes the difference between the actual and desired output, is iteratively learned based on a training data set, and an interpolating response surface M is set up:

$$\mathrm{Y} = \mathrm{M(X)} + \varepsilon. \tag{2.15}$$

The response surface M consists of at least one “hidden layer” composed of processing nodes, referred to as neurons. The inputs are connected to the neurons in the hidden layers, which, in turn, are connected to the output. Each neuron is a nonlinear processor f of its input signals S_i before forwarding it to another layer or the output. Thus the output O of a node is

$$\mathrm{O} = \mathrm{f}\left(\sum_{\mathrm{i}=1}^{\mathrm{n}} \mathrm{w_i S_i} + \mathrm{b}\right) \tag{2.16}$$

Thereby, the weights w_i and biases b are unique for each neuron. The learning phase is an iterative optimization process involving the modification of the weights and biases and the evaluation of the output error. Thus, the structure of an ANN adaptively develops its own basis functions and the corresponding coefficients (Rumelhart et al., 1986; Kimes et al., 1998; Combal et al., 2002a). A drawback of the method is that the network can over-fit the data, although techniques such as pruning or stopping criteria reduce this risk. ANNs are also frequently used for radiative transfer model inversion (chapter 2.2.3). Other machine learning approaches that are used as a transfer function are Support Vector Regression (SVR, see Vapnik, 1999; Durbha et al., 2007; Camps-Valls et al., 2009; Yang et al., 2011; Verrelst et al., 2012a) or, less often, random forest approaches (Powell et al., 2010; Le Maire et al., 2011; Vuolo et al., 2013). No general conclusion can be drawn for the choice of the regression model, as the performance of each model depends on the used VI, ecosystem, site, and field data. However, most studies report that VIs are linearly related to LAI in sparse canopies and non-linearly when high LAI values occur. Further, multivariate and machine learning techniques often outperform univariate techniques (Baret et al., 1995; Broge and Mortensen, 2002; Baret and Buis, 2008; Darvishzadeh et al., 2008c; Atzberger et al., 2010).

Potentials and Limitations

The empirical-statistical approach is often used due to its simplicity, computational efficiency, and the good results that can be achieved if extensive ground measurements are available and if the transfer function is applied on a confined region and known land cover (Gobron et al., 1997a; Cohen et al., 2003a; Colombo et al., 2003; Atzberger et al., 2003a). Apart from its use for LAI mapping, the empirical approach is further indispensable for the upscaling of *in situ* data for validating coarse resolution data (Baret et al., 2003; Morisette et al., 2006). However, there are considerable limitations to the empirical-statistical approach. A prerequisite of a transfer function is the assumption that variations in a spectral signal are caused by variations in LAI only. This assumption is never fulfilled, as canopy reflectance depends on several factors (Dorigo, 2007; Ustin et al., 2009). Explicitly, reflectance is sensitive to variations in space and time (e.g. phenological stages), species composition, and site (e.g. soil properties) and sampling (e.g. atmospheric properties, viewing and illumination geometries) conditions. Further, even if extensive field measurements are conducted, it is nearly impossible to cover all occurring scenarios (Clevers, 1989; Jacquemoud et al., 1995b; Turner et al., 1999). Therefore, no universally valid VI-LAI relationship can be expected. This implies that the derived relationship is only reliable for the data set it is trained on, and new relationships would ideally have to be established for each place and time, which is costly and time-intensive, as corresponding *in situ* measurements are needed. Therefore, empirical relationships are not suitable for global and operational LAI mapping. Partly due to this limitation, increasing interest goes towards RTMs for the retrieval of LAI.

2.2.3. Physical approach

The physical approach is rooted in the understanding and theoretical description of radiation transport through vegetation canopies. Spectral reflectance is the result of scattering and absorbing in the canopy and at boundary layers. Physics-based RTMs aim at providing these processes and relate radiation leaving a vegetation canopy in a given direction to the spectral and structural properties of the leaves and the canopy (Widlowski et al., 2014). An RTM is run in the "forward mode" to calculate reflectances given the specific characteristics of a canopy and observation configurations (see Figure 2-15). The canopy characterization by leaf and canopy parameters is called parameterization. Through parameterization, RTMs can simulate a great variety of vegetation characteristics and sensor acquisition geometries (Dorigo et al., 2007). These explicit input parameters, which can later be directly derived by running the model in the 'inverse mode', are called 'primary variables'. FPAR and the fractional vegetation cover (fCover) have also been estimated as so-called 'secondary variables', as they are combinations of RTM primary variables (Weiss et al., 2000; Combal et al., 2002b). The physical approach was developed since the beginning of the 1980s, concurrently with the empirical approach. First studies showed that the estimation of biophysical and biochemical properties using an RTM from reflectances measured *in situ* is possible given a certain amount of ancillary data on leaf and soil properties (Goel and Strebel, 1983, Goel and Thompson, 1984a, 1984b). The use of satellite data was only pursued in the mid-1990s (Jacquemoud et al., 1995a; Kuusk, 1995a).

Every vegetation RTM is at least composed by a leaf model and a canopy structure model (see Figure 2-15). In addition to this, soil reflectance is crucial for radiation transfer modeling as it describes the lower boundary condition of the canopy with its own spectral properties (see Huete, 1989). It is integrated in the canopy model by spectra measured in the field, spectra taken from the scene, a standard soil spectrum, or by spectra provided by a soil BRF model, e.g. the Hapke model (Hapke, 1981), its successors SOILSPECT (Jacquemoud et al., 1992) or 4SOIL (Laurent et al., 2011). In the works of Atzberger (2003b; 2004) simple empirical relationships and scaling factors have been used to adjust band specific soil reflectances.

Further, a model for the simulation of radiance propagation in the atmosphere can be used to calculate TOA radiance, i.e. the radiance as it would have been measured by a sensor (see e.g. Gastellu-Etchegorry et al., 2004; Baret et al., 2006; Verhoef and Bach, 2007; Lauvernet et al., 2008; Houborg et al., 2009; Laurent et al., 2011). An overview of atmosphere radiation transfer modeling and on established models is given in Grau and Gastellu-Etchegorry (2013). The use of TOA radiance is adopted because atmospheric RTMs are more accurate when run in the forward mode, so that atmospheric, adjacency, and surface directional effects can be incorporated more accurately in the LAI retrieval process (Liang, 2004). Further, in this approach all errors and uncertainties are contained in the LAI simulation process, which makes it easier to study their impact (Laurent et al., 2011; Grau and Gastellu-Etchegorry, 2013). Nonetheless, the use of modeled TOC reflectances together with atmospherically corrected RS data has been directive in the last few decades, which is why the discussion will be limited to the simulation of reflectance at TOC level below. The derivation of LAI is achieved by model inversion. Before the inversion of RTMs is discussed, an overview of leaf and canopy models is given.

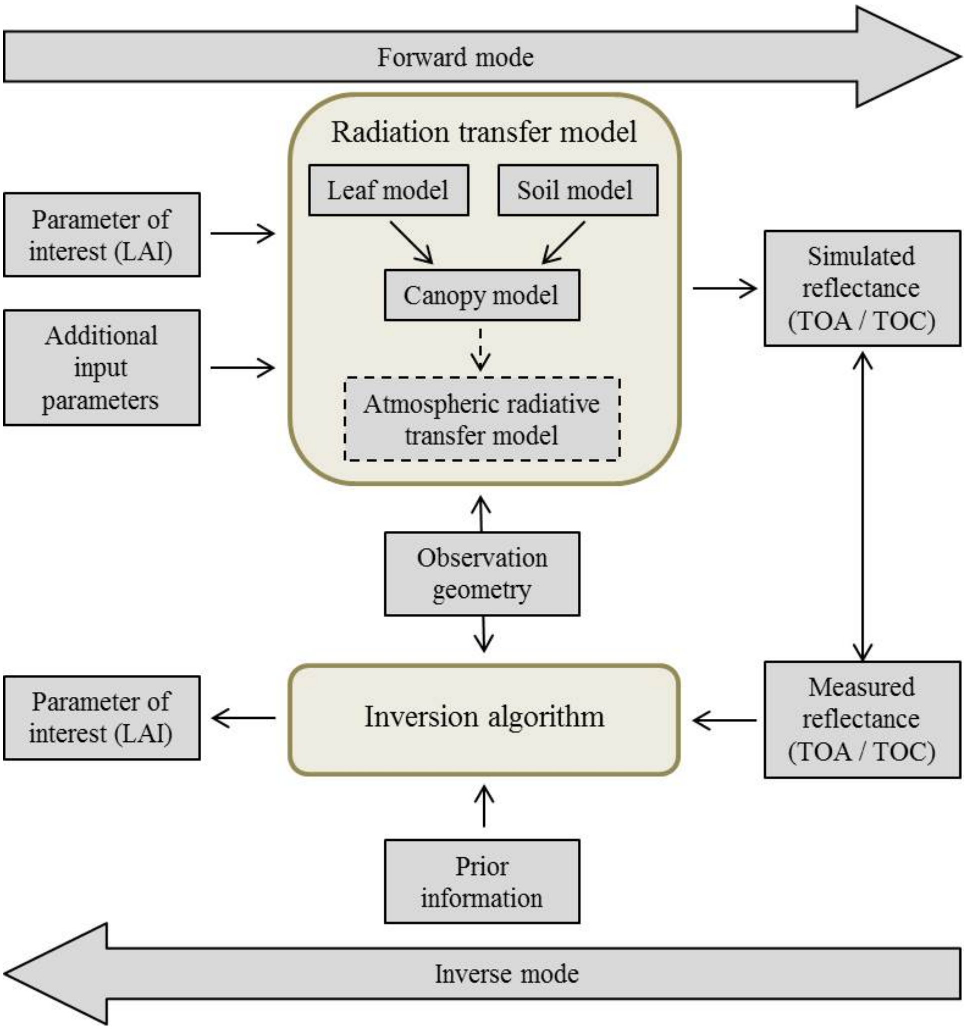

Figure 2-15: Concept of radiation transfer modeling: forward mode (above) and inverse mode (below).

Leaf optical models

The purpose of a leaf optical model is to simulate scattering and absorption of light at plant material depending on leaf biochemical composition and structure. Input parameters to leaf models are at least the concentrations and absorption spectra measured *in vivo* of the most important leaf pigments and water, as well as a refractive index. However, the models differ in the complexity of the modeled leaf structure and distribution of compounds.

The simplest approach is to describe the leaf as a homogeneous medium. This was developed by Allen and Richardson (1968), who published a model based on the theory of Kubelka and Munk (K-M theory, Kubelka and Munk, 1931) that describes the one-dimensional (1D) radiation transfer in scattering media with two parameters, a scattering and an absorption coefficient. Allen and Richardson stated that their theory can be applied to leaves as well as to plant canopies (see below). In their approach, the leaf is considered as one slab of scattering and absorbing material, with incoming light being perpendicular to the leaf. Such models are generally called "N-flux models" (see e.g. Richter and Fukshansky, 1996). An extension of this approach is the "plate model", in which the leaf is composed of one or n homogeneous plates with rough isotropic surfaces in a pile with $n - 1$ intermediate air layers. One of the oldest and most popular plate models is PROSPECT (Jacquemoud et al., 2009, see chapter 6.1.1). In contrast to Allen and Richardson's initial expression, a variable angle of incident light is introduced. It calculates reflectance and transmittance in the spectrum between 400 - 2500 nm based on two types of input variables, the leaf structure parameter N and leaf biochemical content (water and leaf pigments) (Jacquemoud and Baret, 1990). In the following versions, the simulation of reflectance is continuously improved by accounting for further leaf biochemical constituents (Jacquemoud et al., 1996), by the condensation of these components into one parameter ('dry matter', Baret and Fourty, 1997; Jacquemoud et al., 2000), by increasing the model's spectral resolution from 5 nm to 1nm (Le Maire et al., 2004), and by separating chlorophylls and carotenoids (Féret et al., 2008).

This approach is contrasted with more complex but realistic models that take into account the structural heterogeneity of leaves, which is achieved by stochastic, radiosity, or ray tracing methods. The trajectories of photons are simulated, which interact with leaf material according to defined probabilities for scattering and absorption along their way. The model SLOPE (Stochastic model for Leaf Optical Properties Extended for fluorescence, Maier, 2000) is a stochastic approach that approximates radiation transport through 30 layers as transitions between photon states based on Markov Chains (Oehmichen, 2004), while the LEAFMOD model by Ganapol et al. (1998) uses only one layer. A method derived from computer graphics applications is radiosity modeling (Liang, 2004). The best known leaf model of this type is the ABM presented by Baranoski and Rokne (1997). Once a ray hits a leaf, it performs a 'random walk', i.e. can be reflected or scattered multiple times, until it is absorbed or leaves the leaf (Hammersley and Handscomb, 1964). Ray tracing models simulate the propagation of photons through the leaf, taking into account the properties of the cells (shape, size, position, biochemical content) and the optical parameters of the cell constituent. They are therefore the most realistic leaf realizations (Baranoski and Rokne, 1997). An example is RAYTRAN, which can be applied independently of scale (Govaerts et al., 1996). While the strength of these models is their ability to incorporate a lot of information, their drawback is the required detailed description of the cells. This makes them computationally very expensive and inversions difficult to implement.

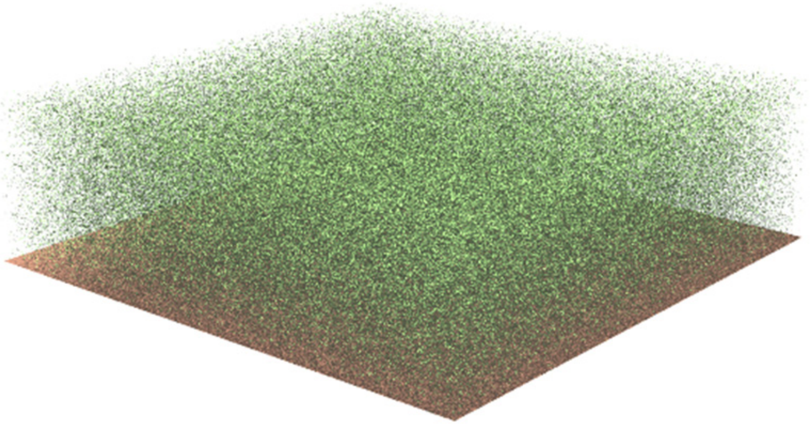

Figure 2-16: Homogeneous vegetation canopy with randomly distributed finite-size scatterers simulated by a 1D model (image downloaded from the RAMI homepage[6]).

A weakness of most leaf models is the ignorance towards the anisotropic reflectance behavior of leaves, although some work on measuring anisotropic leaf BRF and incorporating it in leaf models has been carried out (Jacquemoud and Ustin, 2001; Bousquet et al., 2005; Combes et al., 2007; Comar et al., 2014). Further, biochemical compounds with only relatively small absorption features cannot be accurately retrieved (Fourty et al., 1996), which is however of minor relevance for LAI modeling.

Canopy models

Several canopy models evolved, which can be distinguished according to the degree of detail in representing canopy structures, as well as to the numerical or analytical solution technique used to solve the radiation transfer equations. For a detailed description of radiative transfer equations and their solutions, see Goel (1988), Myneni and Ross (1991), or Verhoef et al. (2007). Most techniques used for leaf modeling are also applied to canopy modeling.

The simplest kind of canopy models are 1D turbid medium model. They rely, as the leaf models, on the approach introduced by Allen and Richardson (1968). The plant canopy is considered a turbid plane-parallel medium (see Figure 2-16), based on a number of simplifications: The canopy is horizontally homogeneous and infinite but vertically variable and finite. It contains infinitely small, flat leaves (comparable to particles) of defined optical properties that are randomly distributed in space. Allen and Richardson's approach considered only two types of radiant fluxes, diffuse upward and downward radiation. In its successor model (Allen et al., 1970) a direct solar flux is also included. Finally, in the Suits (1972) model, directional upwards radiance is considered. The four radiation fluxes are expressed in four differential equations, making this kind of model a 'four stream model'. The Suits model represents leaves as elements with finite size, and the canopy as a mixture of vertical and horizontal leaves. Through extending the Suits model by a leaf inclination distribution function (LIDF) to allow for randomly distributed leaf angles, Verhoef (1984) developed the SAIL (Scattering by Arbitrarily Inclined Leaves) model. The inputs to SAIL are LAI, LIDF, layer thickness, leaf transmittance and reflectance, and a soil spectrum (chapter 6.1.1). It provides canopy BRF and absorption (Goel, 1988).

Other turbid medium models were also developed in the early 1990s, each using different analytical (Verstraete et al., 1990; Pinty and Verstraete, 1991; Knyazikhin et al., 1992;

---

[6] http://rami-benchmark.jrc.ec.europa.eu/HTML/RAMI3/RAMI3.php. Last access: 20.02.2014

Iaquinta and Pinty, 1997) or semi-analytical (Ganapol and Myneni, 1992; Ahmad and Deering, 1992; Gobron et al., 1997b) methods to solve the transport equations. However, SAIL is the most widely used and validated vegetation canopy model (Jacquemoud et al., 2009). It has been improved and extended several times. In 1995, the single-scattering component of direct solar radiation of the Nilson-Kuusk model (Nilson and Kuusk, 1989) was introduced into SAIL in the form of a hot spot parameter forming SAILh (Kuusk, 1991; Kuusk, 1995a). A numerically robust and speed-optimized version (SAIL++) that accounts for multiple scattering was published by Verhoef et al. (2002). To simulate vertical gradients in canopies, e.g. higher leaf area density and pigment concentrations towards the top, Weiss et al. (2001) proposed the 2M-SAIL model. It distinguishes four different layers consisting of fractions of soil, green pigments and brown pigments. Similarly, Verhoef and Bach (2003) propose two layers of different concentrations of brown and green pigments in the GeoSAIL model (not to be confused with the "GeoSail" model, see below). Other versions take into account chlorophyll fluorescence (FLSAIL, Rosema et al., 1991; FluorSAIL, Miller et al., 2005) or can be used for thermal applications (4SAIL, Verhoef et al., 2007).

In 1992, SAIL was combined with the PROSPECT leaf model to form the well-known PROSAIL model (Jacquemoud et al., 2009), which is described in more detail in chapter 6 as it is used in this thesis. By linking the variation of reflectance depending on biochemical leaf contents with its directional variation depending on canopy architecture, PROSAIL is a valuable tool for vegetation characterization. As PROSAIL is a 1D model based on a relatively small number of input parameters, it is computationally effective and invertible. It is especially suitable for representing dense and homogeneous vegetation (Schlerf and Atzberger, 2006; Dorigo et al., 2007). To account for the cases in which these assumption do not apply, e.g. for clumped canopies such as forests or row crops, three-dimensional (3D) methods have been developed.

In geometrical-optical radiation transfer (GORT) models, the canopy is represented by objects of geometrical shapes. To represent the plants, ellipsoids, cones, or cylinders are used (e.g. Strahler and Jupp, 1990; Cescatti, 1997; Widlowski et al., 2006b), or they are constructed from small cubic voxels in a regular grid (e.g. Gastellu-Etchegorry et al., 2004; Béland et al., 2011; Bittner et al., 2012; Grau and Gastellu-Etchegorry, 2013). The spatial distribution of these objects is specified, so that sunlit and shadowed canopy regions can be calculated. This model type is therewith able to handle sparse canopies where shadowing plays an important role. To describe the geometrical objects, additional input parameters are necessary, at least a cover fraction index and a crown shape parameter. The first geometrical model was presented by Li and Strahler (Li and Strahler, 1985, 1986). It constructs a canopy spectrum by linearly combining reflectance from sunlit and shaded tree crowns and backgrounds. This concept was extended by the use of ellipsoidal crown shapes and mutual shading (Li and Strahler, 1992) and by including other sunlit or shaded surfaces (Jupp et al., 1986). Other examples are the Simple Geometric Model (Chopping, 2003), the KUUSK model (Kuusk, 1995b), the approaches of Myneni et al. (1990), of Welles and Norman (1991), or the "4-scales" model of Chen and Leblanc (1997). A review is given by Chen et al. (2000).

Hybrid models represent the canopy as GORT models, with the geometrical objects/voxels no longer being opaque but treated as turbid media to approximate the distribution of scatterers therein (Widlowski et al., 2014, see Figure 2-17). The number of input factors for these models is often increased by the need of describing several horizontal layers. Examples are the Three-dimensional Radiation Interaction Model (TRIM, Goel and Grier, 1988), the model

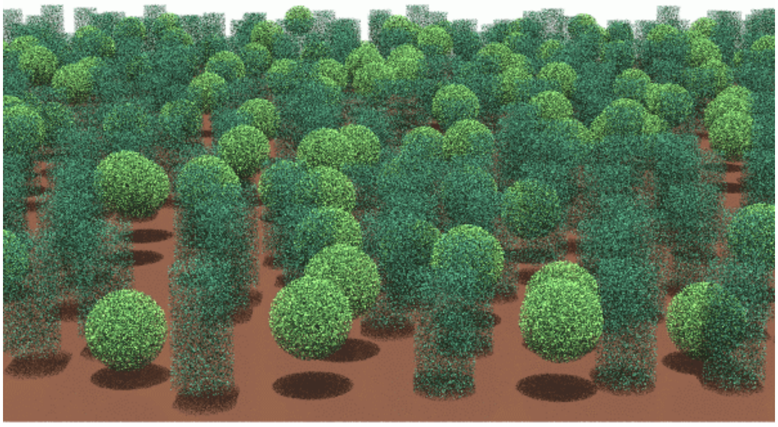

Figure 2-17: Simulated canopy of spectrally and structurally mixed vegetation (from the RAMI homepage[6]). See there and Widlowski et al. (2014) for further examples of simulated homogeneous and heterogeneous canopies, which correspond to the structure of advanced 1D and 3D RTMs.

introduced by Bégué (1992), the Forest Light Interaction Model (FLIM, Rosema et al., 1992), the FRT model (Nilson and Peterson, 1991; Kuusk, 2000), the GeoSail model (Huemmrich, 2001) and the 4SAIL2 (Verhoef and Bach, 2007), both coupled with SAIL. The Invertible FOrest Reflectance Model (INFORM) by Atzberger (2000) is a hybrid model that solves the energy transport based on a stochastic method.

So-called numerical computer simulation models account for location, size, shape, color and orientation of every single object in the canopy by using 3D virtual plants generated from growth simulation algorithms (Allen et al., 2005; Disney et al., 2006; Lamanda et al., 2007; Da Silva et al., 2008; Roupsard et al., 2008). They give a realistic image of canopies and radiation transfer, however, their complexity leads to a high computational demand, which restricted the use of such algorithms for decades (Jacquemoud et al., 2000; Widlowski et al., 2014). Further, inverting numerical computer simulation models is not trivial. Two typical methods are Monte Carlo ray tracing and radiosity methods. Using Monte Carlo ray tracing (e.g. PARCINOPY, Chelle, 1997; DART, Gastellu-Etchegorry et al., 1996; SPRINT, Goel and Thompson, 2000; FLIGHT, North, 1996; Rayspread, Widlowski et al., 2006a; FLiES, Kobayashi and Iwabuchi, 2008), the path of rays through the canopy is calculated through stochastic decisions for each contact, until they are absorbed or leave the scene. Since the number of photons leaving the scene in each direction is small, millions of simulations have to be performed to ensure an accurate BRDF estimation. Radiosity models are widely used in computer graphics for realistic scene rendering. They represent each scattering element in terms of polygons and each polygon is assumed to be a Lambertian surface (Borel et al., 1991; Goel et al., 1991; Chelle and Andrieu, 1998; Qin and Gerstl, 2000). The advantage is that once the radiation transport is solved, canopy reflectance can be simulated from any view angle.

Overall, RTMs become increasingly important in the RS community. Since the 1980s, the ability of radiation transfer modeling in complex canopies has considerably evolved. At the JRC, the comparison program RAMI (RAdiation transfer Model Intercomparison) aims at benchmarking the performance of RTMs. In this program, complex 3D models are used for validating simple RTMs and for testing the impact of approximations made in less complex models (Disney et al., 2000). The results of this initiative are summarized in Pinty et al. (2001; 2004) and Widlowski et al. (2007; 2013).

Leaf and canopy model selection is always a trade-off with regard to the number of input parameters employed (Jacquemoud et al., 2000). The inclusion of many parameters increases the realism of the modeling result but decreases the invertibility and computational efficiency of the model. In cases where the parameters are not adequately known, many parameters will even increase the under-determination of the inversion (see below). A good model is therefore a compromise between realism and simplifications (Nilson and Kuusk, 1989; Kimes et al., 1998; Verhoef and Bach, 2007). The choice of a canopy model depends further on the canopy type under consideration, with particular attention on the way canopy structure is represented, and on the spatial resolution of the RS observation (Pinty et al., 2004; Widlowski et al., 2005; Widlowski et al., 2014). For selection criteria relevant for grassland modeling and an associated literature review see chapter 6.1.2

Inversion techniques

To retrieve canopy parameters from measured reflectances, an RTM needs to be inverted (see Figure 2-14). Due to the complex character of RTMs, an analytical closed-form solution is mostly not possible. Consequently, numerical schemes have to be used for solving the inverted transport equation. These schemes can deal with complex RTMs, since the model is used only in the forward mode. Relating to Equation 2.8 (chapter 2.2.1), which describes the dependencies of surface reflectance in the forward mode, the inverse problem consists in estimating the set of variables $\{a_\lambda, b_\lambda, c_\lambda, s_\lambda, o_\lambda\}$ that produced the observed spectrum R_λ. Some of the parameters influencing canopy reflectance (e.g. LAI of c_λ) are derived given R_λ and other subsystem properties (Goel, 1988; Kimes et al., 2000):

$$c_\lambda = g(R_\lambda, s_\lambda, a_\lambda, b_\lambda, o_\lambda) \tag{2.17}$$

Avoiding the need to retrieve atmospheric properties by using atmospherically corrected TOC data and with full knowledge of the sun and sensor properties, the inverse problem becomes

$$\{b_\lambda, c_\lambda\} = g(R_\lambda, s_\lambda, o_\lambda) \tag{2.18}$$

where s_λ and o_λ contain only fixed parameters. Further, some of the soil (b_λ) and canopy (c_λ) parameters are often known or predictable at a sufficient accuracy and can be fixed with estimates. Thus, only a subset of the parameters in Equation 2.18, called free parameters p, needs to be derived through inversion (Kimes et al., 2000). The number of free parameters p determines the number n of independent equations in the form of Equation 2.17 needed to evaluate them, as n at least has to equal p. If $n < p$, the equation system is under-determined for a unique solution. Additional independent equations are most easily achieved by varying the well-known sun and sensor properties, i.e. by sampling radiation in several viewing directions. Generally, inversion techniques can be classified into two groups, depending on whether the emphasis is put on the match between measured and simulated reflectance, or on the relation of the canopy parameter of interest to the modeled spectra (Goel, 1989; Jacquemoud et al., 2009). A special issue of *Remote Sensing Reviews* (Liang and Strahler, 2000), Tarantola (2005), and Baret and Buis (2008) review inversion theory and methods for LAI derivation. While several aspects influence the selection of an inversion method, it does not depend on the studied canopy type, thus all are potentially suitable for grassland LAI derivation. In the following a short description of the most important techniques – iterative optimization, look-up tables, and neural networks – is given.

Iterative Optimization

Traditional inversion of RTMs uses iterative optimization (Goel, 1988). Multidimensional optimization algorithms search for the set of input variables that leads to the best match between simulated and measured reflectances by iteratively trying different model parameter configurations within a certain range (Figure 2-18). In this regard, a so-called merit or cost function J calculates the dissimilarity between the simulated reflectance R_λ and the measured reflectance $\widehat{\mathrm{R}}_\lambda$, weighted by the variance σ_λ^2 associated to measurements and model uncertainties (Pinty et al., 1990; Jacquemoud et al., 2000; Combal et al., 2002a).

$$J = \sum_{\lambda=1}^{\mathrm{n_{meas}}} \frac{(\mathrm{R}_\lambda - \widehat{\mathrm{R}}_\lambda)^2}{\sigma_\lambda^2} \tag{2.19}$$

The measurement uncertainties are mainly related to sensor and processing errors, while model uncertainties result from model simplifications compared to actual canopies (Koetz et al., 2005b). The minimization of the cost function is then used as a stopping criterion for the optimization. In this regard, the number of free parameters and the number of configurations considered define the size of the inverse problem. Further, the definition of tolerance thresholds is important for optimal performance (Jacquemoud et al., 2009).

There are several minimization techniques available in standard libraries, often classified according to their search strategy and to reliance on the model's partial derivatives. Non-derivative based algorithms include the "conjugate directions" method, which iterates from a single starting point (Goel, 1989; Liang and Strahler, 1993; Liang and Strahler, 1994; Bacour

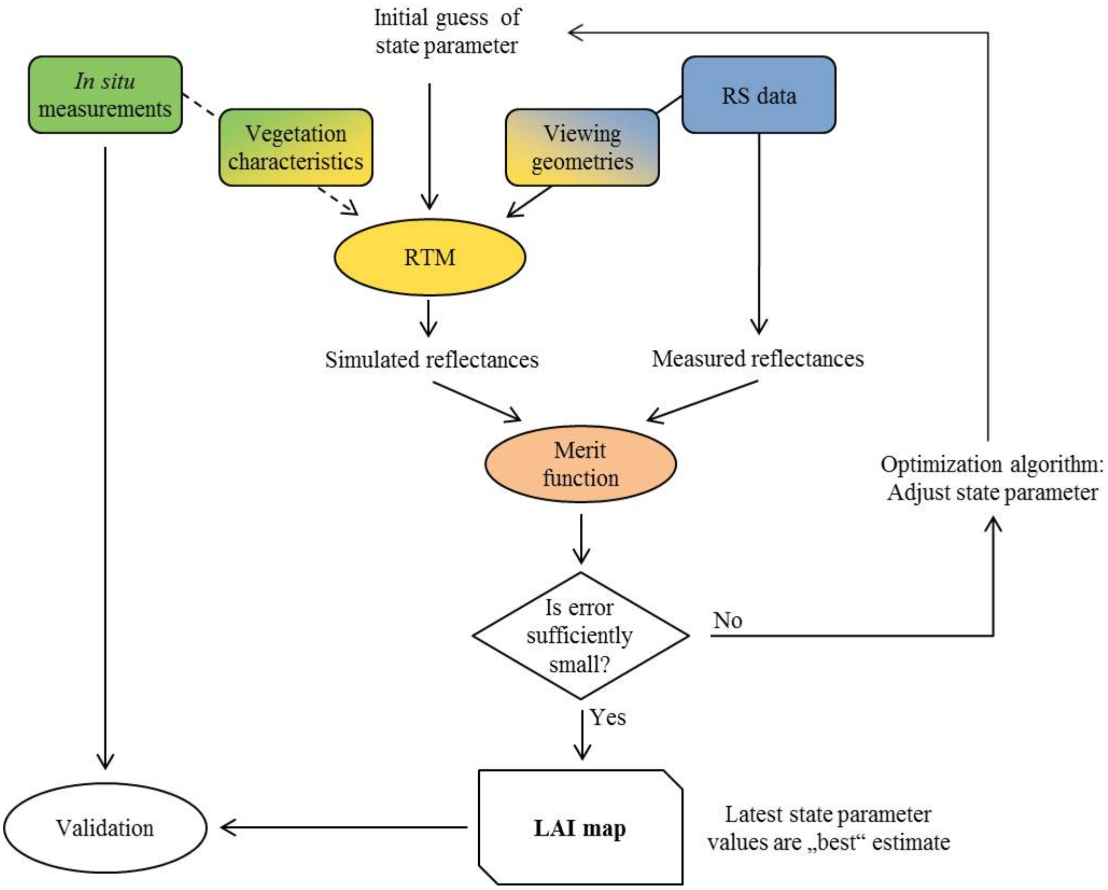

Figure 2-18: Schematic concept of the iterative optimization inversion algorithm. Adapted from Kimes (2000). The 'state parameter' is the parameter of interest, i.e. the LAI, while the 'vegetation characteristics' comprise all other leaf and canopy parameters used in the RTM.

et al., 2002b), or the “simplex” method, which starts from a family of points (Jacquemoud et al., 1994; Privette et al., 1994; Bicheron and Leroy, 1999). The “Steepest-Descent”, “conjugate gradient”, “Newton-Raphson”, or “Quasi-Newton” methods rely on a single starting point and derivative information (Pinty et al., 1990; Iaquinta et al., 1997; Combal et al., 2002a; Lauvernet et al., 2008). In the last decade, Bayesian probability approaches such as the “Markov Chain Monte Carlo” method are increasingly used (Zhang et al., 2005a; Verhoef, 2007). The algorithms differ in their stability and in computation efficiency. Research suggests that the best optimization algorithm varies with the model. The technique has been applied for various vegetation types such as crops (Goel and Thompson, 1984b; Fang, 2003; Laurent et al., 2013), grassland (Privette et al., 1997; Vohland and Jarmer, 2008), and forests (Bicheron and Leroy, 1999; Meroni et al., 2004; Zhang et al., 2005a).

The strength of the iterative optimization approach lies in its simplicity and wide availability, as well as its flexibility and the control the user can maintain over the process. A major drawback of iterative optimization is that it requires an initial guess of the solution to start the search in the parameter space. The correctness of this initial guess can be critical if it causes the solution to get trapped in a local minimum (Qiu et al., 1998; Bacour et al., 2002b; Combal et al., 2002a). The problem can partly be reduced by limiting the range of parameter variation (Lavergne et al., 2007), which however reduces the ability of modeling the natural variability of canopies, or by restarting the optimization algorithm several times at different points in the parameter space, which increases computation time. Similar approaches are genetic algorithms (Jacquemoud et al., 1994; Fang, 2003), which use a population of initial guesses that can be recombined and mutated. Either way, as the RTM has to be rerun iteratively, the computational inefficiency of the approach is a major concern. Thus, although iterative minimization methods proved to be efficient for case studies, they could not be applied operationally over large spatial or temporal domains or for 3D RTMs (Kimes et al., 2000; Kimes et al., 2002; Jacquemoud et al., 2006).

Look-up tables

Look-up tables (LUT) constitute a simple inversion technique also based on the minimum distance between measured and modeled spectra (see Figure 2-19). By running the model

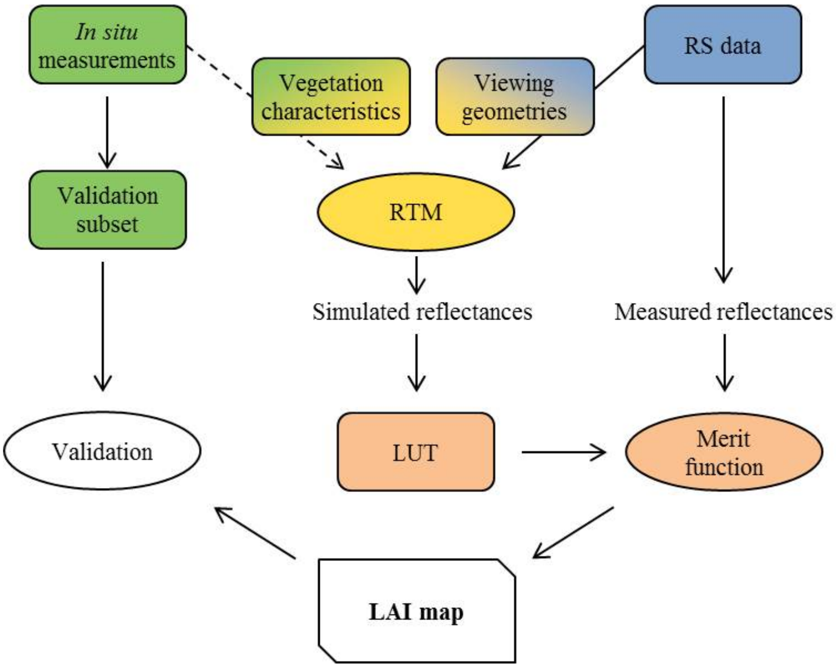

Figure 2-19: Schematic concept of the Look-up table inversion approach.

several times in the forward mode with different combinations of input parameters, a data base with a large number of spectra is computed, a so-called LUT. The aim is to cover all relevant canopy realizations. During inversion, a merit function (see Equation 2.19) calculates the matches between a measured reflectance spectrum and all simulated spectra stored in the LUT. This merit function most frequently is a least squares estimate (LSE) (Rivera et al., 2013; Leonenko et al., 2013b). The parameter configuration that generated the best fit spectrum is then selected as a solution.

The approach has several advantages. It is faster than optimization techniques, as the inversion of each pixel only involves the LUT searching procedure, while the computationally expensive LUT simulation is performed just once. Also, the LUT approach does not require a training phase, which is necessary with machine learning methods and time-consuming in most cases. Apart from the efficiency of the approach, the procedure has the advantage of performing a global search and thus avoiding the danger of getting trapped in a local minimum. This robustness is reinforced by not selecting the parameter set of the single best spectrum as the solution of the inversion, but by deriving the average or median of the parameters of multiple best fitting spectra (Weiss et al., 2000). Further, due to this best fit sample strategy *a posteriori* distribution of the variable of interest can be routinely derived, indicating the reliability of the final estimate (Kötz et al., 2004, see chapter 6.5.3). Another advantage is the easy integration of prior knowledge on the target parameter or on uncertainties into the process (Weiss et al., 2000, see also below and chapter 6.4). There is a range of studies that used LUT inversion to estimate chlorophyll, water content, LAI, fAPAR or fractional cover from RTMs (Weiss et al., 2000; Combal et al., 2002a; Kötz et al., 2004; González-Sanpedro et al., 2008; Knyazikhin et al., 1998; Darvishzadeh et al., 2008b; Leonenko et al., 2013a; North, 2002; Richter et al., 2009; Soenen et al., 2009; Atzberger and Richter, 2012). However, to achieve a high accuracy with this inversion method, the canopy needs to be accurately represented in the LUT. This means that the variable space must be sufficiently and systematically sampled, which increases the LUT size and slows down the estimation procedure. Thus, the parameterization of the model, a realistic distribution of variables, and the step sizes between variable states are crucial (Weiss et al., 2000; Combal et al., 2002a; Combal et al., 2002b). Another drawback e.g. for the processing of RS time series is that each sun and viewing geometry has to be accounted for in the LUT. To overcome this, Gastellu-Etchegorry et al. (2003) suggest interpolating between angles using an analytical BRF model, while Pasolli (2012) uses angle combination classes and associated individual LUTs. Further, when the model and measurement uncertainties are not well known, the definition of the cost function is a critical issue (Verger et al., 2011a; Leonenko et al., 2013b).

Hybrid inversion approaches

The second group of inversion techniques, biophysical variable driven methods, is based on calibrating a statistical relationship over a learning data set consisting of the input and output of an RTM. They are called “predictive”, “semi-empirical”, or “hybrid” approaches, as they combine physical and statistical models (Weiss et al., 2000; Liang, 2004). As the statistical methods described in chapter 2.2.2, inversion consist in adjusting the coefficients of a relationship between the reflectance and the LAI during a calibration phase in order to minimize the difference between this data base parameter value and the values predicted by the inverse model. Once the calibration is achieved, the operational retrieval is rapid and straight-forward (Duveiller et al., 2011b). The difference to a purely statistical approach is that training data for establishing the relationship is not measured by an RS sensor or in the field. Instead, an RTM is used to build a synthetic data set, preserving the data from uncertainties associated with ground and RS measurements. Further, with RTMs a wider range of canopy realizations can be simulated than could be covered by *in situ* measurements (Haboudane et al., 2002; Dorigo et al., 2007; Lauvernet et al., 2008). Due to the highly complex relationships modeled in an RTM, non-parametric machine learning techniques are mostly preferred over simple parametric regressions.

Inversions based on ANNs are the most prominent type of hybrid approaches (see Figure 2-20). An ANN interconnects the synthetic inputs and outputs of an RTM during the learning phase (see chapter 2.2.2 for more details). Then, RS measurements are input into the trained ANN and transformed into biophysical variables (Jacquemoud et al., 2009). ANNs have lately become a popular method of inverting RTMs, mainly because of their high computational speed and their retrieval performance. As the optimization operates directly over the variables of interest, hybrid inversion approaches are potentially more accurate than other techniques (Schlerf and Atzberger, 2006; Bacour et al., 2006; Baret and Buis, 2008). Further, they are less sensitive to model uncertainties (Combal et al., 2002a). Verger at al. (2008) even showed that a single ANN trained across several ecosystems performs in a manner similar to ANNs trained for each ecosystem, which potentially reduces the computational time considerably when working on complex landscapes. As a further advantage, hybrid inversion schemes provide continuous solutions whereas LUTs yield results based on their discrete entries (Duveiller et al., 2011b).

Major drawbacks of ANNs are the time-consuming training phase, the dependency of the retrieval performance on the modalities of the training data set and the network architecture, and the unpredictable behavior of ANNs when an RS signal is not well represented in the training data set. Further, due to their black-box character, they are unsuitable for studying

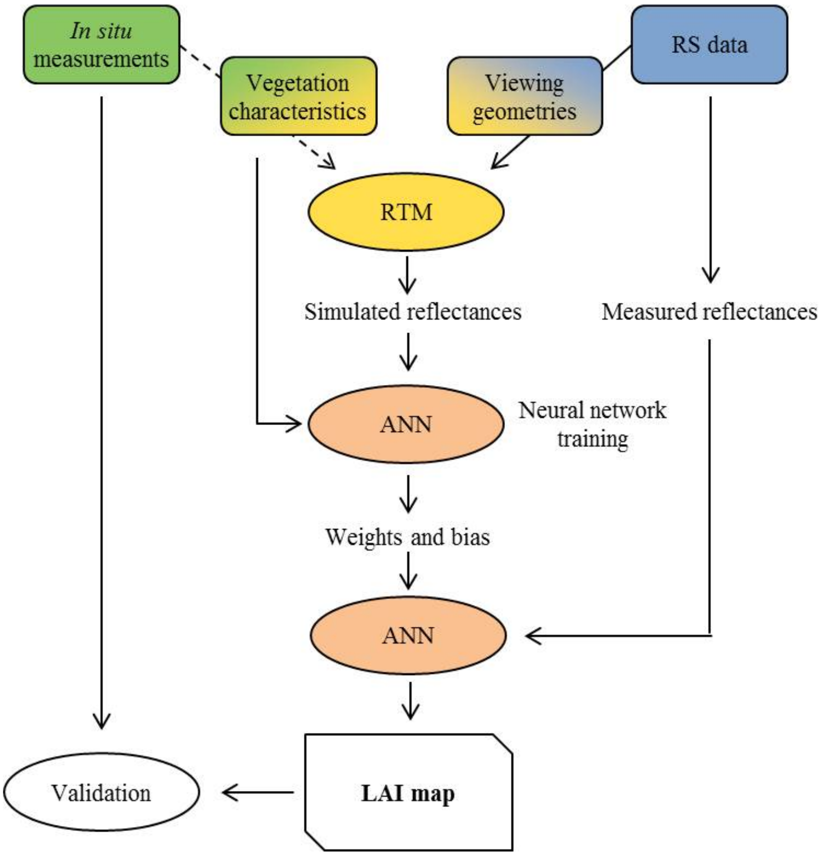

Figure 2-20: Schematic concept of the artificial neural networks inversion approach.

cause-effect relationships. Also, they are tuned for a specific number of inputs, limiting the transferability to other RS data (Schlerf and Atzberger, 2006; Duveiller et al., 2011b; Verger et al., 2011a). There is a wide range of studies that use ANNs with a range of different sensors to determine LAI, gap fraction, fAPAR, or the canopy chlorophyll content (see e.g. Baret et al., 1995; Abuelgasim et al., 1998; Gong, 1999; Weiss et al., 2002; Kimes et al., 2002; Combal et al., 2002b; Atzberger, 2004; Fang and Liang, 2005; Bacour et al., 2006; Verger et al., 2008; Duveiller et al., 2011b). An overview of the method is given by Kimes et al. (1998).

The under-determined and ill-posed nature of RTM inversion

The most serious restriction of RTM inversion is its instability, as it is an under-determined and ill-posed problem. According to Hadamard's postulates, a problem is well-posed if and only if its solution exists, this solution is unique, and depends continuously on the data (Hadamard, 1902). The inversion of RTMs does not fulfill these criteria for two reasons.

First, the equation system is mathematically often under-determined for a unique solution, because the number of unknown parameters p is larger than the number n of independent spectral measurements. Thus, the problem of underdetermination increases with an increasing number of free input parameters. According to Baret and Buis (2008), even a simple RTM requires at least 13 input parameters. Thus, theoretically, at least 13 independent observations (bands or viewing directions) would be required to solve the inversion using RS data. This requirement can mostly not be fulfilled, even if RS sensors could provide a high number of measurements, because of the high correlation between bands and view directions (Gemmell, 2000; Zhang et al., 2002; Verhoef, 2007). If, however, only limited spectral information is provided, the signal can become ambiguous due to compensations between canopy parameter that affect canopy reflectance in a similar way (so-called parameter equifinality). For example, the spectral reflectance of a canopy with low LAI but planophile leaf orientation is very similar to that of an erectophile canopy with high LAI in certain spectral domains (Baret and Guyot, 1991; Jacquemoud and Baret, 1993; Combal et al., 2002b; Atzberger, 2004).

The second aspect is the ill-posedness, which relates to the required continuous dependency of the solution on the data. This means that the more accurately an RTM describes radiation transfer in the canopy, and the more accurate the RS information is, the more accurate the model output will be (Kimes et al., 2000). However, in reality, model and measurement uncertainties do not result in equal uncertainties of the solution, i.e. the solution being near the true solution, but might lead to leaps in the solution space. A continuous dependency of the model output on the input is thus not given (Atzberger, 2004). Especially over dense canopies for which reflectance saturates, a small variation in the input can translate to a large output variation (Combal et al., 2002b; Baret and Buis, 2008). Therefore, retrieval technique for solving ill-posed problems ideally should include uncertainty as an input parameter.

A straight-forward way to reduce the dimensionality of the inverse problem is the coupling of leaf, canopy, and atmosphere models (Lauvernet et al., 2008; Kobayashi and Iwabuchi, 2008; Houborg et al., 2009; Jacquemoud et al., 2009; Laurent et al., 2013). When reflectance and transmittance are provided to a canopy model by a leaf model, not only the number of p decreases, but due to the independence of the remaining variables from wavelength, an increase in spectral sampling in fact reduces the under-determination (Baret and Buis, 2008). Equally, increasing the dimensionality of the RS observation with directional information reduces the problem (Lavergne et al., 2007; Verhoef, 2007; Vuolo et al., 2008). According to Jacquemoud et al. (2000) and Widlowski et al. (2004), especially the retrieval of structural canopy variables benefits from multi-angular observations. However, most RS sensors have a limited number of viewing angles (Knyazikhin et al., 1998), although recently there has been an expansion of sensors providing multi-angular imagery (see chapter 2.3). The combination of several scenes recorded at different angles on consecutive days as provided by MODIS strongly depends on pixel quality and is not available from high resolution sensors (He and Yang, 2013). Thus, increasing independent spectral measurements is not trivial.

Instead, regularization techniques have been introduced to stabilize RTM inversions, which rely on the use of “prior information” to a greater or lesser extent (Combal et al., 2002b). Prior knowledge includes any ancillary information about the “true” distributions of RTM input variables, e.g. land cover type, structural or phenological characteristics, or viewing and illumination conditions. It could be gained from literature, field measurements, model sensitivity (see chapter 6.2), other sensors, or the scene itself (Baret and Buis, 2008). Based on this knowledge, the under-determination is reduced through variables being set, which either are exactly known or have a small influence on the model output, to an assumed real value. The use of *a priori* information is indicated in Figure 2-18 to Figure 2-20 by the dashed arrow between “*in situ* measurements” and “RTM”. A comprehensive overview of regularization techniques is given by Tarantola (2005). Prior information can be introduced to the inversion in different ways. Techniques which try to fit the simulated and measured reflectances using a cost function (LUT and optimization techniques) can be modified by adding an *a priori* vector term to the cost function, creating a Bayesian approach (see e.g. Meroni et al., 2004; Lavergne et al., 2007; Lauvernet et al., 2008; Dorigo et al., 2009):

$$\mathrm{J} = \underbrace{\left(\mathrm{R}-\hat{\mathrm{R}}\right)^{\mathrm{t}} * \mathrm{W}^{-1} * \left(\mathrm{R}-\hat{\mathrm{R}}\right)}_{\text{Radiometric information}} + \underbrace{\left(\hat{\mathrm{V}}-\mathrm{V_p}\right)^{\mathrm{t}} * \mathrm{C}^{-1} * \left(\hat{\mathrm{V}}-\mathrm{V_p}\right)}_{\text{Prior information}} \tag{2.20}$$

where $\hat{V}$ is the vector of the input biophysical variables, V_p corresponds to the vector of *a priori* variable values, R is the vector of RS measuremens, and $\hat{R}$ is the vector of the simulated reflectances. Matrices W and C are the covariance matrices containing the observation and model uncertainties and the uncertainties of the prior information, respectively, as well as the covariance terms (Tarantola, 2005). Each term is weighted by the inverse of its covariance matrix, which represents the Bayesian degree of belief. However, as the uncertainties are often unknown and difficult to estimate in practice, they are assumed to be uncorrelated and W and/or C become diagonal (e.g. Laurent et al., 2013). Note that the first part of the equation is equal to Equation 2.19.

Alternatively, prior information can be introduced to approaches which use a pre-computed data base (LUT and ANN) by adapting range, sampling intervals, and distribution of the input parameters used for canopy realizations (e.g. Darvishzadeh et al., 2008b; Dorigo et al., 2009). In this regard, ecosystem specific parameterizations strongly reduce the ranges of input variables and increase the retrieval performance as long as no misclassification occurs (Baret and Buis, 2008; Dorigo et al., 2009). Otherwise, as proposed by Koetz et al. (2005a), a pre-selection of LUT entries based on the radiometric similarity can be exploited based on a prior guess of the result. Further, LUTs and ANNs can account for model and measurement uncertainties by adding noise to the LUT or learning data set (Combal et al., 2002b).

Constraints can also be derived from spatial or temporal information (Lauvernet et al., 2008). Atzberger (2004) introduced the inclusion of neighborhood signatures of a land use object (agricultural fields). Based on the assumption of a constant canopy structure, intra-field radiometric variability is used in combination with radiometric information to distinguish between planophile and erectophile canopies. This leads to a reduction of the confounding effects between LAI and LAD often observed for RTMs. Based on these findings, Houborg et al. (2009), Laurent et al. (2013), and Atzberger and Richter (2012) use a 2-step inversion approach. The first inversion over an object is used to derive the values of most model parameters for the second, pixel-wise inversion. This reduces the ill-posedness of the second inversion, which focuses on the variable of interest. These methods require RS imagery with a spatial resolution sufficient to detect different pixels within one field.

The introduction of temporal constraints is based on the known dynamic of biophysical variables over time, which can be used to determine the typical ranges of input parameters in a particular development stage (Koetz et al., 2005a). These constraints can be introduced either directly when known, or through additional models such as SVAT or canopy structure dynamics models, which mimic the evolution of vegetation variables over time (Launay and Guerif, 2005; Koetz et al., 2007a; Duveiller et al., 2011b). Kötz (2005a) reported improved parameter estimates, particularly for large LAI values where signal saturation occurs. However, this approach cannot include abrupt changes caused by events such as harvesting, lodging, fire, or pest infestation. Lauvernet et al. (2008) minimized a cost function simultaneously over multi-temporal observation of a patch of reflectances. A certain spatial and temporal stability is assumed for the atmosphere and canopy parameters, respectively, thus reducing the overall number of unknown parameters.

A variety of parameter fixation is the coupling of parameters, which is often performed for leaf water and dry matter content (see e.g. Weiss et al., 2000; Bacour et al., 2006; Duveiller et al., 2011b; Richter et al., 2011). This is based on the knowledge that relative water content in healthy green leaves is about 80 %, so that the water to dry matter ratio is fixed as 4:1. Another option is integrating individual parameters into synthetic parameters at the canopy level. Examples are the canopy chlorophyll content (leaf chlorophyll content × LAI) or total water content (leaf water content × LAI). These variables are physically meaningful, as they correspond to the actual optical thickness of the canopy, and their estimation using RS data has been proven to be more accurate than chlorophyll or water estimation on the leaf level (Jacquemoud et al., 1995a; Fourty and Baret, 1997; Lauvernet et al., 2008).

2.3. LAI products

Advances in radiation transfer modeling have enabled the operational derivation of LAI for about one and a half decades. The derivation of LAI from RS imagery has been a trade-off in this regard: high spatial resolution imagery came to the expense of low revisit frequency. As a high temporal resolution is crucial for monitoring vegetation parameters, so far only coarse resolution data are used for automated LAI derivation. Global LAI is thus provided at about 250 - 1000 m spatial and 4 - 30 days temporal resolution. Improved atmospheric correction, radiometric calibration and model formulation have continuously enhanced their retrieval accuracy, although discrepancies between products and with ground data still remain (Weiss et al., 2007; Garrigues et al., 2008a; Baret et al., 2013). Besides, some regional, data fusion, as well as first global medium resolution LAI products have been developed (Table A-1).

One of the most widely used LAI products is the MODIS LAI at 1 km spatial resolution, which has been made available since 2000. The theoretical basis of the algorithm is given in Knyazikhin et al. (1998). It is based on ecosystems specific 3D formulation of radiation transfer. The inversion is performed using LUTs, with daily imagery derived from MODIS-Terra and/or Aqua acquisitions, and the mean value of all acceptable solutions is retained as the final output value. The daily values are then integrated into one 4-day (both sensors combined) and three 8-day composites (each individual sensor and both sensors combined). If the main algorithm fails (in about 25 - 40 % of all cases), a backup algorithm based on LAI-NDVI relationships is used (Myneni et al., 2002; Yang et al., 2006). Additional per pixel information on product quality is provided. Since its first release, the MODIS LAI product has been widely used and received considerable validation. As the former collection 4 product was reported to have temporal and spatial inconsistencies and to overestimate LAI especially over forests (Cohen et al., 2006; Weiss et al., 2007; Garrigues et al., 2008a), collection 5 was improved in this regard (Kraus, 2008; Sprintsin et al., 2009; Fang et al., 2012).

The Multiangle Imaging Spectroradiometer (MISR) LAI product has been routinely processed since October 2002. It is based on the same 3D RTM and LUT algorithm as the MODIS product, but makes synergistic use of the spectral and directional information collected by MISR. The latest version is the level 3 product. As no backup algorithm is implemented, the algorithm provides LAI retrievals for 60 - 90 % of the input data (Hu et al., 2003; Hu et al., 2007).

Based on global data from the multi-angle POLDER (POLarization and Directionality of Earth Reflectance) sensor on ADEOS, LAI was derived over synthesis periods of 30 days using the PROSPECT Kuusk models and ANN inversion. In total, eight months of POLDER-1 data (Roujean, 2002) and seven months of POLDER-2 data are available (Lacaze, 2005).

CYCLOPES (Carbon Cycle and Change in Land Observational Products from an Ensemble of Satellites) LAI is operationally derived from VEGETATION data at 1 km resolution and with a temporal resolution of 10 days. Its algorithm is based on PROSAIL, with the option of pixels being a mixture of bare soil and vegetation patches. The PROSAIL output is used to train an ANN which is inverted over atmospherically corrected and BRDF normalized daily VEGETATION data, and smoothed with a moving window of 30 days (Baret et al., 2007). Validation and comparisons to other LAI products have shown good performance and stable temporal profiles, even though it suffers from saturation of LAI values larger than 4 (Weiss et al., 2007; Garrigues et al., 2008a; Duveiller et al., 2011b). CYCLOPES LAI has been developed within the CYCLOPES project and its successors “geoland” and “geoland2”, and is now provided as the “LAI Version 0” product in the Copernicus program.

GEOV1 is one of the BioPar products developed within the “geoland2” project (Baret et al., 2010a). It is a version of the CYCLOPES product, with the same spatial and temporal resolution and also based on ANNs, but with different training data. Instead of employing an RTM, the GEOV1 product exploits pre-existing LAI maps, namely the MODIS and CYCLOPES products. Their reflectances and LAI estimates are smoothed and corrected to overcome known deficiencies for low LAI values of MODIS and high LAI values of CYCLOPES, and used as a learning data set for the ANN. Inversion is then performed over VEGEGATION data (Verger et al., 2008; Verger et al., 2011b; Baret et al., 2013). Validation shows that GEOV1 LAI has smooth and intra-annually consistent temporal profiles (Camacho-de Coca et al., 2013). It is provided under the Copernicus program as “LAI Version 1”. Another geoland2 BioPar LAI product is based on MERIS data. It uses PROSAIL in addition to a surface shadow model and an ANN inversion technique, and has a spatial resolution of 300 m and a temporal resolution of 10 days (Bacour et al., 2006). The product is provided for the years 2003 to present at near-real-time for Europe. In addition, on-demand products can be generated on geoland2 sites (Poilvé, 2012).

Another global LAI product based on VEGETATION data is GLOBCARBON, developed by ESA for the years 1998 - 2007. It additionally exploits data from the ENVISAT/ATSR-2 and MERIS (Medium Resolution Imaging Spectrometer) sensors. GLOBCARBON has a spatial resolution of 1 km and provides monthly global LAI maps. The algorithm encompasses a two-step LAI derivation (Deng et al., 2006): preliminary LAI values are derived for six different plant functional types using a land cover classification. Based on this LAI, a BRDF correction is applied to the RS data. The final LAI value is derived using land cover specific statistical relationships with VIs established on the 4-scale GORT model by Chen and Leblanc (1997). LAI is estimated from each sensor for each time interval, and then the monthly median is computed (Plummer et al., 2006). The GLOBCARBON LAI has few missing values, but large spatial and temporal instabilities (Garrigues et al., 2008a). The Canadian Center for Remote Sensing (CCRS) is routinely generating Canada-wide LAI products from AVHRR and VEGETATION at 1 km resolution as 10-day composites using empirical algorithms. However, considerable errors and biases have been reported (Chen et al., 2002a; Fernandes and G. Leblanc, 2005). Rochdi and Fernandes (2010) also introduce an algorithm using empirical relationships to map LAI across Canada, however using 250 m MODIS data.

ECOCLIMAP differs from the other products in that it is a climatology based on land cover maps, climate maps, and NDVI data. It is empirically derived using LAI values extracted from literature which are scaled over the growth period according to AVHRR NDVI dynamics. In this regard, LAI is not computed for each pixel but is estimated for an entire ecosystem (Masson et al., 2003; Champeaux et al., 2005). ECOCLIMAP has weaknesses in describing inter-annual and spatial variations of LAI, and generally overestimates LAI. At Boston University, another monthly LAI product (8 km spatial resolution) based on the AVHRR NDVI time series for 1981 - 1994 was developed using global land cover information and relationships established on a 3D RTM (Myneni et al., 1997; Buermann, 2002).

An important step forward to higher spatial resolution LAI global products has been taken by Ganguly et al. (2012) at NASA, who recently proposed an algorithm for a provisional global LAI product at the 30 m Landsat scale. The implementation is based on a modified MODIS algorithm, and, in addition to the red and NIR reflectances, a SWIR band is used. Based on Landsat 5 and 7 (TM/ETM+) data, LAI has been derived for the years 2004 - 2007 over California. So far, global coverage has not been achieved[7].

2.4. Current research needs

The measurement of LAI in the field and LAI derivation based on remotely sensed imagery has been an active field of research for about four decades. This chapter presented an overview of the relevant methods. Indirect *in situ* measurement techniques have been developed, which still have some shortcomings, but proved to measure LAI handily within a certain accuracy given a sound sampling procedure. Various empirical-statistical techniques have been extensively used although they are still restricted to the conditions that prevailed during the experiment. Also the understanding of the radiation regime within vegetation canopies has strongly increased and led to the development and validation of sophisticated RTMs of varying degrees of complexity.

---

[7] http://landsat.usgs.gov/LAI_Products.php. Last access: February 22, 2014.

Nowadays, the focus lies on developing robust techniques making use of these models. Three challenges that have persisted since the beginning of LAI derivation in this regard are signal saturation, inversion ill-posedness, and the dependency on field data for model tuning. These issues still impair the operational derivation of LAI based on physical as well as empirical-statistical models. Approaches to overcoming these problems, e.g. by scaling or interpolating of non-sensitive spectral signals (Duveiller et al., 2011b; Baret et al., 2013), by using regularization techniques in RTM inversion (Combal et al., 2002b; Laurent et al., 2013; Rivera et al., 2013), or by extracting additional information directly from the RS data (Atzberger, 2004; Lauvernet et al., 2008) have been proposed during the last decade. Another issue is the missing knowledge and management of uncertainties – of the resulting LAI estimates as well as of data and model uncertainties – which are necessary to implement Bayesian inversion approaches and to use the LAI estimates in a range of applications (Baret and Buis, 2008). None of these aspects has been consolidated so far (Verrelst et al., 2014).

New and upcoming multispectral sensor systems, which will combine high revisit frequency with high spectral and spatial resolution, will on the one hand improve the usage of spatial and temporal constraints during inversion by enabling the identification of individual fields and growth trajectories, and on the other hand ease the discrimination of land cover types and thus RTM parameterization due to a reduced amount of mixed pixels (Baret and Buis, 2008; Jacquemoud et al., 2009; Duveiller and Defourny, 2010; Baret et al., 2013). However, with higher resolutions, the computational efficiency of LAI derivation approaches also becomes of greatest interest (Duveiller et al., 2011b). Technical issues such as efficient optimization algorithms, appropriate LUT construction, regularization techniques, or the handling of different observation geometries in one process could be mentioned.

As stated above, the coupled PROSPECT+SAIL model is the most widely used RTM, due to its availability and the extensive investigation of its strengths and weaknesses (Jacquemoud et al., 2009). Shabanov et al. (2000) point out that 1D RTMs are a valid approximation for small and relatively homogeneous canopies. Indeed, some studies have used PROSAIL or one of its versions for crop LAI derivation based on different high resolution data: air-borne RS data (1 - 5 m spatial resolution, Atzberger et al., 2003b; Laurent et al., 2013; Laurent et al., 2014), AVIRIS (Airborne Visible/Infrared Imaging Spectrometer) data (20 m, Jacquemoud and Baret, 1993), Landsat data (30 m, Atzberger, 2004), or CHRIS (Compact High Resolution Imaging Spectrometer) data (34 m, Atzberger and Richter, 2012). However, only few studies analyzed time series of high spatial resolution data, e.g. of SPOT data with 20 m resolution (Duveiller et al., 2011b) and air-borne data of 20 m (Koetz et al., 2005a). In these studies the general usefulness of inversion techniques based on pre-computed reflectance databases for multi-temporal analysis is mentioned, but the advantages, difficulties, and necessary considerations associated with the LUT approach are not discussed. Weiss et al. (2000) and Darvishzadeh et al. (2008b) used a LUT based inversion of PROSAIL and raised specific questions on the LUT and cost function settings, but none of them investigated them in detail with regard to temporal and spatial high resolution RS data.

For these reasons and due to the general requirement of time series information for environmental monitoring purposes, multi-temporal LAI derivation based on the PROSAIL model and LUT inversions are pursued in this thesis. The RapidEye sensor (6.5 m spatial resolution) has been barely used for physical LAI derivation (Vuolo et al., 2010; Vuolo et al., 2012). Furthermore, no study on LAI estimation from RTMs based on high spatial resolution satellite data has been conducted so far in grassland ecosystems that consist of a range of different species. Available grassland studies are all based on data generated using field spectrometers (Dorigo, 2007; Darvishzadeh et al., 2008b; Vohland and Jarmer, 2008). Therefore, the main objective of this thesis is to quantify the performance of RapidEye time series data in a LUT inversion for a heterogeneous grassland landscape over two growing seasons. The potential of the RTM approach is compared to that of empirical-statistical LAI derivation which serves as a benchmark.

3. Study area

In this chapter, the area in which this thesis is conducted is presented. To gain an impression of the variety of grassland occurrences prevailing in this region, the climate and topography as well as the anthropogenic influences that shape the ecological conditions for grasslands are described. The catchments of the River Ammer and its tributary Rott in the Bavarian Alps and alpine foreland cover an area of about 770 km². They are situated between the Lake Ammer and the German-Austrian border at latitude 47°30' to 47°57' and longitude 10°51' to 11°16' and stretch over the administrative districts of Garmisch-Partenkirchen and Weilheim-

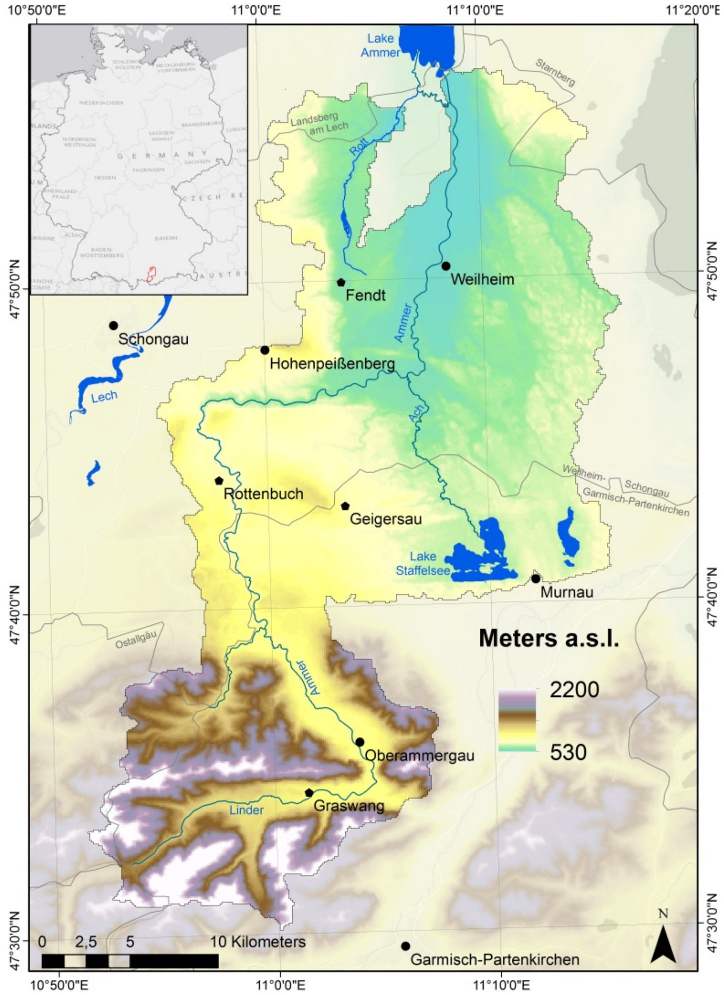

Figure 3-1: Topography of the Ammer catchment. The map shows a digital elevation model (DEM) provided by the DLR based on Shuttle Radar Topography Mission (SRTM) data (see chapter 4.2).

Schongau (Figure 3-1). The River Ammer originates from the Ammergau Alps, situated partly in Bavaria (Germany) and partly Tyrol (Austria). Its headwater is the creek Linder, which sinks into its riverbed between Linderhof Palace and Graswang due to karstic underground and resurfaces as Ammer about 5 km before it passes by Oberammergau. Before entering lower areas near Peissenberg, where the river bed becomes wider, the Ammer has carved a gorge of up to 80 m depth through the molasse hills near Rottenbuch. The river drains into the Lake Ammer, located 35 km south-west of Munich, up to where the length of Linder and Ammer is 84 km. Downstream of Lake Ammer, the river continues as Amper, which flows into the River Isar north of Munich and thus belongs to the drainage basin of the Danube (Rippl, 2011). The catchment is delimited to the west by the catchment of the River Lech and to the east by the catchment of the River Loisach. It is primarily characterized by its topography, which causes a large spatial differentiation in climate, soil, and land use (Smiatek et al., 2012). The highest elevation (Kreuzspitze) is at 2185 m above sea level (a.s.l.) in the Ammergau Alps, and the outflow into the Lake Ammer is at 533 m a.s.l.

The catchments are part of the German Helmholtz Initiative TERENO (TERrestrial ENvironmental Observatories, Bogena et al., 2012). Together with the research stations Schechenfilz (south of Lake Starnberg), Höglwald (near Augsburg), and Scheyern (north of Munich), they form the TERENO *Alps/pre-Alps Observatory*. At the stations Graswang, Geigersau, Rottenbuch, and Fendt (see Figure 3-1) a measurement network collects data about biosphere-atmosphere exchange processes as well as meteorological data, of which the irradiance measurements are used in this thesis (see chapter 4.3.2). The main objectives of the TERENO observatory are the long-term monitoring of global change effects on C-/N-cycles, nutrient deposition, trace gas exchange, vegetation and microbial biodiversity, and Alpine watershed hydrology.

3.1. Climate

Southern Germany is characterized by a warm temperate humid mid-latitude climate with predominating westerly winds throughout the year. Due to the topography of the study area, temperature and precipitation have latitude and height dependent gradients, contributing to the variety of environmental conditions in the study area (Kunstmann et al., 2004). The long-term annual air temperature averages (reference period 1981 - 2010) are around 8 °C in the alpine foreland and around 4.5 °C in the mountainous areas (Figure 3-2). Precipitation rates are relatively high overall and reach their maximum in the summer season. Long-term mean annual precipitation increases from its minimum in the north (~ 1000 mm) to maximum values above 2000 mm in the southern mountain ranges (Figure 3-3). The number of days with snow cover (depth > 10 cm) in the catchment is around 130 days per year (Ludwig, 2000). Winds differing from the common westerlies produce special weather conditions in the alpine foreland: in the winter months, southerly winds, the so-called *Föhn*, cause air masses to descend in the lee of the Alps, bringing warm and dry weather conditions with sometimes stormy winds. Northerly winds, however, often cause cloud formation and heavy precipitation as a result of the forced uplift of the air on the windward side of the mountains. This weather situation with extreme convective precipitation over restricted areas occasionally leads to severe flooding in the Ammer and neighboring catchments, such as in August 2005 or August 2010, due to the fast response of river runoff to precipitation events in Alpine catchments (Smiatek et al., 2012). With regard to the vegetation cover, the climatic conditions in the area inhibit the intensive cultivation of crops but favor grassland and forest ecosystems.

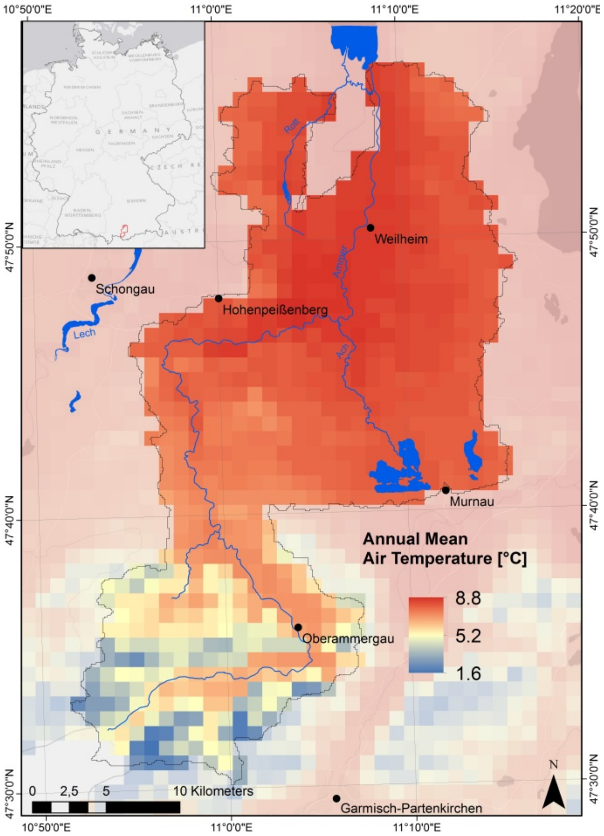

Figure 3-2: Annual long-term average of air temperature in the Ammer catchment for the reference period 1981 - 2010. Data provided by the German Weather Service (DWD)[8].

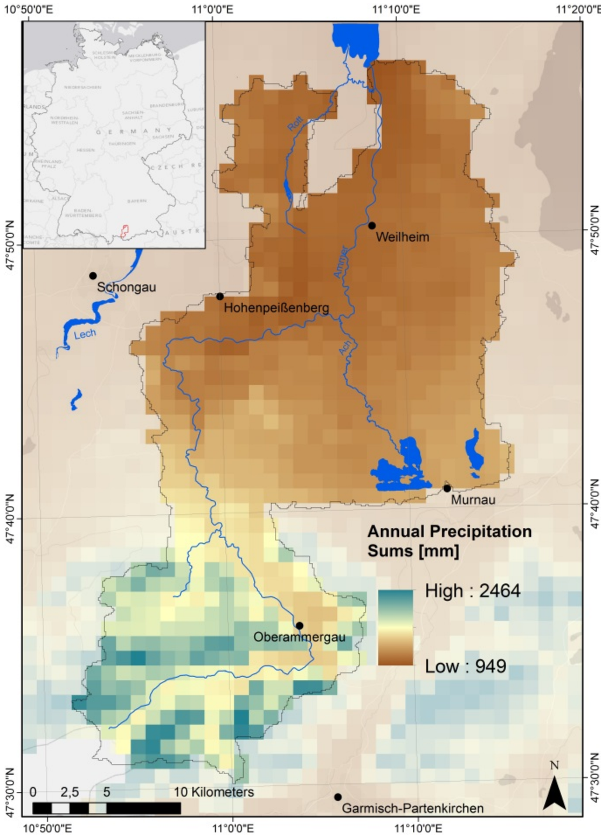

Figure 3-3: Annual long-term average of precipitation in the Ammer catchment for the reference period 1981 - 2010. Data provided by the German Weather Service (DWD)[8].

3.2. Geology, geomorphology and soils

The study area stretches over two major natural regions of Germany: while the southern half is part of the *Bavarian-Tyrolean Intermediate Limestone Alps*, the northern part belongs to the *Subalpine New Moraine Land,* which is a hill country characterized by its Pleistocene glaciations and recent processes (Dongus, 1993). The three main geological units are the lime and dolomite alpine zone in the south, the intermediate flysch zone, and the folded and unfolded molasses in the northern part of the catchment. Soil genesis only started after the end of the most recent ice age (Stolz, 1998).

The region roughly south of 47° 35' N is called the *Ammergau Alps*. In contrast to the rather homogeneous *Northern Limestone Alps* bordering to the south, they consist of complexly stratified and folded series of different facies (Figure 3-4). Lying in this transition zone, the Ammergau Alps' geomorphology is characterized by three different mountain forms (Figure 3-6). The southern part of the Ammer mountain range consists of Mesozoic rocks. In the southernmost part, Triassic Principal Dolomite rocks have the main share, which are characterized by huge walls with rather monotonous summits such as the Kreuzspitze (2185 m a.s.l.). Dolomite rock generates a lot of debris, thus vast debris screes (so called *Griese*) shape the slopes and valley bottoms. The area north of the Graswang valley is dominated by lithographic and *Wetterstein* limestone with accordingly more diverse and rugged mountain formations such as the Klammspitze (1924 m a.s.l.) or the Hochplatte (2082 m a.s.l.). In

---

[8] Data downloaded on March 4, 2014, from http://www.dwd.de/bvbw/appmanager/bvbw/dwdwwwDesktop?_nfpb=true&_pageLabel=dwdwww_result_page&gsbSearchDocId=960246.

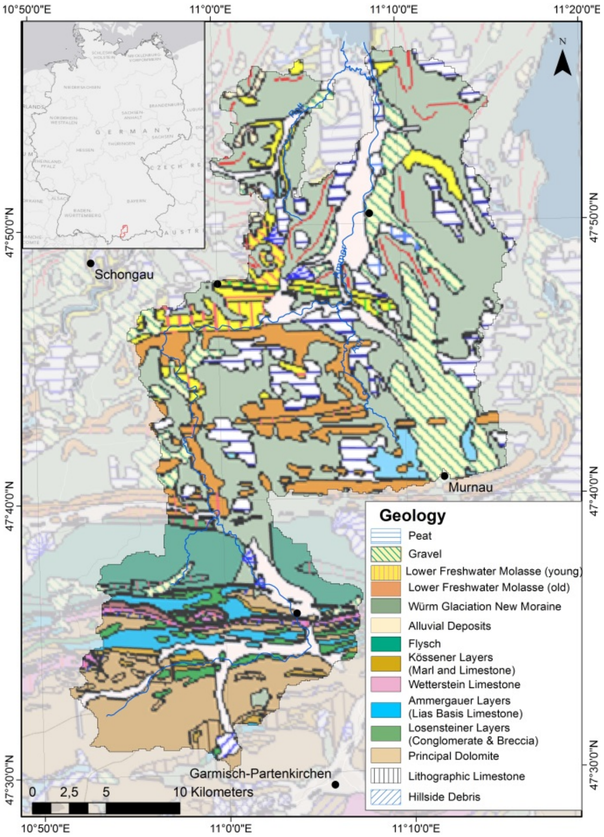

Figure 3-4: Geology of the Ammer catchment. Data provided by the Bayrisches Landesamt für Umwelt (LfU)[9]. The fault zones are indicated as black lines.

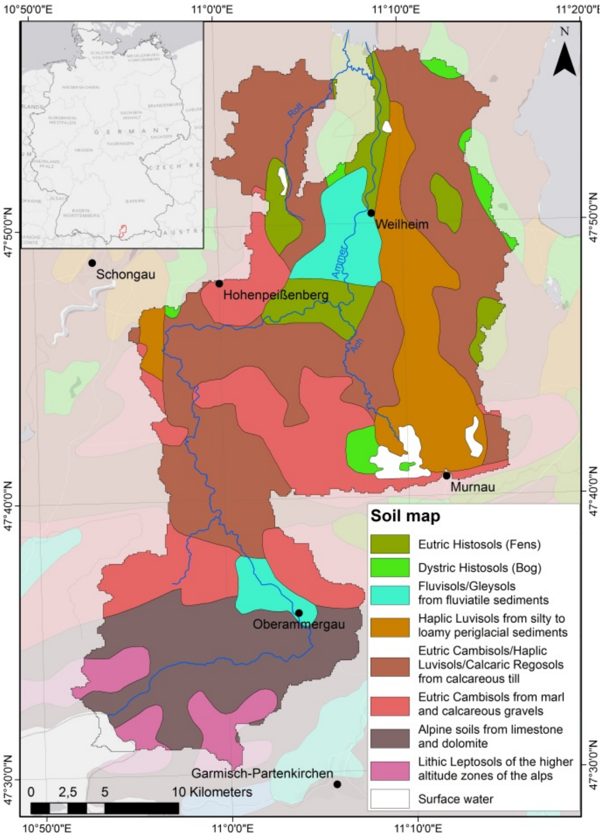

Figure 3-5: Soil Map of the Ammer catchment. The soil map BUEK1000DE (Hartwich et al., 1998) is provided by the German Bundesanstalt für Geowissenschaften und Rohstoffe (BGR)[10].

these areas, only shallow alpine soils sparsely covered by vegetation have developed (e.g. Rendzic and Umbric Leptosols, dark brown and pink signature in Figure 3-5, Hartwich et al., 1998).

The so-called *Flysch Alps* (red signature in Figure 3-5) north of a fault zone at Oberammergau constitute the northern fringe of the Ammergau Alps. Their parent rock consists of Cretaceous subaquatic sediments such as marlstone and calcareous gravels and is therefore quite erosive. This created rather low and round mountain ranges that are almost completely covered by forests such as the Hörnle (1548 m a.s.l.). Their soils, mostly Eutric Cambisols and Podzols, are prone to erosion and landslides (Freudenberger and Schwerd, 1996; Fischer, 2002). In addition to the large geological units, small areas of marl, sandstone, radiolarite, and the debris screes on the valley bottoms contribute to the pedological and hence ecological heterogeneity of this area, which shelters a range of rare species. Not least because of this, but also due to the low human impact in this area, the Ammergau Alps became a nature reserve in 1963 and are still the largest site under the habitats directive (NATURA 2000) in Bavaria (Bundesamt für Naturschutz, 2013, see Figure 3-7).

The area north of the fault zone near Unternogg belongs to the Alpine foreland. It consists of hill country and moorland with landforms such as moraines and drumlins shaped by the last

---

[9] Geological data of Bavaria can be viewed under http://www.bis.bayern.de/bis/initParams.do. Last access: March 13, 2014

[10] Data downloaded on March 4, 2014, from http://www.geoshop-hannover.de/.

Figure 3-6: View of the Upper Ammer Valley with the *Hörnle* and *Aufacker* summits as part of the lower *Flysch Alps* in the background and the *Laber* and *Ettaler Mandl* summits from calcareous rock to the right. The brownish area at the valley bottom is the *Weidmoos*.

glacial period (Würm glaciation) (Frank, 1979; Meyer and Schmidt-Kaler, 1997). The bedrock of the new moraine landscape is Tertiary molasse, which can be further differentiated into a southern part of folded molasses (*subalpine molasses*) and a northern part of undisturbed molasses (*foreland molasses*), with the fault zone near Peissenberg being the border. It is overlaid by Pleistocene sedimentary rock such as gravel (ocher signature in Figure 3-5) and moraine till (red-brown signature) left behind by the Isar-Loisach glacier, which weathered to loamy and sandy Cambisols. Only in a few places can outcrops of the molasse bedrock, such as the Hohen Peissenberg (988 m a.s.l.), be found. Fluvisols and Gleysols (turquoise signature) evolved in depressions and on the fluviatile sediments along the river valleys.

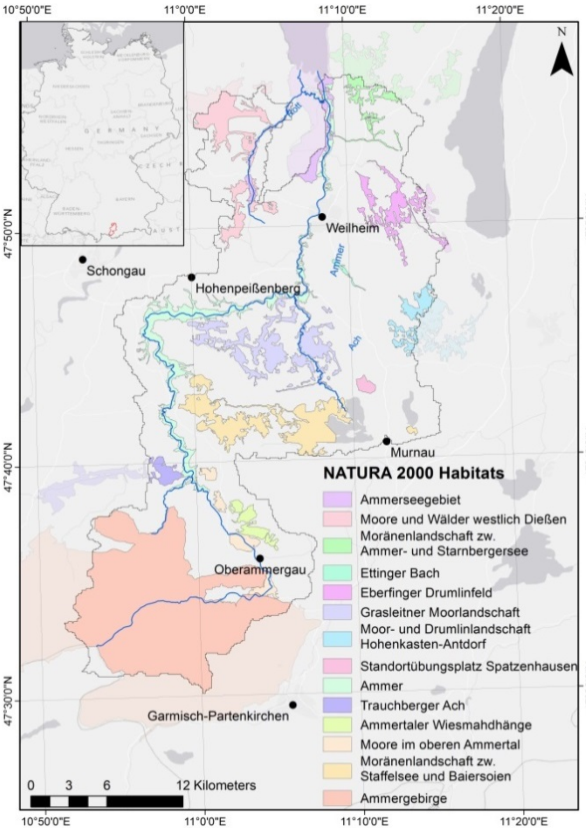

Figure 3-7: Distribution of Natura 2000 sites within the Ammer catchment with their (shortened) German names. The data are provided by the European Environmental Agency[11].

Overall, the pedogenesis in the Ammer catchment resulted in relatively shallow soils unfavorable for crop cultivation, but sufficient for grassland ecosystems. Further, relatively large parts of the study area are covered by fens and bogs, mostly along the river valleys and in the littoral zones of the lakes (green signatures in Figure 3-5, Hartwich et al., 1998). Due to their size and integrity, most of them are protected under the habitats directive. Examples of big fens are the *Weidmoos* and the *Pulvermoos* in the Natura 2000 site *Upper Ammer Valley* (beige signature in Figure 3-7), the *Grasleitner moorland* (purple signature), or the moorlands west of Lake Staffelsee (yellow signature). They include inter alia the habitats 'alkaline fens', 'transition mires and quaking bogs', 'active raised bogs', and 'natural dystrophic lakes and ponds'. These very humid and alkaline areas are covered by grasses and herbaceous species to a great extent, and are thus treated as grasslands in this study as long as they are not covered by standing water (see chapter 4.1.3).

---

[11] Spatial data on the Natura 2000 sites can be downloaded from http://www.eea.europa.eu/data-and-maps/data/natura-2/natura-2000-spatial-data. Last access: March 10, 2014

3.3. Land cover

The rural land cover of the study area is representative of the alpine upland of Central Europe. It is a heterogeneous landscape fragmented by small settlements, forest patches and small-scale agricultural areas. According to the CORINE (COoRdination of INformation on the Environment) land cover classification for the reference year 2006 (CLC2006) provided by the European Union, the Ammer catchment is dominated by agricultural areas (43.7 %) and forests (41.4 %), while only 3.7 % of the area is constituted by urban areas, 4 % are fens and bogs, 4.2 % are transitional shrub-woodland, and 1.8 % are sparsely vegetated areas and bare rock (Figure 3-8). These latter two classes occur mainly above 1200 m in the Alpine areas of the catchment. The high share of forested areas especially in the southern part of the catchment is also caused by topography. These mountain areas have only shallow soils and either too steep or erosion-prone slopes on the Flysch bedrock, and thus are not usable for agriculture. In 2011, 217 829 people lived in the two administrative districts of Garmisch-Partenkirchen and Weilheim-Schongau (Bayerisches Landesamt für Statistik und Datenverarbeitung, 2013a, 2013b), although only 40 % of the area of both districts is covered by the Ammer catchment, excluding big towns such as Garmisch-Partenkirchen. The largest towns inside the catchment are Weilheim (about 21 300 inhabitants), Peißenberg (about 12 300 inhabitants), and Murnau (about 11 500 inhabitants).

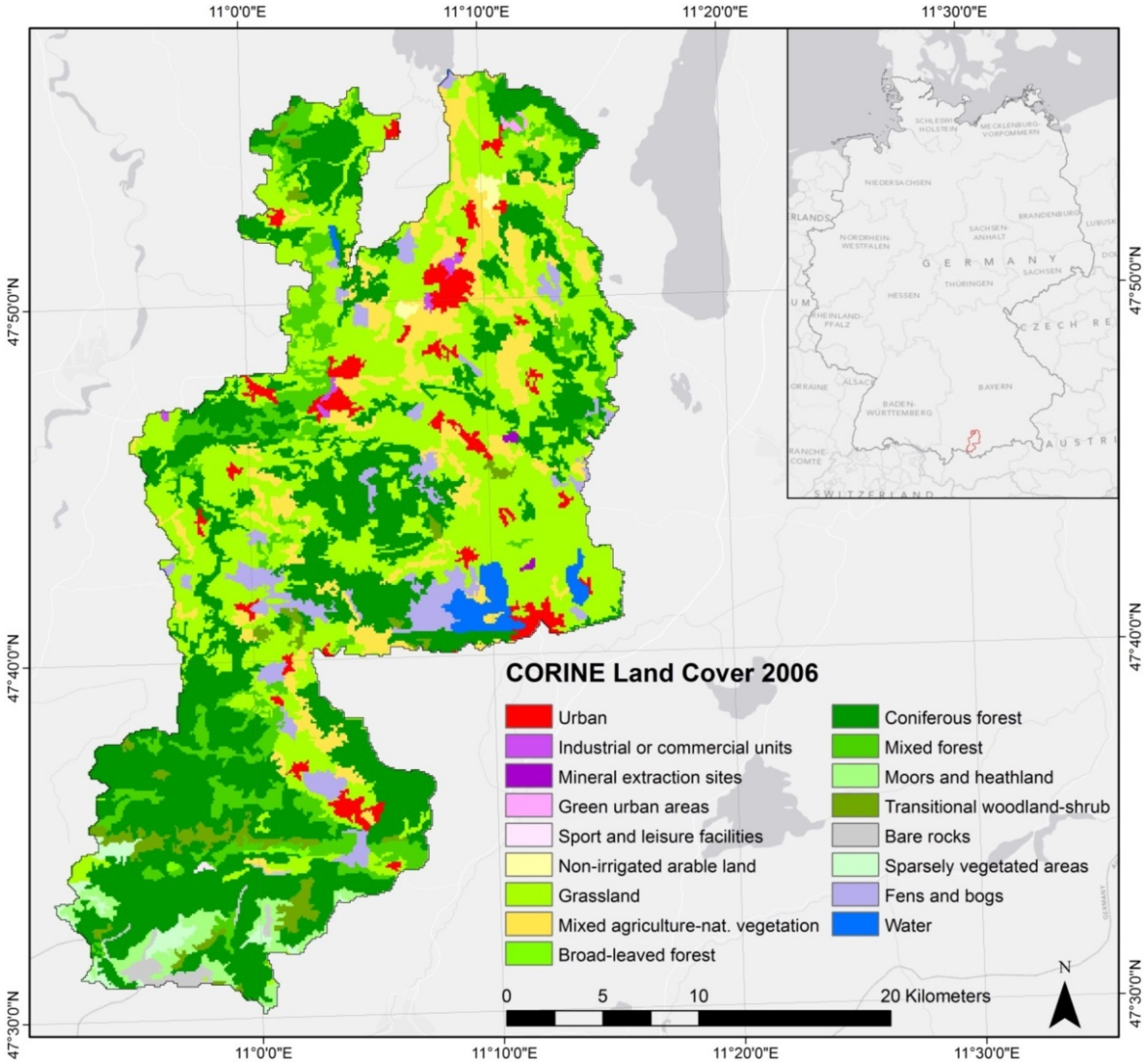

Figure 3-8: Simplified CORINE land cover classification of the Ammer catchment (colors according to official legend) and its location in Germany (upper right).

3.4. Economy

The importance of the individual economic sectors in the districts of Garmisch-Partenkirchen and Weilheim-Schongau (Table 3-1) is in line with the economic structure of Bavaria, although the relevance of agriculture and forestry in both districts is higher than the Bavarian average (0.5 %). As mentioned above, due to the humid climatic conditions, a short growing season length, and the relatively young and shallow soils, the cultivation of field crops is rather unproductive in most agricultural areas in the Ammer catchment (Stolz, 1998). According to the CLC2006, only few fields (6.6 % of the agricultural areas) in the Ammer catchment are used for crop cultivation, which is far below the Bavarian average of about 65 % (Bayerisches Landesamt für Statistik und Datenverarbeitung, 2013c). Following the climatic gradient, the crop fields are rather arranged in the northern part of the catchment and are mostly used for winter wheat and winter barley, rape and forage maize. The major part of the region's agricultural areas is thus grassland used for hay production and cattle livestock farming (see below). The mean proportion of the industrial sector in the districts is slightly lower than the Bavarian average (difference of 0.4 %), and the industrial production is distributed unequally between the northern and the southern parts of the region (Table 3-1, Bayerisches Staatsministerium für Wirtschaft und Medien Energie und Technologie, 2013). Garmisch-Partenkirchen has neither got big firms nor much space for industrial facilities due to the orography, protected areas (more than 50% of the district's area) and vast forested areas. Weilheim-Schongau, however, has better topographical conditions as well as a longer industrial tradition (e.g. pitch coal mining in Peißenberg and Penzberg with its heyday in the 1960s, Balthasar et al., 1975) and a range of medium-sized enterprises.

Apart from the above-average relevance of agriculture and forestry in the Ammer catchment, tourism stands out, especially in the district Garmisch-Partenkirchen. The development of tourism in the region was fostered early on through the construction of the train connection from Munich that reached the town of Murnau in 1879 and Garmisch-Partenkirchen in 1889. Tourism is nowadays an important economic sector and contributes strongly to the region's gross sales (e.g. 18.4 % of the primary income in Garmisch-Partenkirchen for the year 2012, Bengsch and Neumann, 2013). With more than 3 million overnight stays, Garmisch-Partenkirchen ranks under the 10 most frequently visited places in Bavaria. Nature plays an important role for tourism, with the main activities being hiking and skiing (Wagner, 2013). Thus the state of the grasslands in the area is also relevant for this economic sector. Further, the fens played an important role in the economic and touristic evolution of the region, as the extraction of mountain pine peat in the Ammer Valley laid ground to the development of several health resorts. Spa tourism and the associated economic branches such as the health and social services sectors still account for 25 % of all insurable employments in Garmisch-Partenkirchen (Bayerisches Landesamt für Statistik und Datenverarbeitung, 2013b).

Table 3-1: Economic structure of the administrative districts in the Ammer region (differentiated for the districts of Garmisch-Partenkirchen and Weilheim-Schongau; Bundesamt für Bauwesen und Raumordnung, 2007). The share of each sector in the economy of the districts is indicated.

	Garmisch-Partenkirchen	Weilheim-Schongau
Agriculture and forestry	0.9%	1.1%
Industries	19.3%	48.0%
Tertiary sector	79.8%	50.9%

3.5. Grasslands

In contrast to most crops, the grassland ecosystem can be quite productive under humid and rather cold conditions and even develop dense canopy structures with LAI values of up to 10 (Wohlfahrt and Cernusca, 2002; Becker et al., 2007). Although the plant communities of these grasslands are natural, they are often referred to as semi-natural grasslands since almost all European grasslands have been created by agricultural activities to a major extent and are more or less modified by human activity (Silva, 2008). Different fertilization intensities have led to differentiations of plant community and biomass production.

The grasslands in the region are maintained through grazing and cutting regimes, as agriculture consists mainly of dairy and meat production. In the two administrative districts, a total of 93 600 cattle were kept in 2010 (Bayerisches Landesamt für Statistik und Datenverarbeitung, 2013b, 2013c). Grassland communities consist of two thirds of grass species and one third of leguminous and herbaceous species. However, due to different management practices, this ratio and the specific species composition can vary considerably. Meadows are grasslands that are never grazed but cut several times a year for fodder production. This sudden intervention favors grass species and more light resistant herbaceous species. After the first harvest in late spring, manure fertilization is often applied on meadows in the alpine upland. Pastures are grazed by animals, which is a more continuous and selective process and brings forth herbaceous species that are resistant to steps and disdained by cattle. Also here, the nutrient input through animal excretions constitutes a fertilization that in turn favors demanding species, leading to additional spatial differentiation of species composition (Klapp, 1971). Further, pastures can be separated into year-round pastures and rotational grazing systems. The latter are hayfields that are subdivided into grazing lots, which are alternately grazed for 2 - 4 days to allow for regeneration afterwards. In some areas, such pastures are in addition periodically cut to remove weeds and lush vegetation patches of animal rest areas, or to obtain winter fodder (Ellenberg and Leuschner, 2010). In the alpine upland, most pastures are cultivated using these rotational grazing and cutting hayfield systems. With the grazing and/or vegetation cuttings followed by rapid plant re-growth, these grasslands undergo multiple growing cycles within a single vegetation period (Wohlfahrt and Cernusca, 2002).

Apart from the intensively used mesophile grasslands, there are many extensively managed grassland types in the Ammer catchment. Two European agro-environmental schemes that aim to preserve biodiversity, the High Nature Value (HNV) farmland indicator and the habitats Natura 2000 directive are implemented in the area. The designation of both area types relies on the abundance and kind of occurring species or habitats, and especially on grasslands, these areas do overlap. In HNV areas, the aim is to preserve low-intensity agriculture with 1-2 harvests per year and no or little fertilization, as well as the resulting semi-natural biomes (BfN, 2014). The Natura 2000 habitats may be but do not have to be areas used for agriculture. Habitats such as ‘semi-natural dry grasslands‘, ‘species-rich Nardus grasslands’, ‘lowland hay meadows’, and ‘mountain hay meadows’ are characteristic for dry grassland communities on the region’s calcareous bedrock. All of these habitats are of high relevance for rare plant and animal species, and can for example be found in the Natura 2000 site *Ammertaler Wiesmahdhänge* (light green signature in Figure 3-7). Rather humid grassland sites, often situated on alkaline fens and other moorlands, are cultivated hay meadows including the habitats “Molinia meadows on calcareous, peaty or clayey-silt-laden soils” and “hydrophilous tall herb fringe communities”. Large Molina sites are located in the Upper Ammer Valley or north and west of Lake Staffelsee. All these sites are developed and cultivated by man and need regular anthropogenic intervention to prevent the invasion of reed and scrubs. Therefore, they are managed according to specific guidelines that require farmers to mow the grassland no more than once per year (after September 1st), but at least once every second year to maintain the respective habitat type and species composition. Livestock farming and fertilization is not allowed on these meadows (Bundesamt für Naturschutz, 2013).

As shown above, the topography and geology in the Ammer catchment creates a heterogeneous and fragmented landscape. A wide variety of ecological niches is laid out by the microclimate, relief, and soils at relatively small spatial and temporal scales, creating different grassland species compositions (Pauli et al., 2003a). This diversity is extended through the above mentioned farmers' management techniques, differing in their frequency and timing of (selective) plant removal through mowing and grazing. They further increase the high spatial and temporal variability of grassland types and occurrences in the region, as illustrated in Figure 3-9.

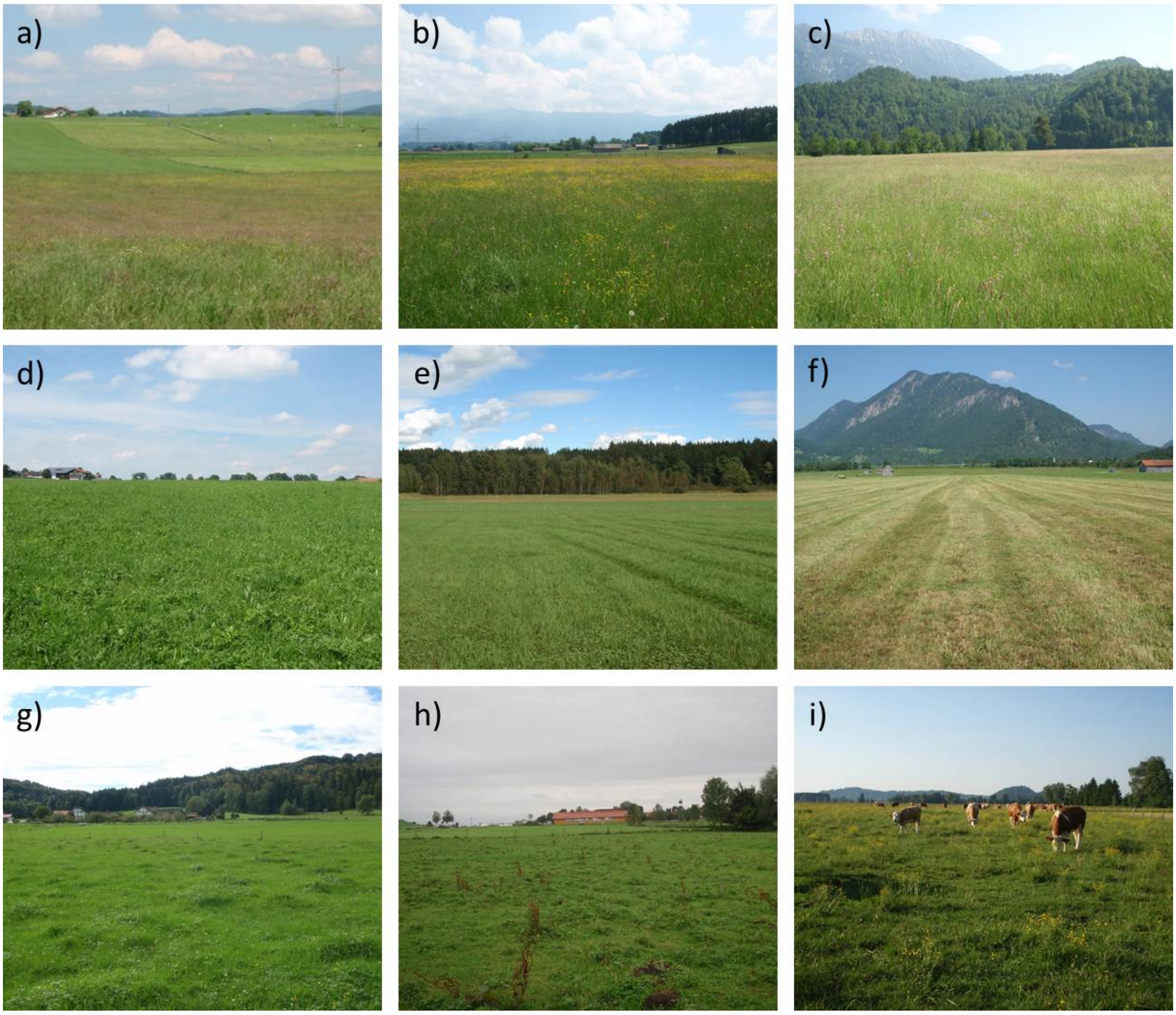

Figure 3-9: Examples of the grassland types and occurrences due to different managing techniques. a) The meadows vary in occurrences on a very small scale. b) and c) Examples of dense meadows shortly before harvest in differently nutritious sites. d) Intensively mowed meadow with a high herbage share. e) and f) Meadows shortly after harvest, with traces from the combine harvester. g) Meadow of a rotational grazing-mowing system still showing patterns caused by pasturing. h) and i) Intensively grazed pastures with reptant herbs and patches of species spurned by cattle. Photos taken in May 2011 (a, b, c, d, f, and i) and September 2011 (e, g, and h).

The productivity and functioning of the different grassland ecosystems in the Ammer catchment can be altered and even lost through land abandonment and consequent afforestation, changes in livestock density, or intensification of grassland management (e.g. through fertilizers, pesticides, and alien grass varieties). The conversion into arable land due to its higher profitability and recent developments such as increased biofuel production are also relevant in the region (Silva, 2008). The state of the grasslands in the alpine upland can thus not be taken for granted, and their monitoring is of high relevance for several reasons (Smit et al., 2008). Firstly, this agro-ecosystem is used for fodder and cattle production, so its surveillance is important for agrarian issues such as yield monitoring, but also for political and economic reasons, as proper grassland management is subsidized e.g. on the Natura 2000 sites. Apart from the feed supply, grasslands are responsible for the supply of a range of ecosystem services, such as reducing erosion by supporting slope stability, regulating water regimes and purifying water from fertilizers and pesticides (Reid, 2005). Further, the conservation of biodiversity in managed agricultural landscapes is of high relevance, as extensive grasslands are among the most species-rich habitats in Europe (WallisDeVries et al., 2002). Grasslands also support cultural services, for example by contributing to a region's cultural heritage and recreational values (Hopkins and Holz, 2006). To ensure these services, the ecological functions of this ecosystem need to cope with a range of global changes. While grasslands are already under great pressure due to the various human activities, alpine ecosystems are assumed to be particularly sensitive to changes in the climate system and ecological changes such as nutrient deposition (Beniston, 2005; Becker et al., 2007; Rammig et al., 2010).

4. Data and preprocessing

In this chapter the RS and i*n situ* data used in this thesis for statistical LAI modeling as well as for RTM calibration and validation are presented. The RapidEye data specifications, their preprocessing and the land cover classification applied to the RapidEye data, which are applied to identify the grassland areas and correct their reflectances, are presented first (chapter 4.1). Chapter 4.2 presents the used digital elevation model (DEM), while in chapter 4.3 the sampling design and the data collected during the field campaigns are summarized.

Figure 4-1 gives an overview of the number of all available data sets and the timing of the *in situ* measurement campaigns (green) with regard to the RapidEye acquisitions (blue) over the study area for the years 2011 and 2012. Each field campaign took between two and seven days, depending on the number and type of measurements conducted. It was intended to have the field measurements well distributed over the growing season in order to cover as many phenological stages as possible. As the fastest changes in natural vegetation occur in spring, measurements were taken more often during this period. The April campaign of 2011 was repeated in 2012, as snow fall and a defective measurement device prevented a sound measurement procedure during the first campaign. Additionally, measurements were conducted in August 2012 to better cover the phenological maximum.

In total, 20 RapidEye images are available for both years. However, this includes all scenes that have even a little coverage of the catchment. Thus, during the two years a complete cover of the catchment is achieved only eight times (Figure 4-2). Only a narrow corridor between approximately 10°55' E and 11°15' E longitude, that is a stripe of 4.3 km width, is covered ten times. Clouds further reduce the spatial information available individually for each scene. The scenes are rarely taken directly at nadir, but the view angles of the scenes do not exceed 15° from nadir. The sun zenith angle ranges from 24.2° to 48.8°. An overview of the acquisition conditions of the RapidEye scenes is given in Table A-2.

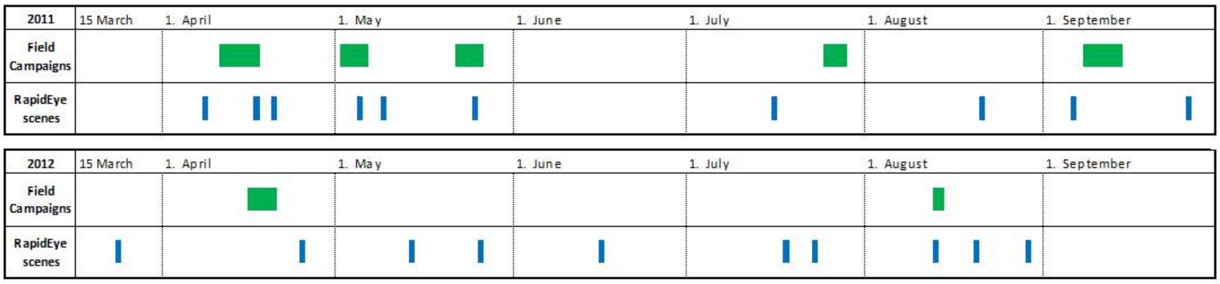

Figure 4-1: Dates of ground measurements and RapidEye acquisition dates. The green boxes indicate the field campaigns while the blue lines indicate the days of the RapidEye acquisitions.

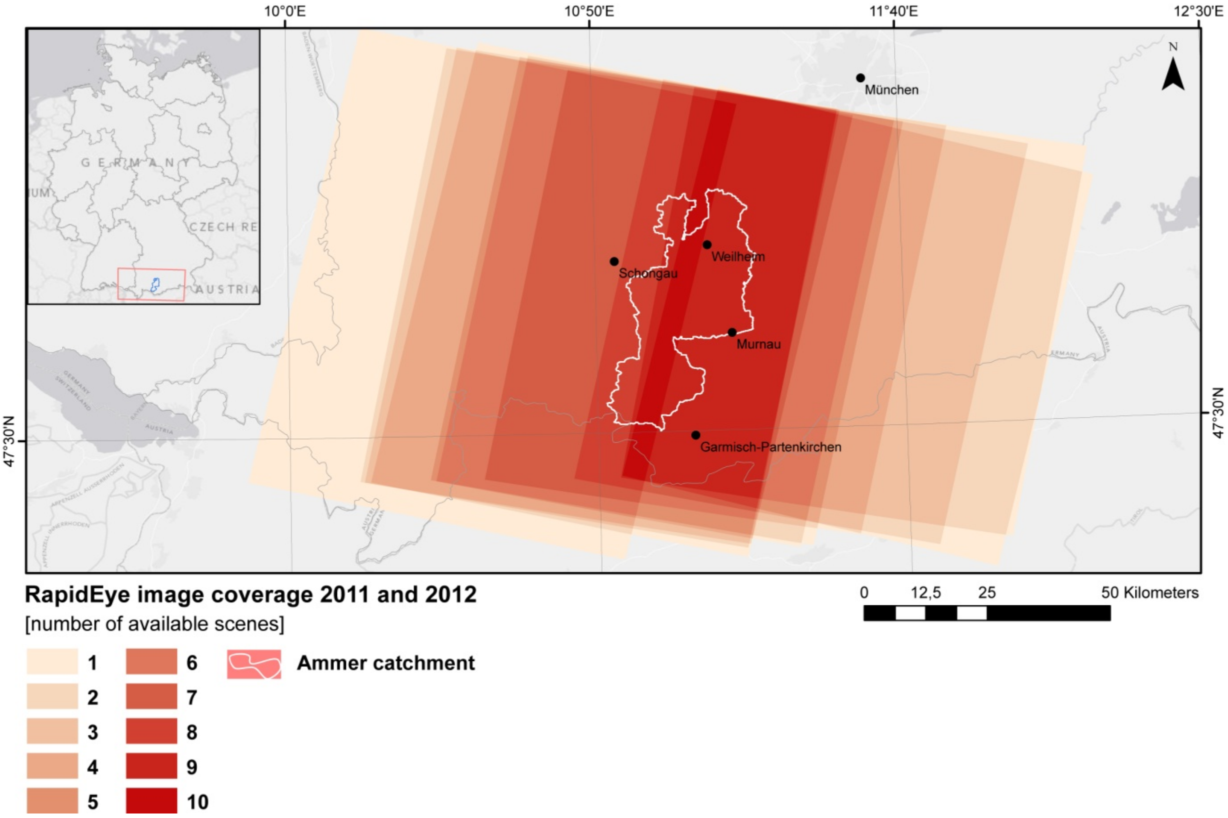

Figure 4-2: Number of available RapidEye scenes in 2011 and 2012 over the Ammer catchment.

4.1. RapidEye data

4.1.1. Data specifications

The RapidEye constellation was launched on August 29, 2008 from the spaceport Baikonur in Kazakhstan by the RapidEye AG and is now run by the company BlackBridge. It consists of five satellites located in the same sun-synchronous orbital plane at an altitude of 630 km. They carry identical sensors that are calibrated equally to one another, hence can be treated identically. The cameras are push broom scanners with five spectral bands in the VIS and NIR domain (see Table 4-1) built by Jena Optronic (Reulke and Weichelt, 2012). In this regard the red edge band is an exceptional feature as up to the time of the RapidEye launch, the MERIS sensor was the only multispectral sensor equipped with a channel in the red edge region. Each of the five linear arrays contains 12 000 sensor elements. With a field of view (FOV) of ± 6.75° about nadir, RapidEye has a swath width of 77 km. The FOV can be oriented across track by up to ±25°. The spatial resolution of RapidEye is 6.5 m. This is converted to 5 m resolution for the level 3 product. 4 million km² of data are recorded by the five sensors

Table 4-1: Wavelengths and band width of the RapidEye bands.

Band	Wavelength [nm]	Bandwidth [nm]
Blue	440 – 510	70
Green	520 – 590	70
Red	630 – 685	55
Rededge	690 – 730	40
NIR	760 – 850	90

every day. The broad swath width, wide field of regard, and the use of five identical satellites enable a high temporal resolution despite the high spatial resolution. Daily images can be recorded in the off-nadir, while the revisit frequency for at nadir acquisitions is 5.5 days. All images are collected, stored, and sent to the receiving station at a radiometric resolution of 12 bit, where they are radiometrically corrected and scaled to 16 bit dynamic range (RapidEye, 2011). With its high spatial resolution, frequent revisits, large area coverage, and the additional red edge band, RapidEye is potentially highly suited for the monitoring of vegetation properties (Tyc et al., 2005).

4.1.2. Data preprocessing

RapidEye imagery is available in two processing levels, the basic product (level 1B data) and the ortho-suite product (level 3A data). In this thesis, level 1B data with a spatial resolution of 6.5 m were used. The bands are delivered as individual NITF 2.0 files. Level 1B data are sensor level data with basic radiometric and geometric sensor corrections (RapidEye, 2011).

At-sensor corrections

The radiometric corrections performed on the level 1B data comprise the correction of radiometric differences between the five detectors, non-responsive detector filling, and the conversion to values directly related to the initial at-sensor spectral radiance. The radiometric calibration is necessary because the sensors convert the signal of incoming energy to a digital number (DN). To convert the relative pixel DNs into absolute radiance values, scaling constants (gain c_1 and offset c_0) are used:

$$\mathrm{L} = \mathrm{c}_0 + \mathrm{c}_1 \times \mathrm{DN} \tag{4.1}$$

The calibration coefficients c_1 and c_0 have been determined during pre-launch for each sensor element of each band and are periodically updated through statistical checks of all recorded image data, additional acquisitions over calibration sites and absolute ground calibration campaigns. The resulting DN values in the RapidEye images correspond to a TOA radiance of 0.01 $\mathrm{W/m^2\ sr^{-1}\mu m^{-1}}$ scaled to 16 bit (RapidEye, 2011).

The basic geometric sensor correction accounts for distortions caused by the internal detector geometries, by the combination of the two sensor chipsets into a virtual array, and by the co-registration of all bands which have imaging time differences of up to three seconds. Additionally, ephemeris corrections are performed. This means that the images are geometrically corrected to an idealized sensor and satellite model, but no terrain model is used in the processing of the 1B products. Therefore, the indicated default image horizontal accuracy of the basic product, which is at least 23 m CE90[12] in areas of higher Ground Control Points (GCP) quality, is only valid for images collected at nadir over flat terrain (RapidEye, 2011). The data used in this thesis have an accuracy of 12.3 - 30.4 m CE90.

Geometric corrections

The overall aim of geometric rectification of RS data is to ensure the spatial comparability of different data sources, in this work of different RapidEye scenes, the DEM, and *in situ* measurements. An overview of sources for systematic and non-systematic geometric distortions is given by Richards and Jia (2006). While the first kind of errors is corrected

---

[12] CE90 is the minimum diameter of the circle centered on all GCPs that contain 90 % of their respective counterparts acquired in the scene.

during the basic geometric corrections of level 1 imagery, non-systematic errors cannot be accounted for automatically and thus require manual corrections. In the Ammer catchment, strong non-systematic geometric distortions are mainly introduced by the terrain. For this reason, in addition to georectification, orthorectification was performed.

As the Rational Polynomial Coefficients (RPC)[13] useful for geo- and orthorectification are encoded in the NITF file subheader, the original data files were used in a first step for orthorectification of each individual band, based on the RPCs and a 30 m SRTM DEM (see below). After the composition of the individually orthorectified bands in a GeoTIFF format, the layer stacks were transformed into the Universal Transverse Mercator (UTM) projection (Zone 32N, WGS 84 datum). As the resulting scenes did not match each other exactly but still showed deviations of up to 40 m in some parts of scenes, the RapidEye image from May 9, 2011 was georeferenced using 14 GCPs collected in the field as well as a first order polynomial warp. The resulting geometric error was less than one RapidEye pixel (RMSE of 0.77). This is higher than the general rule of remaining under half a pixel location error (Richards and Jia, 2006), but could not be reduced due to the complex terrain. Afterwards, all other RapidEye scenes were co-registered to the May 9, 2011 scene.

Masking

In the next step, all water bodies, snow covered areas, clouds, and cloud shadows were masked manually in the RapidEye images. The same water mask was applied to all 20 images, whereas all other masks were created scene-specifically. Manual masking of water became necessary as a wide variety of water bodies – rivers, creeks, lakes and ponds of differing depth and sediment load – with very different spectral properties occur in the study area, which made an automated detection difficult. Clouds were not extracted from the cloud masks delivered with the RapidEye L1B product, as these masks had weaknesses over the bright rock outcrop and snow areas in the alpine areas, as well as in detecting thin clouds and contrails. Cloud shadows could not be identified automatically based on the cloud masks due to the complex terrain. Additionally, snow areas were masked in six of the RapidEye images.

Atmospheric and topographic corrections

As described in chapter 2.2.1, radiance reaching the sensor is influenced by processes that occur during the downward and upward transfer of radiance through the atmosphere, and thus needs to be corrected for these effects. In this thesis, the IDL code of the ATCOR3 software (Richter and Schläpfer, 2012) was used. ATCOR uses large sensor-specific databases (LUTs) of atmospheric correction functions, which are the results of pre-calculated radiative transfer simulations with the MODTRAN5 (MODerate resolution atmospheric TRANsmission) model (Berk et al., 2008). The LUTs cover a wide range and various combinations of aerosol types, water vapor content, visibility, solar angles, and ground elevations. The automatic estimation of the AOD over dark reference pixels in ATCOR was applied in this thesis. Further, the option of having variable AOD in the scene was chosen, as potentially significant visibility differences were assumed for the alpine and foothill areas of the study region. The automatic AOD estimation resulted in visibility ranges between 15 and 70 km for the different scenes (Table A-3). In three scenes, additional haze removal was

---

[13] To gain a relation between image and ground coordinates for every pixel, each sensor relies on a model, i.e. a set of equations incorporating information such as platform altitude, viewing angle, and sensor focal length. To approximate this relationship without inverting the sensor model, RPCs (Rational Polynomial Coefficients or Rapid Positioning Coordinates) are used in analytical models (Xiong and Zhang, 2009).

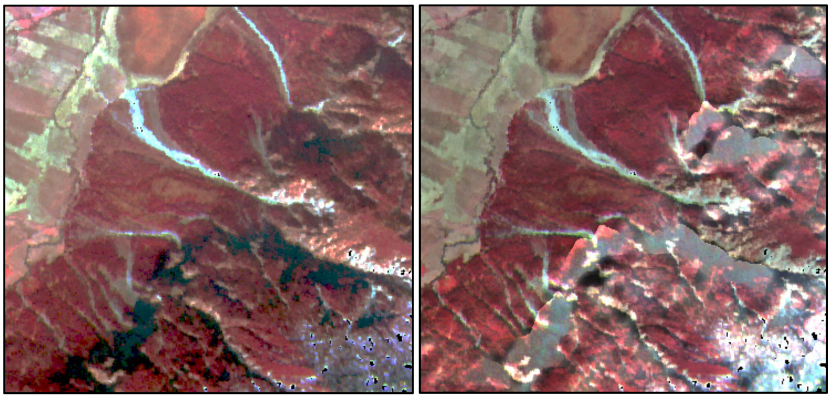

Figure 4-3: Example of overcorrection effects due to topographic correction in steep, shaded terrain (right image) in comparison to the original scene (left image). Shown is a subset of the April 8, 2011 RapidEye scene in the Loisach Valley near Oberau, band combination 5-3-2.

applied. The rural aerosol type was chosen for the corrections, as well as the mid-latitude summer atmosphere, which corresponds to a 2-3 cm water vapor column. The range of adjacency effects, which accounts for the adjacency radiation L_{adj}, was set to 0.1 km.

Due to the rugged terrain in the alpine region of the study area, topographic correction is necessary. The aim of topographic correction is twofold: to account for L_{ter} on the surface reflectance and to normalize the reflectances to the viewing direction, thus to create reflectances as they would have been measured over flat terrain. The ATCOR3 program provides the possibility of topographic corrections concurrently with the atmospheric correction by incorporating a DEM. The DEM enables a BRDF correction as well as the calculation of L_{ter} based on a sky view factor[14] (Richter and Schläpfer, 2012). However, no satisfying results could be achieved for the RapidEye scenes. Very steep, shaded slopes were strongly overcorrected, probably due to the extreme viewing geometries and the bright limestone background (see Figure 4-3). This overcorrection on faintly illuminated areas with local solar zenith angles above 60°, caused by the usual but unfitting assumption of an isotropic reflectance behavior, is also mentioned by Richter and Schläpfer (2012). Furthermore, the use of the relatively high resolution slope and aspect maps derived from the DEM led to artefacts (stripes) in the corrected image even on flat terrain. Although this problem is also mentioned in the ATCOR manual and the selection of a larger kernel size is recommended, the smoothing of these maps prior to their application in the topographic correction did not solve the problem entirely, but simultaneously falsified the BRDF correction by reducing the high frequency spatial information.

Therefore, a different strategy was pursued. No topographic correction was applied to the RapidEye images to avoid introducing the above mentioned errors. Instead, the ATCOR2 code for flat terrain was used and the local viewing and illumination geometries were included directly in the RTM forward and inverse runs (see chapter 6.4). For the classification and the empirical-statistical approach, the subtle spectral differences due to exposition were assumed negligible in comparison to measurement errors and noise, especially as the LAI samples used for training are located mostly in flat terrain. To still account for the strong elevation differences in the study area which are influencing the dimension of the atmospheric column and thus the length of the radiation path through it, the study area was segmented in three elevation zones (Figure 4-4, hatching signatures). Each elevation class covers an altitude range of 400 m, for which the average ground elevations (760 m, 1290 m, 1680 m) were used in the ATCOR2 processing of the respective

---

[14] The sky view factor V_{sky} determines the fraction of the hemispherical diffuse sky flux (1 indicating a full hemispherical view) and 1- V_{sky} determines the fraction of radiation L_{ter} reflected from surrounding mountains onto the considered pixel (Richter and Schläpfer (2012).

image segments. All other ATCOR parameters were kept identical. After the individual atmospheric corrections of the three elevation segments of each scene, the segments were mosaicked. This procedure neglected the influence of the terrain reflected radiation L_{ter}, but was nevertheless recommended in personal communication with Mr. Richter. The adjacency radiance L_{adj} is still accounted for in the ATCOR2 procedure.

In a last step the preprocessed 2011's April 17 and April 20 scenes were mosaiked, as each of the scenes covered half of the study area and were sufficiently close in time.

4.1.3. Land cover classification

A land cover map for the Ammer catchment was derived from multi-temporal RapidEye imagery using the random forest (RF) classifier. Each supervised classification relies on pairs of land cover observations (*responses*) and associated spectral characteristics (*predictors*). These characteristics are called features, and a classification is performed by generating rules that assign a land cover class to specific features. Classifiers can be divided in parametric and non-parametric methods, determined by their dependence or independence from assumptions on the statistical distribution of the input data (Hastie et al., 2009).

RF is a non-parametric ensemble of decision tree classifiers. Decision trees need to be trained (*built*) before they can be used to assign (*predict*) land cover classes based on RS data. They are hierarchical schemes that split the feature space into sub-spaces using binary decisions. At each decision (*node*) a certain threshold value of a single feature is used to split the data set into two subsets. Thereby, the aim is to increase the purity of the response values in the two subsets, which can be achieved and automated using statistical metrics. Following this scheme, the resulting subsets are split, in turn. Terminal nodes (*leaves*) are reached when the response variables in the node consist of a single class, or if further splitting is constrained (e.g. by specifying a minimum amount of pixels per node), in which case the class label is assigned to the majority class within the node (Breiman, 1998). Apart from their fast generation compared to other iterative methods, decision trees have several advantages. First of all, there is no need to reduce the feature space beforehand to the most important and preferably un-correlated features, as the most significant feature is automatically selected at each split (Breiman, 2001). Further, the tree construction is resistant to noise and outliers. Since not only continuous but also ordinal and nominal scaled data can be included as predictors, the approach is directly applicable to multi-source RS and geographic data (Seni and Elder, 2010). The ability of treating different spectral profiles of a land cover class by assigning them to different leaves is a further asset, especially given the omitted topographic correction, which probably amplifies the spectral within-class variability. However, a drawback of the approach is its sensitivity to the influence of single features, and the resulting variance of the predictions. A slight change in training data can lead to a different tree architecture. Thus, to optimize the robustness of the approach, to avoid over-fitting, and to increase the prediction accuracy, decision tree ensembles are normally used (Ho, 1998).

Ensembles are created by building multiple trees in parallel and independently by randomly changing their construction parameters and finally combining the predictions of the trees based on majority voting. This is on the one hand achieved in the RF classifier by *bagging*, i.e. training each tree in the forest on a different training data set randomly sampled from the original data (referred to as 'bootstrap aggregation', Breiman, 1996, 2001). On the other hand *boosting* is applied, which consists of randomly sub-setting the features available for splitting at each node from the feature vector (Ho, 1998; Chan and Paelinckx, 2008). Tree-based ensemble classifiers, and thereby especially RF, have repeatedly proven to be effective for land-cover classifications (Pal, 2005; Watts and Lawrence, 2008; Hüttich et al., 2011; Löw et al., 2012).

The RF classifier in this thesis was built using the "randomForest" package implemented in the R statistics language (Liaw and Wiener, 2002). For classification, three RapidEye scenes (May 9, July 16, and September 6) were used. A multi-temporal classification approach was chosen, as some of the land cover classes, for example "winter wheat" and "grasslands", show similar spectral signatures in advanced development stages, but distinctly different phenologies (continuous grassland vegetation cover vs. bare soil of harvested crops). The scenes were stacked into one data frame together with three VIs which were derived from each scene, namely the NDVI, SAVI, and the NDVI with the red edge band substituting the red band ($NDVI_{re}$), resulting in a 24 layer feature space.

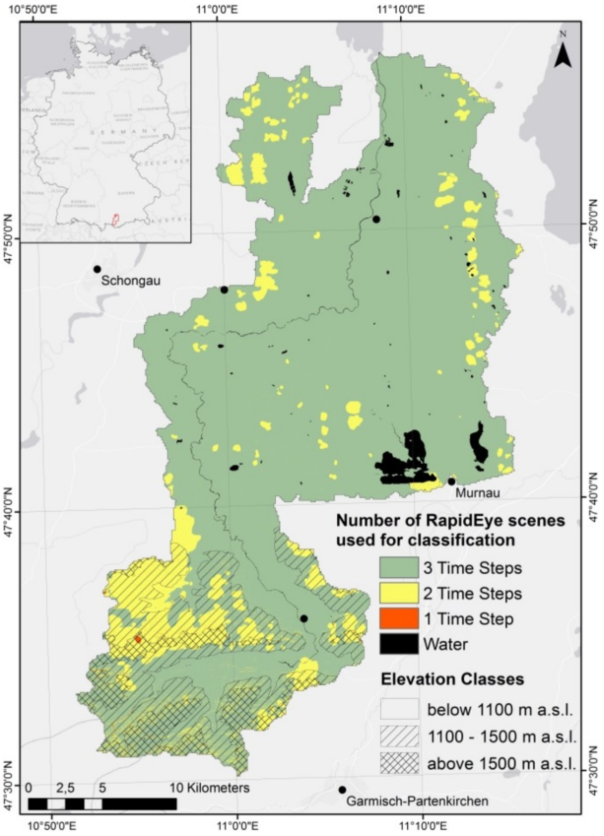

Figure 4-4: Number of RapidEye scenes used for classification and elevation classes used for atmospheric correction of each pixel.

The training and validation data were collected *in situ* as well as derived visually within the RapidEye scenes with the help of Google Earth imagery. As water bodies, snow, clouds, and cloud shadows had already been masked manually, the remaining land cover classes in the area were 'rock/concrete', 'forest', 'grassland', 'moor', as well as the field crops "rape", "maize", and "wheat". 298 polygons covering about 83 000 pixels were marked first, as the selection of polygons is a quick and robust procedure. However, as the number of collected pixels per class varied strongly due to different shares of the classes in the area and the different sizes of land cover objects and the associated polygons, random subsets of 3 000 pixels were drawn per class from the polygons for training as well as for testing. This was done by splitting the 298 polygons into two groups and then drawing 3 000 pixels per class from each group. Although on the one hand this poses the risk of grouping all small and all big polygons of a land cover class, which might restrict the number of available pixels for training and validation, it ensures on the other hand that pixels from the same land segment (e.g. field or forest patch) are not used for both training and validation, which seemed more relevant. Indeed, the above mentioned bottleneck was only seldom reached, and only for the rather small classes of rape, maize and wheat, and 3 000 pixels could be drawn for training and validation of most classes.

The number of trees within the RF was set to 500 in order to achieve convergence (Löw et al., 2013). For bagging, the size of the sampling subset was defined as two thirds of the training data set, and the number of features to split the nodes during boosting was set to five, which is the rounded square root of the number of input features, as commonly recommended (Liaw and Wiener, 2002; Gislason et al., 2006). The remaining third of training data, which is not used for the construction of the tree, is automatically used for testing the tree. The

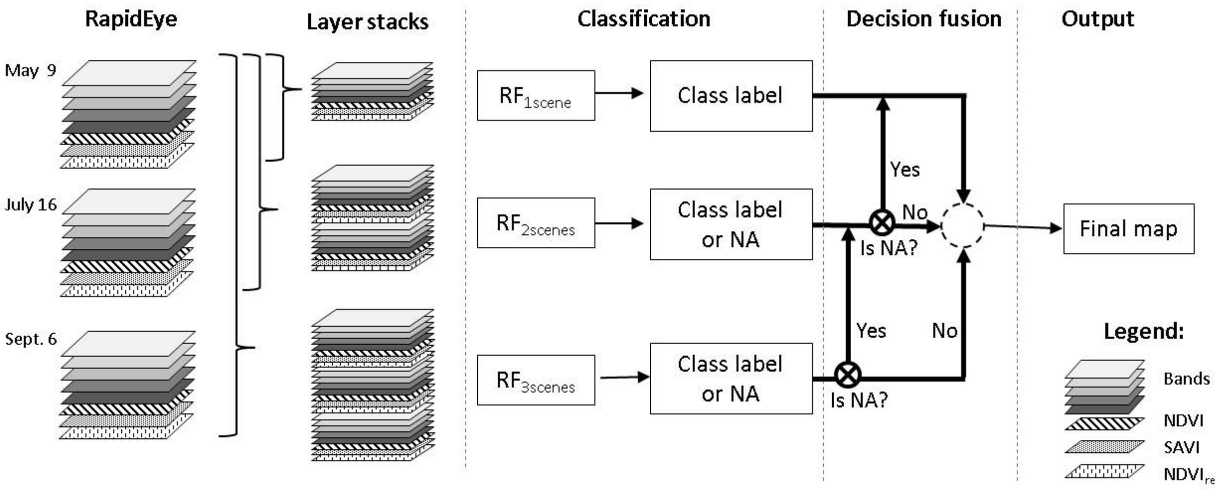

Figure 4-5: Workflow of the multi-temporal classification and iterative mosaicking procedure based on the randomForest classifier. The layer stack just based on the May 9 scene is not affected by missing values due to clouds or snow and therefore provides a classification result for every pixel.

error measure derived from this sample is called out-of-bag (OOB) error and equals an n-fold cross-validation. The stabilization of the OOB error after several tree generations indicates the stabilization of the prediction (Hastie et al., 2009). However, studies showed that the OOB is a rather conservative error assessment (Breiman, 2001; Gislason et al., 2006). Therefore, the independent test set for the class-wise validation has been used additionally.

As the use of a stack of three RapidEye scenes (having different cloud and snow covers) increased the amount of pixels in the stack with missing values in at least one of the layers, which creates an NA output, an iterative classification and mosaicking procedure was applied (see Figure 4-5). Additionally to the three time steps layer stack, the same RF classification was performed on a two time steps stack (May 9 and July 16) as well as on the single May 9 scene which had no missing values from masking. Using an iterative rule set, the classifications were composed afterwards by filling the NA value gaps of the three-scene classification with values of the two-scene classifications, or, if no data were available in this map either, with the single-scene classification. Figure 4-4 shows that the classification of most areas could rely on three scenes (86.1 %, green signature) while only a minor area (0.15 %, orange signature) consists of information from only one time step.

The resulting land cover map is displayed in Figure 4-6. The landscape structure with its rather small agricultural parcels, the forest fragments, and the fen and bog areas as well as the settlements are represented with a high level of detail. The overall test set error of the three scene classification is 3.4 % (OOB error: 0.1%), the error of the two scene classification is 6.4 % (OOB error: 0.3%), and the overall test set error of the single classification scene is the highest with 8.8 % (OOB error: 2.0 %; see Table 4-2, Table A-4, and Table A-5). With regard to the combined classification, these accuracies are valid for the respective areas indicated in Figure 4-4. Thus, apart from its use for filling cloud gaps, the multi-temporal classification ensured higher classification accuracy for most pixels of the map. The confusion matrices show the number of correctly classified pixels on the diagonal in relation to the omission and commission errors for each individual class. As this thesis focuses on the grassland class, special interest lies on the error of this class (Table 4-2). In the three scene classification, its commission error is 2.0 % and thus even lower than the overall error. Most confusion occurred with the moorland class, which is caused by the high spectral

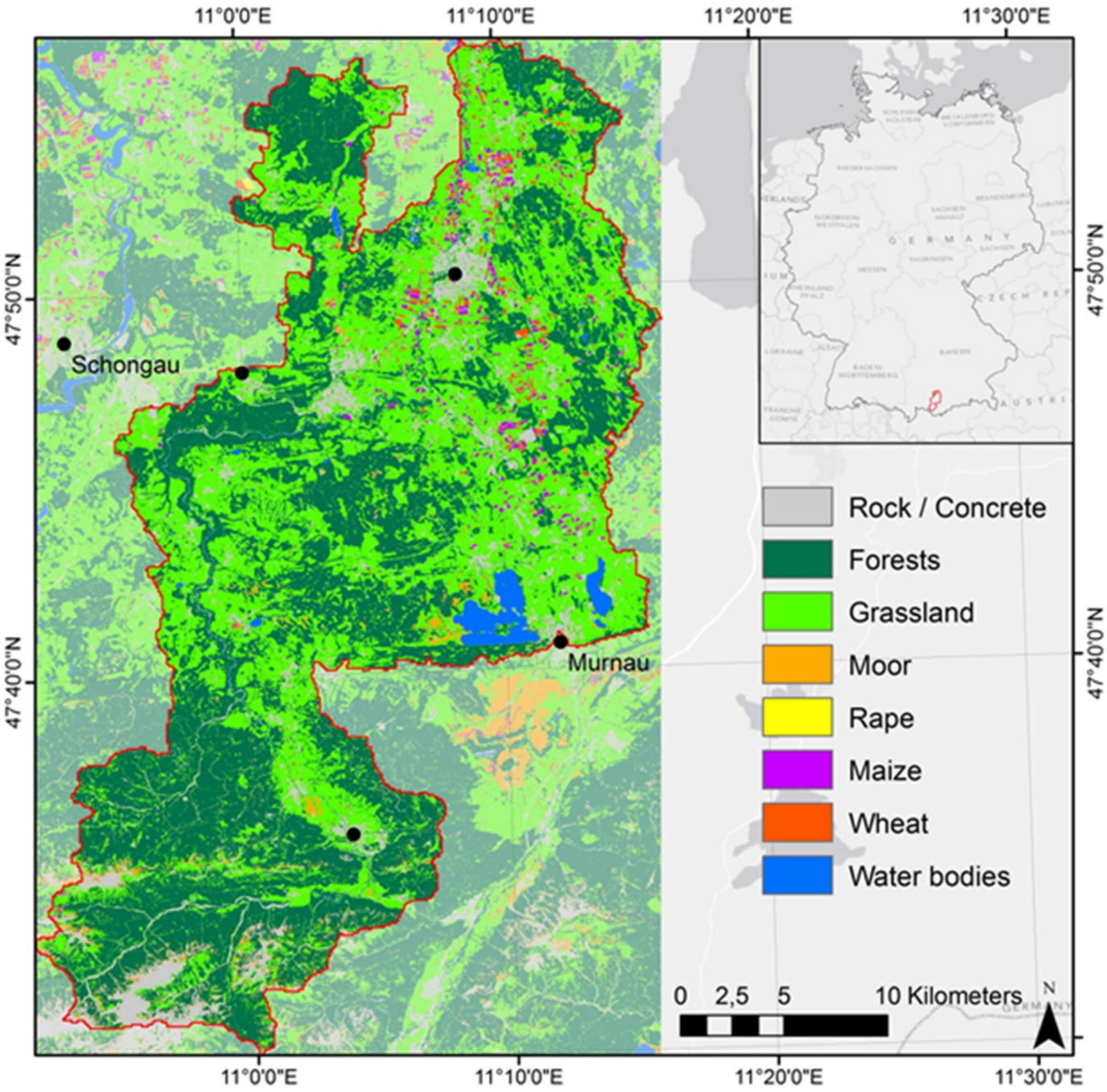

Figure 4-6: Land cover classification of the Ammer catchment based on a mosaic of different random forest classifications.

Table 4-2: Confusion matrix for the land cover classification based on 3 RapidEye scenes (May 9, July 16, and September 6), i.e. covering 86.1 % of the study area. The overall test set error rate is 3.4 %.

	Rock / Concrete	Forest	Grassland	Moorland	Rape	Maize	Wheat	N° validation pixels	Commission Error [%]
Rock / Concrete	2926	2	40	3	2	0	27	3000	2.47
Forest	0	2988	12	0	0	0	0	3000	0.40
Grassland	2	37	2939	22	0	0	0	3000	2.03
Moorland	0	0	239	2514	0	247	0	3000	16.2
Rape	6	0	5	0	1695	0	0	1706	0.64
Maize	0	0	0	8	0	2992	0	3000	0.27
Wheat	0	0	0	0	0	0	2676	2676	0.00
N° classified pixels	2934	3027	3235	2547	1697	3239	2703		
Omission Error [%]	0.27	1.29	9.15	1.30	0.18	7.63	1.00		3.4 %.

resemblance of the moorland and grassland ecosystems. Both biomes consist to a great extent of Poaceae and herbaceous species. Their occurrence differs mostly by the varying land management. Thus, it can be argued that these classes are rather land use than land cover classes, and this blurred class definition caused these misclassifications. However, in most cases grassland areas were wrongly assigned to moor, which translates to the high grassland omission error of 9.2 % and to the high commission error of the moor class of 16.2 % (Table 4-2). As in this thesis analyses have only been performed on the grassland areas, this means that some grasslands in the study area are omitted, but at least no other land cover is accidently treated as grassland. The land cover map was finally used to create a grassland mask and to replace all other land cover pixels with NA values.

4.2. Digital elevation model

In this thesis, a DEM was used for the correction of atmospheric and orographic effects as well as for the derivation of local viewing and illumination geometries (chapter 6.3). The data set is a 1 arc sec (~30 m) resolution DEM based on Shuttle Radar Topography Mission (SRTM) data provided by the DLR (German Aerospace Center). The distinguishing feature of the SRTM DEM is that it was the first global elevation data set at medium resolution levels and entirely produced with a single technique. The mission provides DEM data between 60°N and 57°S based on the synergistic use of the US C-band (5.6 cm) system and the German/Italian X-band system X-SAR (synthetic aperture radar, 3.1 cm), which were processed by NASA (National Aeronautics and Space Administration), DLR, and the Italian Space Agency, respectively. Both sensors were on board the *Endavour* shuttle during an eleven days mission in February 2000 and were simultaneously operated. Sensors were installed in a stereo arrangement, i.e. both instruments' receivers were flying on parallel tracks to their antennas (separated by a 60 m mast), thus viewing the earth's surface from slightly different angles. Due to this, they provided two interferometric SAR data sets from which surface elevation was derived based on the phase difference measurements of the two signals by triangulation (Rabus et al., 2003; Farr et al., 2007). The two radars produced data sets of different spatial resolution, coverage, and accuracy and are processed into one DEM.

The DEM vertical accuracy requirements of 16 m absolute and 6 m relative error are valid at 90% confidence level, as well as the requirement of maximum absolute 20 m displacement for the horizontal accuracy. The relative accuracy describes the error in a local 225 x 225 km area, while the absolute value stands for the absolute difference from true height throughout the mission (Rabus et al., 2003). As dense forests may not be penetrated by the radiance to the ground level, the DEM will not correspond to the ground surface in those areas but rather provides elevation measurements from near the top of the canopies. In addition, smooth surfaces such as lakes often do not scatter enough energy back to the sensor and thus may have higher errors (Farr et al., 2007). However, water bodies and forests are excluded from the analysis, and given the high relief energy in the study area these errors do not alter the overall topography. The original data use WGS84 as the horizontal and vertical datum. They were projected to UTM and resampled to the 6.5 m RapidEye resolution for further usage.

4.3. Field measurements

In this subchapter, the sampling design, measurement methods as well as the resulting *in situ* LAI values are described, which are referred to as LAI_{insitu} in this thesis. Intensive field measurements were performed during the growing seasons of 2011 and 2012. The overall aim was to generate a validation data base to assess the accuracy of both LAI derivation methods.

Thereby, the field data sampling was designed in a way that ensured they could be used for LAI validation on different scales. Further, field measurements are needed for the establishment of transfer functions (see chapter 5.1) as well as for the parameterization of the RTM (see chapter 6.3). A special focus was put on the assessment and comparison of different algorithms for deriving LAI indirectly from light transmittance measurements.

4.3.1. Sampling design

Five measuring campaigns where conducted in 2011 (April 11 - 17, May 2 - 6, May 22 - 27, July 25 - 28, and September 8 - 14), however, the weather conditions and a defect sampling instrument prevented reliable indirect LAI measurements during the first campaign. In 2012, two field campaigns were conducted during April 16 - 20 and August 13 - 14. For easier reference, these seven periods are in the following termed calendar weeks 15, 18, 21, 30 and 36, as well as 16 and 33, respectively (see Figure 4-1).

When performing ground-based measurements for collecting reliable, representative and sufficient field data, the spatial sampling design is of major importance. In this thesis, three criteria where especially considered:

- *Sample size* – To establish statistically sound transfer functions and validation protocols, a sufficient number of data across the entire value range should be sampled. Ideally, the number of measurements is related to the error variance. A high number of random samples would thus be preferable in this context. However, the sample size is often rather determined by pragmatic considerations, and no strict rule on minimum sampling size is available (McCoy, 2005). However, as it was intended to derive transfer functions for the individual scenes, 20 plot measurements per campaign were considered the minimum requirement (Köhl et al., 2011).
- *Scale issue* - To validate a RS based map of a certain resolution, the sampling units need to be scaled and spread correspondingly, in a way that field data do on the one hand represent all conditions composing the pixel reflectance, and can on the other hand be compared directly to individual pixels or groups of pixels. This can be problematic for coarse resolution data, as many measurements are needed to derive an integrative value. However, there is also a lower spatial limit, as for example indirect LAI measurements – relying on repeated hemispherical sensor measurements – cannot be conducted on a very small area of a few meters. To circumvent both issues, the measurements were arranged within a two-stage nested design with such distance between them that single measurements can be treated individually over several scales, but still allow for up-scaling. This scheme is also recommended by the CEOS (Committee on Earth Observation Satellites) Land Product Validation group and the VALERI (VAlidation of Land European Remote sensing Instruments) project (Baret et al., 2003; Morisette et al., 2006). For consistent upscaling, the complete sampling area should be relatively homogeneous, i.e. the biophysical variable / radiometric values should change only marginally within one plot. This implied that only those areas were considered that consist of homogeneous land cover on a kilometer scale, which strongly reduced the amount of feasible areas in the heterogeneous landscape.
- *North-south gradient* – It was intended to cover the altitudinal and thus climatic gradients in the study area in order to cover the corresponding differences in phenology and grassland management. The sampling sites were therefore distributed

across the Ammer catchment, which reduced convenience and the overall number of visited plots. Further, no plots could be selected in the high mountain region of the Graswang Valley, for reasons of accessibility, prolonged snow cover, and insufficient spatial homogeneity of the alpine meadows.

Four grassland sampling sites ('plots') were selected in the study region (see Figure 4-7). The relative homogeneity of the plots was determined beforehand by calculating the variance of Band 3 of a Landsat 5 TM scene from July 2009 of the study region in a 1 km x 1 m moving window. Not all sites were investigated during each campaign due to time constraints. In week 30, the site in the Murnauer Moos was not visited. In week 33 only the Fendt site and meadows in the surrounding were covered due to a simultaneous air-borne mission which was restricted to this small area. Furthermore, the Haunshofen site was shifted about 0.8 km to the east after the campaign in week 21 to increase the homogeneity of the site.

Each plot had an area of 750 x 750 m in order to cover 3 x 3 MODIS 250 m pixels, i.e. a target pixel and the close surrounding, for potential upscaling procedures to the MODIS scale while accounting for adjacency effects (Baret et al., 2003). To cover the grassland variability in each plot, several elementary sampling units (ESUs) are distributed within, each situated in an individual meadow. Special attention was paid to a sufficient distance of the ESUs from field boundaries to avoid border effects (McCoy, 2005). According to VALERI, the ESUs should be spread spatially equally within a plot to improve the geostatistical variable estimation. The center square should be more densely sampled. While during the first few campaigns, five ESUs were chosen per plot as suggested in Si et al. (2012), this was identified as insufficient after the third campaign. Hence, the number of sampled ESUs was continuously increased

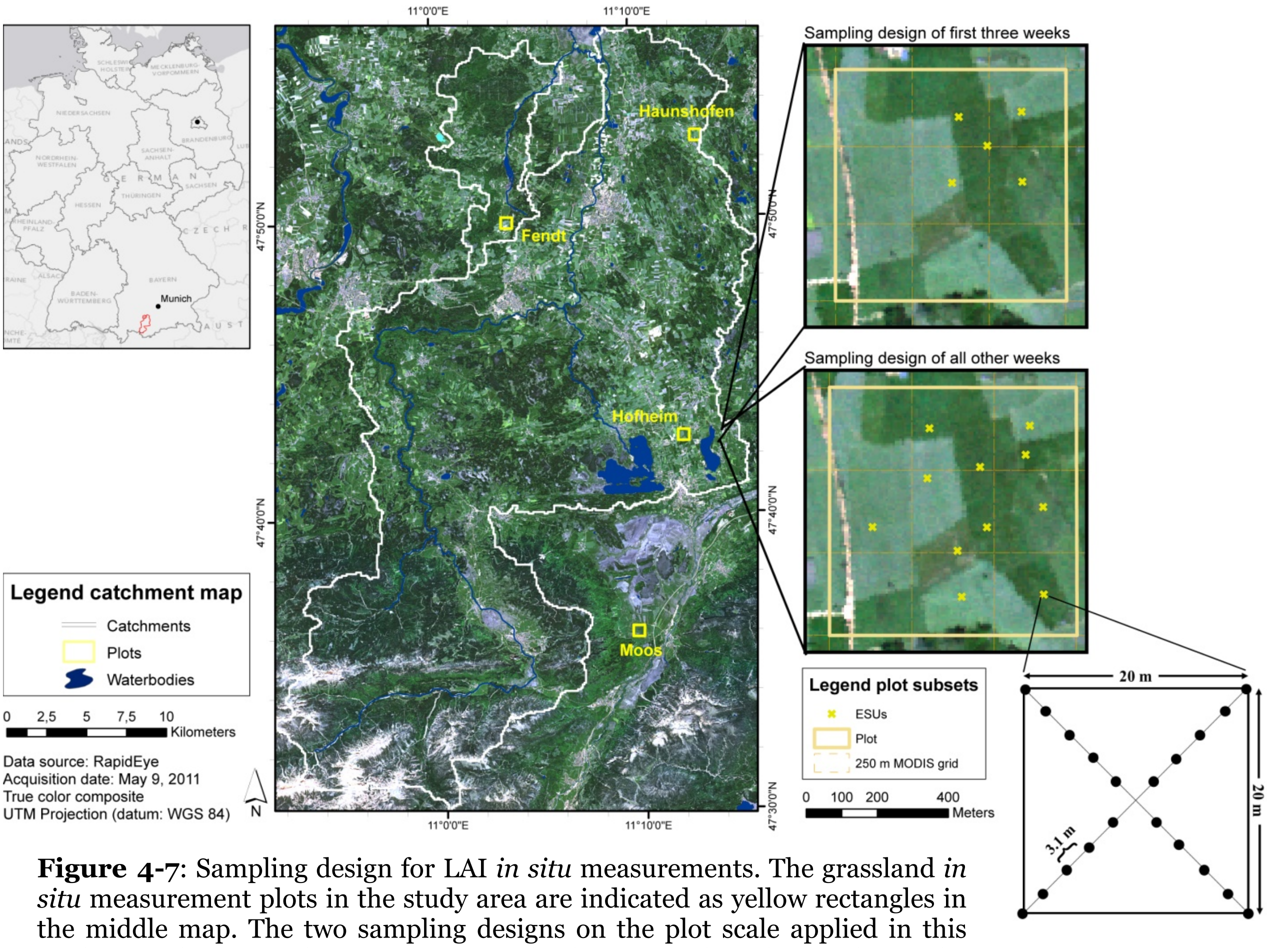

Figure 4-7: Sampling design for LAI *in situ* measurements. The grassland *in situ* measurement plots in the study area are indicated as yellow rectangles in the middle map. The two sampling designs on the plot scale applied in this study are shown in the zoom insets. The bottom right scheme shows the sampling design at the ESU scale.

Table 4-3: Number and kind of measurements conducted during the field campaigns.

Week	Number of ESUs	Number of valid samples					
		LAI indirect	LAI direct	MTA*	Chlorophyll	SLA / LMA	Canopy height
2011							
15	20		5		12	5	20
18	20	19	4	19			15
21	20	20	4	20			19
30	26	26		26			25
36	33	33	6	33		6	33
2012							
16	29	29	2	29			
33	22	22		22	22	10	

*The MTA is also the input parameter to the LIDF used in the RTM (chapter 6).

during the following campaigns (see Table 4-3) through additional student help, the reduction of sampled parameters, and more experienced measurement devices handling. The ESUs constitute an area of 20 x 20 m, covering about 3 x 3 RapidEye pixels (see e.g. Justice and Townshend, 1982). Within every ESU, 20 measurement points were arranged on two diagonal transects, constituting a cross sampling scheme. This scheme is not significantly different in its representativeness from random sampling (Garrigues et al., 2002), but offers rather short paths and thus quick sampling.

4.3.2. Measurement of biophysical parameters

LAI and MTA

The general principles and available instruments for LAI measurements are already summarized in chapter 2.1. Here, the methodology that was actually implemented in this thesis is described. For indirect LAI measurements, the LAI-2000 PCA (see Figure 2-4) as well as the software FV2200 (LI-COR, 2009) were used. The LAI-2000 relies on the Beer-Lambert extinction law, which describes the attenuation of the radiation in a canopy (Monsi and Saeki, 1953). Light attenuation can be expressed with LAI, the mean projection of unit leaf area $G(\theta)$, the normalized path length through canopy in direction θ ($1/cos\theta$), and the transmission probability $\mathrm{P}(\theta)$ (see chapter 2.1.2), as

$$\mathrm{LAI} * \mathrm{G}(\theta) = -\ln \mathrm{P}(\theta) * \cos\theta \tag{4.2}$$

under the assumption, that only light that is not intercepted by plant material reaches the ground. Therefore, only visible light (320 – 490 nm) is measured, for which the amount of reflected or transmitted light is low. The transmittance probability $P(\theta)$ is estimated by comparing measured light intensities above (A) and below (B) the canopy using a fisheye lens (Jonckheere et al., 2004; Weiss et al., 2004). Within each ESU, 20 B measurements were conducted at the sampling points, while the A measurements were repeated only four times just before the first of five B readings, assuming stable irradiance conditions for these five measurements, which normally took about two minutes. As the transmission information is needed explicitly for single directions, the field of view of the optical hemispherical sensor head of the LAI-2000 is divided into five concentric ring detectors i, each covering an angle range centered around the angles 7°, 23°, 38°, 53°, and 68°, thus having five constant $\overline{\theta}_i$ values (see Figure 4-8 and Table 4-4).The left-hand term of Equation 4.2 is equivalent to the

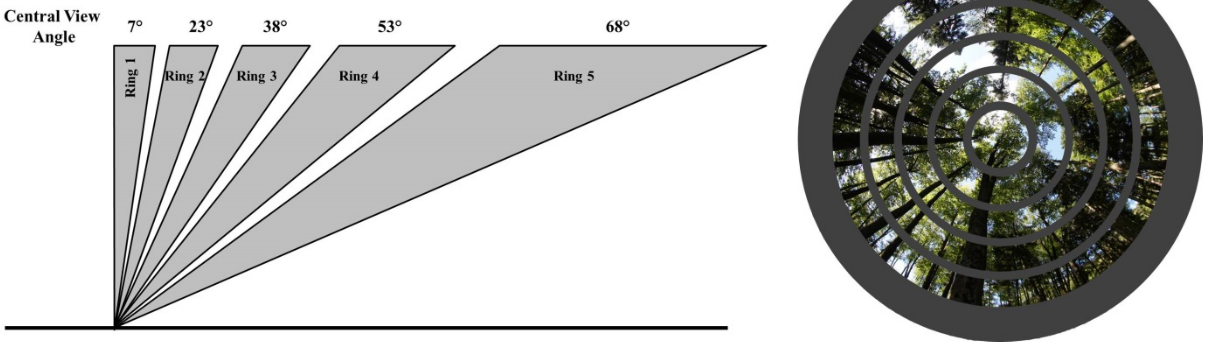

Figure 4-8: Viewing angles of the LAI-2000 PCA sensor. While the left sketch (adapted from LI-COR, 2009) shows the five viewing angles in a cross-section, on the right an example of the sections 'seen' by the detector rings is given.

number of contacts made by a probe passing through the canopy at an angle θ and is therefore called contact number κ. The LAI-2000 derives κ_i of each ring by dividing the logarithm of the A and B readings ratio in each ring i by the respective path length $S(\theta_i)$:

$$\overline{\kappa_i} = \frac{\frac{1}{n}\sum_{i=1}^{n} -\ln(\frac{B}{A})}{S\theta_i} \tag{4.3}$$

There are several empirical approaches implemented in the LAI-2000 to derive LAI from $\overline{\kappa_i}$. The two most widely used approaches, the *Miller* and the *Lang* method, were investigated in this thesis in more detail. Miller (1967) demonstrated that LAI can be calculated with Equation 2.6 if $P(\theta)$ observations are available over the angle range 0 to π/2. Integration over these directions is achieved in the LAI-2000 instrument by means of the sensor rings, which cover nearly the entire hemisphere and due to which the $\sin\theta d\theta$ term of Equation 2.6 is constant. This term is implemented in the instrument as so-called weighting factors W_i representing the coverage of the hemisphere of each ring:

$$W_i \ = \ \mathrm{d}\theta_i * \sin\overline{\theta_i} * const \tag{4.4}$$

with $\mathrm{d}\theta_i$ being the respective angle width in radian units, $\overline{\theta_i}$ being the central angle of each ring, and *const* being a scaling constant of 1.58 in the 5-ring case in order to normalize the weights to unity (see Table 4-4). The LAI is calculated as twice the sum of the contact number κ_i in each ring, weighted with the respective W_i factor:

$$\mathrm{LAI}_{Miller} = 2\sum_{\mathrm{i}=1}^{5} \overline{\kappa_{\mathrm{i}}} * W_{\mathrm{i}} \tag{4.5}$$

Table 4-4: Central angles, angle widths, and weighing factors of each LAI-2000 sensor head ring.

Ring	$\overline{\theta}$ [°]	$d\theta$ [°]	$d\theta$ [rad]	$\sin\theta$	W_i
1	7	12.2	0.213	0.212	0.041
2	23	12.2	0.213	0.391	0.131
3	38	11.8	0.206	0.616	0.200
4	53	13.2	0.230	0.798	0.290
5	68	13.2	0.230	0.927	0.337

This method is referred to as the "LAI-2000 method" in the instrument's manual, as it is the algorithm implemented in the portable console. In this thesis, the approach is called "Miller method", because it is close to the original formulation (Miller, 1967; Weiss et al., 2004).

Based on Equation 4.2, Lang (1987) proposed another algorithm for computing LAI without requiring the leaf angle distribution $G(\theta)$ and with no need for all values of $\kappa(\theta)$. By assuming that $G(\theta)$ is approximately linear with θ and has a value near 0.5 at θ = 57.3° over a wide range of canopy structures (Figure 4-9), Lang showed that the $\kappa(\theta)$ function is quasi linear:

$$\kappa(\theta) = a + b\theta \tag{4.6}$$

where a and b are the empirically derived slope and intercept of a linear approximation of the projected leaf area $G(\theta)$. Thus, by simply interpolating a value of κ for θ= 57.3°, Lang derives:

$$\mathrm{LAI_{Lang}} = 2 * (a + b) \tag{4.7}$$

In the LAI-2000, the $\overline{\kappa_i}$ values are used to fit a linear relationship. The most significant difference between the approaches thus is that Lang's algorithm weights all rings equally in fitting the linear approximation, while the Miller's algorithm weights the rings according to their hemisphere coverage, which can, however, introduce errors as plant elements are generally not randomly distributed over the hemisphere in a real canopy, but rather in the outmost ring. For both algorithms, the plot LAI value was derived by logarithmical averaging over the 20 B measurements according to Lang and Xiang (1986) and Weiss et al. (2004) in order to reduce LAI underestimation due to clumping (chapter 2.1.2).

It has been observed that the Miller method underestimates the actual effective LAI, and the reason for this has been assumed in most studies to be increased foliage scattering effects in the fifth ring and a corresponding overestimation of gap fraction (Chason et al., 1991; Chen and Black, 1991; Fassnacht et al., 1994; Dufrêne and Bréda, 1995; Wilhelm et al., 2000; Chen et al., 2006). These authors suggest discarding one or two of the outer rings of the LAI-2000 sensor for LAI calculation. Planchais and Pontailler (1999), however, contradict this assumption and show that no bias in scattering with high θ exists. Instead, they state that the underestimation of LAI is caused by clumping and that the counterbalancing effect of

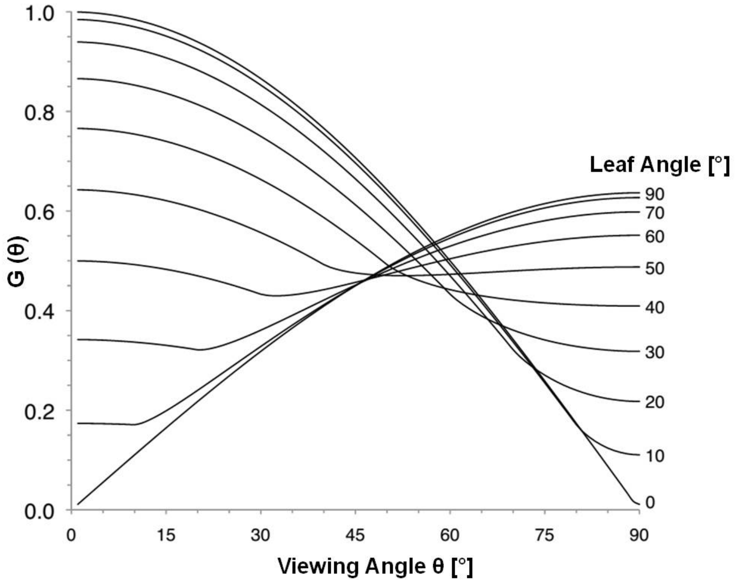

Figure 4-9: Theoretical relationship between projected foliage area and viewing direction for various foliage inclination angels. According to Wilson (1959).

discarding observations at higher viewing angles results from producing an error in the estimation of the leaf projection function $G(\theta)$ and thus of the MTA. Leaves are supposed to be more erect than they are, which results in an increased LAI estimate. As this error is variable with θ, it is however not a stable clumping correction procedure. Unfortunately, their analysis only relies on data derived using the Lang algorithm, and neither this nor other studies have tested different LAI-2000 algorithms in grassland canopies. Thus, in this thesis all combinations of derivation algorithm and rings are tested to assess the difference between the two algorithms ($LAI_{Miller-5}$ and LAI_{Lang-5}, respectively) and between the four and five rings settings ($LAI_{Miller-4}$ and LAI_{Lang-4}, respectively).

Weiss et al. (2004) and Leblanc and Chen (2001) further plead for the use of a single direction measurement for LAI derivation. However, using one single ring does not allow for the derivation of leaf angle distributions, which also had to be collected in the field. Therefore, this technique was not taken into account. The LAI-2000 PCA can calculate the MTA of the foliage given a LAI value by solving equation 4.2 for $G(\theta)$:

$$G(\theta) = \frac{\kappa(\theta)}{\mu S(\theta)} \tag{4.8}$$

whereby $\mu S(\theta)$ corresponds to the LAI estimate in each ring. Figure 4-9 shows the idealized relationship between the projected foliage area $G(\theta)$ and the viewing direction for various foliage inclination angels for an ideal canopy with random azimuth leaf orientation (Wilson, 1959; LI-COR, 2009). The MTA is calculated using an empirical polynomial relating inclination angle to the slopes of this idealized curves after Lang (1986).

The 360° azimuthal field of view of the sensor can introduce errors to the measuring procedure. One unwanted effect is the shadow of the operator in the image, which can be restricted using view caps. A 270° view cap was used on the sensor lens in this thesis (see Figure 4-10 a). Another issue is the risk of heterogeneous conditions viewed by the sensor, which can be caused by brightness gradients in the sky or especially by strongly clumped canopies. Therefore, larger view caps are often used in row crops and forests (Nackaerts et al., 2000). An actual problem for the measurement of grass canopies is the close proximity of the sensor head to the vegetation elements as the LAI-2000 responds non-linearly to light interception by close foliage, which could not be avoided, however (Hyer and Goetz, 2004).

Ideally, the LAI-2000 PCA measurements should be made under diffuse light conditions, i.e. under homogeneously overcast skies or close to sunrise or sunset, because these conditions

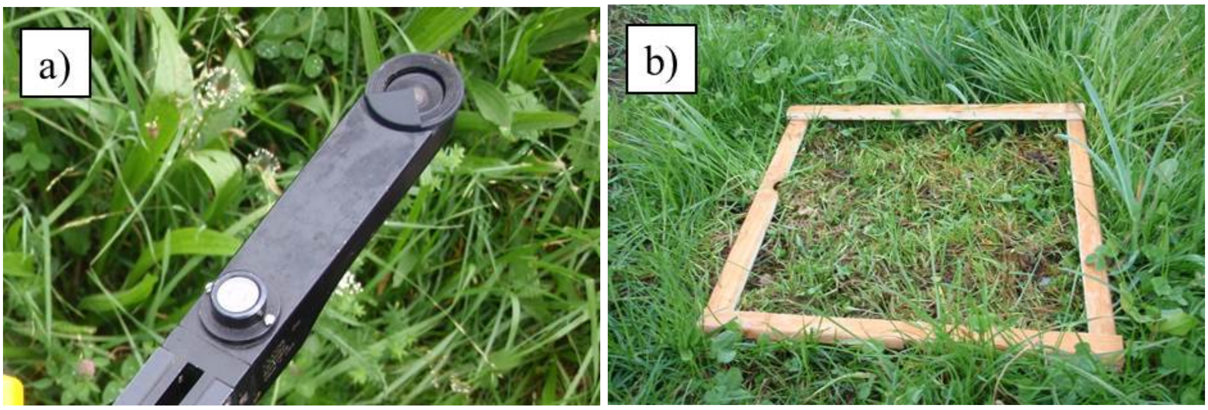

Figure 4-10: LAI *in situ* measurements. a) LAI-2000 sensor head with 270° view cap. b) Direct LAI measurement by clipping the above ground biomass.

are closest to the assumption that leaves are exclusively absorbing radiation. Light reflected from the canopy to the sensor would add to the recorded radiation below the canopy and lead to an underestimation of LAI (Leblanc and Chen, 2001). In addition, heterogeneous skies and rapidly changing conditions should be avoided (Hyer and Goetz, 2004).

Due to the workload, these recommendations could however only partly be taken into account. Measurements were conducted during overcast conditions as well as under direct sunlight, in which case the sensors head and the canopy under investigation were shaded. To ensure similar conditions the sensor head was always pointed away from the sun, with the observer/sun direction being masked using the view cap (LI-COR, 2009, see Figure 4-10 a.) Measurements for which the light intensity below the canopy exceeded the above value due to changing light conditions or operator errors were later excluded from the calculations. As a result, the averaged LAI value of each ESU relies in 75 % of all cases on 20 single measurements, in 23 % on 19-16 measurement pairs, and only in 2 % of all cases on less than 16 measurements. The LAI values were therefore considered to be representative of the respective ESU. The footprint of the LAI-2000 PCA depends on the view angle of the sensor, i.e. the number of sensor rings used, and the canopy height (LI-COR, 2009). In view of the fact that the canopy heights measured in the field range from roughly 3 to 40 cm, the theoretical area seen by the sensor is a circle with a radius of 0.11 - 1.5 m. The effective range can be further reduced by foliage. Hence, about 3 m distance is kept between each sample point to guarantee statistical independence.

Although the LAI-2000 cannot distinguish photosynthetic active leaf tissue from other plant elements as discussed in chapter 2.1.2, in this thesis, the term LAI is still used, as in grasslands most vegetation parts seen by the sensor are green leaves. However, the canopy elements are not randomly distributed in space, which is one of the basic assumptions behind LAI retrieval algorithms (Chen and Black, 1992). Due to this clumping, the indirectly derived LAI has to be seen as *effective* LAI and is expected to underestimate the *true* LAI from destructive sampling (LAI_{destr}), even though a logarithmic averaging procedure was chosen. Further, underestimation is caused by vegetation elements not completely fulfilling the above mentioned assumption of absorbing all radiation in the VIS. The bias introduced by residual scattering effects is estimated to be around 8 % (Leblanc and Chen, 2001). Thus, while indirect measurement methods are useful for assessing temporal or spatial relative LAI variation, they require an extra calibration for absolute accuracy (Cutini et al., 1998; Planchais and Pontailler, 1999; Wilhelm et al., 2000; Jonckheere et al., 2004).

The LAI-2000 measurements are corrected in this thesis using direct LAI measurements. LAI_{destr} was determined at 21 ESUs by destructive sampling. However, five values from week 15 could not be used as no correct respective LAI-2000 measurement was available due to malfunctioning of the instrument, so 16 data pairs were available. The collection of more samples would have been desirably, but was not possible due to the high workload of manual LAI measurements and the need of measuring the leaf area immediately after harvesting.

At each sampling point, an area of 30 cm x 30 cm was chosen within the ESU and the complete above ground biomass was harvested (see Figure 4-10 b). The sampled subsets were selected considering their representativeness of the ESU. The samples where immediately packed into plastic bags and stored within a cooler until storage in a refrigerator. On the same day in each case, the harvested leaves were laid out on a white background in such a way that no overlap existed between adjacent leaves, flattened by a glass pane and photographed from nadir with a digital camera. In some cases, a scanner was available which was used to gain a picture of the flattened plant elements instead. In a last step, these images were manually segmented into foliage and background pixels (see as example Figure 2-3). The number of pixels belonging to the foliage class was related to the total area of the picture, and summed up in case the samples could not fit within one photograph. For the LAI determination, no distinction was made between harvested green and senescent plant material, an assumption that is however in line with the LAI-2000 measurements.

Dry matter, water, chlorophyll content, canopy height, and diffuse radiation

In calendar weeks 15, 36 and 33, a drying oven and precision scale was available. They were used for two purposes (see Table 4-3): in weeks 15 and 36, the workload of directly measuring LAI was reduced by taking three subsets of the whole biomass of one sample. These were weighted, laid out and photographed in order to determine the LAI of the subset. Subsequently the samples were stored in thin paper bags to prevent lightweight plant parts from being blown away, dried in the oven at 90 °C for 12 hours, i.e. until they were constant in weight, and weighed again. The LAI was then scaled to the total harvested, dried, and weighed biomass by using the samples mean SLA (see chapter 2.1.1). This procedure was additionally applied to samples taken in week 33, although those samples did not represent a defined area, so they could not be used to estimate the plot LAI. Nevertheless, the total of 21 samples collected in the field during the three weeks were used to determine the leave's water content and the LMA as well as its reciprocal SLA from the comparison of the fresh and dry weights (Landsberg and Gower, 1997; Jonckheere et al., 2004).

The chlorophyll was measured once in spring 2011 and once in summer 2012 at a total of 34 EUSs. The chlorophyll content was measured indirectly using a SPAD-502Plus chlorophyll meter (Konica Minolta Sensing Inc., Japan). The SPAD determines the relative amount of chlorophyll a + b by measuring the absorbance of the leaf at two wavelengths (650 nm and 940 nm). Using these two absorptions, the SPAD calculates an index which is highly correlated to the amount of chlorophyll present in the leaf (Konica Minolta). SPAD measurements were repeated at each measuring point in the ESUs at a randomly selected leaf. The most common species (e.g. grass species, clover, dandelion, plantain) and different positions in the canopy (i.e. sun and shade leaves) were selected for the measurements. The SPAD value was derived as the average of the 20 leaf readings. Several authors have published functional relationships between SPAD values and selected plant species (e.g. Markwell et al., 1995: soybean and maize; Guimaraes et al., 1999: tomatoes; Si et al., 2012: grassland). In this thesis, the exponential relationship according to Si et al. (2012) was used, as it was explicitly established for mixed grassland.

Additionally, the canopy height was measured at each of the 20 sampling cross points during the campaigns in 2011. In order to obtain a representative sample, the leaves were selected with reference to the abundances of the plant species in a 10 cm radius around each sampling point. Total solar radiation as well as diffuse radiation were measured continuously at 10 minute intervals at the three TERENO stations *Graswang*, *Fendt* and *Rottenbuch* (see Figure 3-1) using Sunshine Pyranometers (Delta-T Devices Ltd, Burwell, UK).

4.3.3. Results of *in situ* measurements

Due to changing circumstances in sampling design, manpower, available instrumentation, and weather conditions, the kind and number of measurements that could be conducted varied between the campaigns. The unpredictable satellite coverage due to the high number of cloudy days in the study area as well as the irregular RapidEye pass over times further reduced the number of field measurements that could be used for training and validation purposes (see chapter 5.1). While the kind and number of all measurements is summarized in Table 4-3, the descriptive statistics of the results is presented in Table 4-5.

LAI and MTA

The LAI-2000 PCA values ($n = 148$) vary with the four LAI derivation algorithms, the *Miller* and the *Lang* method applied to four and five of the LAI-2000 sensor ring measurements, in their mean (2.2 - 2.6) and their range (0.3 - 0.4 to 6.1 - 7.7). All data sets show a non-normal, right-skewed distribution. The comparison of the tested derivation algorithms reveals very high correlations[15] between the accordant measurement values (correlation coefficient r_s between 0.97 and 0.99).

However, the absolute differences between the LAI estimates increase for higher values, resulting in a mismatch of 7 - 25 % for LAI measurements larger than two (see Figure 4-11). As expected, the two 4-ring algorithms (orange and blue signature) produce continuously higher values, which, according to Planchais and Pontailler (1999), is caused by an overestimation of the MTA. To determine if the LAI algorithms produce significantly different results, the non-parametric Wilcoxon signed-rank test was applied (Bauer, 1972). The Wilcoxon test showed that in almost all cases the choice of algorithm significantly affects the derived LAI value ($p < 5.9e^{-07}$, two-tailed test). Only the $\text{LAI}_{\text{Miller-5}}$ and $\text{LAI}_{\text{Lang-5}}$ (violet and green signatures in Figure 4-11) show no statistically significant difference. This suggests that LAI *in situ* data collected using the LAI-2000 PCA using different algorithms and especially different hemisphere coverages cannot be equated in absolute terms, and that the discussion of the algorithm used is crucial for every LAI *in situ* investigation.

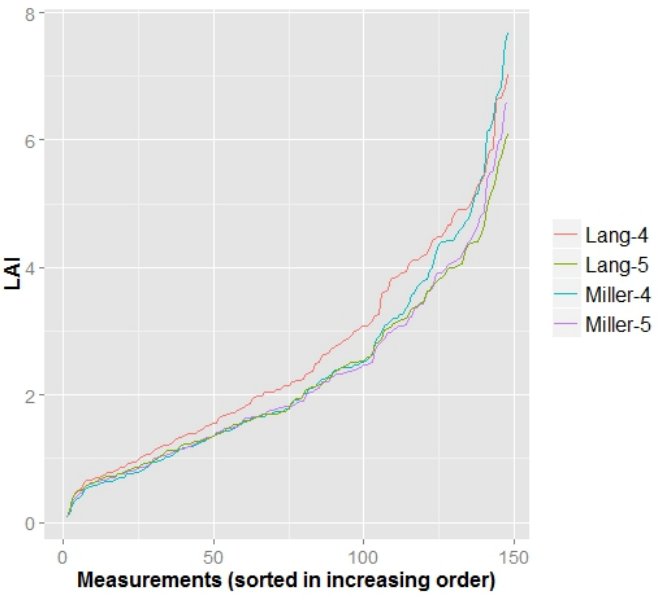

Figure 4-11: Comparison of the four tested LAI derivation algorithms, the Miller and Lang algorithms using the same transmission measurements from four or five of the LAI-2000 sensor rings. The derived LAI values are sorted in the order of the increasing Miller-4 algorithm results to show the increasing mismatch with higher LAI values.

---

[15] As the LAI-2000 *in situ* measurements are not normally distributed, Spearman's *rho* statistic (Spearman (1907) is used.

The LAI_{destr} values derived from destructive sampling range from 1.5 to 6.5 with a mean of 3.6 and thus seem to cover all prevailing grassland occurrences from freshly harvested to very dense meadows. The comparison between directly and indirectly measured LAI reveals an underestimation of the true LAI by nearly 50 % on average by the indirect methods. This strong underestimation is caused by canopy clumping (see discussion in chapter 2.2.2) and in fact also in this thesis the highest discrepancies between directly and indirectly measured LAI values occur on heterogeneous, strongly grazed pastures with reptant herbs and patches of species spurned by cattle (see photographs h) and i) in Figure 3-9). These meadows with a high degree of clumping on a canopy scale have a relatively high average coefficient of variation (CV) of 83 % within the 20 transmittance measurements. Apart from the inappropriate use of the Poisson model, the overall low measurements are also caused by the design of the LAI-2000 device. In very low canopies, the sensor cannot be placed completely underneath the vegetation, and, due to the height of the sensor head itself, the lower 3 - 4 cm of upright plants are not in the sensor's field of view. In very dense canopies the LAI-2000 also tends to underestimate the true LAI, due to its decreasing sensitivity to small changes of the optical signal in dark conditions. An asymptotic saturation level is reported to be reached by the PCA at a value of about 5 (Gower et al., 1999; Jonckheere et al., 2004). Hence, a correction using directly measured LAI is indispensable (Brantley et al., 2011).

Due to their high correlation with each other, the different LAI-2000 values correlate overall similarly well with the corresponding *in situ* measurements (LAI_{Lang-4}: $r_S = 0.779$, LAI_{Lang-5}: $r_S = 0.786$, $LAI_{Miller-4}$: $r_S = 0.762$, $LAI_{Miller-5}$: $r_S = 0.755$). Although the derivation of higher LAI values using a 4-ring algorithm might seem desirable to counterbalance the general underestimation of the LAI-2000 instrument, accepting this error in contact number estimation is no appropriate approach to correct for clumping (Planchais and Pontailler, 1999). Instead, the similar results of the two 5-ring approaches indicate that the use of all sensor rings increases the stability of LAI derivation. Finally, as the Miller method has been criticized in the literature for overweighting transmission in the outmost ring (Garrigues et al., 2008b), the LAI_{Lang-5} values were used for correction with the directly measured LAI_{destr} values.

A linear model fit between LAI_{destr} and LAI_{Lang-5} (Figure 4-12) was used to correct the underestimation of the 121 indirectly measured LAI values that will be used as LAI_{insitu} for further analysis, as suggested by Chason et al. (1991), Wilhelm et al. (2000) and Brantley et

Table 4-5: Summary statistics of the biophysical parameters sampled *in situ* for all measurements.

	LAI_{destr}	LAI_{Lang-5}	LAI_{insitu}	MTA*	Chlorophyll [µg cm^{-2}]	Water content [%] / [cm]	SLA / LMA [cm^2 g^{-1}] / [g m^{-2}]	Canopy height [cm]
Minimum value	1.5	0.4	1.5	38	13.6	75.7 / 0.016	153.2 / 27	3.3
Maximum value	6.5	6.1	7.5	90	31.4	87.9/ 0.043	363.8 / 65	39.4
Mean value	3.6	2.4	3.6	64	24.9	81.2/ 0.021	213.6 / 50	15.5
Standard deviation	1.9	1.4	1.5	10.5	4.3	3.0/ 0.006	51.4 / 10	8.0
n	16	149	149	149	34	21	21	112

* The MTA is also the input parameter to the LIDF used in the RTM (chapter 6).

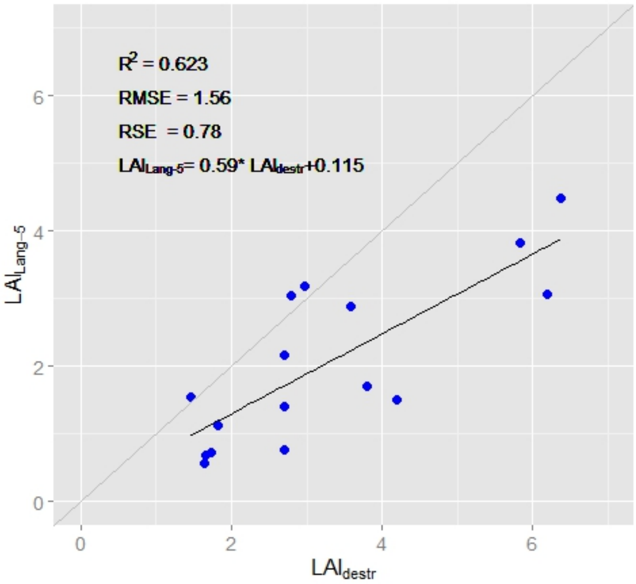

Figure 4-12: Comparison between directly measured LAI (LAI_{destr}) and indirect LAI derived using the Lang method implemented in the LAI-2000 instrument (LAI_{Lang-5}).

al. (2011). The descriptive statistics of the LAI_{Lang-5} values as well as the corrected LAI_{insitu} values are summarized in Table 4-5. It can be seen that the corrected LAI values fit the distribution of LAI_{destr} quite well, especially the minimum and mean values. The scaling produced some very high values during the summer months, which are however not unrealistic. The value distributions of the individual sampling weeks are shown in Figure 4-13. While the general increase of LAI over the phenological phase is represented in overall lower spring values (weeks 16 and 18) and higher values in the summer months (weeks 30, 33, and 36), the week 21 values do not stick to this pattern. This is caused by the timing of the first grassland harvest in mid-May 2011. The MTA measurements vary widely between leaf angles of 40° and 90°, with a higher average leaf angle in spring (67.7°) than in summer (59.7°), which is probably caused by the different timing of the growth phases of grasses and herbs.

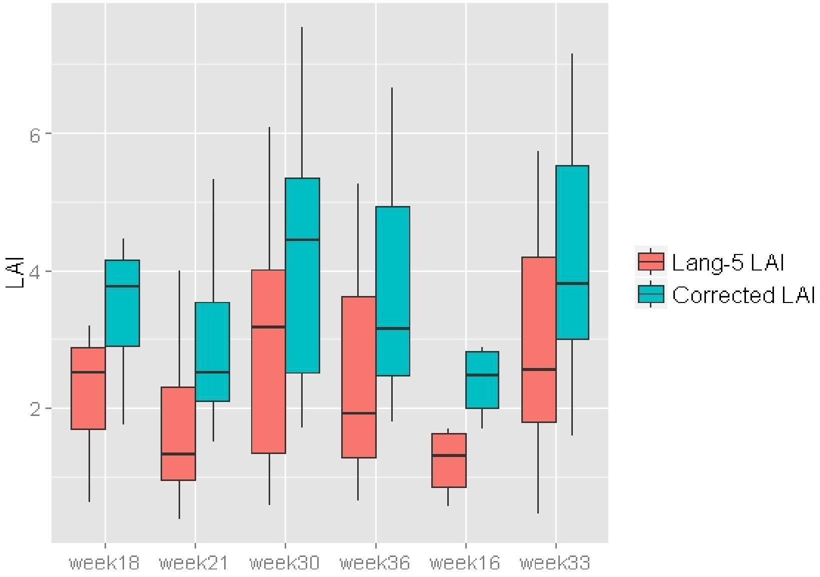

Figure 4-13: Distributions of the LAI *in situ* values differentiated per week. The measured LAI-2000 PCA values using the Lang-5 algorithm are shown in orange, while the distributions of the corrected LAI values are shown in blue.

Dry matter, water, chlorophyll content, canopy height

The chlorophyll measurements range from 13.6 to 31.4 µg cm^{-2}, with a mean value of 24.9 µg cm^{-2}. Overall, these values are rather low compared to other grassland studies. While Vohland and Jarmer (2008) only measure slightly higher values (mean of 25.7 µg cm^{-2}), Si et al. (2012) measure a mean chlorophyll content of 30.2 µg cm^{-2}, with values ranging from 21.9 to 37.0 µg cm^{-2}. A very similar grass chlorophyll mean value (30.1 µg cm^{-2}) but a wider range (17.1 - 49.7 µg cm^{-2}) is reported by Darvishzadeh et al. (2008b). For crops, even higher values are frequently measured (see e.g. Daughtry, 2000; Ruecker et al., 2006; Atzberger and Richter, 2012). It is also peculiar that the spring and summer measurements show only a little difference in mean value (April: 21.6; August: 26.8). These results indicate either an incorrect use of the SPAD instrument or of the relationship used to relate SPAD values to chlorophyll content.

The water and dry matter content values show the expected behavior. The water content mean of 81.2 % is very close to the 80 % relative water content commonly assumed for a wide range of applications (see e.g. Lauvernet et al., 2008; Duveiller et al., 2011b). For the dry matter content, it is harder to judge the plausibility of the measured value of 50 (±10) g m^{-2}, as only few literature values are available. While there are some studies measuring crop dry matter content (e.g. Atzberger and Richter, 2012, mean LMA = 79.2 g m^{-2}), the values in the only RS study on grassland LMA values published (Vohland and Jarmer, 2008, mean LMA = 428 g m^{-2}) seem exceptionally high. Ecological studies such as He et al. (2010) report higher grassland LMA values (mean = 94 g m^{-2}), and also a meta-analysis of Poorter et al. (2009) indicates higher mean LMA (72 g m^{-2}) for graminoids. This underestimation of LMA could result from an overestimation of the samples' LAI, given that the water content range seems correct. The canopy height measurements on the other hand show a reasonable range and variation (Wohlfahrt et al., 2001). Chlorophyll, water content, SLA, height, and irradiance values and ranges were used in this thesis to improve the parameterization of the RTM (see chapter 6.3).

5. LAI derivation using empirical-statistical models

In this chapter, the potential of LAI derivation from RapidEye data based on empirical-statistical models is investigated. As described in chapter 2.2.2, these models search for consistent relationships between the LAI and the spectral signature of vegetation. Based on such a relationship, spatially continuous RS reflectance measurements are converted to LAI (see Figure 2-13). Empirical-statistical methods have the disadvantage of relying on field data (Dorigo et al., 2007). However, they produce accurate results if representative field data are available and if they are applied over a confined area and known land cover (see e.g. Haboudane, 2004; Brantley et al., 2011). Therefore, these models serve as benchmark models against which RTMs can be compared (Kimes et al., 1998), and it is as such that they are used in the framework of this thesis.

For this comparative purpose, the overall aim of this chapter is to identify and assess robust and accurate statistical relationships based on six field campaign data sets that are used with six corresponding RapidEye scenes to establish transfer functions for LAI derivation. LAI varies over time due to phenology and environmental conditions, which makes a multi-temporal analysis of surface reflectance necessary to identify changing vegetation states and, accordingly, potentially changing relationships to RS data. As only few studies have investigated the seasonal development of LAI using statistical methods so far, and as none of them used RapidEye data for LAI derivation in grasslands, estimation of grassland LAI in the Ammer catchment during different phenological stages is performed in this work based on repeated ground- and satellite-based measurements. This availability of multi-temporal *in situ* and RapidEye data enables the analysis of three aspects related to multi-temporal vegetation monitoring:

- *Transferability*: Which error has to be expected when using a transfer function established at one point in time to derive LAI at other acquisition dates?
- *Data set combination*: Does the combination of data sets from different dates strengthen the statistical relationships? How many data sets should be combined? Are there ideal collection times to gain reliable estimates over the entire vegetation period?
- *Potential of the red edge band*: To which extent does the use of the red edge band in VIs enhance the relationship to the LAI measurements?

After establishing transfer functions based on different VIs and statistical models for each RapidEye scene, for several data set combinations, and for all scenes combined (chapter 5.1), the accuracy of the derived LAI is assessed. The results of LAI derivation based on single data sets are described and discussed first (chapter 5.2.1). The temporal transferability of the established models is analyzed in chapter 5.2.2, and the usefulness of combined data sets for model transfer in chapter 5.2.3. A comparison of selected VIs is performed to assess the potential of the red edge channel (chapter 5.2.4), followed by some conclusions (chapter 5.3).

5.1. Establishment of transfer functions

For each of the field measurement campaigns, a temporally matching Rapid Eye scene was selected (see Table 5-1). As is stressed by Morisette et al. (2006) and Lee et al. (2004), to build a meaningful relationship between phenologically varying vegetation and remotely sensed data, the field campaigns must be achieved within a short time period centered on the satellite acquisition date. This is of particular importance in variable ecosystems such as grasslands that are intensively used for mowing and pasturing. This condition was fulfilled for May 25 and August 13 scenes, as the field campaigns were conducted on the RapidEye overpass day. For the May 9 and September 6 scenes, a time lag of 5 days between acquisition and the middle date of the campaign was achieved, while for April 15 and July 16 scenes, the closest field data were acquired 7 days later and 10 days earlier, respectively. For these scenes, special care was taken to check the $\mathrm{LAI}_{\mathrm{insitu}}$ - RS relationships regarding plausibility. Based on this check, some LAI measurements had to be excluded from further analysis, as at some ESUs the land cover had obviously changed between the *in situ* observation and the satellite image acquisition due to mowing or pasturing. In one case, the RapidEye scene did not cover all *in situ* measurements. This affected a total of 29 $\mathrm{LAI}_{\mathrm{insitu}}$ measurements (7, 2, 1, and 19 measurements in weeks 18, 21, 30, and 16, respectively) resulting in 121 usable data pairs. Data pairs of $\mathrm{LAI}_{\mathrm{insitu}}$ and reflectance observations were generated by relating the GPS points positioned in the field to pixels in the georeferenced RS scenes. A 3 x 3 pixel mean filter was applied to the RapidEye data before reflectance extraction, thus corresponding to the size (20 m x 20 m) of the ESUs.

The spectral information of the RapidEye bands was transformed to VIs in a first step to enhance its sensitivity to LAI variations (see chapter 2.2.2). There is no agreement in the literature about which VI is best suited for estimating LAI, and a range of different VI types have been identified to relate to LAI using empirical and modeled data (see e.g. Jacquemoud et al., 2009, or He et al., 2006, for a review). Therefore, several VIs have been selected from

Table 5-1: Data pairs of RapidEye scenes and *in situ* measurements.

Week	Date of RapidEye acquisition	Time lag [days] between RS acquisition and *in situ* measurements	Number of usable LAI observations
2011			
18	09.05.	- 5	13
21	25.05.	0	18
30	16.07.	+ 10	25
36	06.09.	+ 5	33
2012			
16	25.04.	- 7	10
33	13.08	0	22

the literature to account for different vegetation densities and potential influential factors in the regression analysis. The first group of VIs consists of ratio indices such as the SR and the NDVI, as well as modifications of these correcting for soil and atmosphere influences (Kaufman and Tanre, 1992; Roujean and Bréon, 1995). Ratio VIs are the most widely used VIs for LAI derivation and have been shown to be robust over a wide range of conditions (Chen and Cihlar, 1996; Berterretche et al., 2005). The second group of indices includes purely orthogonal indices that have been developed to minimize the soil background influence by establishing a soil line (Richardson and Wiegand, 1977). For the calculation of these indices, an average soil line has been sampled from each RapidEye scene.

Hybrid VIs such as the SAVI and a range of SAVI variations (Huete, 1989) constitute the third type of indices. VIs employing the red edge band form the fourth group of indices, as they show promise in improving LAI estimation in dense canopies (Lee et al., 2004; Brantley et al., 2011; Potter et al., 2012). To test the benefit of the RapidEye red edge band, several rather new and partly experimental VIs were used. The red edge NDVI (Gitelson and Merzlyak, 1994) and the modified red edge SR (Sims and Gamon, 2002) substitute the red band used in the original VIs by the red edge band. Viña and Gitelson (2005) evaluated that the NDVI_{re} overcomes the saturation effect of the NDVI in dense vegetation. The principle of exchanging the red band for the red edge band is also pursued by Ehammer et al. (2010), who introduced two red edge ratio VIs and tested their performance on irrigated crop land in Central Asia. Conrad et al. (2012) focused on the shape of the reflectance curve in the red - red edge - NIR domain. They introduced the indices *Curvature*, characterizing the direction and intensity of the spectral curve curvature in the red edge, *Length*, i.e. the Euclidian distance that is spanned by the three reflectance values, and *Relative Length*, which relates the *Length* to the distance between the red and the NIR reflectance. The fifth group of indices includes modified chlorophyll indices. These indices, which employ the green and sometimes the red edge band, were originally developed to react sensitively to variations in chlorophyll content. However, some modified chlorophyll VIs have also been reported to be strongly responsive to variations in LAI (Daughtry, 2000; Haboudane, 2004). A total of 25 indices were tested. An overview of the used VIs, their formulas and references is given in Table A-6.

As mentioned earlier (chapter 2.2.2), there is no single best relationship between LAI and VIs, and there are a wide variety of published empirical LAI models. Therefore, four univariate statistical models were employed and compared in this thesis to identify the model with the highest explanatory power for each data set. Linear, qudratic polynomial, exponential, and power models were assessed. Logaritmic relationships were discarded after poor results had been achieved in preliminary studies (Asam et al., 2013). Multiple regressions were reported to achieve higher model fits than unvariate models (Baret et al., 1995; Darvishzadeh et al., 2008c). However, the use of these techniques was renounced here, as the individual VIs are partly highly correlated (inducing the problem of multicollinearity, see Field et al., 2012). Further, the direct comparison of uni- and multivariate models using e.g. the coefficient of determination R^2 is insignificant, complicating the model selection. Finally, the use of a simpler model with fewer predictors is always favored in inferential statistics (Field et al., 2012).

The different regression models were computed for each index, for all six individual data sets, and for combined data sets. This means that the time series field and satellite data sets – or parts thereof – are considered as a single dataset. For the combination of data sets, several aspects were considered. Firstly, to generally test the transferability of the regression models to other acquisition dates, six data sets were generated, each leaving out one other sample on whose corresponding RapidEye VIs the function was to be applied. Secondly, spring (April 25, May 9, May 25) and summer (July 16, August 13, September 6) data sets were created to test for the transferability between seasons. To measure the accuracy loss caused by reducing the sampling density by half or two third, but still covering different phenological phases, data sets containing three (April 25, May 25, and August 13 scenes, and May 9, July 16, and September 6 scenes) and two (April 25 & July 16, April 25 & August 13, April 25 & September 6, May 9 & July 16, May 9 & August 13, May 9 & September 6, May 25 & July 16, May 25 & August 13, May 25 & September 6) samples were generated. Together with the single data sets and the set combining all data, this resulted in 26 different data sets.

To assess the accuracy of a statistical model, two aspects have to be investigated (Field et al., 2012): Is the model a valid fit to the data, and can it be generalized to other samples? To assess the validity of the regression, several aspects have to be considered. According to Burt et al. (2009) and Field et al. (2012), there are three basic requirements on the fitted model residuals that need to be fulfilled for further inferential analyses. The residuals have to be

- normally distributed with a mean equal to zero. The Shapiro-Wilk test (Royston, 1982) was used to assess whether the residuals distribution differed significantly from a normal distribution.
- homoscedastic, which means that the variance of residuals should be constant. The Breusch-Pagan test (Breusch and Pagan, 1979) was used to assure homoscedasticity of the residuals.
- independent. To test for correlations between residuals, the two-sided Durbin-Watson test (Durbin and Watson, 1971) was used.

For these tests, the 0.05 confidence level was chosen for acceptance of the null hypothesis. Further, results of the t-test and the F-test were used to check if the regression coefficients and the coefficient of determination R^2, respectively, were significantly different (significance level $p < 0.1$) from being null, and thus if they had an explanatory value for the predicted outcome. The strength of the model fit was investigated using R^2. Models not fulfilling the residual assumptions and not reaching the significance level for the model coefficients were discarded from further analysis. They are indicated as blank spots in Table A-7.

Apart from fulfilling these prerequisites, the generalizability of the model has to be assessed to ensure that it can be used for inferences beyond the sample of the collected data. Ideally, a second independent data set would be used to validate the model. However, the collection of field data is very laborious (see chapter 2.1), leading to generally small sample sizes. Due to this, there is a trade-off between using all available observations to develop a robust regression model and having no independent observations to test the model, versus excluding a predetermined number of observations for testing, but having a less robust model. To overcome this, cross-validation methods were used in this thesis in order to provide an unbiased estimation of model accuracy (Richter et al., 2012a). To assess the model fit, the adjusted coefficient of determination R^2_{adj} is used. This value indicates the loss of predictive power (*shrinkage*) of the model when applied to the population from which the sample is drawn. This value is generally lower than R^2 and can be negative. In the R language, it is calculated using Wherry's equation (R Development Core Team, 2008). To further measure the prediction error associated with the transfer function, cross-validation has been used to estimate the $RMSE_{cv}$. This is done by iteratively dividing the sample in two mutually exclusive subsets, fitting the model to the larger part of the samples and using the remaining values (the *holdout set*) for validation. K-fold cross-validation with k=10 has been reported to achieve better results for model validation than bootstrap and leave-one-out procedures (Kohavi, 1995; Borra and Di Ciaccio, 2010). However, for some of the very small samples used in this thesis (n_{min} = 10), a 10-fold sampling is equal or close to a leave-one-out procedure. Hence, in these cases, k was scaled linearly down to 5 for the smallest data set to achieve a good compromise between prediction bias and variance (Kohavi, 1995). The subsets were drawn randomly, and the cross-validation procedure was repeated 50 times and averaged to generate $RMSE_{cv}$. The relative cross-validated RMSE ($rRMSE_{cv}$) relates the RMSE to the samples mean and thus indicates the cross-validated model error in percentage.

5.2. Results of LAI derivation using statistical models

5.2.1. Single data set analysis

Overview of all tested LAI-VI relationships for the individual data sets is given in Table A-7. For each scene, R^2_{adj} as well as the significance level α of each VI performing in each model is listed. The highest R^2_{adj} values, i.e. the best fit and those fits with a maximum of 5 % less explanatory power, are printed in bold. Blank spaces indicate VI-model combinations that did not achieve a significant relationship or violated at least one regression assumption. For the single data sets, no valid relationship could be established in 8.5 % of all cases. Although the model types failed almost equally as often, some differences exist for the different VIs and data sets. The success rate for the data sets varied between 82 and 98 %, but could not be linked to the sample size or a phenological phase. With regard to the indices, several VIs could establish sound relationships in every case, although some (MSR2, MSR_{re}, Curvature, rLength, and MCARI, see Table A-6 for abbreviations) did not in 20 - 40 % of all cases.

A valid and strong fit was found for each scene. Figure 5-1 displays the scatter plots of the respective best-fitting model for each date. The overall explanatory power of the models, with R^2_{adj} values ranging from 0.64 to 0.86 ($p < 0.001$), is high. The cross-validated prediction errors $rRMSE_{cv}$ of 10.4 to 27.8 % also seem reasonable, although the target accuracy (see GCOS, 2006, and Drusch et al., 2010) of 10 % is clearly not met for some of the data sets (May 25, July 16, August 13). The relatively low explanatory power of the fit for the May 9 scene might be on account of the small sample size, its narrow range of measured LAI values (1.8 - 4.5), and especially some outliers. The July 16 scene also seems to be distorted by outliers in the high LAI and VI value ranges, while the concave shape of the model fit of the May 25 scene indicates signal saturation of the MSR_{re} index. As it was mentioned in chapter 2.2, saturation is the effect of radiation emerging from the canopy without remaining sensitive to increasing LAI, impairing the estimation of high LAI values (Baret and Guyot, 1991; Sellers et al., 1996; Turner et al., 1999; Liang, 2004; Duveiller et al., 2011b). Gobron et al. (1997a) explain that this happens when the canopy is optically not thin enough to allow an illumination of the underlying soil.

Apart from these restrictions, the strength of the respective regression models compare favorably with other studies. In grassland, R^2 values of up to 0.44 (He et al., 2006), 0.68 (Friedl et al., 1994), 0.79 (Fan et al., 2009), or 0.82 (Frank and Karn, 2003) were achieved based on common broad-band indices or transformations. Darvishzadeh et al. (2008c) improved the relationship between LAI and two narrow-band VIs (R^2= 0.63) by using SMR (R^2= 0.66) and PLS (R^2= 0.69). Using CCA, R^2 values of up to 0.54 (Cohen et al., 2003b) and

2011

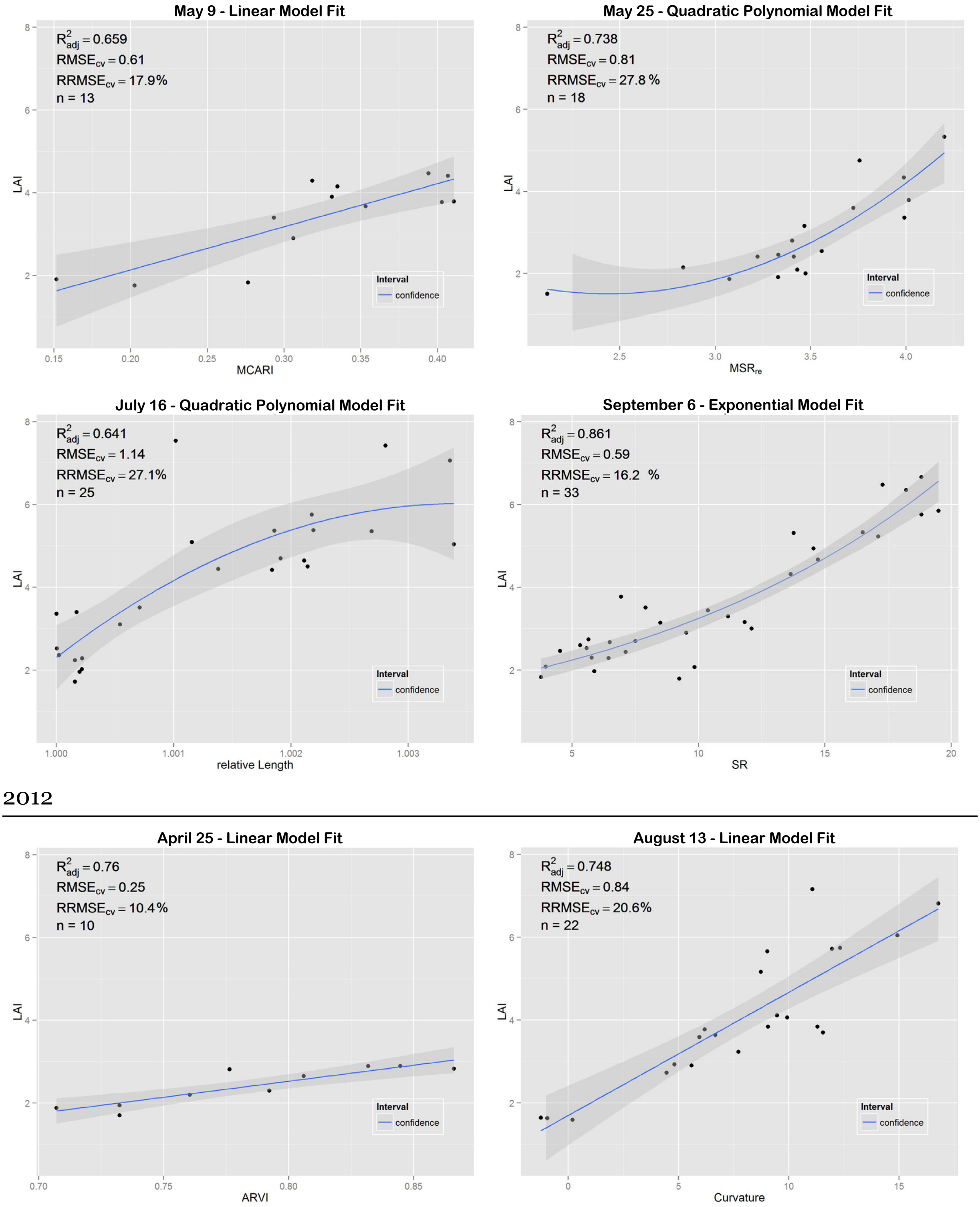

Figure 5-1: Best fitting LAI-VI relationship of the six single data sets, showing the adjusted coefficient of determination R^2_{adj}, the cross-validated absolute and relative root mean squared errors ($RMSE_{cv}$ and $rRMSE_{cv}$), as well as the 95 % prediction confidence intervals in grey.

0.63 (Cohen et al., 2006) with Tasseled Cap parameters or up to 0.6 with hyperspectral indices (Lee et al., 2004) were established. Although in this thesis, it is not the R^2 but the R^2_{adj} measure, which is generally lower, that is used, the accuracies are in the upper range of those results. The efficiency of the rather simple models and broad-band VIs used in this thesis is hence satisfying.

With regard to the models and VIs used for LAI estimation, no universal recommendation can be given, as the regressions show a diverse picture for the different scenes (Table A-7). No model or VI can be identified that fits best for all data sets. The linear models achieved the highest R_{adj}^2 ($p < 0.001$) for three of the scenes (April 25, May 9, and August 13). In the other scenes (apart from May 25), the linear models also have R_{adj}^2 values quite similar to those of the more complex models, and are thus useful for a rather conservative LAI estimation. In the May 25 and July 16 scenes, quadratic polynomial models fit best. The highest result for the September 6 scene is achieved by an exponential model. This mixed performance of different statistical models is in accordance with the varying findings in the literature, where the best results for an LAI–VI relationship were obtained with linear (Colombo et al., 2003), exponential (Hansen and Schjoerring, 2003; Wang et al., 2005; Yang et al., 2007; Vuolo et al., 2013), power and quadratic (Ehammer et al., 2010), or even cubic (Turner et al., 1999) models. This also supports the assumption that the LAI-VI relationship changes during one vegetation period, which has already been suggested for forest LAI (e.g. Wang et al., 2005; Heiskanen et al., 2012; Potithep et al., 2013). However, the pattern in the temporal order of the best fitting model shapes is not consistent (see Figure 5-1). The spring season is dominated by linear model fits (April 25 and May 9). Increasing vegetation densities would then hypothetically lead to a better fit of non-linear models due to saturation, which is indeed the case in the scenes of May 25, July 16, and September 6. However, the convex curve fitted to the July 16 data rather indicates an oversensitive VI than VI saturation. The August 13 model shape is linear, which indicates either that the relationship is distorted by outliers or that saturation is already reduced by senescence in mid-August. However, the September 6 scene regression is again exponential, representing a rather decreasing VI sensitivity with higher LAI values. It is hence not possible to derive a characteristic model shape development over the season from these observations. The fact that even temporally close relationships are not described by similar models supports the observations summarized by Dorigo et al. (2007) that statistical models are shaped by the canopy, soil, atmosphere, and illumination conditions that prevailed during data sampling and are hence restricted to them.

The respective best fitting VI also varies considerably for the different data sets (Table A-7). While the ratio indices as well as some hybrid and red edge indices achieve highest fits for the April 25 scene, the VIs performing the best fit by far in the May 9 scene are the modified chlorophyll indices. The red edge indices are the only ones achieving significant results in the following sample (May 25). In the July 16 scene the red edge indices fit best again, while in the August 13 and September 6 scenes also orthogonal and ratio indices achieve equally high R_{adj}^2 values. This variation in VIs suggests that the spectral canopy characteristics sampled during the different scenes vary in such a way that different band transformations are needed to unmask the LAI-VI relationships. Although the NDVI has been widely used for decades, it is shown here that LAI can be derived more accurately by other indices. The NDVI has 10 - 40 % less explanatory power than the respective best fitting VIs, apart from the April 25 scene, which supports the findings of Lee et al. (2004). An improvement of the NDVI-LAI relationship during senescence as observed by Eitel et al. (2011) and Tillack et al. (2014) cannot be confirmed, probably as they attributed this behavior to a decrease in chlorophyll content, which is not reached yet in grasslands by the beginning of September. He et al. (2006) concluded for grassland that ratio-based and soil-line related VIs performed better than chlorophyll corrected VIs, which can be confirmed apart from the May 9 scene.

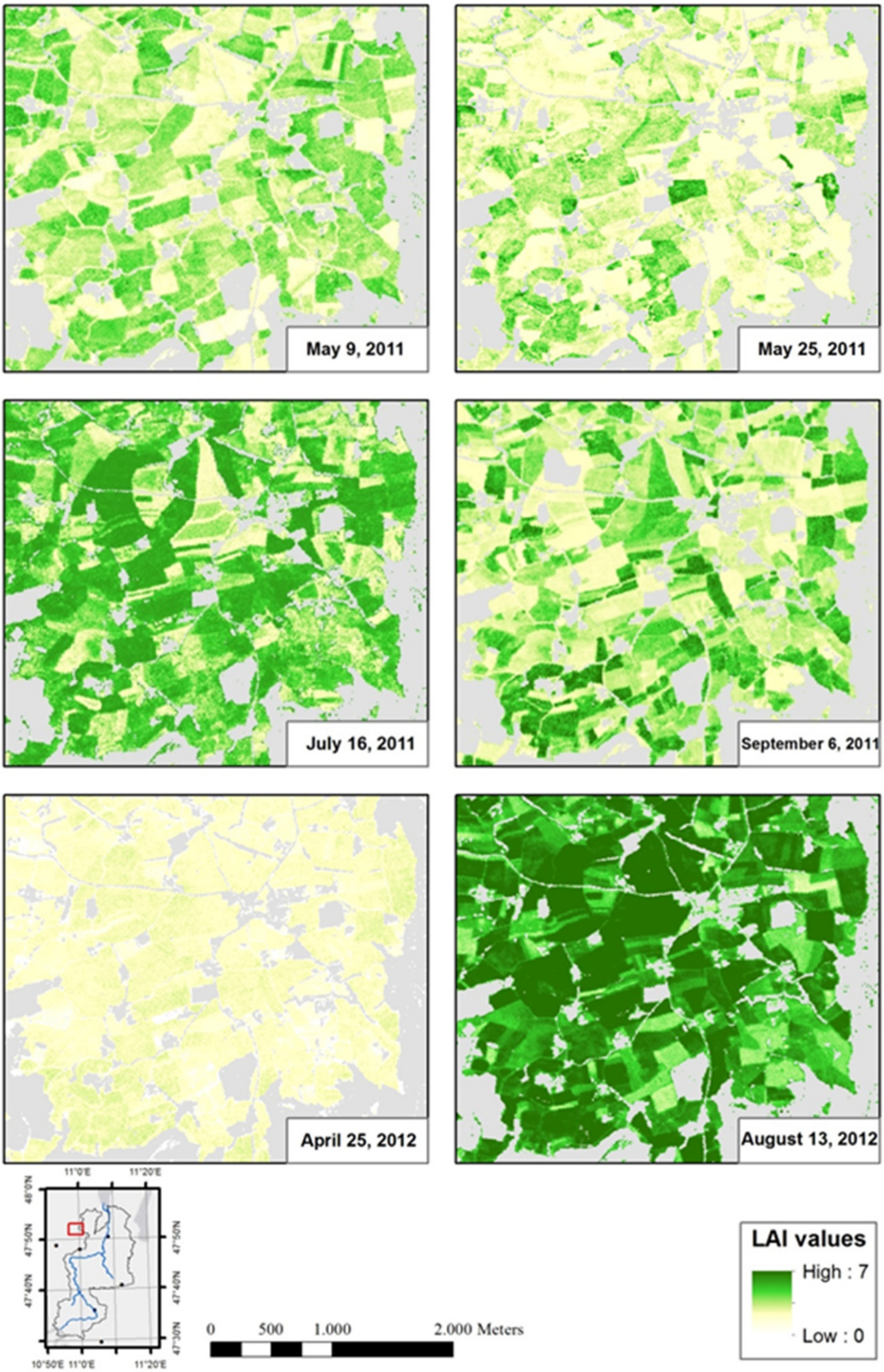

Figure 5-2: Subsets of the statistically derived LAI maps for the six field campaign dates.

Table 5-2: Summary of the statistics of the respective best model fit for each data set. n indicates the size of each data set, $R^2_{adj}$the adjusted coefficient of determination, $RMSE_{cv}$ the absolute cross-validated RMSE, $rRMSE_{cv}$ the RMSE, and α the significance level of the model fit: 0.1 '.' 0.05 '*' 0.01 '**' 0.001 '***'0.

	n	VI	Model	Function	R^2_{adj} α	$RMSE_{cv}$	$rRMSE_{cv}$
April 25	10	ARVI	linear	$LAI = -3.67 + 7.75 * ARVI$	0.76^{***}	0.25	10.4
May 9	13	MCARI	linear	$LAI = 0.05 + 10.43 * MCARI$	0.66^{***}	0.61	17.9
May 25	18	MSR_{re}	poly	$LAI = 8.07 - 5.39 * MSR_{re} + 1.11 * MSR_{re}^2$	0.74^{***}	0.81	27.8
July 16	25	rLength	poly	$LAI = -320705 + 639242 * rLength - 318534 * rLength^2$	0.64^{***}	1.14	27.1
August 13	22	Curv	linear	$LAI = 1.70 + 0.30 * Curv$	0.75^{***}	0.84	20.6
September 6	33	SR	expo	$LAI = 1.55 * e^{SR*0.07}$	0.86^{***}	0.59	16.2
all scenes	121	RDVI	expo	$LAI = 0.48 * e^{RDVI*3.52}$	0.48^{***}	1.08	30.1
all but April 25	111	RRI2	poly	$LAI = -2.81 + 2.59 * RRI2 - 0.2 * RRI2^2$	0.50^{***}	1.09	29.5
all but May 9	108	ARVI	poly	$LAI = 8.97 - 27.62 * ARVI + 27.06 * ARVI^2$	0.49^{***}	1.12	31.0
all but May 25	103	MSR2	poly	$LAI = 1.04 + 0.14 * MSR2 - 0.001 * MSR2^2$	0.46^{***}	1.14	30.6
all but July 30	96	Length	poly	$LAI = 3.83 - 16.22 * Length + 34.88 * Length^2$	0.65^{***}	0.84	24.6
all but Aug. 13	99	ARVI	poly	$LAI = 10.69 - 31.7 * ARVI + 29.35 * ARVI^2$	0.42^{***}	1.13	32.3
all but Sept. 6	88	SARVI	expo	$LAI = 0.65 * e^{SARVI*2.96}$	0.39^{***}	1.18	32.9
April 25, May 25, Aug. 13	50	RRI1	poly	$LAI = 6.47 - 5.05 * RRI1 + 1.3 * RRI1^2$	0.65^{***}	0.85	25.5
May 9, July 16, Sept. 6	71	RRI2	linear	$LAI = -1.22 + 1.46 * RRI2$	0.58^{***}	1.00	26.4
April 25, July 16	35	MSR_{re}	poly	$LAI = 17.85 - 11.73 * MSR_{re} + 2.26 * MSR_{re}^2$	0.40^{***}	1.40	37.8
April 25, Aug. 13	32	DVI	expo	$LAI = 0.51 * e^{DVI*4.34}$	0.72^{***}	0.86	24.2
April 25, Sept. 6	43	Curv	poly	$LAI = 2.11 + 0.01 * Curv + 0.01 * Curv^2$	0.81^{***}	0.64	19.3
May 9, July 16	38	NDVI	power	$LAI = 8.02 * NDVI^{3.38}$	0.39^{***}	1.24	31.4
May 9, Aug. 13	35	Length	power	$LAI = 15.4 * Length^{1.81}$	0.72^{***}	0.79	20.6
May 9, Sept. 6	46	SR	expo	$LAI = 1.55 * e^{SR*0.07}$	0.79^{***}	0.65	18.3
May 25 July 16	43	SR	linear	$LAI = 0.13 + 0.37 * SR$	0.51^{***}	1.16	31.6
May 25, Aug. 13	40	$NDVI_{re}$	poly	$LAI = 12.7 - 63.9 * NDVI_{re} + 89.93 * NDVI_{re}^2$	0.70^{***}	0.82	23.2
May 25, Sept. 6	51	RRI1	poly	$LAI = 5.28 - 3.38 * RRI1 + 0.88 * RRI1^2$	0.78^{***}	0.67	19.7
spring	41	RRI1	poly	$LAI = 10.98 - 7.52 * RRI1 + 1.6 * RRI1^2$	0.43^{***}	0.96	32.7
summer	80	ARVI	poly	$LAI = 7.71 - 23.66 * ARVI + 24.58 * ARVI^2$	0.59^{***}	1.04	26.5

The overall analysis of the single time step R^2_{adj} values shows that the differences in regression strength between the VIs is, on average for the individual data sets, 2 - 30 times larger than the differences in between the model types. The same is true for the coefficients of determination of the combined data sets (see below). This observation suggests that the careful selection of a VI sensitive to the variable of interest at a certain point in time is of higher importance than an extensive selection of the model type.

In the upper part of Table 5-2, the statistical figures and the established transfer function of the respective best fitting model for each date are specified. These functions were applied to map LAI based on the six RapidEye scenes. The scatterplots between field and satellite estimates of LAI are shown in Figure A-1. A subset of each generated LAI map is displayed in Figure 5-2. In the LAI maps, individual fields can be well distinguished. They show a heterogeneous, temporally and spatially variable pattern of growth stages due to the phenological development as well as varying grazing and mowing cultivations and intensities.

Vegetation density follows the seasonal trend with a maximum in August. The late May 25 scene stands out with considerably reduced LAI values in comparison to the May 9 scene. This is caused by anthropogenic influences, as, due to the prevalent weather conditions in 2011, most parcels were mowed for the first time in mid-May.

5.2.2. Temporal transferability of statistical relationships

After LAI maps have been derived under these best-case conditions, i.e. using data collected in the field simultaneously with an RS observation, in this section the frequently encountered situation of having a satellite image but no field data is simulated. The aim is to quantify the error that is introduced to LAI estimation under such conditions. As described in chapter 3.5, the diverse management techniques in the study area result in a broad range of vegetation states at nearly any point in time. In theory, this is an advantage with regard to the establishment of transferable relationships, as this would enable *in situ* measurements of a wide range of LAI values at almost every point in time over the entire vegetation period. Based on these wide ranges and similar variances of LAI, robust and therewith transportable transfer functions could thus be established. To verify this assumption, the established transfer functions (see upper part of Table 5-2) were used on the respective VIs (i.e. the VIs by means of which the functions have been established) of the other scenes to test for their temporal transferability. Their prediction potential for LAI at other points in time has been measured against the available field data, hence using the RMSE and rRMSE (RMSE / mean value of the reference measurements).

The six single transfer functions achieve variable results when applied to other data sets. The resulting error rates are summarized in the upper part of Table 5-3. It can be observed that the use of a transfer function established on a single field campaign data set increases the associated prediction error in all but one case. However, the rRMSE values of the LAI estimates range from 12 % in the best case up to 102 % for one data set, which corresponds to an LAI RMSE of 2.5 in this scene. This high error variance (the error being doubled, tripled, and increased even higher in a third of all cases each) complicates the derivation of an overall error magnitude introduced by function transferability to other RS scenes. The error tends to be higher when a spring or summer data set is used for LAI prediction in the respective other season. However, for the models of the May 9, May 25, and September 6 scenes, this connection is inverted with mostly higher prediction errors for the chronologically closer dates. With regard to the individual data sets, the July 16 transfer function yields the highest average error (70%), which can be explained by its extraordinary model shape and its large absolute LAI values (see Figure 5-1). Further, the field data sampled very early and very late in the year (April 25, May 9, September 6) transfer with a similar average error (44 - 52 %). Especially in the first two scenes, the transfer is probably hampered by the small LAI value range. The May 25 and August 13 scenes (linear and polynomial model fits) achieve the lowest errors of around 35 %. The sampled LAI values of April 25 are predicted with the highest errors, probably due to the overall low value range.

It can be concluded from this experiment that the use of a transfer function on another RS scene is always unfavorable, as it will highly probably increase the prediction RMSE to over 1. This disproves the above mentioned general assumption of temporally stable transfer functions in grassland due to its high variability. Although it is possible to measure low and moderate LAI values *in situ* at every point in time (see Figure 4-15), extremely high values can neither be sampled nor reproduced for every date. Instead, these results confirm the impression generated by Figure 5-1 that the different models are fit to different densities, biochemical conditions, and canopy structures in different vegetation stages. If a regression model transfer cannot be avoided, however, i.e. LAI can only be sampled once during a season, this sampling should be conducted in early or late summer to cover a wide data range, and carefully screened for outliers afterwards. In spring, the data range of LAI values is too narrow, and measurements in mid-summer tend to be affected by saturation. Further, a linear or a similarly conservative regression model should be used to prevent extreme LAI estimations. The effect of regression model transferability has not been quantified in other studies so far, which impedes a comparison of these results. Vuolo et al. (2013) test the spatial transfer of LAI models, but use model parameters calibrated on the whole season, not on individual points in time.

5.2.3. Combined data sets analysis

As shown above, the use of transfer functions based on data from a single point in time on other scenes does mostly not yield acceptable results. Thus, the motivation to combine data sets collected during several measurement campaigns is to increase the validity and robustness of relationships used for LAI derivations at other points in time. For field crops, this approach has often been pursued in order to integrate all development stages of the plants in the regression model (e.g. Ehammer et al., 2010; Rinaldi et al., 2010). The respective best fitting regression functions trained on the above-mentioned data set combinations (see Table 5-2) have thus been analyzed for their regression strength to test the possibility of deriving robust statistical relationship transferable in time, and to identify the number and timing of field campaigns needed.

In a first step, the performance of a regression model based on all available *in situ* measurements is tested. The 2011 and 2012 data sets are thereby treated as one season's time series. The R^2_{adj} of the model fitted to all available data is considerably lower than that of the single time steps (see Table 5-2) and the relative prediction errors are overall higher than those achieved with the scene-adapted models (Table 5-3). While the mean error of the individual models is 17.9 %, the rRMSE$_{cv}$ of the combined data set is 30.1 %. Aggregating all available field data for building a regression model would only reduce the LAI mapping error for one scene (July 16). Scenes for which the rRMSEs are around 20% show even lower prediction errors for the individual data sets. This reduction of model strength when combining data sets has also been observed by Vuolo et al. (2013) and Wang et al. (2005).

As the "all scenes" regression model is thus no suitable replacement for the adapted models, it would be of higher interest if gaps within a time series could be filled based solely on the satellite image and on combined field data sets of the same vegetation period. Thus, different scenarios of field data availability are tested also in this chapter. Therefore, a "leave-one-out" experiment has been applied to each scene's data set. Polynomial model have almost exclusively achieved the best fits on these data sets, as other models had to be rejected due to the non-compliance of the residuals normality test in many cases. The R^2_{adj} and rRMSE$_{cv}$ values of these models are quite similar to those of the "all scenes" combination, varying around 0.49 and 30.2 %, respectively (Table 5 2). Only the data set leaving out the July 16 scene achieves a noticeably better model fit and an RMSE$_{cv}$ below 1, indicating a possible distortion introduced by the July 16 data. The rRMSEs of the "interpolated" LAI values vary greatly between 21.7 and 92.6 % (Table 5 3). Two gaps can only be deficiently filled by the use of a model based on the remaining time series data. The LAI of April 25 has been almost impossible to predict using another date's model (see upper part of Table 5 2), and it is also predicted with an error of 92.6 % in this experiment. With its overall very low values and

Table 5-3: Prediction errors of transfer functions applied to other points in time based on the individual and combined field data sets. Shaded cells indicate that no model transfer has been performed as the data sets have been used for training. The ‘all scenes’ data set is an exception

rRMSE [%] **Transfer function of**	**Used on VI of**					
	April 25	May 9	May 25	July 16	August 13	September 6
April 25		42.1	47.3	61.2	52.0	56.0
May 9	91.8		41.5	40.4	34.4	31.3
May 25	12.0	33.2		54.6	41.1	25.9
July 16	102.0	65.8	92.7		29.9	58.7
August 13	50.4	33.7	43.3	34.6		21.1
September 6	96.7	22.8	29.0	34.7	37	
all scenes	57.9	20.4	31.5	37.9	20.9	20.2
all but April 25	92.6					
all but May 9		26.6				
all but May 25			33.4			
all but July 30				41.1		
all but Aug. 13					24.8	
all but Sept. 6						21.7
April 25, May 25, Aug. 13		29.4		45.8		26.6
May 9, July 16, Sept. 6	126.5		23.6		47.7	
April 25, July 16		56.9	70.6		28.4	75.2
April 25, Aug. 13		20.6	33.0	47.4		29.9
April 25, Sept. 6		25.6	23.8	45.9	26.7	
May 9, July 16	96.9		37.8		28.3	22.8
May 9, Aug. 13	41.7		30.8	43.3		25.0
May 9, Sept. 6	94.2		29.0	35.1	35.6	
May 25, July 16	123.8	34.0			46.5	23.6
May 25, Aug. 13	42.5	32.8		44.1		25.7
May 25, Sept. 6	31.9	25.2		44.5	26.7	
spring				47.9	29.1	20.8
summer	82.3	31.1	33.8			

narrow data range (LAI = 1.7 - 2.9) but at the same time rather high VI values (see Figure 5 3), it obviously cannot be reproduced properly. The other exception is the July 16 scene. Despite the good model fit established on the remaining five data sets, this date’s LAI is estimated with a high error (41.1 %). This result strengthens the above-mentioned observation that the data set is distorted by outliers. Apart from these two dates, LAI can be predicted using the other times steps’ regression models with an error of around or below 30 %. This equals the accuracies achieved using all data sets and represents an accuracy loss of approximately 10 % when filling a time series gap compared to the ideal use of coincident *in situ* measurements.

In the next step, the performance of the empirical-statistical approach when further reducing the number of field campaigns by half or by two thirds is analyzed. This corresponds to the use of three or two combined *in situ* measurement data sets (see middle part of Table 5-3). The three data set combinations were created by evenly distributing the dates over the season, while for the two data set combinations, different spring and summer scenes were joined based on the findings of preliminary analyses (Asam et al., 2013). With regard to the R_{adj}^2 values, the two different "three scenes" models are comparably strong. The prediction results are once again biased by the large prediction error on the April 25 data set. Leaving this result unconsidered, the two models perform similar well, with rRMSEs between 23.6 and 47.7. In both cases, the vegetation maximum exhibits the largest prediction errors.

From solely investigating the R_{adj}^2 and $rRMSE_{cv}$ of the two date combinations, it can be seen that any regression model trained on the July 16 data achieves considerably lower results than the others. Their rRMSEs are also higher on average (54 %) than those of the other data sets (36 %). The LAI estimations for the July 16 scene have a correspondingly high error rate, which is not the case for the other mid-summer scene (August 13) and is thus probably not caused by saturation. As observed before, the April 25 data are mostly not reproducible with a reasonable error rate. Leaving the April 25 error rates unconsidered, the average rRMSEs of all models (apart from the April 25 & July 16 scenes combination) vary around 33 %. This indicates an approximately 15 % prediction improvement by using two data sets instead of only one measurement campaign randomly placed during the vegetation period. In several cases, this might be caused by the low sample size when using only one time step. No considerable difference can be found between the uses of two, three or five data sets. With regard to measurement timing, the combinations with the latest campaign (September 6) achieve better results overall than those of the mid-summer scenes (July 16 and August 13).

These results suggest that the use of only two *in situ* data sets is sufficient for LAI time series derivation if an increased error rate of approximately 33 % is accepted. This is also an option if no robust regression model can be established on a single data set. As only models covering both, the spring and summer seasons, have been used so far, the transferability of models established on either one is tested last (see bottom part of Table 5-3). The establishment of valid regression models has been more difficult for the spring combination, as the residues of most tested models have not been normally distributed (most p > 0.05). Comparing the two model fits, the summer data sets combination yields better results (R_{adj}^2 equals 0.43 and 0.59, see Table 5-2). However, this difference in model strength could also be explained by the sample size, which is twice as big for the summer sample. With regard to the LAI estimation error, the two models yield similar figures (32.5 %, once again leaving the April 25 scene unconsidered). This surprisingly good performance of the spring model might be explained by the relatively high LAI *in situ* values of the May 25 scene (up to five), and indicates a reduced importance of field measurement timing when several data sets are combined.

5.2.4. Red edge potential for LAI derivation

As mentioned above, only few studies have used RapidEye data for the characterization of vegetation canopies so far (see e.g. Ehammer et al., 2010; Eitel et al., 2011; Friese et al., 2011). None of them quantified or discussed the benefits of the red edge band for LAI derivation. Especially with regard to new and upcoming sensors such as WorldView-2 or Sentinel-2 (DigitalGlobe, 2010; Drusch et al., 2012), which are equipped with one or more red edge bands, the potential of this spectral domain for vegetation parameter mapping is of high interest. Therefore, the impact of the use of the RapidEye red edge band is assessed in this thesis by comparing the statistical modeling results based on conventional VIs and their respective red edge equivalents, in which the red band is substituted by the red edge band. Three VI pairs (SR – RRI1, NDVI – $NDVI_{re}$, and MSR2 – MSR_{re}) are based on the respective same formula including the red band or red edge band (see Table A-6). All single data sets and all models were included in this analysis, however, only the models which achieve significant results ($p < 0.01$) were considered. As not a single significant model could be established for the May 9 scene using one of the above-mentioned indices (see Table A-7), no comparison could be performed for this scene. With this reduction to five scenes' data, the analysis was conducted on 60 VI pairs.

Regarding the regression modelling presented in this chapter, the additional value of the red edge band is striking. In Table 5-4, the model results of the VI pairs are presented, with the higher R^2_{adj} value printed in bold in each case. In 88 % of all VI comparisons, the red edge VI yields stronger relationships than the respective original VI. Averaged over all 60 VI comparisons, the $rRMSE_{cv}$ could be decreased by 5.4 % by using a red edge VI. Although the red edge VIs could establish no valid models in 20 - 40 % of all cases as mentioned in chapter 5.2.1, they were robust in those cases where the respective conventional VIs failed. Regarding the other VIs used in this thesis employing the red edge band, i.e. the experimental indices *Curvature*, *Length* and *relative Length* proposed by Conrad et al. (2012) and the MCARI (Daughtry, 2000), further analysis also seems promising. Each of these VIs achieved highest

Table 5-4: Comparison of regression R^2_{adj} values established using SR, MSR2, and NDVI with their red edge band equivalents. Only significant model results ($p < 0.01$) were included in the comparison.

		R^2_{adj} values					
Model	Week	SR	RRI1	MSR2	MSR_{re}	NDVI	$NDVI_{re}$
linear	April 25	0.63	**0.72**	0.65	**0.73**	0.74	0.74
	May 25	0.37	**0.57**	0.33	**0.61**		**0.45**
	July 16	0.51	**0.63**	0.35	**0.61**	0.48	**0.62**
	August 13	0.62	**0.70**	0.56	**0.71**	0.53	**0.64**
	September 6	**0.83**	0.79	0.74	**0.76**	0.62	**0.72**
power	April 25	0.67	**0.71**	0.69	**0.72**	0.72	**0.73**
	May 25	0.38	**0.68**	0.35	**0.70**		**0.62**
	July 16	0.51	**0.63**	0.37	**0.61**	0.50	**0.63**
	August 13	0.63	**0.72**	0.58	**0.72**	0.59	**0.70**
	September 6	**0.82**	0.81	0.74	**0.78**	0.71	**0.77**
exponential	April 25	0.59	**0.69**	0.59	**0.70**	**0.72**	0.72
	May 25	0.41	**0.71**		**0.73**		**0.66**
	July 16	0.49	**0.62**	0.32	**0.61**	0.51	**0.63**
	August 13	0.57	**0.71**	0.48	**0.72**	0.61	**0.71**
	September 6	**0.86**	0.83	0.68	**0.80**	0.74	**0.80**
polynomial	April 25	0.74	**0.74**	**0.81**	0.76	0.74	**0.75**
	May 25		**0.73**		**0.74**		**0.69**
	July 16	0.50	**0.61**	0.35	**0.59**	0.52	**0.61**
	August 13	0.61	**0.71**	0.60	**0.71**	0.61	**0.71**
	September 6	**0.86**	0.82	0.74	**0.80**	0.78	**0.81**

results on at least one of the data sets and thus indicates a useful sensitivity to certain conditions. The shape indices were especially successful for very dense vegetation (July 16 and August 13). Such an improved ability to establish statistical relationships when using the red edge channel was also observed by Tillack et al. (2014) for some phenological phases in forest canopies, although they did not compare structurally identical indices and yielded lower R^2_{adj} values on the whole.

5.3. Potential of statistical models for LAI derivation

In chapter 5, the potential of LAI derivation from single and combined RapidEye data based on empirical-statistical models was investigated. The usefulness of repeated *in situ* measurements and RapidEye images is proven by high R^2_{adj} (0.64 - 0.86) and corresponding low prediction errors (RMSE$_{cv}$: 0.25 - 1.14, rRMSE$_{cv}$: 10.4 to 27.8 %) of most of the established statistical models. The high spatial resolution of the RapidEye data enabled the distinction of LAI variabilities within and between fields, and hence the direct relation between different canopy states and associated reflectances. However, with such high spatial resolution data, local disturbing factors such as changing viewing geometries, canopy gaps, and saturation, also might have a potentially high influence on this relationship.

These modeling results are in the upper ranges of other LAI derivation studies and thus satisfying, but with rRMSE$_{cv}$ and absolute RMSE$_{cv}$ values above 10 % and 0.5, respectively, which do not yet meet the target requirements determined by GCOS (2006) and the GMES user committee (Drusch et al., 2010). Generally, it would therefore be of high interest to test in further research whether the accuracies achieved with the empirical-statistical method over grassland can still be improved, e.g. by using other models, different *in situ* measurement methods, or a more detailed field sampling strategy, or whether this method will always be restricted by the underdetermined problem (see chapter 2.2.3) of deriving a single canopy variable from the spectral signature of a surface.

It was further deduced in this chapter that the proper selection of a VI is more important for a sound regression model than the selection of a mathematical model type. With regard to the potential of RapidEye's red edge band, it was concluded that the red edge clearly strengthens the LAI-VI relationships and improves the LAI prediction. The derived maps show that LAI varies strongly over space and time due to phenology and managing practices. The relation between field-based and satellite-based measurements also changes over the season. Different VIs and models should therefore be used for estimating LAI during the year. This supports the reasoning of Dorigo et al. (2007), who state that empirical-statistical relationships are restricted to the conditions that prevailed during RS and field data acquisition. Further, these investigations revealed inconsistencies and problems with the July 16 data set, which seems to be influenced by outliers. Therefore, a proper outlier screening (see Field et al., 2012) is highly recommended for empirical-statistical LAI modeling.

The test on temporal transferability of regression models reveals an associated rRMSE$_{cv}$ increase from on average 20% for the data sets on which the function has been established, to on average of 49 % if used on other points in time. Compared to the ideal use of the contemporaneous *in situ* measurements, this result represents an accuracy loss of 30 %. If such a procedure cannot be avoided, the training data set should be sampled in early or late summer, screened for outliers and used in a conservative regression model. However, for a rigorous analysis of optimal measurement times, the identical sample sizes for each campaign would be ideal to prevent reduced model performances due to changing sample sizes and insufficiently sampled variance ranges. These aspects should be considered for future work. The analysis further showed that there are phenological phases for which LAI cannot be reproduced using other field data. In none of the transferability experiments models that were established on other single data sets proved to be suitable for LAI estimation from the earliest scene (April 25). These periods of rapid change, i.e. green-up and senescence, are thus only properly simulated using corresponding field data.

With regard to data set combinations, the union of all six available data sets results in higher LAI estimation errors than the respective individual models. The prediction error is 31.5 % on average and thus similar to the average accuracies that can be achieved when interpolating time series gaps based on the respective other five scenes (rRMSE = 30.2 %). This error does also not increase when using only half or one third of the available field measurements. From this series of experiments, it can be derived that the LAI derivation for a date in time for which no *in situ* measurements are available is improved by approximately 15 % when two measurement campaigns are conducted instead of only one. Further campaigns do not significantly reduce the estimation error. With regard to the timing of field measurements, the R_{adj}^2 values of the models including a spring scene and the late summer scene (September 6) achieve highest results, so that this combination is recommended for efficient and representative field measurements.

6. LAI derivation using the PROSAIL model

The second LAI derivation approach pursued in this thesis is the physical modeling of LAI using an RTM. As presented in chapter 2.2.3, RTMs simulate the interactions of radiation with vegetation elements and the soil while traveling through the canopy, i.e. absorbance, reflectance and transmittance. Based on these processes, the radiation leaving a canopy can be related to its spectral and structural properties (Widlowski et al., 2014). In LAI retrieval procedures, the RTM is run first in the forward mode to calculate reflectances given specific canopy and observation configurations. This canopy characterization by biophysical and chemical input parameters is called parameterization. By iteratively changing the parameterization, RTMs simulate the spectra of a great variety of vegetation conditions (see Figure 6-1). In the second step, which is referred to as inversion, the canopy spectrum with its parameters (including LAI) most similar to the measured reflectances is selected by spectral matching or by a statistical relationship over the RTM input and output (Dorigo et al., 2007).

The advantage of LAI modeling using RTMs is its independence from field measurements. If data on canopy characteristics are available from *in situ* observations, this might improve the

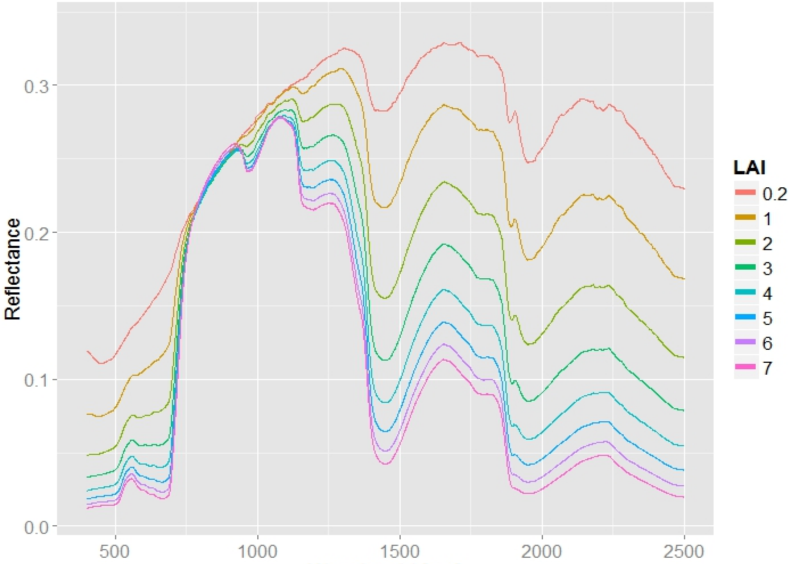

Figure 6-1: Effect of LAI on PROSAIL canopy reflectance (θ_s = 30°, θ_o = 0°, φ_r = 0°, ALA = 60°, C_{ab} = 35 µg cm^{-2}, C_{ar} = 10 µg cm^{-2}, C_w = 0.02 cm, C_m = 0.01 g cm^{-2}, N = 1.5, bf = 0.5, hs = 0.11, C_{bp} = 0.3, skyl = 0.13. For abbreviations see Table 6-1).

LAI modeling, as it can be used as "prior information" for parameterization. However, the workflow of physical LAI derivation does not rely on it. This enables an automated LAI derivation and thus time series generation. Further, several factors influencing the canopy reflectances, such as the soil reflectance, the illumination and observation geometry, or the canopy structure, are explicitly accounted for in an RTM. Additionally, some inversion techniques allow for the simultaneous derivation of several biophysical leaf and canopy parameters, and provide pixel-wise quality information on the LAI modeling.

Despite these advantages, RTMs have so far never been used for the derivation of grassland LAI from high spatial resolution multi-spectral RS data (see chapter 2.4). In view of the expected increase in availability of high spatial resolution RS data over the next few years, the aim of this chapter is to assess the potential of this data type for physical LAI derivation of (semi-)natural grasslands in comparison to empirical-statistically derived LAI (chapter 5). Additionally, the use of some innovative approaches, namely a global sensitivity analysis, the use of additional input features, and the mapping of pixel-wise LAI estimation uncertainties is analyzed.

Figure 6-2 displays the workflow of the physical LAI derivation algorithm used in this thesis. The preprocessing of the RapidEye data used as input for model inversion was presented in chapter 4.1. With regard to physical LAI modeling, Dorigo et al. (2007) state that LAI retrieval accuracy depends on the selection of an appropriate RTM, an RTM parameterization well adapted to canopy conditions and system geometry, and on the inversion procedure. These are also the main points that are presented in this chapter (see right part of Figure 6-2). In the first subchapter 6.1, the characteristics and the suitability

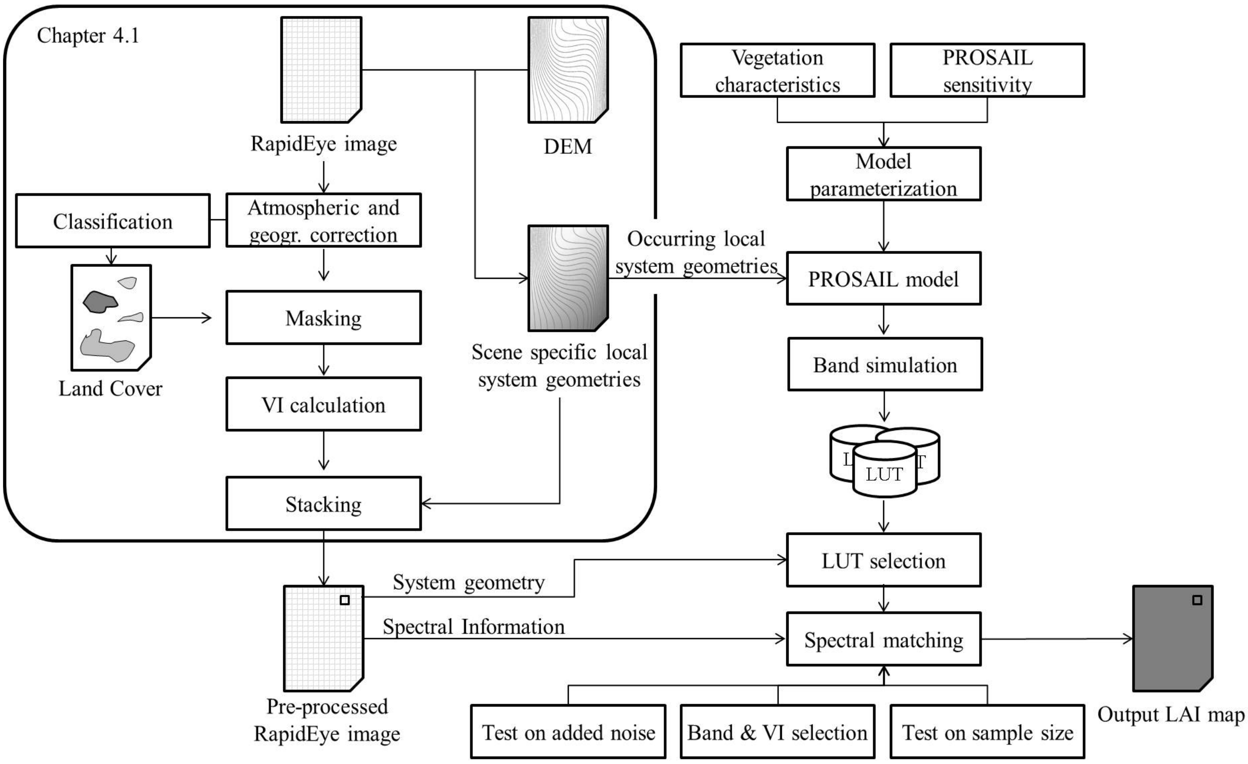

Figure 6-2: Flowchart of the LAI retrieval algorithm used in this thesis. The left part illustrates the RapidEye preprocessing chain, the steps involved in the establishment of a scene specific local system geometries layer (see chapter 6.4) are depicted while in the middle. On the right, the model set up (parameterization, LUT generation) and inversion procedure (spectral matching as well as optimization techniques "feature selection" and "sample size") discussed in this chapter are shown.

specifically of the PROSAIL model (Jacquemoud et al., 2009) used in this thesis are discussed. In order to optimize the parameterization of the most influential model parameters, a sensitivity analysis is performed in a next step (subchapter 6.2). The gained information is used together with the vegetation characteristics described in chapter 4.3 for model parameterization (subchapter 6.3). Next, the integration of topographic information (see chapter 4.2) within the model setup is assessed in subchapter 6.4. Subchapter 6.5 describes the tested inversion and regularization strategies, namely the selection of the LUT approach as well as of a cost function for the spectral match, the test on multiple solution sample sizes, spectral feature selection, and the addition of simulated noise. Subchapter 6.6 summarizes and discusses the results of physical LAI modeling. In subchapter 6.7, conclusions on the potential and challenges of the procedure are drawn.

6.1. The PROSAIL model

6.1.1. Model characteristics

Due to the high diversity in leaves and vegetation canopies, a wide range of leaf and canopy models has been developed (see chapter 2.2.3). The selection of an appropriate model from this variety for the canopy under consideration is crucial for accurate LAI derivation (Dorigo et al., 2007). According to Weiss et al. (2000), the choice of the RTM has to meet at least two requirements: it has to allow a fair representation of the canopy architecture, but manage to do so with a minimum of input information. Further, the computational efficiency is important when time series of high spatial resolution data are analyzed. Limiting the number of parameters increases model stability. A higher number of model parameters that need to be specified inevitably increases the model output uncertainty, as the exact specifications of these parameters is generally not known und varies strongly among canopy types. RTM complexity is hence always a trade-off between realism and accuracy, as it is ambiguous whether an increase in model realism would outbalance the retrieval uncertainty produced from a more complex combination of parameters. LAI modeling in this thesis is facilitated by the facts that only a single ecosystem is investigated, and that grassland canopies exhibit a high level of randomness. The latter favors the use of a model that represents the canopy as randomly distributed vegetation elements, i.e. turbid medium models (see chapter 2.2.3).

The PROSAIL model was chosen here, which is a nonlinear 1D turbid medium RTM. As outlined in chapter 2.2.3, the PROSAIL model (Jacquemoud et al., 2009) combines the most widely used leaf model, PROSPECT (Jacquemoud and Baret, 1990), with the most widely used vegetation canopy model, SAIL (Verhoef, 1984, 1985), and is itself the most popular

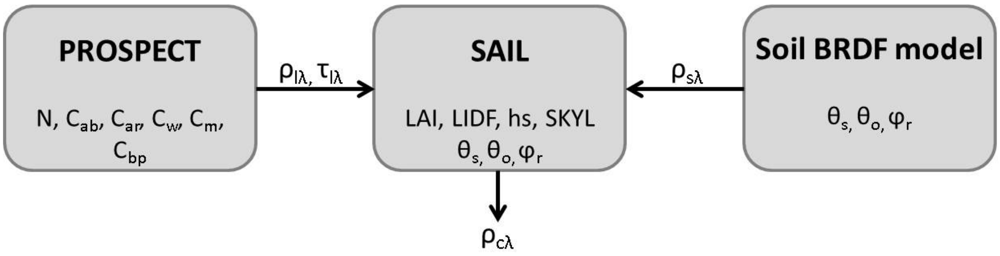

Figure 6-3: Schematic structure of the PROSAIL model. The abbreviations indicate the PROSAIL input parameters (N = leaf structure coefficient; C_{ab} = chlorophyll a +b content, C_{ar} = carotenoid content, C_w = equivalent water thickness, C_m = dry matter content, C_{bp} = brown pigments content, LIDF = leaf inclination distribution function, *hs* = hot spot, SKYL = ratio of diffuse incident radiation). ρ is the reflectance and τ the transmittance of leaves ($_l$), soil ($_s$), and canopy ($_c$) that are wavelength dependent, θ_s and θ_o are the sensor and observer zenith angles, and φ_r is the relative azimuth angle. Adapted from Jacquemoud et al. (2009).

coupled leaf-canopy RTM. The structure of the model is depicted in Figure 6-3. The version used here is coded in MATLAB and is freely available[16].

PROSPECT simulates the leaf directional–hemispherical reflectance and transmittance in the spectrum between 400 - 2500 nm with a 1 nm spectral resolution (Le Maire et al., 2004). It represents leaves as a pile of n homogeneous absorbing plates with rough isotropic surfaces separated by $n - 1$ intermediate air spaces. Within the plates, the absorption elements are assumed to be randomly distributed. The specific absorption coefficients of the different molecules, the surface roughness parameter, as well as the refractive index of leaf material were determined empirically and are stored in the model data base (Jacquemoud and Baret, 1990). PROSPECT is thus a deterministic model. In this thesis, the PROSPECT 5b version with a separate treatment of chlorophylls and carotenoids is used (Féret et al., 2008). Model variables are the leaf structure parameter N, specifying the average number of "plates" and thus of air-cell wall interfaces within the mesophyll, the dry matter (C_m) and water content (C_w), as well as the biochemical constituents chlorophyll (C_{ab}), carotenoid (C_{ar}), and brown pigments (C_{bp}) (see Table 6-1). C_m comprises cell wall molecules such as cellulose and lignin, while C_{bp} represents the polyphenol pigments responsible for senescence. PROSPECT has been improved, applied, and validated in several studies (Fourty et al., 1996; Jacquemoud et al., 1996; Baret and Fourty, 1997; Bousquet et al., 2005).

SAIL is an analytical canopy reflectance model that represents the canopy as a plane-parallel, horizontally uniform and infinite but vertically variable and finite slab. The canopy contains infinitely small leaves randomly distributed in space, between which multiple scattering occurs (Verhoef, 1984, 1985, 2002). For the development of canopy reflectance models and SAIL derivatives, see chapter 2.2.3. In this thesis, the numerically robust and speed-optimized model version 4SAIL was used (Kuusk, 1985; Verhoef, 1998; Verhoef et al., 2007). The leaf transmittance and reflectance are provided by the PROSPECT model (see Figure 6-3), while the canopy architecture is specified by LAI, LIDF, and the hot spot parameter *hs*

Table 6-1: Input parameters of the PROSAIL model subdivided into PROSPECT and SAIL parameters. The symbol column contains the parameter abbreviations used throughout this text and the unit column indicates the parameters' units.

Symbol	Parameter	Unit
PROSPECT variables		
N	Leaf structure coefficient	-
C_{ab}	Chlorophyll a +b content	$\mu g*cm^{-2}$
C_{ar}	Carotenoid content	$\mu g*cm^{-2}$
C_w	Equivalent water thickness	cm
C_m	Dry matter content	$g*cm^{-2}$
C_{bp}	Brown pigments content	-
SAIL variables		
LAI	Leaf area index	m^2*m^{-2}
LIDF	Leaf inclination distribution function	°
hs	Hot spot parameter	$m*m^{-1}$
ρ_{soil}	Soil reflectance	-
SKYL	Diffuse/total incident radiation	-
θ_s	Solar zenith angle	°
θ_o	Observer zenith angle	°
φ_r	Relative azimuth angle	°

---

[16] Downloaded from http://teledetection.ipgp.jussieu.fr/prosail/. Last access: May 12, 2014.

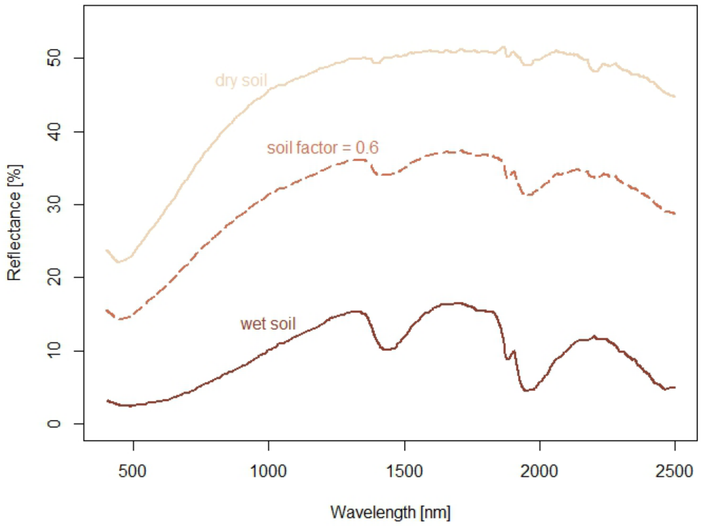

Figure 6-4: PROSAIL soil spectra. The wet and dry soil spectra are stored in the PROSAIL model, and a brightness factor (*bf*) is used to scale between the two. Wet (and thus dark) soil corresponds to a *bf* of zero, while dry soil corresponds to a *bf* of one.

(see Table 6-1). In this model implementation, LIDF is either assumed ellipsoidal and specified by its MTA (Campbell, 1990) or can be represented by a more complex 2-parameter LIDF model (Verhoef, 1998). hs is a single-scattering component of direct solar radiation connected with the finite size of leaves in a canopy, thus partly correcting for the infinitesimal size assumed in SAIL. It is implemented to better describe the hot spot effect and is estimated as relative leaf size, thus relating the average leaf size to canopy height (Nilson and Kuusk, 1989; Kuusk, 1991). Further inputs to 4SAIL are the spectral properties of the soil ρ_s that can be externally provided by a soil model (Figure 6-4) or spectra sampled in the field or from RS data. In this thesis, a standard Lambertian soil spectrum stored in the model was used in combination with a soil brightness factor (*bf*) that scales the spectrum between dark and bright soils (see Figure 6-4). The three angles solar zenith θ_s, observer zenith θ_o, and relative azimuth φ_r define the system geometry of the radiation transport. SAIL provides the four radiance streams including TOC HDRF and BRF in a first step, from which the directional reflectance is calculated by relating both reflectances to the sum of direct (E_{sun}) and diffuse irradiance (E_{sky}) using the SKYL factor and the global radiation according to François et al. (2002). Additionally, fPAR and albedo are output variables of PROSAIL (Jacquemoud et al., 2009). The eventual specification of all parameters is presented in chapter 6.3.

PROSAIL links the spectral variation of canopy reflectance depending on leaf biochemical contents with its directional variation depending on canopy architecture. This link is essential, as the SAIL model alone cannot be inverted over several wavelengths (see chapter 2.2.3). The use of multispectral data in SAIL would lead to an under-determined system because three unknowns (leaf reflectance, leaf transmittance, and soil reflectance) are wavelength dependent input variables to SAIL, which thus have to be estimated at each wavelength in addition to the canopy structure variables (see Figure 6-2). The inversion of SAIL alone at a given system geometry therefore requires at least three times as many observations as wavelengths, which makes a robust inversion of SAIL impossible unless several viewing angles are available, which is normally not the case with RS data. Thus, the use of a leaf model does not only enable the consideration of biochemical leaf constituents, but also reduces the dimensionality of the inverse problem by imposing a spectral constraint on the inversion process (Jacquemoud et al., 2009).

6.1.2. PROSAIL suitability for grassland LAI

Since its publication in 1992, PROSAIL has been extensively used and validated. In a first step, model outputs have been successfully compared to measured spectra over different biomes and at different scales (see e.g. Major et al., 1992; Jacquemoud et al., 1995a; Andrieu, 1997; Danson and Aldakheel, 2000; Schlerf et al., 2007). Due to its high accordance with measured spectra, it has been particularly useful for the evaluation and design of VIs (Baret et al., 1995; Broge and Leblanc, 2001; Haboudane, 2004; Zarco-Tejada et al., 2004; Chaurasia and Dadhwal, 2004; Le Maire et al., 2008). However, most applications of PROSAIL aim at deriving biophysical parameters from vegetation canopies. For LAI derivation, PROSAIL was inverted against spectral information gained from hand-held spectroradiometers (e. g. Jacquemoud et al., 1995a; Casa and Jones, 2004; Dorigo, 2007; Darvishzadeh et al., 2008b; Le Maire et al., 2008; Vohland and Jarmer, 2008), air-borne and spaceborne hyperspectral data (e.g. Jacquemoud et al., 1994; Jacquemoud et al., 2000; Weiss et al., 2002; Atzberger et al., 2003b; Meroni et al., 2004; Vuolo et al., 2008; Laurent et al., 2013; Laurent et al., 2014), high spatial resolution multispectral RS data (e.g. Atzberger, 2004; Koetz et al., 2005a; Soudani et al., 2006; Vuolo et al., 2010; Duveiller et al., 2011b; Atzberger and Richter, 2012), and medium to coarse resolution data (e.g. Zarco-Tejada et al., 2003; Lacaze, 2005; Zhang et al., 2005a; Bacour et al., 2006; Baret et al., 2007; Pasolli et al., 2011). In most of these studies, PROSAIL was used for crop characterization, although the number of studies focusing on forests and other natural vegetation canopies increased over the recent years. These applications led to the development of a range of ecosystem-adapted PROSAIL model variations (see chapter 2.2.3).

PROSAIL has been reported to achieve accuracies similar to those of more complex reflectance models (Weiss et al., 2000; Jacquemoud et al., 2000; Bacour, 2002; Widlowski et al., 2007; Widlowski et al., 2013). PROSAIL thus proved to be a good compromise between accurate results and robust performance. As it is based on a relatively small number of input parameters, it is invertible and computationally effective (Jacquemoud et al., 2000). Representing dense and homogeneous vegetation in which small single vegetation elements (Shabanov et al., 2000; Goel and Thompson, 2000; Schlerf and Atzberger, 2006; Dorigo et al., 2007), it is highly suitable for grasslands. Additionally, its extensive documentation makes PROSAIL an attractive choice. For these reasons, the PROSAIL model was chosen for reflectance simulations. Next, a framework for the parameterization of PROSAIL suitable to the different RapidEye scenes had to be established. To render this model set-up efficient, a sensitivity analysis (SA) of the PROSAIL model was performed first.

6.2. PROSAIL sensitivity analysis

6.2.1. Types of sensitivity analysis

The aim of an SA is to apportion the variations in the output of a model to variations of different input parameters (Saltelli, 2000). For an RTM, each parameter's contribution to the canopy reflectance variance must be quantified in each wavelength. The motivations to gain such information are diverse (Saltelli, 1999). Firstly, systematic model simulations are necessary to verify that the model behaves as expected. Secondly, an SA indicates whether the model is suitable for the intended use. Parameters which do not noticeably impact the model outcome can also not be retrieved accurately during inversion. Further, the sensitivity of an RTM towards measurement errors can be assessed (Goel, 1988). Finally, with regard to the design of sensors and satellite missions, SAs are relevant for the identification of optimal wavelength ranges and viewing directions for biophysical parameter derivation.

In this thesis, the most important aspect is the identification of influential input parameters in the RapidEye spectral bands, which is crucial for an efficient model parameterization. Parameters for which a small variation causes large RTM output variations must be modeled in small increments to ensure the simulation of all prevailing canopy spectra in the scene and hence the precise derivation of this parameter during inversion. At the same time, a detailed differentiation of non-impacting variables which do not generate significantly different model outputs would only increase inversion ambiguity and decrease computational efficiency and should therefore be omitted. Thus, the level of detail at which a parameter should be adjusted has to be relative to its impact on the canopy radiance. Further, the SA aims at identifying suitable or potentially negligible spectral bands and additional valuable features.

Although some SAs of the PROSAIL model have been conducted during the last few decades, they either did not cover the whole parameter space, delivered only qualitative results, or focused on parameters or spectral ranges not relevant for LAI retrieval. The simplest kind of SA is a series of simulations performed by sequentially changing one input parameter at a time over a reasonable range while retaining the other parameters unchanged, and monitoring the relative change in model response (Saltelli, 1999). An example is given in Figure 6-1, as for the generation of the canopy spectra shown in the figure all parameters other than LAI were kept constant to highlight canopy reflectance changes due to LAI variation only. This kind of SA is called “one-at-a-time” (OAT) or “local”, as it is run at a given central point in the input parameter space (Saltelli et al., 1999). To gain quantitative measures of relative parameter importance, the sum of squared differences between a “standard canopy” case and each perturbation is calculated for each parameter. Such local SAs have been performed for the PROSPECT model by Zarco-Tejada et al. (2003) and Ceccato et al. (2001), for the SAIL model by Major et al. (1992) and Mu et al. (2008), and for PROSAIL by Jacquemoud (1993), Zarco-Tejada et al. (2003), Vohland and Jarmer (2008), Darvishzadeh et al. (2012) and Wang et al. (2013). Modified versions of this method have been used on other RTMs by Privette et al. (1996) and Bicheron and Leroy (1999), who varied the parameters by 10 % around a standard reflectance distribution, and Asner (1998; 2000) and Privette et al. (1994), who additionally performed a principal component analysis on the variances. Combal et al. (2000) used a statistical method, while Laurent et al. (2011) analyzed the partial derivatives of the relative model output with respect to the input parameters.

However, these local SA approaches are limited (Saltelli, 2008). First, because a fixed baseline parameter set has to be defined for this analysis, which is often arbitrary, and any conclusion drawn on parameter importance is only legitimate around the baseline case. Second, a local SA is not comprehensive, because variations in the model output due to interactions between the parameters cannot be detected. Interactions describe effects in which variance of the model output due to one parameter depends on the level of another parameter. The combined change in two parameters may produce a greater effect than the sum of effects from either parameter alone (Bacour, 2002). Encountering no interactions is highly unlikely under natural conditions, because canopy biophysical and biochemical properties often co-vary (Jacquemoud, 1993; Jacquemoud et al., 2009).

Thus, so-called “global” SAs should be used for sensitivity evaluations. In a global SA, the parameters are not only varied locally around a mean value, but over their entire plausible range. Additionally, parameter distribution functions can be specified for each of the model parameters, so that information on focus ranges can be included. Further, in global SAs, the input parameters vary simultaneously so that interactions between them can be quantified.

Global SAs have not been performed extensively on RTMs. One global SA method that has been applied to PROSAIL is the Design Of Experiments for Simulation (DOES) (Bacour et al., 2001; Bacour et al., 2002a; Bacour, 2002). The motivation to use DOES is to handle the potentially large number of model runs generated by simultaneous parameter variations. A statistical method is used to define a few model settings that cover the entire parameter space. In doing so, DOES aims at maximizing the information extraction while reducing the number of simulations by factors of up to 300. However, DOES estimates the input parameters' effects with respect to an empirical linear model connecting model input and response, which reduces its usability for nonlinear models (Saltelli et al., 1999). Further, it does not explicitly quantify the effects of interactions. Therefore, another method, the Extended Fourier Amplitude Sensitivity Test (EFAST, Cukier et al., 1973; Saltelli et al., 1999), was used in this thesis.

6.2.2. The extended Fourier amplitude sensitivity test

Concept of EFAST

Ceccato et al. (2001; 2002) and Bowyer and Danson (2004) were the first to apply EFAST, a method developed in chemistry, in a RS context and to PROSAIL. EFAST is a variance-based method that determines the fractional contribution of each x_i of a set of n input parameters $x = (x_1, x_2, \dots, x_n)$ to the variance V of the output of any model $y = f(x)$ from their conditional variances. Parameter combinations are also sampled systematically from the parameter space in this approach, with all x_i varying simultaneously. The core feature of EFAST is that the model's multidimensional parameter space is explored by a suitable search-curve defined by a set of parametric equations (see Figure 6-5):

$$\mathrm{x_i}(\mathrm{s}) = \mathrm{G_i}(\sin \omega_\mathrm{i} \mathrm{s}) \tag{6.1}$$

where s is an independent scalar, G_i are transformation functions for each parameter, and ω_i is a set of ideally incommensurate frequencies associated with each parameter. As can be seen from Figure 6-5, the G_i functions used here are sets of straight lines, which results in uniform sample data distributions. Expressing $f\big(x_1(s), x_2(s), \dots, x_n(s)\big)$ as $f(\mathrm{s})$, and expanding $f(\mathrm{s})$ in a Fourier series, the multidimensional parameter space is reduced to a one-dimensional integral employing the Fourier coefficients A_{ω_i} and B_{ω_i} (Saltelli et al., 1999):

$$f(\mathrm{s}) = \sum_{\omega_\mathrm{i}=-\infty}^{+\infty} \left\{ A_{\omega_\mathrm{i}} \cos\, \omega_\mathrm{i}\, s + B_{\omega_\mathrm{i}}\, sin\, \omega_\mathrm{i}\, s \right\} \tag{6.2}$$

Each axis of the parameter space is hence explored with a frequency ω_i, i.e. each x_i oscillates periodically at a different frequency ω_i, so that the search curve could hypothetically pass through every point in the input space using incommensurate ω_i (Figure 6-5). In practice, the frequencies are commensurate (for more details see Saltelli et al., 1999) and the curve describes a closed path (see Figure A-2). The Fourier transformation finally allows for a decomposition of the model output variance V_i as function of the input parameter i, as

$$V_\mathrm{i} = 2 \sum_{p=1}^{+\infty} \Lambda_{p\omega_i} \tag{6.3}$$

where $\Lambda_{\omega_i} = A^2_{\omega_i} + B^2_{\omega_i}$, hence the computation of partial variances involves only the sum of squares of the Fourier coefficients at the fundamental and all harmonics p of ω_i. If x_i has a strong influence, the oscillation of the model output at frequency ω_i is of high amplitude.

This method can thus be compared to an analysis of variance (Cukier et al., 1973). EFAST decomposes the total variance V of the model output in a three-parameter case as

$$V = V_1 + V_2 + V_3 + V_{12} + V_{13} + V_{23} + V_{123} \tag{6.4}$$

where V_1 is the variance of input parameter 1, V_{12} is the variance of interaction between parameters 1 and 2, and V_{123} is the variance of interaction between parameters 1, 2, and 3. The partial variances V_1, V_2, and V_3 represent the contribution of individual parameters to the model output and are called first-order variances. In EFAST, the ratio between the i^{th} first-order variance and the total variance V is called *main effect* or *first-order index* S_i and represents the percentage of the output variance that is accounted for by the specific input parameter i, averaged over variations in other input parameters:

$$S_i = \frac{V_{\text{i}}}{V} \tag{6.5}$$

The *second- and higher-order* variance terms and corresponding indices S_{ij} represent the percentage variance caused by parameter interactions. They are derived from the frequencies not used for the computation of V_{i}, as these contain the residual variances. A measure for the variance due to one individual parameter and all its interactions is the so-called *total order index* S_{Ti}, which comprises all partial variances, thus for the three parameter case:

$$S_{T1} = \frac{V_1 + V_{12} + V_{13} + V_{123}}{V} \tag{6.6}$$

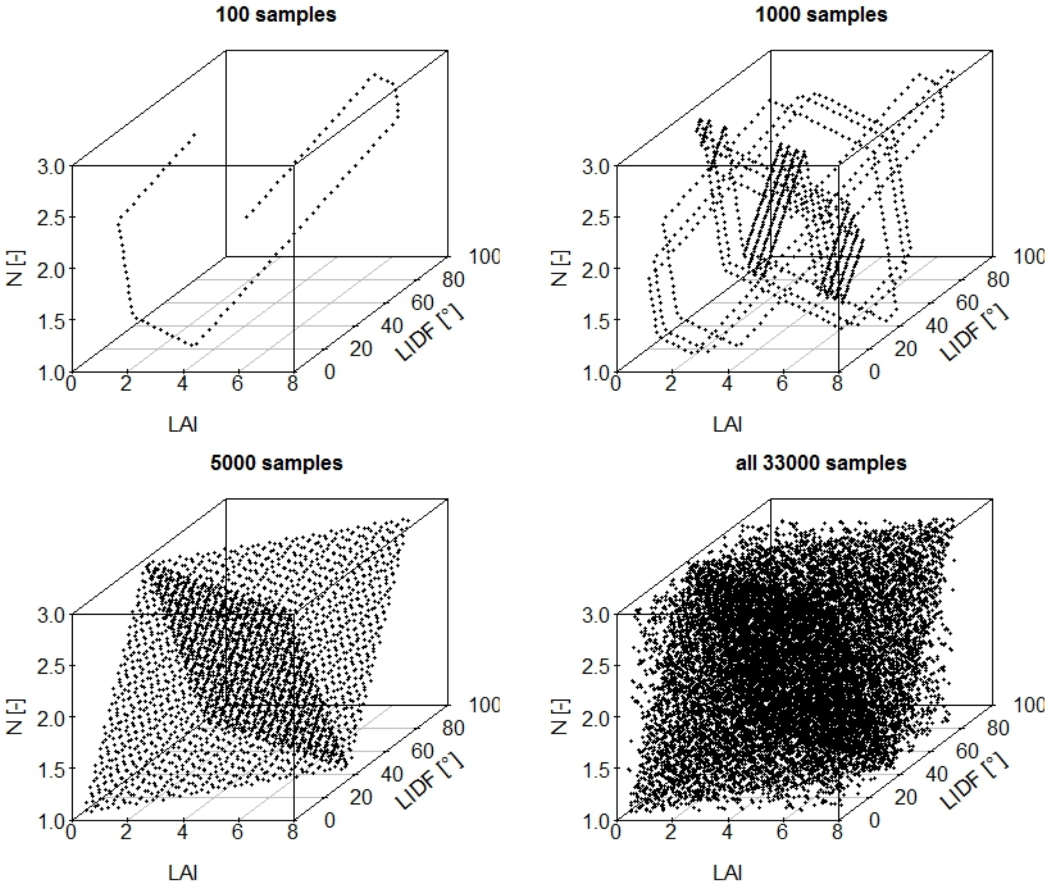

Figure 6-5: Example search-curve of the EFAST algorithm scanning the 3D LAI, LIDF, and N parameter space, ideally using a set of incommensurate frequencies so that the curve can pass through every point in the space (bottom right plot). To illustrate the irregular path of the search-curve, the parameter values sampled for the first 100, 1000, and 5000 PROSAIL runs are shown.

As such, the total index quantifies the degree of additivity of the model and its sum over all parameters is generally higher than one, as interaction effects between parameters 1 and 2 are counted in both S_{T1} and S_{T2}. To make more efficient use of the model runs, additional random phase-shifts were introduced by Saltelli et al. (1999), which enable the generation of different search curves, over which the variances are finally averaged. The phase-shifts are depicted as black areas in Figure A-2 due to the significantly higher frequencies.

Thus, EFAST is an information-rich approach that allows full exploration of the input parameter space, accounting for interactions, nonlinear responses, and self-verification. The main advantages of EFAST are its robustness and its computational efficiency (Saltelli et al., 1999). EFAST has been applied to PROSPECT and PROSAIL to assess the parameters influencing canopy reflectance in two selected wavelengths (Ceccato et al., 2001; 2002) or on the entire spectrum (Bowyer and Danson, 2004), with special focus on the leaf water content. However, to the knowledge of the author, it has not yet been applied to the PROSPECT5+4SAIL model versions, and no sensitivity analysis has been performed so far for the spectral configurations of the RapidEye sensor. Therefore, PROSAIL sensitivity was assessed by calculating the first-order, interaction, and total-order indices for the entire spectrum as well as for the five RapidEye bands using the *fast99* function of the “sensitivity” R package provided by Pujol et al. (2013). Further, the impact of LAI variations on selected VIs was tested as performed by Ceccato et al. (2001; 2002)(Ceccato et al., 2001), although not for designing a VI but to identify suitable additional spectral features for model inversion. The *fast99* default settings (M = 4, ω values as given by Saltelli et al., 1999) have been used.

The ranges used in the EFAST SA, between which the canopy parameters are sampled, are specified in Table 6-2. For the LIDF, the ellipsoidal 1-parameter implementation was used. The parameter ranges were similar to those of other studies (Bacour, 2002; Bowyer and Danson, 2004) and cover the entire realistic ranges of each parameter (Jean-Baptiste Féret, personal communication). During the design of the experimental plan, 11 parameters – thus all PROSAIL parameters but the viewing angles – were randomly drawn 3 000 times following a uniform distribution. This procedure resulted in 33 000 canopy realizations. The

Table 6-2: Ranges of the PROSAIL variables used in the global SA. In between these ranges, the parameters are uniformly sampled. Viewing angles were held constant.

Parameter	Unit	Lower Bound	Upper Bound
PROSPECT variables			
N	-	1	3
C_{ab}	$\mu g{*}cm^{-2}$	10	90
C_{ar}	$\mu g{*}cm^{-2}$	2.5	22.5
C_w	cm	0.008	0.035
C_m	$g{*}cm^{-2}$	0.002	0.02
C_{bp}	-	0	0.5
SAIL variables			
LAI	$m^2{*}m^{-2}$	0.1	7.5
LIDF	°	5	85
hs	$m{*}m^{-1}$	0.01	0.3
bf	-	0	0.9
SKYL	-	0.05	0.4
θ_s	°	30	
θ_o	°	5	
φ_r	°	80	

system geometry, that is, the sun and sensor zenith as well as the relative azimuth angles, were fixed, as only mono-angular data were used in this thesis. Instead, the mean of the sun and observer zenith angles of the RapidEye scenes as well as the most frequent relative azimuth angle (see Table A-2) were used to gain information relevant to the available data. For investigation of the directional reflectance sensitivity of the PROSAIL model, the reader is referred to Gobron et al. (1997b), Asner (1998), Gastellu-Etchegorry et al. (1999), Bacour et al. (2001), Bacour (2002), and Wang et al. (2005).

Results of EFAST

The first order main effects, interactions, and total order indices of the eleven input parameters on PROSAIL reflectance in the VIS and NIR spectral range are shown in Figure 6-6. While the wavelengths are given on the x-axis, the y-axis displays the respective index values of the main effects (top), interactions (middle), and total effects (bottom). The first-order index describes spectral variations due to variations of the respective parameter, and a high interactions index value indicates that variations of a parameter at a certain wavelength strongly depend on the levels of other parameters. With regard to the first-order effects, the parameters LAI, LIDF and the soil factor *bf* have the largest influence in total, although they show considerable variation over the spectrum. The LAI plays an important role, accounting for over 20 % of the model output variance in the VIS between 400 and 700 nm and in the SWIR beyond 1400 nm, while its influence is reduced in the NIR. The influence of the soil *bf* varies around 15%, with a minimum between 750 and 1000 nm. The largest variances (20 - 70 %) in the NIR and in the SWIR are generated by the LIDF. The diffuse irradiance factor SKYL is only relevant in the blue and green regions. The hot spot parameter barely influences the model output, which was to be expected given the chosen viewing geometry far off the hot spot region ($\varphi_r = 80°$). The PROSPECT parameters play a minor role overall, but show some characteristic influences (see chapter 2.2.1), e.g. chlorophyll content C_{ab} in the green and red edge wavelength ranges, dry matter content C_m in the NIR, or water content C_w between 1200 and 1900 nm. Overall, sums of the first-order indices are between 0.65 and 0.85, indicating that the remaining variance is caused by parameter interactions.

The interaction effects show a slightly less variable behavior. Overall, most interactions occur in the VIS. The three most important parameters LAI, LIDF and soil brightness have rather constant partial variances due to interactions around 10 - 20 %, with narrow ranges of increased interaction effects in the green, red edge, and NIR. While the interaction effects of the canopy model parameters are rather lower than the first-order indices, those of the leaf model parameters are mostly as high as their first-order effects. Ceccato et al. (2001) found that only small interactions occur between leaf parameters. This indicates that the interactions observed here are caused by the scaling effect, which all leaf constituents undergo as the leaf area increases. The total index incorporating all first- and higher-order indices underlines the ranking observed for the first-order indices, with the LAI, LIDF and soil brightness accounting for the largest parts of the variance, while the leaf parameters influence the reflectance to a lesser extent in the sensitive wavelengths.

Compared to other global SAs performed on the PROSAIL model, some similarities as well as some differences could be observed. Overall, evaluation of the EFAST results was difficult, as no comparable study using all parameters and all wavelengths exists. The comparison with the EFAST results of Ceccato et al. (2002) is limited to two wavelengths, as they only analyzed the reflectance at 820 nm and 1600 nm. Further, they included the viewing angles as well as the leaf reflectance and transmittance instead of the individual leaf parameters.

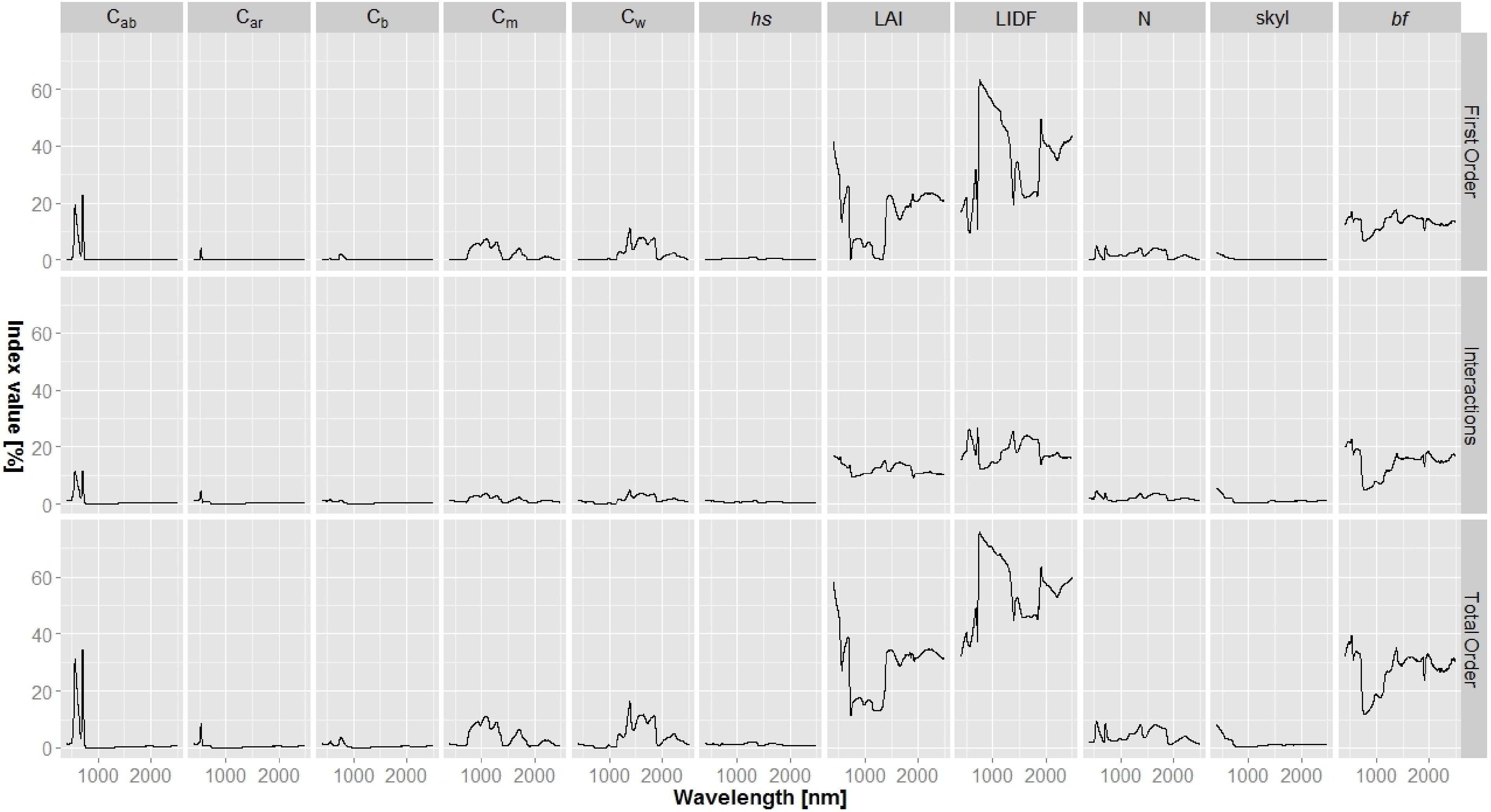

Figure 6-6: Sensitivity analysis results for the entire spectrum: the graph shows the variance of PROSAIL outputs which consists of the first-order index (top), which describes spectral variations due to variations of the respective parameter, interactions (middle) which contain variations due to the joint variation of parameters, and total order index (bottom plot), which is the sum of the first-order and all higher-order indices, of all PROSAIL parameters. 33 000 canopy realizations have been analyzed based on a uniform parameter distribution.

Indeed, these parameters which, have no direct equivalent in the above presented analysis (ρ_l, τ_l, θ_s), have the largest influence on the model output (25 - 40 %) in their study, leaving only small portions for LAI, LIDF and the soil factor (total indices of 12 - 17 %), contradicting the results achieved above. In the EFAST study of Bowyer and Danson (2004), the LIDF and the soil parameter were fixed, precluding a direct comparison of parameter influences therein as well. Although the pattern of the LAI contribution was rather similar to the one detected here, the relative influence of leaf parameters was strongly increased, which might have been caused by the overall reduced number of parameters.

Other published PROSAIL SAs also find a high sensitivity of the model to variations in the parameters LAI and LIDF. However, the DOES (Bacour et al., 2001; Bacour et al., 2002a; Bacour, 2002) identified the largest influence of both parameters in the NIR and a reduced importance of the LAI in the VIS, which is directly opposed to the sensitivities reported above. A comparison of the importance of the soil factor is difficult, as the results in the different studies of Bacour et al. varied. However, it can be stated that the influence of the soil parameter was low overall (<10 %) according to the DOES experiment (apart from the results in Bacour et al., 2001) and in contrast to the EFAST results. The interactions assessed in these studies did also not exceed 10 % of partial variances. The largest deviation has to be observed for the influence of the chlorophyll parameter, which did not exceed 17 % in this study, but accounts for up to 60% of the reflectance variation in the VIS and was the prevailing factor controlling the reflectance according to Bacour et al. (2001). Compared to the results of the local SAs performed by Jacquemoud (1993) over the 400-2500 nm range, quite similar results could be observed for the leaf model parameters and the LIDF, although the results for LAI differ strongly, with the predicted strongest effect of LAI being in the NIR. This was caused by the low average leaf angle value (40°) used in his base case scenario, as an increase of the area of such flat leaves would naturally influence the scattering in the NIR while rather erectophile leaves would not, illustrating the drawback of the OAT approach.

The fact that different results were achieved in this SA compared to other approaches might well be explained by the varying model settings of each analysis. Furthermore, this was the first analysis of the PROSPECT5+4SAIL model versions using EFAST, and the different LIDF implementations for example can lead to differences in the model response. The partially strong discrepancies in the very few different SAs of the PROSAIL model suggest that further research is needed in this field.

To assess the importance of the different input parameters on reflectance in the available RapidEye bands, the EFAST SA results were summarized for the simulated RapidEye band reflectances (see Table 6-3 and Figure 6-7). Naturally, the same trends as for the spectrum analysis described above could be observed, with the canopy structure parameters LAI and LIDF and the soil parameter first-order indices together accounting for approximately 60 - 75 % of variance in the model output. Parameters such

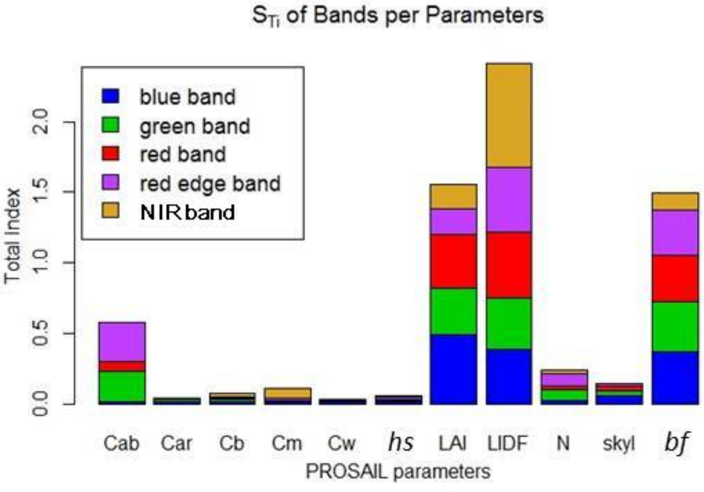

Figure 6-7: PROSAIL parameter influence on the RapidEye reflectances. The high relevance of the LAI, LIDF, and *bf* parameters is clearly illustrated.

Table 6-3: Sensitivity analysis results for the five RapidEye bands: first-order, interactions, and total indices, which measure the respective influence on the model output variance, specified in percent. re = red edge.

	First-order indices (%)					Interactions (%)					Total order indices (%)				
	blue	green	red	re	NIR	blue	green	red	re	NIR	blue	green	red	re	NIR
PROSPECT															
N	0.1	3.9	0.5	4.6	1.5	2.0	4.2	2.2	3.6	1.2	2.1	8.1	2.6	8.2	2.7
C_{ab}	0.2	13.3	3.4	18.3	0.0	1.5	8.4	3.2	9.3	0.1	1.7	21.7	6.6	27.5	0.1
C_{ar}	0.1	0.3	0.0	0.0	0.0	1.4	1.1	0.8	0.4	0.1	1.6	1.4	0.8	0.4	0.1
C_w	0.0	0.0	0.0	0.0	0.0	1.1	0.8	0.8	0.4	0.1	1.1	0.8	0.8	0.4	0.1
C_m	0.0	0.0	0.0	0.4	4.6	1.1	0.8	0.8	0.7	2.6	1.1	0.8	0.8	1.1	7.2
C_b	0.0	0.4	0.0	0.6	1.1	1.1	1.4	0.8	1.0	0.8	1.1	1.7	0.9	1.6	2.0
SAIL															
LAI	32.9	17.7	25.2	4.0	7.0	16.1	15.1	13.2	14.4	9.6	49.1	32.8	38.3	18.4	16.6
LIDF	20.7	10.9	28.4	19.3	61.3	18.2	25.2	18.4	26.3	12.4	38.8	36.1	46.8	45.5	73.7
hs	0.1	0.2	0.1	0.5	0.4	1.2	1.1	0.9	1.0	0.6	1.2	1.3	1.0	1.5	1.0
bf	15.1	15.3	14.4	15.0	7.0	21.7	20.0	19.2	16.9	5.2	36.8	35.3	33.6	31.9	12.2
skyl	1.8	1.3	0.7	0.6	0.1	4.1	2.4	2.2	1.1	0.3	6.0	3.7	2.9	1.7	0.5

as the water content C_w, the carotenoid content C_{ar}, or the brown pigment content C_{bp} only marginally influenced the reflectance in the VIS and NIR, as their effects are either naturally small or their absorption bands are not met. The sensitivity of reflectance to the chlorophyll content C_{ab} in the green and red edge bands constituted an exception in this regard.

Besides the RapidEye bands, the sensitivity of the model in some of the VIs successfully used for empirical-statistical LAI derivation (see chapter 5) has been investigated. Figure 6-8 gives an impression on the overall sensitivities of seven different VIs in comparison to the RapidEye bands. It shows the reduced influence of the soil brightness on the VI variances. The effect of LAI differs across the VIs. The increased sensitivity of red edge VIs ($NDVI_{rededge}$, RRI1, Curvature) to canopy chlorophyll content is clearly shown.

Conclusions from the EFAST analysis

It is possible to draw several conclusions for the model suitability and parameterization from Figure 6-7 and Figure 6-8. The results for the entire spectrum depict characteristics of the spectral behavior of vegetation as described in the literature and thus indicate that the PROSAIL model output is a valid representation of vegetation canopy reflectance. Furthermore, the prominent role of the LAI over large parts of the spectrum shows that the model is generally suitable for modeling the influence of LAI on the canopy radiance, and thus also for deriving LAI in the inverse mode. The relatively high importance of the LAI in the SWIR also indicates the high potential of bands situated in these wavelengths ranges provided e.g. by the upcoming Sentinel-2 sensor.

With regard to RTM parameterization, the parameters LAI, LIDF and soil *bf* need to be especially carefully parameterized, as they had a large influence on the model output. This means that the parameter ranges need to cover all occurring states at small intervals to reproduce the associated canopy reflectances, but at the same time should be matched as closely as possible to the assumed true value, as even small variances might lead to a largely different output. The chlorophyll content C_{ab}, the dry matter content C_m, leaf structure N, and diffuse irradiance parameter SKYL should also be varied during parameterization, although their influence was reduced compared to the canopy and soil parameters and thus the number of variable levels can be smaller and with larger intervals. The parameters C_{ar}, C_w, C_{bp} and *hspot* could be fixed to a mean value, as their variance will not influence the modeled reflectances at a relevant rate, hence increasing the accuracy of LAI estimation and reducing the necessary number of model runs (Goel, 1988).

This analysis resulted in the use of six free parameters[17]. Further information available from the EFAST results is the identification of useful and negligible bands and features, which can be used to reduce model complexity further, as the number of free parameters determines the number of independent equations needed to create a well-determined inversion problem (see chapter 2.2.3). An appropriate band selection has been reported to improve RTM inversion, for example because some bands may contain particularly high noise levels (Bacour et al., 2001; Meroni et al., 2004; Schlerf and Atzberger, 2006). As can be seen from Figure 6-8, the RapidEye bands were not equally sensitive to LAI variations. Based on these results, it could be suggested to exclude the red edge and NIR bands from further analysis and to the alternatively use VIs. However, in inverted RTM modeling, all parameters are estimated simultaneously by choosing the canopy realization that produces the most similar reflectances. In addition, the parameter levels influence each other, as indicated by the partially high interaction indices. Therefore, the spectral features used for RTM inversion should not only be sensitive to LAI, but also to the other influential parameters, that is, LIDF, chlorophyll and soil brightness, to identify the fitting canopy structure. Furthermore, when analyzing the correlations between the bands and VIs discussed here (see Figure A-3), the red edge and NIR bands correlate only moderately strong (r = 0.2 - 0.6 except for one case) with the other bands, i.e. they carry different information, while the VIS bands correlate with about 0.8. Further, some studies have stressed the high importance of the NIR reflectances for LAI derivation (see e.g. Rivera et al., 2013). Despite their reduced sensitivity to LAI, the red edge and NIR bands were therefore kept for LAI derivation. From the same Figure A-3, the overall medium correlation coefficients of the RVI and the Curvature indices to the

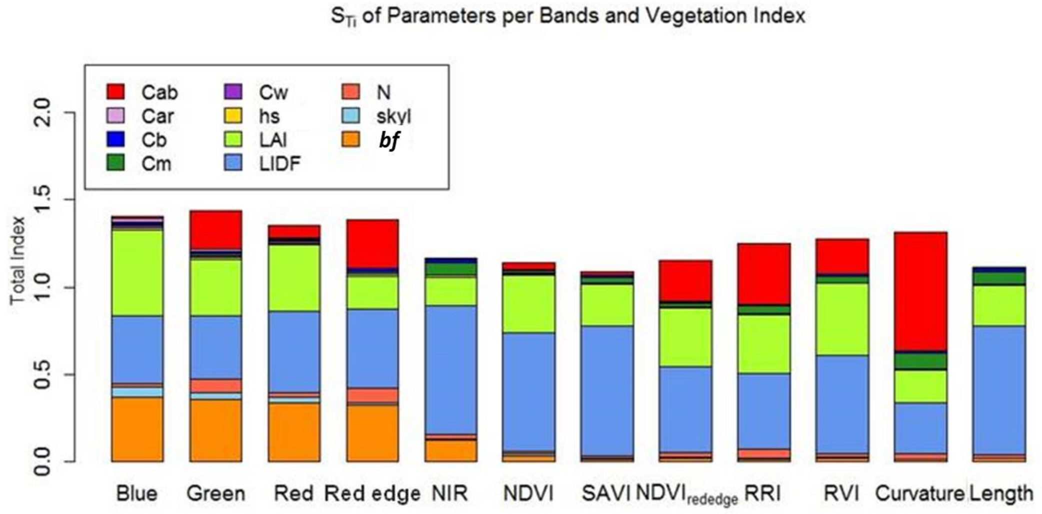

Figure 6-8: RapidEye band reflectance and VI sensitivities to the PROSAIL parameters. For each spectral feature, the total indices of the individual parameters are stacked above each other to show the overall sensitivity of each feature to changing leaf and canopy conditions and to illustrate the influence of each parameter.

---

[17] It will be shown below that the SKYL parameter can be fixed.

RapidEye bands (0.63 and 0.54 on average) can be derived. These medium strong correlations as well as their high aggregated total index values and increased sensitivity to chlorophyll content (Figure 6-8) suggest that the VIs might enhance the inversion sensitivity to the target biophysical parameter and increase the robustness of the matching procedure. Therefore these two VIs were chosen together with all RapidEye bands, resulting in seven spectral features used for further analysis in RTM inversion.

6.3. Parameterization of PROSAIL

By running the PROSAIL model several times with changing input parameters, an ensemble of canopy reflectance simulations can be built. The range and rate at which the parameters are changed is defined through a parameterization framework. In doing so, the aim is to cover all occurring vegetation states and at the same time to reduce the underdetermined and ill-posed nature of RTM inversion. To overcome these problems, different regularization techniques exist (see chapter 2.2.3). One approach used in this thesis was the introduction of *a priori* knowledge on the PROSAIL variable ranges and sampling intervals (see e.g. Combal et al., 2002b; Baret and Buis, 2008). Further, if a variable is perfectly known, it should be considered as a fixed constant. These restrictions reduce the number of canopy realizations and thus the risk of parameter equifinality, i.e. the phenomenon whereby similar reflectance spectra are generated from different model settings (Kimes et al., 2000). The definition of ranges is generally carried out for each ecosystem individually (see e.g. Knyazikhin et al., 1998; Dorigo et al., 2009). In this regard, one advantage of using high spatial resolution RS data is that they enable the identification of different land covers at a low rate of mixed pixels. This helps considerably in refining the prior information on the typical ranges of canopy biophysical parameters. However, it should be noted that while the managed grassland canopies in the Ammer catchment were spatially mostly homogeneous within one field, they were not with regard to the entire landscape for which the canopy characterizations have to be specified (see chapter 3.5). For that reason, a strict parameter limitation (as it would be possible for crops) was not feasible, but a rather tolerant parameterization had to be chosen to cover all canopy states occurring at a time. Nevertheless, *a priori* knowledge was used as far as possible for defining the ranges of variation of the RTM input parameters. An alpine grassland specific parameterization was hence generated based on knowledge about the grassland ecosystem under investigation. In the following, the PROSAIL parameterization for every RapidEye scene based on the EFAST SA, *in situ* measurements, and values used in studies conducted in similar conditions (see Table A-8 for a review) is discussed.

From the set of leaf model parameters, only C_{ab}, C_m, and N were varied in the model. The *in situ* chlorophyll measurements (see chapter 4.3.3, Table 4-5) were lower than other chlorophyll concentrations C_{ab} reported in the literature (see e.g. Ruecker et al., 2006, and Daughtry, 2000, for crop chlorophyll). Furthermore, C_{ab} was only measured in the field at two points in time. Therefore, the upper range of the C_{ab} parameterization was chosen according to other PROSAIL studies conducted in crop and grassland ecosystems (see Table A-8), with ranges even for grassland studies between 1 and 100 µg cm^{-2}. The range of C_{ab} was variable over the season, as the chlorophyll content commonly varies with the plant cycle, with a rather narrow range of lower values in spring (10 - 40 µg cm^{-2}) and a wider range in summer (20 – 80 µg cm^{-2}) sampled at constant intervals of 10 µg cm^{-2}. The wide summer range with rather low values was chosen to account for the occurrence of freshly mown meadows covered by freshly exposed shade leaves, as well as for extensively used meadows without fertilizer treatments.

The *in situ* measurements of the dry matter content C_m (0.0027 - 0.0065 g cm^{-2}) were realistic but slightly lower than those found in the literature. As the dry matter content measurement procedure is indeed prone to underestimation due to the loss of material during harvesting, drying, and weighing, the leaf mass was sampled between the lower bound of 0.004 g cm^{-2} and an upper bound of 0.012 g cm^{-2}. C_m was sampled three times within this range constantly over the entire season.

The structure parameter *N* cannot be measured physically and empirical relationships to SLA are not continuous (see Ceccato et al., 2001, for a discussion), so the selection of this parameter was purely based on literature values. Other grassland studies (Table A-8) used relatively wide *N* ranges between 1 and 2 to account for the large number of different species. As these species are mainly monocots, they have rather thin leaves, which correspond to *N* between 1 and 1.7 (Jacquemoud, 1993; Bousquet et al., 2005). Therefore, in this work, *N* is sampled between 1.3 and 1.9 in steps of 0.3 for all RapidEye scenes.

The remaining PROSPECT parameters C_{ar}, C_w, and C_{bp} were fixed based on the findings of the EFAST analysis. According to one author of the PROSAIL model (Jean-Baptiste Féret, personal communication) the C_{ab}/C_{ar} ratio is about 4, so the carotenoid C_{ar} value was varied over the season according to the mean of the C_{ab} ranges between 4 and 12 µg cm^{-2}. The water content C_w value was fixed at 0.02 according to the *in situ* data (see Table 4-5), because the absorption of leaf water does not significantly influence the canopy reflectance in the spectral range used. A rather high constant brown pigment C_{bp} value of 0.4 was chosen (the realistic value range being 0 to 0.5) to account for the relatively high amount of dead material in natural grasslands (see e.g. He et al., 2006) and for manure remnants on intensively used meadows and pastures.

The setting of the canopy model parameters was mainly driven by the *in situ* values sampled during the measurement campaigns. As it is the variable of interest, highest emphasis was put on the selection of the LAI data ranges. *In situ* measurements showed that the LAI ranges vary considerably over the season, although the minimum value always remained below 2 due to repeated mowing events throughout the year (see Figure 4-15). Therefore, the lower bound of LAI was fixed at 0.2 for all points in time, while the maximum value was linearly interpolated between the maximum LAI values measured during the individual measurement campaigns (plus about 0.5 LAI to account for measurement uncertainties). For the spring and autumn scenes before and after the *in situ* measurement dates, a moderate decrease of maximum LAI was assumed. Based on this, LAI was dynamically increased from 3.6 in late March to 7.0 in July, and reduced again to 5.2 at the end of September, which is in accordance with ranges used in other studies (see Table A-8). These ranges were sampled at very small intervals of 0.2, which led to a large number of model runs in the summer scenes.

The parameterization of the highly influential leaf angle distribution function LIDF parameter proved to be the most challenging aspect. For crop canopies, constraining the LIDF to a narrow realistic value range is feasible, as the canopy structure is spatially homogeneous and quite accurately measureable (see e.g. Koetz et al., 2005a). A grassland canopy, however, can consist of a large number of species with potentially very different leaf angles, such as erectophile grasses and planophile or reptant species such as clover or plantago species. Furthermore, as the species compositions of the alpine grasslands of the Ammer catchment vary significantly due to different management practices, the mean of all measurements would also not be representative for all grasslands. Therefore, the LIDF was selected from a rather wide range of values based on field and literature data. The lower bound of the LIDF range was set to 36° for spring and 30° for summer scenarios according to the mean *in situ* minimum values of both seasons (46° and 41°, respectively, minus 10° to account for measurement uncertainties). Although a maximum MTA of 90° was measured in the field using the LAI-2000 PCA during each campaign, a purely erectophile canopy is an unrealistic value for grasslands. Literature values for grassland MTA are also rather low (see e.g. Darvishzadeh et al., 2008b: 55°). As a compromise, the upper bound was set to 78° (except for the late September scene, for which it was set to 72°), which is in the range of values that was used in RTMs for crop simulations (see e.g. Vuolo et al., 2008; Atzberger, 2010; Atzberger and Richter, 2012). MTA was sampled in 6° intervals and used in the ellipsoidal one-parameter LIDF, which has the advantage of being a continuous function (Campbell, 1986, 1990).

The remaining canopy parameters, i.e. the hot spot parameter *hs* and the ratio of diffuse to total incident radiation SKYL parameters, were fixed. The *hs* parameter for the four scenes in 2011 for which field data were available was assessed relating the average leaf size (assumed to be 2 cm) to the measured mean canopy height, resulting in *hs* values between 0.1 and 0.14. For the remaining scene simulations, a value of 0.1 was selected, which seemed acceptable given the low range of variability in *hs* and as sensor geometries are far from the hot spot direction. The ratio of diffuse to total incident solar radiation (SKYL) was calculated for each scene based on continuous radiation measurements at the three micrometeorological TERENO stations *Graswang*, *Fendt* and *Rottenbuch* (see chapter 4.3.3). To quantify SKYL, the total and diffuse radiances measured during half an hour around the RapidEye over-flight time at the three stations were averaged.

The settings of the soil brightness factor *bf* were barely limited, as soil conditions may vary strongly both temporally and spatially (see e.g. Lauvernet et al., 2008). To define the ranges

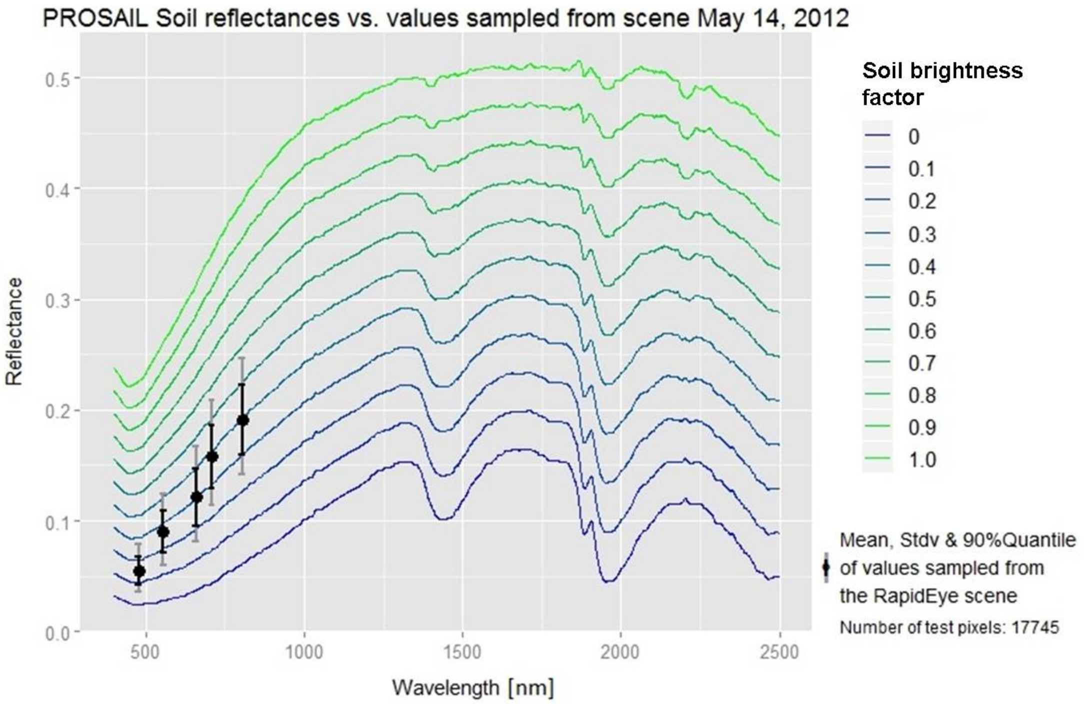

Figure 6-9: PROSAIL soil spectra compared to RapidEye soil reflectances sampled from the May 14, 2012 scene. To cover all soil conditions prevailing in the RapidEye scenes, the scene-specific PROSAIL parameterizations include all brightness factor levels that lie within the 90 % quantile of the observed spectra in each wavelength.

of *bf* for each scene, between 6000 and 18000 soil reflectance samples were taken manually from areas within each RapidEye image, which were visually identified as "bare field" (as proposed in Richter et al., 2012b, or Verrelst et al., 2014). The selected reflectances were then compared to the soil reflectances in the VIS and NIR at several brightness levels stored within PROSAIL (see Figure 6-9). In order to cover the full realistic range but not parameterize too wide due to outliers, the levels covered by the 90 % quantiles of the soil samples were selected in a first step. Further, one *bf* step towards lower values was added to account for potential darker soils underneath vegetation cover due to higher wetness.

The ranges and interval values of all PROSAIL input variables used in the model runs for all dates are listed in Table A-9. For all parameters, a uniform distribution within the corresponding range was used as in Laurent et al. (2011), Koetz et al. (2005a) and Darvishzadeh et al. (2008b) (see Weiss et al., 2000, for the discussion of alternative sampling approaches). This parameterization resulted in 33 516 to 198 450 variable combinations for the different time steps, which is within the range of other studies that use a similar number of free parameters (e.g. Richter et al., 2012b: 49 152; Leonenko et al., 2013b: 90 404; Weiss et al., 2000: 100 000; Darvishzadeh et al., 2008b: 100 000; Wang et al., 2013: 190 080; Kötz et al., 2004: 130 000; Duveiller et al., 2011b: 204 800).

6.4. Integration of topographic conditions

The remaining three PROSAIL parameters which have not been specified so far, the solar zenith, observer zenith, and relative azimuth angles, required special treatment. Laurent et al. (2014) showed that it is favorable to use the original (not nadir-normalized) RS data in RTM modeling, which requires the simulation of reflectances using the scene's system geometries. However, geometry information provided with the RapidEye data refers to the ideal case of flat terrain, and would thus have to be topographically corrected to account for local changes in the viewing and illumination geometries. This topographic correction of the RapidEye data did not achieve satisfactory results, as mentioned in chapter 4.1.2. Thus, to derive a pixel-wise sun and sensor angles map corrected for the terrain, the topography of the Ammer catchment is taken into account. The local slope and local aspect angles were extracted from the SRTM DEM (see 4.2) over the entire study area and combined with each individual RapidEye scene's system geometry (see Figure 6-10). While the relative azimuth angle φ_r between the sun and the sensor does not change due to topography, the local sun and sensor zenith angles $\theta_{o_{local}}$ and $\theta_{s_{local}}$can be derived from the aspect and slope angles at position (x, y) according to Richter and Schläpfer (2012) by:

$$\theta_{o_{local}}(x,y) = \cos^{-1}(\cos\theta_o * \cos\theta_{topo}(x,y) + \sin\theta_o * \sin\theta_{topo}(x,y) * \cos(\varphi_{topo}(x,y) - \varphi_o)) \quad (6.7)$$

θ_o is the sensor zenith angle, θ_{topo} is the terrain slope, φ_o is the senor azimuth angle, and φ_{topo} is the terrain azimuth. While this is the formula for correcting the sensor view angle, using this equation with the respective sun angles delivers $\theta_{s_{local}}$. An approach presented by Pasolli (2012) produces nearly identical results:

$$\theta_{o_{local}}(x,y) = \theta_o + \left(\cos^{-1}\left(\cos\left({}^{\pi}/_{2} - \theta_{topo}(x,y)\right) * \cos\left(\varphi_{topo}(x,y) - \varphi_o\right)\right) - {}^{\pi}/_{2}\right) \quad (6.8)$$

Equation 6.8 was thus used in this thesis to derive raster layers of the pixel-wise local sun and sensor zenith angles for each RapidEye scene. Both layers were combined into one layer and added to the RapidEye data sets. Pixels with $\theta_{s_{local}} > 90°$ were masked in the RapidEye scenes, as completely shaded hills do not provide sufficient spectral information for RTM inversion. Further, the angle information was quantized in steps of 5 degrees to reduce the number of occurring viewing geometries in the scenes to a manageable quantity. From this procedure, 104 - 157 different combinations of sun and sensor zenith angles are derived for the different scenes in this thesis (see Table A-9). These combinations were then used, in turn, to parameterize θ_o and θ_s in the PROSAIL model.

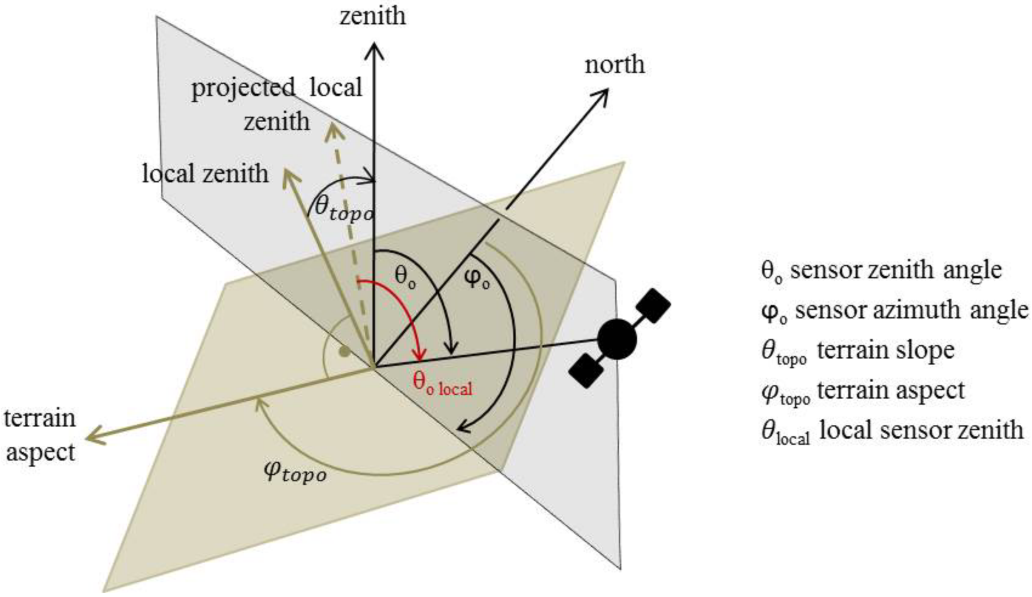

Figure 6-10: Representation of the sensor viewing geometry for an inclined surface due to topography. The same conditions hold for the sun illumination geometry. Compare to Figure 2-10 for viewing geometries over flat terrain.

6.5. PROSAIL Inversion

As mentioned above, the selection and configuration of an appropriate and robust inversion procedure is the third important aspect for accurate LAI derivation using an RTM, besides the model suitability and parameterization (Dorigo et al., 2007). In this chapter, the chosen inversion approach is justified first (chapter 6.5.1). Then, several optimization strategies in LUT-based RTM inversion that have been proposed in the literature are tested, namely the applied cost function (chapter 6.5.2), multiple best solutions (chapter 6.5.3), added noise, and additional features (chapter 6.5.4).

6.5.1. LUT inversion approach

For an overview of the different inversion approaches, i.e. iterative optimization, LUTs and ANNs, and their respective assets and drawbacks, see chapter 2.2.3. Generally, inversion techniques based on pre-computed reflectance databases, thus LUTs and ANNs, are preferred compared to iterative optimization methods, because they are not prone to getting trapped in local minima, and because the RTM is only used in the direct mode, which is less time consuming (Rowland et al., 2001; Combal et al., 2002b; Koetz et al., 2005a; Bacour et al., 2006; Dorigo et al., 2007). With regard to accuracy, the two approaches have also been observed to perform similarly (Richter et al., 2012b). However, with regard to computational efficiency, both, the LUT and ANN approach, still have limitations. For both methods, data bases have to be established first. LUT inversion then involves an LUT searching procedure for each pixel, which can be time consuming if large data bases are used and if the inversion is applied to a large number of pixels. While the pixel-wise ANN inversion itself is very quick, the ANN training can take a lot of time because many trials are required to choose the most adequate network architecture, and to validate it (Combal et al., 2002b). This becomes especially critical if many different local system geometries occur in one scene due to topography or due to the use of mosaics (e.g. MODIS data), as individual ANNs need to be trained based on individual LUTs for each geometry (Dorigo et al., 2007). Leaving the viewing angles as free parameters for training an ANN is not an option, as this would lead to a strong under-determination of the inversion. Thus, the time expenditure of both approaches might get high under certain circumstances, which, however, has never been compared for high spatial resolution data.

One basic motivation to use the LUT approach is the simplicity of the approach. It is easy to implement, and during LUT inversion, the calculation of the spectral distances, the performance of individual bands, and the selection of solutions can be monitored and altered at any point. This contributes to the understanding of the procedure and to the identification of errors, and thus enables the improvement of parameterization and/or inversion. Another benefit of using LUTs is that all model parameters are estimated, that is, e.g. the leaf angle, chlorophyll and water content or soil conditions are retrieved in addition to LAI, while an ANN retrieves only one variable of interest. The gained additional information might be useful for various applications such as plant growth. Further, as a more complete picture of the vegetation canopy is given, the variability and plausibility of the other output parameters can indicate inconsistencies within the LAI estimate. Moreover, the LUT approach is less sensitive to errors from measurements or models (Kimes et al., 2000; Chen et al., 2003) and does not generate highly unpredictable output values (as it is possible using ANNs, see Baret et al., 2013), because its output will always be within the bounds of the model parameterization. An advantage of both approaches is that *a posteriori* uncertainties of the variable of interest can routinely be derived, indicating the reliability of the final estimate. Baret et al. (2013) showed that a theoretical performance can be derived for each biophysical variable using ANNs. However, with the LUT approach, such information can even be derived pixel-wise by analyzing a subset of the "best solutions" (see e.g. Rivera et al., 2013).

Due to the sum of these arguments, LUTs are generated using the parameterization framework described above. Thereby, the number of variable combinations defines the number of entries (i.e. lines) in the LUT. From each of the simulated PROSAIL spectra, the band-equivalent reflectances of the five RapidEye bands are calculated in a next step using the band specific spectral response curves, i.e. the weights for the bands over all wavelengths (BlackBridge, 2012, see Figure 6-11). These band-equivalent reflectances were further used to calculate the VIs mentioned above (RVI and Curvature), which were stored in the LUTs together with the band reflectances. The dimension of the LUT is thus determined by the number of free parameters (LAI, LIDF, *bf*, C_{ab}, C_m, N), the number of parameter variations, and the number of spectral bands and VIs. For each of the system geometry angle combinations occurring in one RapidEye scene, an individual LUT covering all parameterizations had to be generated, since each LUT is specific to the sensor view and sun directions for which it is designed. During inversion, the local system geometry information stored with the RapidEye data is used in a first step to select the fitting LUT from the LUT ensemble of each time step (see Figure 6-2). The selected LUT is then used for the pixel-wise spectral matching.

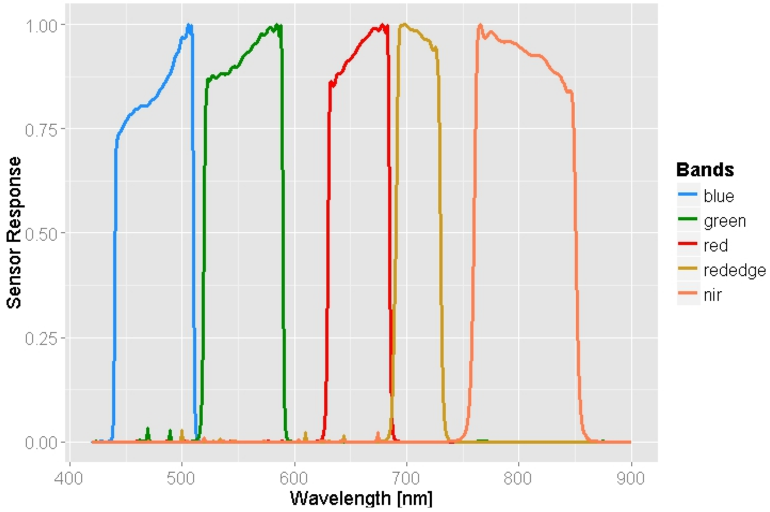

Figure 6-11: Spectral response curves of the RapidEye Sensor. Note that the data for each band have been normalized for that band. Based on data from the BlackBridge spectral response curves document (BlackBridge, 2012).

However, the size of the LUT is critical, as a small LUT may not consider all realizations, while an inversion on a very large LUT is time-consuming. However, Darvishzadeh et al. (2012) showed that the LUT size does not significantly influence biophysical parameter retrieval (see chapter 6.5.3).

6.5.2. Least squares estimate cost function

LUT-based RTM inversion consists in finding the simulated reflectances that match best with the reflectances measured by the sensor in all bands. Such an optimization problem is solved by the use of a so-called cost function. The question of how this “best match” is defined is discussed in this chapter. Traditionally, the minimum distance between the modeled and measured reflectances has been identified using a LSE (Rivera et al., 2013). Leonenko et al. (2013b) were the first to question this approach and reviewed over 60 alternative statistical measures as cost function for the derivation of biophysical parameters using RTM inversion. They argue that the LSE method is based on assumptions (such as the maximum likelihood estimation with a Gaussian distribution of residuals), which are often violated in physical modeling due to uncertainties in instrument calibration, atmospheric corrections, or simplified assumptions in the RTM. Three families of alternative cost functions were introduced: information measures, minimum contrast, and M-estimates. It should be noted that some of these cost functions have additional parameters that need to be tuned, which is an optimization problem in itself. Rivera et al. (2013), Leonenko et al. (2013a) and Verrelst et al. (2014) adopted these measures, but drew rather different conclusions. For both, simulated and MODIS data, Leonenko et al. (2013b; 2013a) found that statistical distances other than LSE (the Bregman, Hellinger, and Arimoto divergences for broadleaf forests, Bregman divergence, power divergence, and Pearson chi-squared measure for needle leaf forests) resulted in better LAI estimation using the FLIGHT model (North, 1996). Verrelst et al. (2014) also observed that the LSE was not the best performing cost function, in this case for crops, but that the cost function ‘Trigonometric’ achieved highest accuracies for LAI derivation. Rivera et al. (2013) on the other hand identified the classical LES as best-performing function for LAI derivation in crops albeit its theoretical limitations, if noise and the mean of multiple solutions are introduced (see below).

These studies hence suggest a range of different best performing algorithms. Additionally, the studies identified different optimal cost functions for different parameters, and for cases in which all parameters should be retrieved with the highest overall accuracy (Leonenko et al., 2013b; Rivera et al., 2013), thus any choice has to be tested for each application individually. These differing results indicate that further research is needed in this field, especially with regard to the different kinds of error distributions (see Leonenko et al., 2013b). For that reason, a simple LSE-based distance measure is used in this thesis.

When using the LSE measure, the question arises whether the spectral distance of each band should be normalized. This is not clarified in the literature, as studies supporting both approaches have been published (see e.g. Weiss et al., 2000; Meroni et al., 2004; Colombo et al., 2008; Soenen et al., 2009 for the use of normalized bands, and Koetz et al., 2005b; Darvishzadeh et al., 2008b; Richter et al., 2009; Laurent et al., 2011; Atzberger and Richter, 2012; Si et al., 2012, for LAI derivation without normalization). However, two arguments in favor of normalization do apply to the data used in this thesis. Firstly, a normalization of bands increases the weight of the VIS bands as it reduces the emphasis of bands that have the largest absolute reflectance values, an effect which might be desirable given the results of the SA (see chapter 6.2.2). Secondly, normalization is practically inevitable if other features such as VIs are used, as those values most often exceed reflectance values (see e.g. Pasolli, 2012). Hence, the cost function to be minimized in this thesis was defined as the sum of the squared differences between modeled and observed reflectances normalized by the observed value, giving the normalized squared error (nSE):

$$nSE = \sum_{i=1}^{n_s} \left(\frac{R_{meas\ i} - R_{mod\ i}}{R_{meas\ i}} \right)^2 \tag{6.9}$$

In this equation, R_{meas} are the RapidEye reflectances, R_{mod} are the simulated reflectances, and n_s is the number of spectral bands. For each canopy realization, the nSE was calculated and sorted. Once the minimum distance between the observed and the simulated spectra is identified, the LUT entry with the respective parameter levels that have been used for the generation of the reflectances is selected. Traditional LUT inversion derives the LAI value associated with the simulated spectrum which is the closest match with the remotely sensed spectrum, i.e. the minimum nSE in this case.

6.5.3. Multiple LAI solutions and uncertainty measures

Under ideal imaging and modeling conditions, one single best inversion solution would return the best LAI estimation. The procedure can, however, become instable when noise affects the RS data or when the RTM result is not unique due to the above mentioned parameter interactions and spectrum compensating effects between them. Small variations in the modeled reflectances can be associated with large leaps in the parameter space in this regard, so that the single best solution can be distinctively different from the next best solutions.

Multiple solution samples

Thus, the robustness and accuracy of the inversion can be increased by not selecting the parameter set of the single best spectrum as output, but by deriving the parameters of multiple best fitting spectra, which, as a subset of the LUT, is called multiple solution sample. The benefit of selecting several LUT entries close to the absolute minimum has been shown by several authors (see Weiss et al., 2000; Combal et al., 2002a; Koetz et al., 2005a; Darvishzadeh et al., 2008b; Soenen et al., 2009; Vohland et al., 2010; Richter et al., 2011; Darvishzadeh et al., 2012; Wang et al., 2013; Verrelst et al., 2014). Further, a confidence level around the final estimate can be derived pixel-by-pixel by analyzing the distributions of the spectral distance measure values and of the LAI values within the multiple solutions sample (see Rivera et al., 2013).

The actual size of the sample of multiple best solutions as well as the statistical measure according to which the final estimate is calculated are crucial, but different strategies and numbers are reported in the literature for LAI derivation. The sample can either be defined by a fixed number of all cases (see Weiss et al., 2000; Combal et al., 2002b), as a certain percentage of all cases (see Wang et al., 2013; Verrelst et al., 2014), or by a threshold corresponding to measurement and model uncertainties (see Knyazikhin et al., 1998; Soenen et al., 2009). In absolute numbers, optimal sample sizes between ten (Combal et al., 2002a) and 250 (Darvishzadeh et al., 2012) entries have been identified as being optimal for LAI derivation, while the best LUT fraction percentage varies between 1% (Verrelst et al., 2014) and 20 % (Koetz et al., 2005a; Vohland et al., 2010; Richter et al., 2011).

Uncertainty thresholds for the definition of the multiple solution sample were rejected in this thesis due to the missing knowledge on model and measurement uncertainties. Further, fixed sample sizes were not used because the considerable variability in the number of LUT entries for the different RapidEye scenes (chapter 6.5.1) would result in quite different information contents used for different scenes. In this context, a percental sample size for all LUTs seemed to be the most appropriate approach. The optimal percental sample size was identified using a subset of the available *in situ* data, i.e. the LAI data of three of the six field campaigns (May 25, July 16, and September 6, 2011). The list of nSE values obtained over the five RapidEye bands for each reference pixel is sorted, and different percentage sample subsets are tested for inversion. As the literature suggests that the consideration of multiple solutions influences the result only up to a selection of approximately one fourth of the model realizations (e.g. Rivera et al., 2013), and that the largest variations in accuracy occur in the lowest percentage ranges of selected cases (e.g. Weiss et al., 2000; Darvishzadeh et al., 2012), 26 percentage values between 0.001 % (representing the single best solution case) and 25 % were realized, with finer intervals of up to 1.0 % in the lower range. For each sample size, the range of possible LAI solutions is retained.

In some applications, such as LAI input to land surface models, it may be acceptable to specify a range of LAI values. In most other situations, however, it is desirable to provide just one solution. With regard to the statistical measures used for the derivation of a single value from the subset of multiple possible solutions, most of the above mentioned studies rely on measures of central tendency, i.e. on the mean or median of the LAI value distribution within the sample. Only few authors use different methods, such as Vohland et al. (2010), who apply a weighted mean, or Soenen et al. (2009), who use ancillary information (e.g. topography measures) to further reduce the potential solutions to those that match both reflectance and ancillary conditions. However, also in this regard, no preferred measure is identified in the literature. In this thesis, the mean and the median were tested, by calculating both measures for the different multiple solution subsets and comparing the resulting LAI values derived at the field campaign plots to the *in situ* values, i.e. calculating the RMSE for each scene and sample size. The RMSEs generated through this analysis are shown in Figure 6-12 for the three measurement campaigns' data sets and the respective RapidEye reflectances. Apart from the differences in absolute RMSE values for the three scenes which are not discussed here, it is remarkable that for each data set a different optimal sample size is identified, ranging between 0.1 % and 25 %. The July and September scenes show a rather similar behavior with a global minimum. For the May 25 scene, however, the derived minimum RMSE value is generated with the largest tested sample size of 25 %, so no final statement regarding the optimal size can be made, as the RMSE might drop further with larger samples. Presumably, the behavior of this scene's LAI accuracy is rather due to scene-specific uncertainties in the RS or field data. An average LAI value derived from more than 25 % of all simulated cases cannot represent a specific canopy state. Thus, this large sample size is not adopted for further analysis. Instead, the percentage value minimizing the RMSE averaged over all three data sets, 0.5 %, is chosen for further analysis.

As can further be seen from Figure 6-12, the RMSE values do not differ much between the mean and median LAI values, and no statistical measure performs overall better than the other. Based on this ambiguous result, the median has been selected as statistical measure for generating the final LAI maps for three reasons: First, the median value is less influenced by outlier values than the mean. Second, the median LAI is a value that can actually be found in the multiple solution sample, while e.g. the mean of a bimodal LAI distribution within the solution sample is no LAI for which a corresponding modeled spectrum is a close match to the RS spectrum. Finally, the small interval of 0.2 at which the LAI has been specified during parameterization allows for a gradual LAI estimation also without the use of mean values.

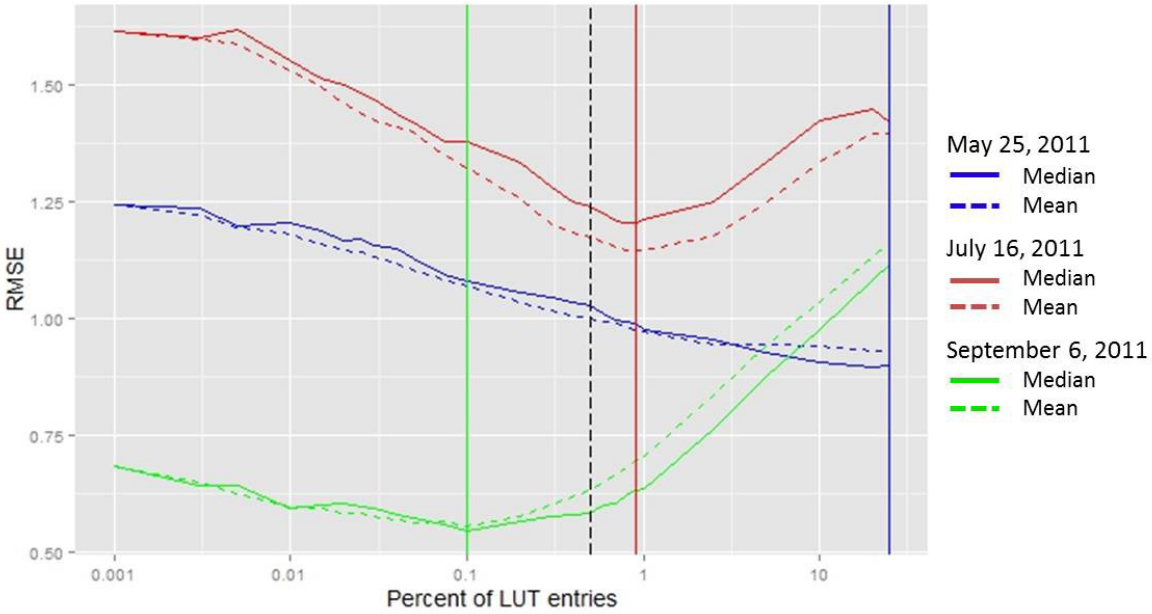

Figure 6-12: RMSE between modeled and measured LAI as a function of the percentage of selected cases in the LUT. The vertical solid lines mark the respective minima achieved for three *in situ* data sets, while the black dashed line marks the overall minimum (0.5 %). Note that the x-axis is logarithmically scaled.

Uncertainty measures of the inversion approach

As mentioned above, a multiple solution sample provides further information through the use of descriptive statistics on the sample's distributions of *nSE* and LAI values. The residuals of the spectral match indicate the degree of mismatch between the observed spectrum and the LUT spectra. Thus, the spectral distances, which is characterized here by the nRMSE (derived from the respective *nSE* values) between simulated and measured spectra, and by the standard deviation (SD) of the selected nRMSEs, provide parameter-independent information regarding the uncertainty of the inversion process (Kötz et al., 2004; Rivera et al., 2013). The LAI SD of the sample can be interpreted as the uncertainty of the LAI estimate itself, as it outlines the variability encountered within the multiple solutions, i.e. the ill-posedness of the inversion (Kimes et al., 2000). Since the SD directly depends on the magnitude of LAI, alternatively the LAI CV can be used. It maps the relative uncertainty of LAI derivation and allows for a comparison of inversion performance across all maps (Rivera et al., 2013).

As these measures are available for each pixel, they are a spatially explicit uncertainty measures, and several quality layers for each LAI map can be generated. Thereby, the measures complement each other. For example, a large RMSE between the selected simulated and measured spectra would either indicate that the specific canopy type is not well covered by the LUT, or that the measured spectrum is affected by errors, either of which would reduce the reliability of the inversion result, even though the SD of the LAI estimates is small. On the other hand, a large LAI SD in combination with a low RMSE SD would indicate a close spectral match with a measured spectrum, which is however ambiguous, i.e. an ill-posed inversion. The statistical measure also indicates a reduced robustness of LAI inversion in this case. This illustrates how these different measures can help to identify the source of error of LAI derivation. Thus, apart from the median LAI, the nRMSE of the selected median LAI, the SD of all nRMSEs, the SD of LAI, and the CV of LAI are output of the RTM inversion in this thesis and used for flagging uncertain LAI estimates. Such inversion quality information is only seldom analyzed in the literature (see e.g. Dorigo, 2007; Rivera et al., 2013; Verrelst et al., 2014), and generally only based on a single measure.

6.5.4. Improvement of spectral model input features

As mentioned in chapter 2.2.3, both, reflectances generated by a RTM and vegetation signals recorded by RS systems, can only be modeled or measured to a certain degree of accuracy. While assumptions simplifying the radiation transport through the canopy introduce errors to simulated reflectances, spectral measurements are influenced by atmospheric conditions and corrections, radiometric calibration, or BRDF normalization (Baret et al., 2007). This implies that an RTM actually predicts a domain around the model output to which the “true” reflectance belongs. For RS reflectances, it is also only possible to specify a range around a measured reflectance including the “true” value. Both domains are difficult to minimize, as the different uncertainties would need to be individually and precisely quantified (Baret and Buis, 2008). Uncertainties associated with RTMs are very complex and result in highly structured errors (Verger et al., 2011a).

Added spectral noise

Adding noise to the simulated canopy reflectances, as it has been pursued in a few studies so far, can however be seen as a regularization technique to at least partly account for uncertainties attached to spectral measurements. In most of these studies (e.g. Combal et al., 2002b; Bacour et al., 2006; Baret et al., 2007; Lauvernet et al., 2008; Richter et al., 2011) relative Gaussian noise of about 2.5 % to 4 % is added to the simulated reflectances irrespective of wavelength to account for instrumental noise (Nieke et al., 1999). Koetz et al. (2005a) additionally introduced wavelength dependent errors of up to 10 % in the blue band to account for atmospheric influences. Verger et al. (2011a) considered the structure of RS data uncertainties in more detail and argue that atmospheric correction, radiometric calibration, and instrumental noise result in multiplicative and additive uncertainties, which are both wavelength-dependent and wavelength-independent. Therefore, Verger et al. (2011a) suggest a noise generation approach in which both additive and multiplicative white Gaussian noise, band-dependent as well as band-independent, is considered :

$$R_{noisy}(\lambda) = R_{sim}(\lambda) * [1 + \varepsilon(0, \sigma_{rel}(\lambda)) + \varepsilon(0, \sigma_{rel}(all))] + \varepsilon(0, \sigma_{abs}(\lambda)) + \varepsilon(0, \sigma_{abs}(all)) \quad (6.10)$$

$R_{noisy}(\lambda)$ corresponds to the degraded band-specific reflectances in the LUT, $R_{sim}(\lambda)$ to the LUT reflectances simulated by the RTM, $\varepsilon(0, \sigma)$ represents a normal distribution with a mean value equal to zero, $\sigma_{rel}(\lambda)$ being the relative uncertainty applied to band λ, $\sigma_{rel}(all)$ being the relative uncertainty applied to all bands, $\sigma_{abs}(\lambda)$ the absolute uncertainty applied to band λ, and $\sigma_{abs}(all)$ the absolute error applied to all bands. This approach is also implemented here, as also the noise affecting the RapidEye data is of additive and multiplicative nature (BlackBridge AG, personal communication).

The influence of added noise on the five RapidEye bands was again tested on three of the six RapidEye scenes (May 9, May 25, and September 6), for which concurrent *in situ* data are available[18]. As variance coefficients, Verger et al. (2011a) use fixed relative and absolute values (4 % and 0.01, respectively) irrespective of individual bands. For the application described here, it would be favorable to use the specific signal-to-noise ratio of the original RapidEye data (Reulke and Weichelt, 2012), which however cannot be assumed unchanged after the preprocessing and resampling steps (see chapter 4.1.2). Therefore, noise levels were derived from the respective RapidEye scenes by sampling reflectances from visually homogeneous areas. Per scene, approximately 4000 pixels from around 10 different objects (agricultural fields and meadows) were derived, and for each object the absolute and relative SD were calculated. As it has to be assumed that by sampling pixels from a scene not only noise, but also natural variability is recorded, only the coefficients of the object showing the smallest relative and absolute SD values were selected for each scene. This value was assumed to be closest to the true spectral noise. The derived values range between 0.002 and 0.01 for the absolute values and 1.9 and 9.3 for the relative values. As no knowledge on the band-dependent and the band-independent uncertainties existed, the respective lowest absolute and relative band-specific noise levels of each scene (i.e. 0.003 and 2.0 %, 0.003 and 1.9 %, as well as 0.002 and 3.0 %) were treated as band-independent variances $\sigma_{abs}(all)$ and $\sigma_{rel}(all)$, while the differences between these values and the band-specific coefficients (ranging between 0 % and 6.3 %) were treated as band-dependent variances $\sigma_{abs}(\lambda)$ and $\sigma_{rel}(\lambda)$. The used noise levels are thus rather conservative estimates in the range of other literature values.

For testing the influence of these noise levels on the LAI retrieval accuracy, three different approaches are pursued. Firstly, the LUTs are affected with noise by applying Equation 6.10 on each LUT entry individually and therewith slightly changing the simulated reflectance values, and subsequently used for inversion, similarly to most of the above mentioned studies. Further, as suggested by Richter et al. (2012b), the noise modeling was applied to the LUTs 50 times, resulting in 50 LUTs containing slightly different reflectances. From these 50 LUTs, LAI was derived in two different ways. On the one hand each LUT was inverted individually and LAI was derived by calculating the mean LAI of the 50 LAI estimates output. On the other hand, the entries of all 50 LUTs were joined together into one LUT and used for inversion, which generates one LAI estimate. For all inversions, the optimal multiple solution subset size of 0.5 % identified above and the median solution were used.

---

[18] The May 9 scene was selected for this test instead of the July 16 scene as it has a smaller LUT and thus fewer computation effort was required for affecting the LUT reflectances with noise.

The overall LAI prediction error for all three RapidEye scenes was slightly reduced on average by 3.7 % from an RMSE of 0.82 to 0.79 for all three tested LAI derivation approaches using noisy LUT reflectances. This prediction error decrease is rather low compared to other studies (e.g. Verger et al., 2011a; Richter et al., 2012b). Thus, as this small error reduction is associated with a rather high computational effort of noise simulation for the many and partially large LUTs, the use of added noise is abandoned in this thesis. Nevertheless, further systematic evaluations of the role of added noise in grassland LAI derivation in combination with different noise levels, multiple solution sample sizes, and cost functions might result in further improvements. Without aiming for the noise level of a specific sensor, Rivera et al. (2013) and Verrelst et al. (2014) evaluated the influence of noise at levels between 1 - 50 and 1 - 30 %, respectively. Both studies attested an improved biophysical parameter derivation through adding noise to the simulated spectra, but they also stressed the fact that the optimal noise levels depend on the selected cost function and multiple solution approach. Therefore, further analysis on noise influence on LAI in grasslands could also be expanded by taking into account such interactions.

Test on additional spectral features

Another approach to reduce the uncertainty associated with the spectral features which are used as input to the RTM inversion is the additional use of VIs as input, which are less sensitive to influences that disturb the spectral signal (see chapter 2.2.2). The benefit of using additional VIs in the inversion procedure has been tested based on all four RapidEye scenes of 2011 for which concurrent *in situ* data are available. The rationale behind this is on the one hand to increase the dimensionality of the multi-spectral RS data, reducing the ill-posedness of the inversion. On the other hand, the integration of information on vegetation properties highlighted by VIs might increase the robustness of the spectral match. Nevertheless, only very few RTM inversion studies used VIs as additional spectral features (Pasolli et al., 2011). VIs have been implemented by calculating the VI values based on the modeled and measured RapidEye band. While the overall LAI retrieval RMSE by the sole use of the five RapidEye bands is 0.93, the additional use of the RVI reduced the RMSE to 0.89. The use of the Curvature index as well as of both indices together with the RapidEye bands increased the RMSE to 1.05 and 1.20, respectively. Therefore, the RVI was chosen as additional band, resulting in six inversion features, which matches the number of free PROSAIL parameters.

6.6. Results of LAI derivation using the PROSAIL model

In the following, the performance of physical LAI derivation using the PROSAIL RTM is presented. First, the similarity of the modeled and measured reflectances is evaluated. Then, the resulting LAI maps are described and their accuracies are assessed using *in situ* LAI measurements that coincide with six of the RapidEye images. In a next step, the spatial patterns of LAI derivation accuracy are discussed based on inversion uncertainty measures and additional canopy parameters, with special focus on the most challenging canopy occurrences. In the fourth subchapter, the generated LAI time series are evaluated.

6.6.1. Comparison of RapidEye and PROSAIL reflectances

In a first step, the ranges and distributions of the simulated reflectances and of the corresponding RapidEye reflectances are compared in each band and for each scene, since the capability of the RTM to properly simulate the canopy spectra and the consequential spectral match is a prerequisite of model inversion (Baret and Buis, 2008). Hence, the range of simulated data necessarily needs to contain the range of the observed data, since a meaningful spectral match is not possible if the measured spectrum is not covered by the LUT. Further, significantly different data ranges indicate that many simulation runs were carried out in vain during the construction of the LUT. Regarding the distributions of the simulated and modeled spectra, a high similarity is unlikely to be due to the uniform sampling of the parameter spaces during parameterization, which aimed at covering all parameter levels and all possible combinations on the one hand, and probably rather normally distributed real-world observations on the other hand. Hypothetically, a high similarity of distributions would be desirable, because it indicates that the ecosystem under investigation is well represented. Further, it increases the chances of finding a suitable match for most measured reflectance values and the chances of a successful inversion for the spectral signals that can result from confounding parameter influences. However, *a priori* knowledge on the RS reflectances distributions and on the necessary parameterization scheme to achieve similar reflectance distributions is normally not available.

In Figure 6-13, a random sample of grassland pixel reflectances measured in the five RapidEye bands of the July 16, 2011 scene is compared to the reflectances simulated by PROSAIL given the scene-specific parameterization. The simulated reflectances are taken from the LUT that was generated using the system geometry closest to the geometry of the RapidEye acquisition (θ_s= 27.5°, θ_o= 17.5°). Accordingly, the RapidEye reflectances were taken only from completely flat pixels, and the sample has the same size as the corresponding LUT. The density plots show clearly differing ranges and distributions in the five bands. According to a Kolmogorow-Smirnow test performed on the data set pairs, the null hypothesis that the samples are drawn from the same distribution had to be rejected for each band in this example. The same analysis is also presented in a more dense form using boxplot graphs for each of the six RapidEye scenes for which concurrent *in situ* data are available (Figure A-4). The simulated reflectances and the measurements also show some distinct differences here. A pattern similar for all scenes is evident from these figures: in the VIS, the simulated reflectances are on average a bit lower than the RapidEye grassland reflectances, but cover a wider range overall. This means that the VIS reflectances occurring in reality are

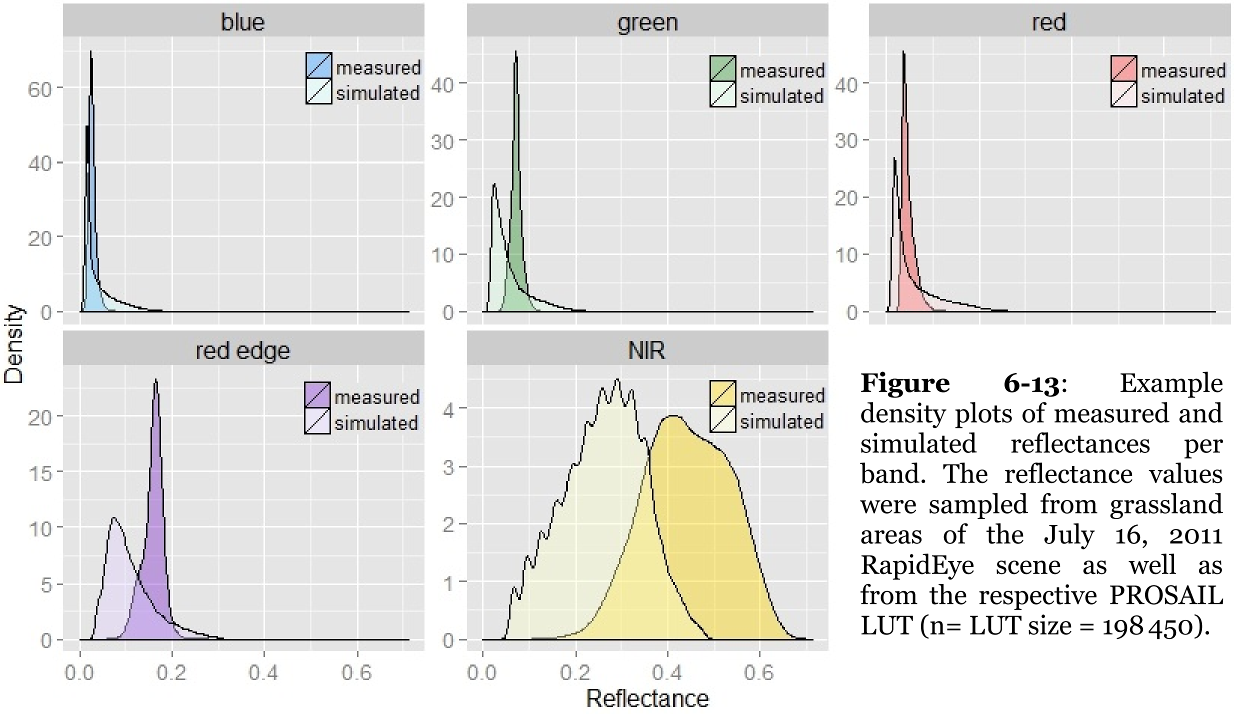

Figure 6-13: Example density plots of measured and simulated reflectances per band. The reflectance values were sampled from grassland areas of the July 16, 2011 RapidEye scene as well as from the respective PROSAIL LUT (n= LUT size = 198 450).

covered by the LUT and can be closely fitted to a solution by the cost function. However, a large part of the LUT entries containing low reflectance values and corresponding canopy parameters is only seldom selected as best fit, while the majority of RapidEye reflectances fit best to a relatively small number of canopy realizations that produced higher reflectances. This VIS distribution shift, which is most distinctive in the green, might either be caused by an inadequate parameterization (e.g. too low C_{ab} rates or LAI values), or by inadequate RapidEye preprocessing (e.g. atmospheric correction). Alternatively, Vohland and Jarmer (2008) also mention inconsistencies between simulated and the measured grassland reflectances in the VIS, and attribute this to the chlorophyll absorption coefficients used in PROSPECT, which may not be true for many grassland plant species. Yet, without contemporaneous *in situ* canopy spectral measurements using a spectroradiometer, the question of which distribution is closer to reality cannot be conclusively solved. Further, the narrow distributions of the measured VIS reflectances may have negative consequences on LAI derivation using PROSAIL. In chapter 6.3, it was observed that the influence of LAI on the PROSAIL output is largest in the VIS. In turn, a small variability in VIS reflectances leads to a small variability of the LAI estimates.

The situation is different, however, for the simulated red edge and especially the simulated NIR reflectances, which are on average significantly lower than the observed reflectances. In this case, it is clear that the RapidEye measurements are more in the range of realistic grassland NIR reflectances (cf. e.g. Darvishzadeh et al., 2008b; Vohland et al., 2010), i.e. that the PROSAIL NIR reflectances are too low. Most importantly, the PROSAIL simulations do not span the data range of RS reflectances in the NIR, preventing a close cost function match for high remotely sensed NIR reflectances. This has two implications: first, this great difference between the measured and modeled reflectances will put an emphasis on the NIR reflectance during inversion, as the nSE_{NIR} will have the largest share in the overall nSE value of each LUT entry. In this context, the normalization introduced in the cost function proves valuable, as the influence of this error is somewhat reduced by it. Second, for pixels with a high NIR reflectance, the closest simulated NIR reflectances correspond to only a small number of canopy realizations generated probably by extreme input parameters. As these few cases will most probably be selected due to the high influence of this band as soon as a pixel's NIR reflectance is above the highest simulated NIR value, this leads to an 'artificial'[19] saturation effect over dense vegetation, however not necessarily returning the highest existing LAI level in the LUT.

This partly strong mismatch between modeled and measured reflectance ranges reveals possibly important restraints for accurate LAI derivation. In general, the insufficient representation of the meadows and pastures by PROSAIL could suggest that the selected RTM is unsuitable for grassland canopies. Dorigo (2007), however, achieved a satisfying fit between PROSAIL results and grassland spectra. Thus, alternatively, it might be caused by unsuitable parameterization e.g. by including too low LAI or C_{ab} values, too high LIDF values or unrealistic soil spectra. With regard to the reflectance distributions, as mentioned above, the uniform sampling scheme used for PROSAIL parameterization can be revised. Alternative, e.g. Gaussian, sampling strategies focusing on more frequent spectral ranges have been suggested e.g. by Weiss et al., 2000, Dorigo et al., 2007, Hedley et al., 2009, and Duveiller et al., 2011b.

---

[19] This „artificial“ saturation resulting from missing high reflectance simulations in the LUT should not be confused with the RS signal saturation resulting from insufficient light transmittance through dense canopies.

6.6.2. PROSAIL LAI derivation results and accuracy

Based on the above described model set-up and optimization of the inverted PROSAIL model, and the RapidEye data described in chapter 4.1, a two-year high spatial resolution LAI time series, i.e. 19 LAI maps, was generated for the Ammer catchment. Additionally, maps displaying further canopy characteristics such as the leaf chlorophyll content or the mean leaf angle were generated. These data sets are useful for comprehensive descriptions of the vegetation cover, such as differentiating spectrally similar but structurally different canopy types (e.g. grassland and moorland), or estimating ecological processes and disturbances.

Figure A-5 displays the LAI map derived from the May 9, 2011 scene and gives an impression of the landscape structure and spatial variability of LAI. In the mountainous south-western part of the catchment, only few grassland areas exist. They can be distinguished into valley bottom areas with a high LAI, and mountain pastures with overall lower LAI, which are not intensively used. Following the further course of the Ammer River, different grassland habitats around Unterammergau (see Figure 3-7) such as the *Ammertaler Wiesmahdhänge* with LAI values around 5, and the *Moore im oberen Ammertal* with a comparably lower LAI can be distinguished. In the alpine foreland to the north, significantly more areas are covered by grassland. These meadows and pastures have an overall higher LAI, as they are more intensively managed. The map also displays the partly strong spatial differences in between fields resulting from these managements. In the northern part of the catchment, the grassland area is somewhat reduced due to a higher settlement density and more areas which are used for crop cultivation.

In Figure 6-14, subsets of six of the 2011 and 2012 LAI maps derived from the inverted PROSAIL model are displayed to illustrate the spatial and temporal dynamic of the grassland areas. The strong seasonal changes and spatially very heterogeneous occurrences of the managed alpine grassland LAI are well displayed. Overall relatively low LAI in April (bottom left) is followed by an increase in biomass from May onwards (upper left). As observed in chapter 5.3, LAI is lower locally at the end of May due to the first harvest in mid-May 2011. In these three spring scenes, the LAI distributions of individual parcels can be well differentiated, although the discernibility is reduced in some areas by high intra-field variability. LAI again strongly increases and characterizes very dense canopies in mid-July and especially mid-August. In these maps, the high LAI areas are very homogeneous and at the same maximum level, which might indicate saturation. This phenomenon might be caused by an RS signal saturation over dense canopies in the traditional sense (see chapter 2.2), but also by the missing number of LUT entries representing high NIR reflectances observed above. The September scene displays homogeneous fields at reduced and spatially variable LAI levels, which seems more realistic.

To quantify the accuracy of the derived maps, LAI values are compared to the *in situ* measurements. Measured and estimated LAI from the six field campaigns and the six RapidEye scenes are shown in Figure 6-15, analogous to the statistically derived LAI in Figure A-1. As for the empirical-statistical approach, a 3 x 3 pixel mean filter was applied to the resulting LAI maps before extracting the LAI values used for validation in order to spatially match the area over which the LAI data have been measured *in situ*. The results differ considerably for the different scenes (see also Table 6-4). In most cases, a medium to strong positive linear relationship exists between the estimated and measured values with R^2 values between 0.5 and 0.8. Only for the May 25 scene could no meaningful relationship be established. This is the same scene that also showed the unexpected behavior during the

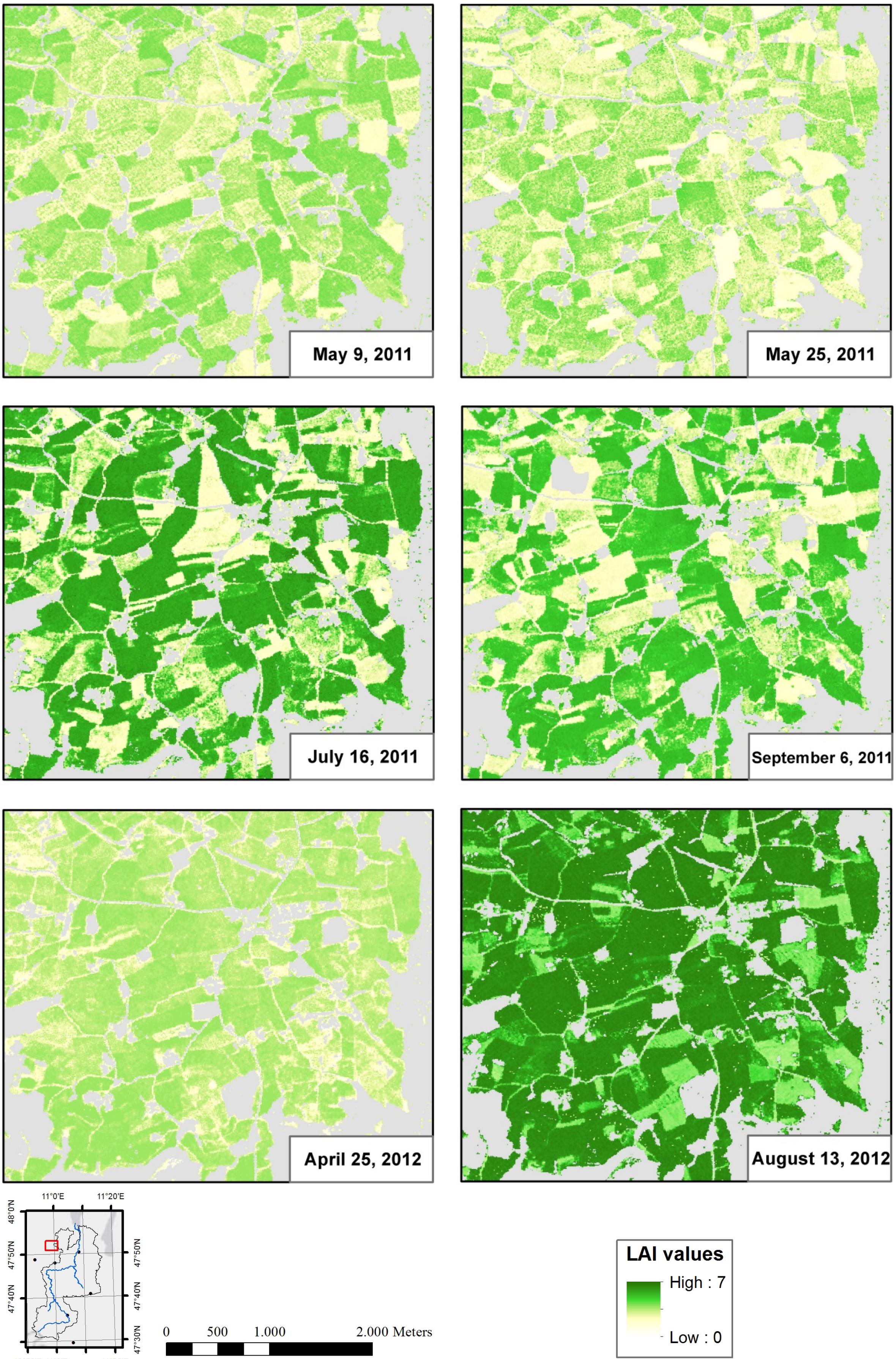

Figure 6-14: Subsets of the physically modeled LAI maps for the six field campaign dates in 2011 and 2012. LAI is scaled equally in all maps and the same subsets, time steps, and legend scaling as for the statistically derived LAI in Figure 5-2 is used.

2011

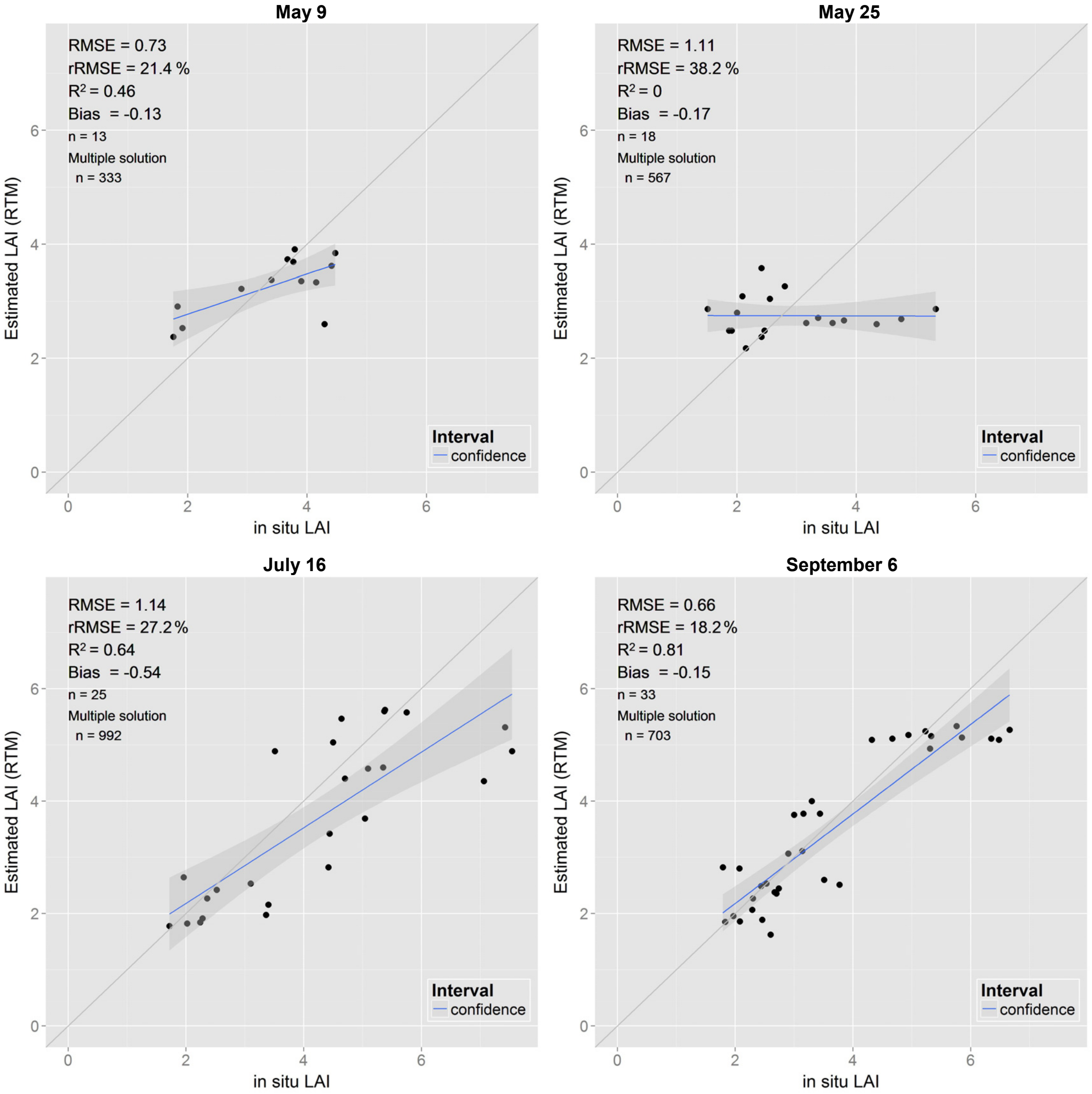

2012

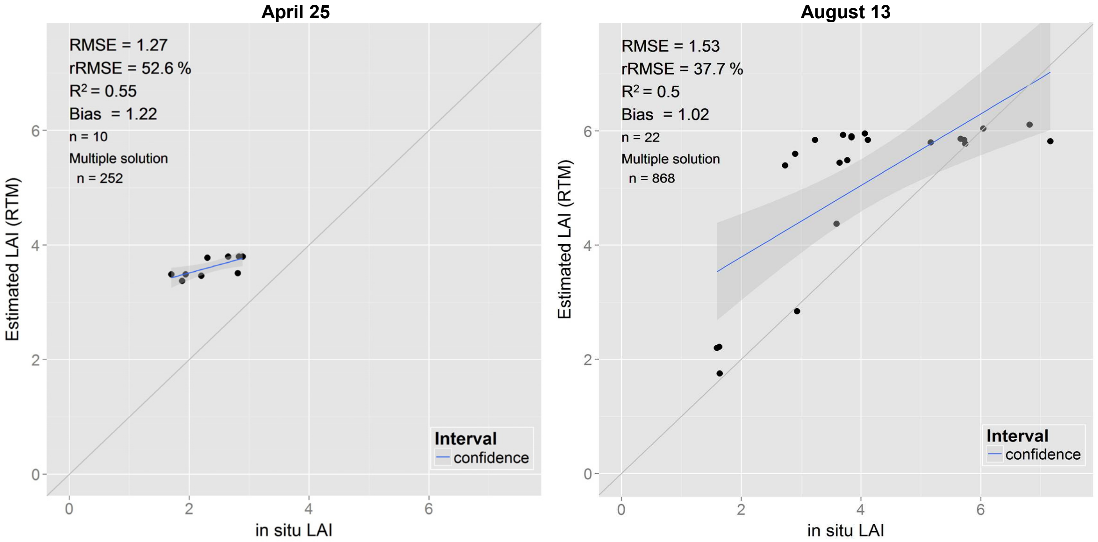

Figure 6-15: Performance of the PROSAIL LAI estimates evaluated against *in situ* data for the six field campaign dates. The confidence interval indicates the interval estimate of a fitted linear model, "n" indicates the number of *in situ* measurements and "Multiple solution n" gives the size of the multiple solution sample from which the final solution is selected by the median.

Table 6-4: Summary of LAI and LIDF retrieval accuracy generated using the PROSAIL model for each field campaign date. "n" is the number of in situ measurements, R^2 indicates the strength of the linear model fit, and α the significance level of the model fit: 0.1 '.' 0.05 '*' 0.01 '**' 0.001 '***'0.

		PROSAIL LAI				PROSAIL LIDF
	n	R^2	α	RMSE	rRMSE [%]	rRMSE [%]
2011						
May 9	13	0.46	*	0.73	21.4	41.2
May 25	18	0.0		1.11	38.2	50.1
July 16	25	0.64	***	1.14	27.2	43.0
September 6	33	0.81	***	0.66	18.2	36.9
2012						
April 25	10	0.55	*	1.27	52.6	42.6
August 13	22	0.50	***	1.53	37.7	40.7
All scenes	121	0.50	***	1.09	30.3	42.7

multiple solution sample size test (see chapter 6.5.3). LAI was derived in the May 9, July 16, and September 6 scenes with a relative RMSE (rRMSE = RMSE / mean value of the reference measurements) in the range of 20 - 30 %. The September 6 scene stands out with an RMSE of 0.66 and an rRMSE below 20 %. In the remaining scenes (May 25 and August 13), the errors are around 40 %. The explanatory power of the April 25 LAI estimates with about 50 % rRMSE is strongly reduced. In most cases, LAI is overestimated at lower LAI values (<2-3). Additionally, the scatter plots of the summer scenes (July 16, August 13, and September 6) reveal that LAI tends to saturate at higher LAI values (> 5-6). In the May 9, May 25, and September 6 scenes, this reduced accuracy of very low and very high values is balanced, and these scenes accordingly have only a low negative bias. The July 16 scene, however, has a high negative bias, while in the two 2012 scenes, the RTM almost always overestimates *in situ* LAI. Overall, two limitations can be observed in these results, which on the one hand concern the missing modeling of very low LAI values during early spring but also for most of the other scenes. On the other hand, the reproduction of very high LAI, i.e. the selection of LAI values from the upper range of each parameterization, is also impaired.

On average, the results of the inverted PROSAIL RTM fit the grassland LAI measured *in situ* with an R^2 of 0.5 (see Table 6-4 and Figure A-6). LAI can be derived with a 30 % error rate and a slight positive bias. These error rates are clearly above the target accuracy of 10 % (GCOS, 2006; Drusch et al., 2010). A direct comparison of the results to other grassland LAI studies using high spatial resolution multispectral RS data in an inverted RTM is not possible, as to the author's knowledge no such study exists. However, based on HyMap data, Dorigo (2007) achieves a relative accuracy of 46 % for grassland LAI derivation. Using spectroradiometer measurements[20], Vohland and Jarmer (2008) derive grassland LAI with

---

[20] The comparison of LAI estimates derived from multispectral RS with air-borne or *in situ* hyperspectral data is naturally impaired, due to the fewer measurement distortions, higher canopy homogeneity, and the availability of more bands using spectroradiometer data. However, the number of bands must not be overrated. Although increasing the number of bands does lead to increased spectral dimensionality, this increased dimensionality does not necessarily imply increased information content. Verhoef (2007) reports that a nadir looking hyperspectral sensor contains up to 12 independent data dimensions, while this dimensionality significantly reduces as noise levels increase. Further, the additional dimensions offered by spectroradiometers appear to contribute mainly to improved estimates of biochemical leaf parameters.

an rRMSE of 36 %, Dorigo et al. (2009) with an rRMSE of 35 %, and Darvishzadeh et al. (2008b) with an rRMSE of approximately 33 %[21]. Darvishzadeh et al. (2008b) further observe an accuracy decrease by 61 %, with an increasing number of grassland species from one to four species, indicating the relevance of the heterogeneity of a canopy for LAI retrieval accuracy. The number of species occurring in the grasslands of the Ammer catchment exceeds four by far. Hence, the results presented here also illustrate the fact that radiation transfer modeling becomes more challenging in diverse ecosystems with a high spatio-temporal variability compared to monocultures.

Indeed, for physical LAI estimates of agricultural fields using high spatial resolution RS data, a range of 15 - 20% is currently regarded as the achievable accuracy (Baret, 2010). Within the crop LAI literature, errors range from 8 - 10 % (Richter et al., 2011) to 10 - 15 % (Houborg et al., 2009; Atzberger and Richter, 2012; Rivera et al., 2013) to 30 % (Duveiller et al., 2011b; Vuolo et al., 2012; Verrelst et al., 2014). However, as stated by Rivera et al. (2013) and Verrelst et al. (2014), these partially high accuracies were only achieved for single crops, and the algorithms would not be applicable to multi-species canopies or more natural ecosystems Further research on grassland properties which are more difficult to derive should therefore be continued in order to mitigate these limitations associated to grassland LAI mapping.

6.6.3. Analysis of spatially explicit inversion uncertainty

A first step towards the identification of model shortcomings but also of RS data deficiencies which might cause the above mentioned limitations in physical LAI modeling is taken by investigating the spatially explicit uncertainty measures introduced in chapter 6.5.3, as well as maps of other parameters that strongly influence the canopy reflectance (see chapter 6.2.2) exemplarily for the September 6, 2011 scene. This sort of analysis is a recent development and has only been conducted by Dorigo (2007), Rivera et al. (2013) and Verrelst et al. (2014) so far. Figure 6-16 displays some canopy parameters as well as the statistics of model inversion for a subset of the scene.

While no large variations occur overall, the nRMSE[22] (bottom left plot) is above average in some, but not all, cases of high LAI estimates. Indeed, the areas of increased misfit between the selected LUT entry and the RapidEye reflectances are almost exclusively very dense canopies with very high RVI values (not shown). As was mentioned above, very high NIR reflectances are not well covered by the LUTs, and these thus are the areas where NIR values above approximately 0.5 lead to a large nRMSE and which are hence affected by saturation. The SD of the nRMSE values indicates the span of RMSE values in the multiple solution sample, i.e. it is low if it was possible to identify many closely fitting LUT entries and high if the best 0.5 % of all solutions also include strongly deviating spectral properties. It is depicted in the bottom middle plot of Figure 6-16 and shows that mostly fields other than those with high absolute nRMSE values are affected. These fields coincide with very sparsely vegetated areas strongly influenced by the soil signal. This increased difficulty to generate a close match over sparsely vegetated areas has also been observed by Rivera et al. (2013). Further, the inset histogram in the upper left plot shows a rather bimodal distribution, which

---

[21] The rRMSE in the study of Darvishzadeh et al. (2008b) is derived using the range of the reference measurements for normalizing the RMSE instead of the mean value. The rRMSE has therefore been recalculated using the reference data's central value published in this study. As the true mean of the *in situ* data is not known, however, this can only be considered an estimate.

[22] Note that not the RMSE but the nRMSE is indicated due to the normalization implemented in the cost function. Thus, the nRMSE values do not represent the absolute spectral distance between modeled and measured reflectances but are increased in the order of two to three.

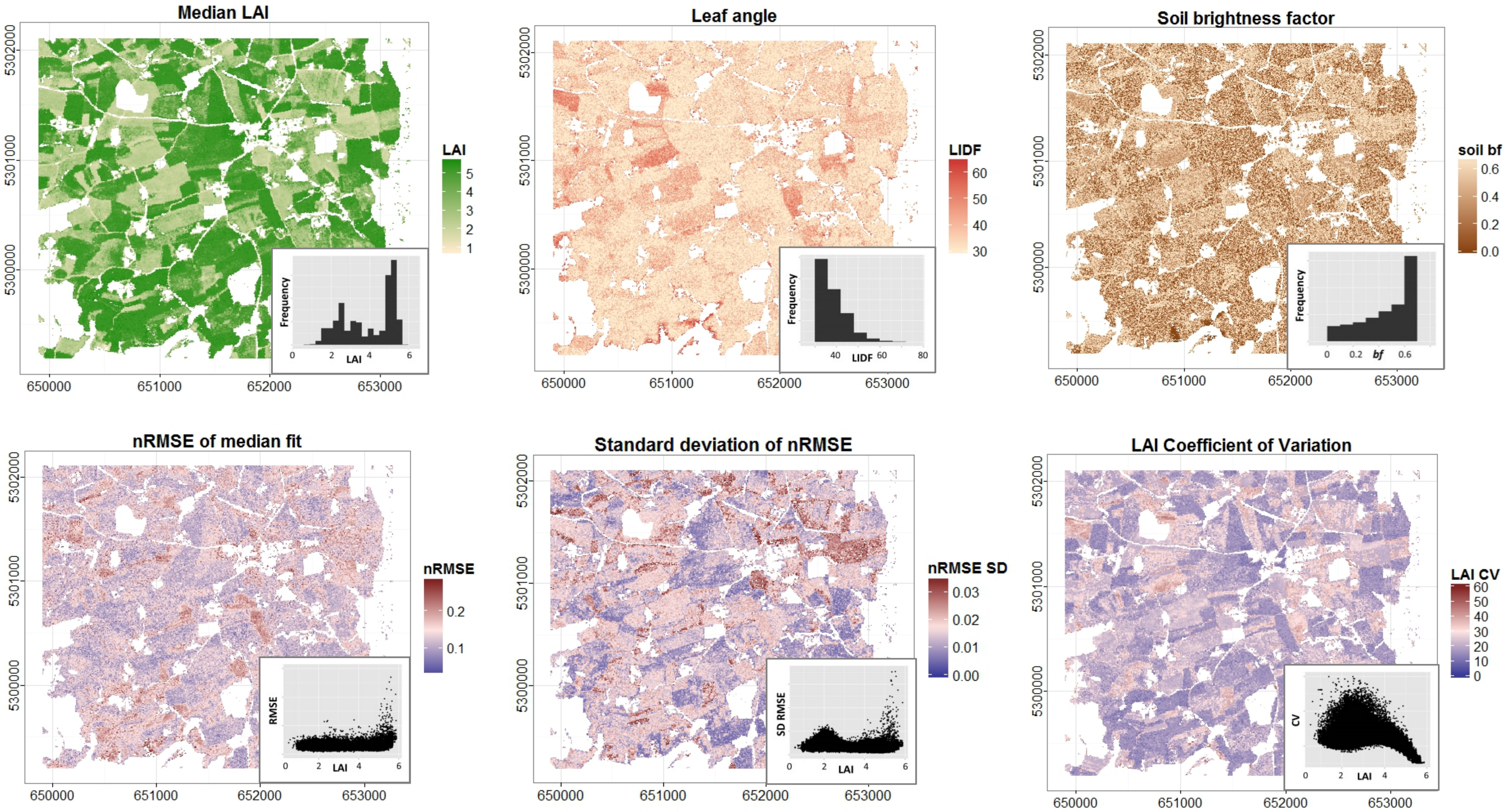

Figure 6-16: LAI, leaf angle, soil brightness factor (top row) as well as uncertainty measures (bottom row) for a subset of the September 6, 2011 scene. The nRMSE of the median fit indicates the average residual between the measured reflectances and the reflectances associated to the selected LUT entry, which is the median LAI of the multiple solution sample. The SD of the nRMSEs indicate the span of nRMSE values in this sample, while the LAI CV illustrates the range of LAI estimates the multiple solution sample. The inset scatter plots show the parameter distributions (top row) and the respective relationship with the estimated LAI (bottom row).

indicates that mostly LAI values around 2.5 and 5 have been selected. This distribution can be observed for most scenes and is especially distinct for the summer scenes (Figure A-8). These observations confirm the above mentioned difficulties with modeling very high and very low LAI values and can be localized.

Analyzing the SD and the CV of the LAI values included in the multiple solution sample provides information on the reliability of the LAI estimate itself. Despite the large nRMSE SD, the SD of LAI is lowest (0 - 0.5 LAI) on most of the sparsely vegetated areas (not shown), i.e. a wide range of different spectra obviously resulted in similarly low LAI estimates. This suggests that the occurring, possibly quite different soil spectra of the RapidEye scenes are not well covered by the LUTs, but still sufficiently different from a vegetated canopy to prevent confusion. Over the more densely vegetated areas, the LAI SD varies around one. Finally, the LAI CV (bottom right plot in Figure 6-16) is overall low over areas of high LAI estimates (0 - 20 % of variation), but increases with lower LAI values (see inset scatter plot) for some of which a higher risk of parameter equifinality, i.e. of compensating effects between RTM parameters, obviously exists. On the one hand this means that high LAI values are estimated with high reliability, although this “reliability” is partly caused by the above mentioned “artificial” saturation in the modeled NIR reflectances. On the other hand it indicates that during the estimation of medium and low LAI values, the median LAI is selected out of a relatively wide range. This impedes the derivation of extreme values, as in these areas the median value will represent the center of the range (see also Combal et al., 2002b, for a discussion of this problem). This might explain the reduced ability of the approach of mapping LAI values below 2 (see Figure A-5).

As mentioned above, other PROSAIL parameters that strongly influence the canopy reflectance should also be analyzed in order to assess the quality of a RTM inversion. The LIDF, C_{ab} and soil *bf* proved to be the other most influential parameters of the PROSAIL model and are therefore investigated in more detail. Spatializing the LIDF estimates shows that the within-field variability of LIDF is low, which is in accordance with assumptions presented by Atzberger (2004). Especially for dense fields, a small average leaf angle between 30 - 40° has been selected by the procedure. Only for some fields with low LAI, LIDF values of 50 - 60° are selected. This is probably caused by the rationale that model runs based on small leaf angle values produce the highest NIR reflectances. The leaf angle values measured in the field at each ESU using the LAI-2000 PCA are strongly underestimated by the physical approach (see Figure 6-17). It has however to be mentioned that, while the indirect LAI-2000 PCA LAI estimates have been corrected using directly measured LAI, the leaf angle values were not recalculated afterwards, although they might change with LAI according to equation 4.11. The accuracy of the *in situ* LIDF values thus has to be questioned. Nevertheless, other studies found in the literature (Table A-8)

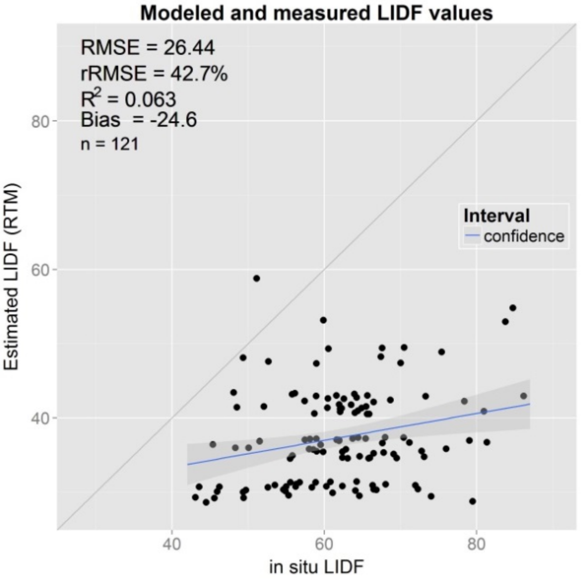

Figure 6-17: Scatterplot of all *in situ* LIDF measurements vs. PROSAIL LIDF estimates. Note that the RTM LIDF values are spread slightly around their true values to better indicate the value distribution.

also generally assume higher LIDF values for crop and grassland model parameterization, so that a certain LIDF underestimation can still be assumed to be valid. However, no direct validation of the LIDF outcome of PROSAIL exists yet, which is why the absolute evaluation of these results is not possible.

As all PROSAIL parameters are estimated together, and as LAI and LIDF have strong compensating effects on each other (see e.g. Jacquemoud, 1993), a potential LIDF underestimation of densely vegetated areas has implications on LAI estimation. A high leaf angle value would entail a higher LAI estimate for the same pixel reflectance. As estimated LAI of the dense fields in the subset are already very close to the maximum LAI value used for parameterization of this September scene, however, this suggests that either the LAI or the LIDF was parameterized too narrowly. Atzberger (2004) also shows that low LIDF values result in higher LAI estimation errors, as the saturation situation is more quickly. Finally, when analyzing the PROSAIL estimation errors of LAI and reached LIDF for each scene (see Table 6-4), it is apparent that the LIDF rRMSE is lowest for those scenes for which the LAI could also be predicted with the lowest rRMSE. The quality of both parameters is thus interdependent. In conclusion, LIDF parameterization plays a very important role for biophysical parameter estimation using RTMs, but is at the same time often disregarded.

The wide range of crop and grassland LIDF values and distribution types suggested in the literature, varying between 20 and 80 °, and between uniform, Gaussian, or spherical distributions, also indicate the fact that knowledge on this parameter is still sparse. Further investigations should therefore focus on the characterization of the leaf angle distribution in the field (see e.g. Koetz et al., 2007b, Hosoi et al., 2009, and Béland et al., 2011 who use terrestrial LIDAR (LIght Detection And Ranging) for LIDF measurements) in order to improve the definition of LIDF values for RTM parameterization.

The physically modeled leaf chlorophyll contents (Figure A-7) are homogeneously low (20 - 30 $\mu g*cm^{-2}$) for the whole area except for very few pixels in densely vegetated areas. These C_{ab} estimates, which are also very low in comparison to other grassland studies (Vohland and Jarmer, 2008), are probably caused by the above mentioned high RapidEye reflectances compared to the modeled reflectances. A low chlorophyll value is compensated by other PROSAIL parameters, such as a high LAI or a low LIDF, both of which are observed in this thesis. However, low assumed C_{ab} concentrations also increase the influence of the soil in the model output since leaf transmittance is inversely related to C_{ab} (Atzberger, 2004), which can distort the modeled signal.

Finally, the soil *bf* map (upper right plot in Figure 6-16) is rather noisy in contrast to LAI and LIDF, and boundaries between parcels are less distinctive. It is difficult to assess the plausibility of these estimates, as on the one hand soil reflectance can be assumed to be homogeneous within a single field, which normally consists of the same soil type and experiences the same treatment and weather conditions. On the other hand, especially in a non-flat landscape, small-scale differences in soil humidity cannot be excluded. Nevertheless, this observation might indicate instabilities in RTM inversion. The introduction of spatial constraints on *bf* as suggested by Atzberger (2004) or the use of *in situ* soil spectrometer measurements might potentially reduce this instability. Overall, the analysis of the associated parameter maps reveals some shortcomings. However, as Rivera et al. (2013) showed, the simultaneous estimation of multiple biophysical parameters using one inversion strategy is not the best choice, but different cost functions and inversion setups should be individually optimized per variable of interest. It can therefore be assumed that the LIDF, C_{ab} and soil *bf* parameters are derived with reduced accuracy using an approach which has been continuously optimized for LAI derivation.

The analyses of the quality layers associated with the derived LAI maps confirm the observation that the inverted PROSAIL model reproduces medium high LAI values well. However, it has a reduced ability of mapping very high and very low LAI values, which are marked by either high inversion nRMSE values or high nRMSE SD and LAI CV values. To visualize these challenging aspects, the modeled LAI values at two ESUs are further investigated. Figure 6-18 represents two cases of LAI overestimation selected from the especially weakly modeled May 25, 2011 scene, compared to the *in situ* values and to photographs taken in the field. Indeed, some differences can be observed with regard to LAI overestimation by physical LAI modeling. In the upper row of Figure 6-18, the area of a pasture is depicted which has some bare areas caused by grazing. On this plot, an LAI of 1.8 has been measured, which is overestimated by the PROSAIL model by 0.7 LAI. The bottom row of the figure, however, shows a different kind of sparsely vegetated meadow, which results from harvesting. For these areas, LAI overestimation is distinctively more pronounced, as the measured LAI of 1.5 is reproduced by values around 2.8. While on both ESUs, the soil signal will play a prominent role, litter, brown plant material, and stubbles additionally distort the canopy spectrum on the second ESU. Presumably, these spectra are not covered by the LUT and their simulation would need a highly specifically adapted parameterization of the C_{ab}, C_{b}, and soil *bf* values, i.e. stratified LAI modeling. Very similar restrictions in LAI derivation have been observed by Dorigo (2007), who noted a reduced average accuracy in LAI derivation using spectroradiometer measurements for the phenological types ‘meadow-cut’ and ‘pasture’ (around 60 %) in comparison the type ‘meadow-long’, which is modeled with an accuracy of about 80 %.

With regard to LAI underestimation and saturation effects, the misfit of the modeled and measured NIR reflectances has already been mentioned. The use of the median value out of a

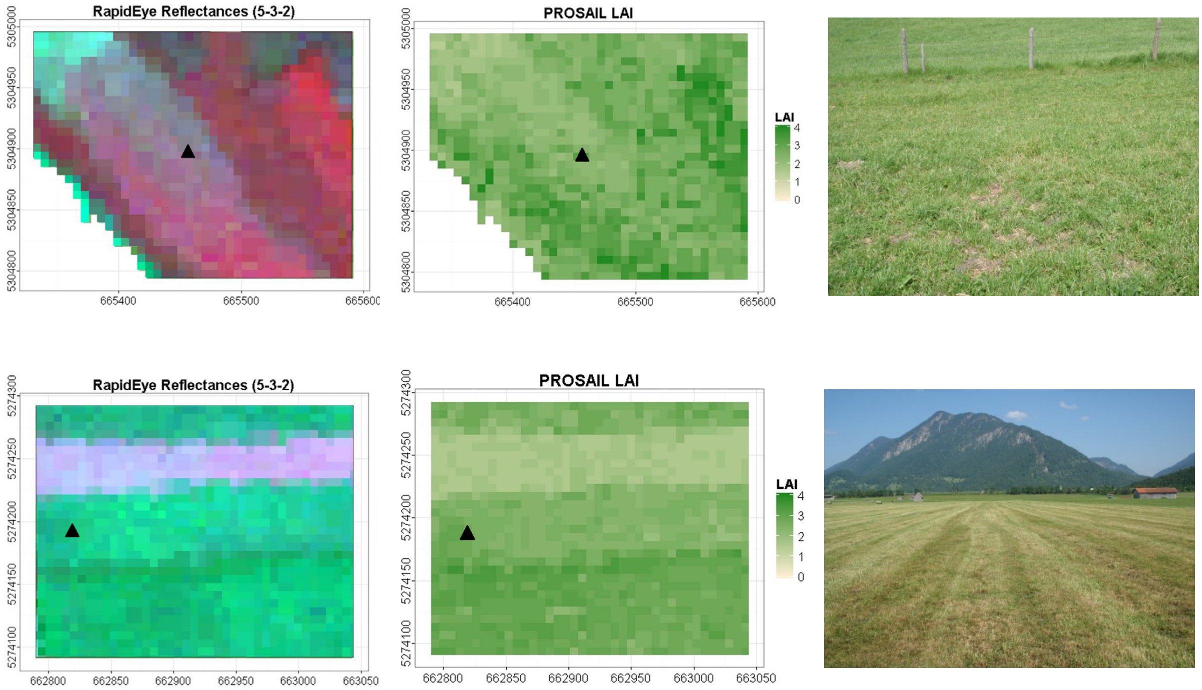

Figure 6-18: Examples of low LAI grassland overestimated by the PROSAIL model. In the upper row, a sparsely vegetated pastures is shown, while in the bottom row the subset depicts a freshly harvested meadow. The ▲ symbols mark the positions of the ESUs. The photographs were taken on May 24 and 25, 2001, respectively.

multiple solutions sample also influences the mapping of very high values, i.e. highest values are omitted. Thus, although saturation occurs, the upper range of possible LAI values is not met in any scene. While these analyses point towards limitations caused by the model, some areas of the May 25, 2011 scene are an example for the intrinsic limits of LAI derivation from RS data. For this spring scene, the RTM seems to be non-sensitive to high LAI values (see Figure 6-15). As an example, a subset of the ‘Hofheim’ plot is shown in Figure 6-19. On both ESUs, a high LAI (4.3 and 4.8, respectively) was measured, but the modeled LAI at these pixels are rather low (2.6 and 2.7, respectively). The RapidEye reflectances are also low in these areas (see middle plot) despite the dense and healthy vegetation observed in the field. Especially the green and red edge reflectances are reduced by about 20 %. A closer look at the canopy structure (right plot) reveals, however, that the grassland under observation is high and characterized by a large amount of grasses, i.e. erectophile species. In such conditions, more shadows are prevalent and photons might get trapped in the canopy more frequently, which leads to a reduced canopy reflectance (see e.g. Madeira et al., 2001). The photograph in Figure 6-18 further shows that many species, and especially grasses, were blooming during this measurement campaign, which reduces the greenness of the canopy. In this case it hence seems that the vegetation spectrum as seen by the RapidEye sensor is distorted from the outset, so that a simple RTM which does not explicitly take into account non-green vegetation elements or a heterogeneous canopy structure could not physically derive the LAI value based on a spectral match. Four of the five highest *in situ* LAI values of this campaign data set are located within such dense and blooming meadows, which is nearly one fourth of all validation data for this scene. In combination with the many low LAI values measured in the field shortly after the first harvest mid of May (see Figure 6-18), which are not properly reproduced by RTM inversion, this lead to the very high prediction error of almost 40 % in this scene.

In this context the measurement errors associated with the sensor signal-to-noise ratio and atmospheric effects should also be mentioned as sensor intrinsic limitation (Combal et al., 2002b). The July 16, 2011 scene, for example, for which LAI retrieval accuracy is rather low, was partly influenced by haze and cirrus clouds, which could influence the TOC reflectances despite the conducted sensor calibrations and atmospheric corrections. However, no further analysis has been conducted in this direction. To sum up, it can be stated that several factors negatively influence the performance of physical LAI estimation, which would have to be addressed individually at differing stated of the procedure.

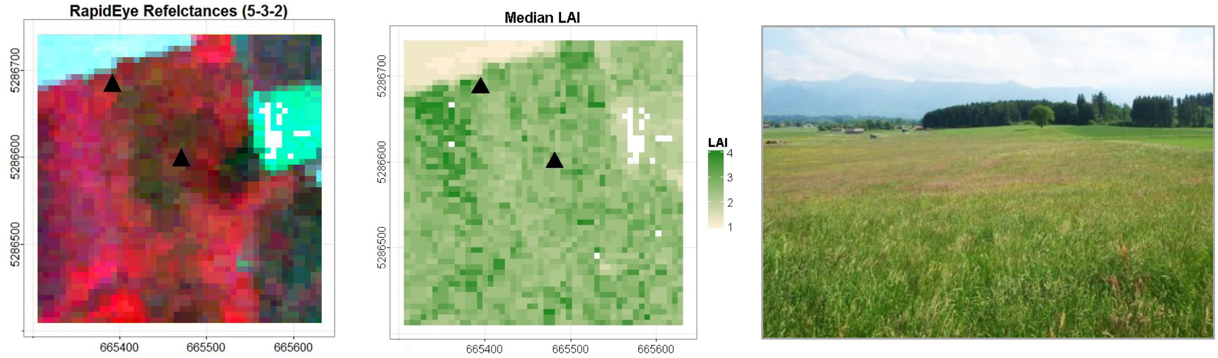

Figure 6-19: Example of grassland signal alteration during the blooming period. In the middle plot, the physically derived LAI map is shown, while the ▲ symbols mark two of the ESUs. In the left plot, the RapidEye data used as input for the inversion are displayed in a NIR-red-green false color composite. The photo on the right was taken on May 23, 2011 from the position of the upper left ESU and illustrates the canopy state during the RapidEye acquisition.

6.6.4. Derivation of a RapidEye LAI time series

The generation of 19 high spatial resolution LAI maps of the Ammer catchment for the years 2011 and 2012 enables the analysis of the temporal dynamics of individual grassland fields in the study region and the assessment of the temporal resolution of the RapidEye time series. Figure 6-20 shows the LAI time series (red signature) based on the available RapidEye scenes of a meadow at the TERENO Fendt site (47°49'58.48"N, 11° 3'38"E) in the Ammer catchment, which is mapped in the right-hand side inset map. At the Fendt station, a hemispherical camera was installed in the field to monitor the canopy development and especially LAI reduction due to mowing at a daily rate (star signature in the inset). As the camera had to be taken out of the meadow before mowing but was not always returned immediately afterwards, the timing of mowing can only be localized around several days of the year (DOY) in some cases. Additionally, *in situ* measurements were conducted at the Fendt site during the field campaigns.

The RapidEye time series match the LAI measured *in situ* on this plot relatively well, apart from the spring LAI in 2012. Some measurements covering the high density states just before mowing would be needed to derive an overall estimate on RapidEye LAI time series accuracy. With regard to the temporal variability of the plot, it can be seen that the sudden LAI reductions due to mowing are fairly well reproduced, although the last harvests of the season in September are never covered. One harvest in 2011 (around DOY 170) is not represented by the course of LAI derived from the RapidEye data available and also in 2012 one additional scene in the beginning of July would be necessary to differentiate between the second and third mowing. The growth and re-growth cycles of this meadow are thus sketched nicely to a

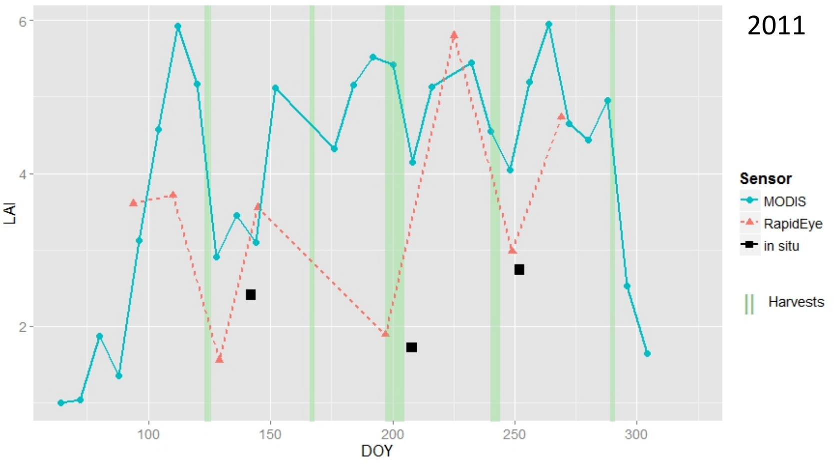

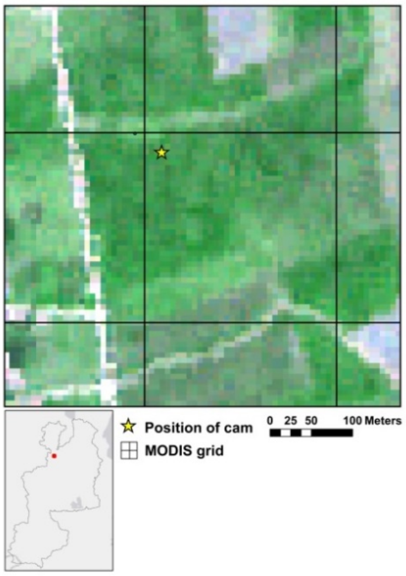

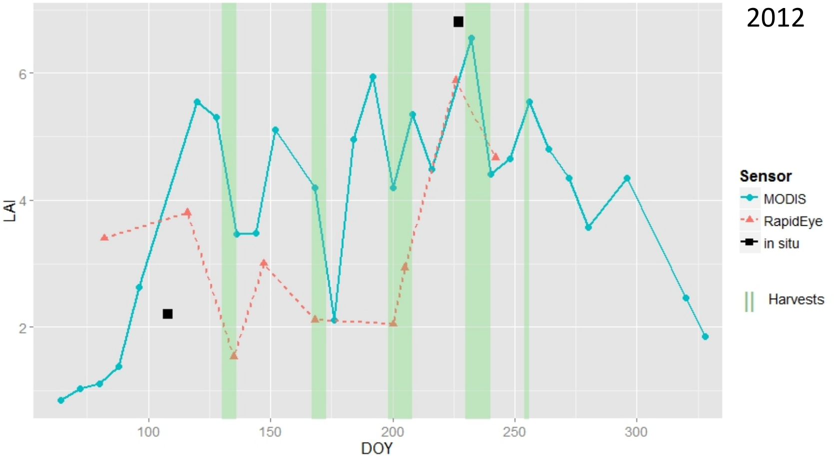

Figure 6-20: LAI time series at the Fendt station based on RapidEye and MODIS data. The phenological cycles of 2011 (above) and 2012 (below) are shown, while the map inset indicates the position of the camera as well as the selected MODIS pixel. The black ■ symbol represent LAI measured *in situ* at the site, while the stripes shaded in green depict the timing of mowing.

certain degree, but not completely reproduced. Further, Figure 6-20 shows that acquisitions earlier and later during the year would be needed to reproduce the LAI values prevailing during spring and autumn.

To further assess the quality of the RapidEye time series and for comparison with a coarser scale LAI product in this fragmented landscape, LAI time series based on MODIS data for the same area are shown. This time series were generated according to the algorithm described in Pasolli et al. (2011) at the Institute for Applied Remote Sensing at EURAC[23] based on daily MODIS Terra surface reflectance data (MOD09). The LAI time series was also derived using an LUT based PROSAIL inversion. To better capture the spatial detail, only the bands with the highest spatial resolution (red and NIR at 250 m resolution) are considered. Based on these, three VIs, namely the SR, NDVI and the EVI, were calculated and used as additional features for inversion. The preprocessing of the data consisted of an 8-day composite generation to reduce the occurrence of cloudy scenes. In being a regional LAI product, the data differ from the global MODIS LAI product (see chapter 2.3) in their higher spatial resolution and the regionally adapted model parameterization. Its improved performance with respect to standard LAI products was shown by Pasolli et al. (2011).

Nevertheless, the MODIS time series overestimates *in situ* as well as RapidEye LAI estimates in most cases. LAI reductions due to mowing are indicated by local minima, but the absolute minimum values are not reproduced. This is at least partially caused by the spatial heterogeneity within the MODIS pixel, which also includes a differently managed pasture as well as part of a maize field in the southern part. These reflectance contributions probably influence the non-linear estimation process of LAI (see e.g. Garrigues et al., 2006). Irrespective of this, the 8-day MODIS LAI time series reflects the temporal pattern of green-up and senescence and the sudden LAI reductions caused by mowing well. The slight deviations in the timing of the LAI reduction from the RapidEye data (see e.g. around DOY 200 in 2011, where high MODIS LAI is still provided while the RapidEye data already show a low LAI value) might be caused by the 8-day composite generation so that the indicated date does not necessarily reflect the day of acquisition for each pixel. Overall, this high frequency time series information could be used for the fitting of RapidEye or other high spatial resolution time series interpolation in future work.

6.7. Potential of physical modeling for RapidEye based LAI derivation

In this chapter, the potential of the PROSAIL model for the derivation of high spatial resolution grassland LAI was presented and evaluated. The model was adapted to a grassland ecosystem based on literature values, own field studies and a global sensitivity test. The resulting LAI maps provide detailed information on the spatial biomass distribution within the Ammer catchment as well as on intra-field LAI variability. The temporal dynamic of individual grassland parcels caused by management activities can also be monitored to a reasonable degree based on the RapidEye time series. The PROSAIL model proved to be an adequate RTM during model set-up due to the limited number of input parameters and its computational efficiency, and the chosen LUT inversion process allowed for testing and implementing a range of regularization techniques that aimed at stabilizing the procedure. The established LUTs for the different phenological phases can be further used to derive additional LAI maps for other years in the Ammer catchment or in similar grassland

---

[23] See at http://www.eurac.edu/en/research/institutes/remotesensing/default.html. Last access: June 19, 2014

landscapes in Central Europe as long as the local system geometries of the used RS scene are represented.

Overall, LAI maps could be derived from the individual RapidEye scenes using PROSAIL with an rRMSE of 20 - 40 %, which is comparable to the accuracies achieved in the few existing other grassland studies, which are, however, based on hyperspectral data measured *in situ* or air-borne and therefore of a theoretically higher quality. The most often neglected leaf angle estimates were also validated using field data, which revealed an underestimation of this parameter by the RTM inversion and stresses the importance of a regular evaluation of this highly influential canopy parameter.

Using multiple solutions during LUT inversion, a range of uncertainty measures was derived for each pixel. These quality layers provide spatial information on the physical LAI modeling procedure and were used on the one hand to identify grasslands areas for which LAI was estimated with a high reliability, and on the other hand to identify especially challenging cases, namely the mapping of extremely high and low LAI values. This information can be used for the improvement of shortcomings in the parameterization and inversion setup. However, it was also shown that both cases, i.e. over- and underestimation of LAI, are also partly caused not by modeling inadequacies but by highly unexceptional canopy occurrences such as blooming or plant litter on freshly harvested meadows. The uncertainty measures can further provide the basis for a backup procedure using empirical relationships or spatial interpolation in future work.

The implementation of physical LAI modeling involves a wide range of technical aspects. However, the importance and setting of these individual adjustment possibilities strongly depend on the ecosystem under investigation and the used data types and qualities (see e.g. Verrelst et al., 2014). With regard to these technical details, it was shown that some regularization methods, for example the newly introduced additional VI as an input feature, improved the inversion performance to a large extent. The use of a multiple solutions sample could also reduce the overall error in LAI modeling, and the identified sample size of 0.5 % of all LUT entries proved to be a good compromise between inversion robustness and model sensitivity to the spectral signal. The addition of simulated noise to the LUT reflectances did not significantly improve the modeling results in this study, but might well improve the LAI derivation robustness based on other data sets. Thus, in further studies the interactions of these optimized regularization techniques should be considered, and extended to the analysis of alternative cost functions, in order to further strengthen the RTM inversion.

LUT inversion proved to be useful and easily adaptable to such optimization tests as all regularization techniques, apart from the test for additional VIs, could be applied to the pre-computed LUTs. Furthermore, it delivers acceptable results and provides very valuable information on the inversion quality. Nevertheless, with regard to computational efficiency, the use of the LUT approach has to be questioned. The generation and inversion of LUTs is computationally very expensive, which is especially problematic when individual LUTs have to be generated for different system geometries. Hence, the wide parameterization resulting in a large number of LUT entries, the need to generate about 100 different LUTs per scene to account for topography, and the large amount of pixels (approximately 35 M) constituting the Ammer catchment, brought the LUT approach to its limits. To enable operational physical LAI modeling, a reduced pixel count would therefore be an option. In contrast to the high spatial resolution of the RapidEye data, simulated lower resolution data used in a preliminary study (Asam et al., in press) showed that with a spatial degradation to 20 m and 30 m resolution, thus Sentinel-2 or Landsat 8 type data, computation time was reduced by about 80 and 90 %, respectively. Alternatively, the use of ANN inversion could be tested, especially since the use of fixed observation geometries for LAI derivation under different viewing geometries has recently been successfully used (Duveiller et al., 2011b).

As this is the only LAI derivation study on a larger grassland area, i.e. heterogeneous and partly natural canopies with different phenological stages, it highlights the specific difficulties associated with physical LAI modeling in this ecosystem type. It is crucial to note that the canopy conditions of the managed alpine grasslands are very heterogeneous within one scene. Therefore, even though an individual meadow is spatially homogeneous and thus feasible to be characterized by an RTM, the LUT has to be generalized to all possibly prevailing conditions, which introduces uncertainties. Although this was aspired using a wide parameterization, the mismatch in simulated and measured reflectance data as well as the analysis of the LAI and LIDF output maps suggests that some parameterizations might need to be specified over even broader ranges. The parameterization of the RTM when working on grassland thus plays a crucial role. More *in situ* measurements of grassland canopy parameters and especially of reference spectra as well as the test of other parameter sampling schemes for parameterization are therefore suggested. Nevertheless, given the high spatio-temporal variability of this ecosystem, a significantly more specialized parameterization as it is used for crops cannot be applied. Instead, the implementation of further pixel-based regularization techniques such as two-step LUT inversions, or the use of first-guess values to reduce the LUT (e.g. based on chlorophyll-VIs empirical relationships, see Dorigo, 2007) could be further investigated for an improvement of LAI derivation in such a spectrally heterogeneous landscape.

The focus of this work lay on the derivation of the LAI. However, it was shown that using an RTM, LAI is always estimated in combination with and depending on a range of other biophysical parameters. Physical modeling is thus a comprehensive approach and enables an easy adaptation of the developed algorithm to other potential variables of interest. Not least due to this capacity, the use of RTM in RS vegetation analysis applications will likely increase over the next few years. On the one hand, approaches such as the ARTMO[24] tool box (Verrelst et al., 2011; Verrelst et al., 2012b) published during the last few years aim at automated modeling of leaf and canopy properties and will strongly promote the use of RTMs in the RS community. On the other hand, upcoming sensors with a sufficient spatial resolution for the analysis of small-scale landscapes will probably foster the use of such techniques. Their improved revisit times will enable the mapping of rapid changes in vegetation conditions due to phenology or management techniques. Additionally, the availability of further spectral bands in the NIR, as they are provided e.g. by the Sentinel-2 sensor, are very promising for improved physical LAI modeling as reflectance between 1000 nm and 1400 nm is highly sensitive to LAI (see chapter 6.2). Further, the improved radiometric qualities and refined techniques for the removal of atmospheric effects will most likely also reduce the inaccuracies introduced to RTM (Jacquemoud et al., 2009) by measurement errors and thus foster the development of improved physical modeling approaches.

---

[24] Online provided under http://ipl.uv.es/artmo/. Last access: June 16, 2014.

7. Synthesis on LAI derivation using high spatial resolution remote sensing data

The potential of high resolution RS data for grassland LAI derivation and associated optimization possibilities, which were evaluated over a heterogeneous alpine landscape, are of high interest for future automated LAI derivation procedures. A two year LAI time series, i.e. 19 LAI maps based on 20 RapidEye scenes, was generated using radiation transfer modeling, and six LAI maps were derived using an empirical-statistical method. In the following subchapters, the results of the modeling activities are synthesized with regard to the research questions and future research activities.

7.1. Assessment and comparison of empirical-statistical and physical LAI modeling

1) How does the selection of VIs and regression models impact the statistical modeling of LAI and how well can these models be transferred to other points in time?

Overall, LAI mapping accuracies of 70 - 90 % could be achieved for the six RapidEye scenes for which contemporaneous training data were available using empirical-statistical modeling, which is within the upper range of other statistical grassland LAI derivation studies. The systematic test of 25 VIs and four statistical model types revealed that the differences in regression strength between the VIs are, averaged for the individual RapidEye scenes, 2 - 30 times larger than the differences between the model types. The explanatory power of different VIs varied by 20 - 60 % for the individual models and field campaign data sets. This suggests that in this thesis the selection of a VI is more important for the establishment of a sound transfer function than the identification of the best mathematical model fit. Especially indices that employed RapidEye's red edge band strengthened the LAI-VI relationships and improved the LAI prediction, which was shown for the RapidEye bands based on a comprehensive model comparison. However, no clear conclusion on which VI to use can be drawn, as the respective best VI varied throughout the phenological season.

These seasonal differences in best performing VI and model type already indicated a limited temporal transferability of the regression models. Indeed, the modeling error proved to increase to 49 % on average when using a regression transfer function on RS data from different dates. The combined use of several data sets to create a regression which is used for LAI derivation at a different time step reduces this LAI estimation error to 30 - 35 % on average. Thus, reduced *in situ* LAI measurement labor comes at the cost of LAI time series error rates being increased by 10 - 30 % as long as at least two campaigns are conducted. These analyses indicate that a model calibration phase, i.e. the testing and identification of a best fitting combination of mathematical model and VI, is also necessary for empirical-statistical LAI modeling. Further, the approach is not suitable for automated derivation of LAI time series if LAI accuracies higher than 50 % are to be achieved.

In this context it was also shown that not only the selected VI and statistical model potentially influence the LAI estimation, but that also the techniques applied in the field sampling instrument, in this study the Miller and Lang algorithms applied on a differing number of directional light transmittance measurements, can strongly influenced the LAI measured *in situ* (see chapter 4.3.2). Thus, in order to achieve highly accurate and reliable LAI products, further efforts must also be put into the improvement of *in situ* LAI measurement techniques, in measurement standards which also comprehend suggestions with regard to the derivation algorithms used in these techniques to ensure their comparability, and in the establishment of continuously monitored validation sites. Being used for validation purposes, LAI *in situ* measurements must also meet and at best fall below the 10 % error rate. The continuous calibration of indirect LAI measurements as well as the improvement of conventional measurement techniques and instruments are hence necessary.

2) Which RTM settings are most relevant for establishing an adapted and robust LAI derivation procedure, and which grassland specific limitations occur during inversion?

As LAI derivation using multispectral RS data is an ill-posed problem and thus unstable, special interest lies in assessing the improvements that can be achieved through model settings and inversion regularization techniques. A global sensitivity analysis, the EFAST approach, was applied to PROSAIL over the 400 - 2500 nm spectrum as well as on the simulated RapidEye bands and selected VIs in order to identify the most important model parameters and most sensitive spectral features. The results of this analysis are plausible but in parts different from other SAs. Therefore, further research should be based on the gained results in order to achieve a comparison with an identical model setting and to evaluate the EFAST approach and PROSAIL parameter importance over the relevant spectral range. Based on these results, in a next step several techniques for increasing the robustness of the approach, namely the use of a multiple sample solution, the selection of the statistical measure of central tendency, the use of VIs as additional features, and synthetic noise, were tested. The upper part of Table 7-1 summarizes the achieved improvements by indicating the range of RMSE that resulted from the different model inversion settings. The selection of an ideal multiple solution sample size as well as of a suitable additional spectral feature reduced the average RMSE by up to 0.5. The influence of added noise and the selection of either statistical measure (mean or median) was however not relevant for LAI modeling in this study.

Despite the optimized model settings reduced the overall modeling error, notable differences in LAI estimation accuracy were still found for the different scenes. While in the best case (September 6), LAI is estimated with an RMSE of 0.66, the worst LAI estimates are modeled with an RMSE of 1.14 in the July 16 scene (see middle part of Table 7-1). These differences could result either from the only model setting which was variable for the different scenes – the PROSAIL parameter ranges– or from the remotely sensed reflectances, assuming that the

LAI measured *in situ* represents the true LAI. Although the question which of these aspects caused these large differences cannot be conclusively answered without contemporaneous *in situ* spectroradiometer reflectance measurements for each scene, the observed spectral mismatches between the simulated and measured reflectances (see chapter 6.6.1) could give an indication. Indeed, this misfit does not vary considerably between the different scenes (see Figure A-4 and the lower part of Table 7-1), although the seasonally adapted model parameterization changed between time steps. The model parameterization always seems to miss the observed spectral at the same degree. Also with regard to the LAI value distributions observed for the different scenes, no consistent relationship to the modeling accuracy could be observed, as the LAI in the three worst scenes with an rRMSE above 30 % exhibit normal, left-skewed, and bimodal distributions (see Table 6-4 and Figure A-8). Thus, the differences in model accuracy are probably caused by characteristics of the individual RapidEye scenes. This can on the one hand include errors associated with the sensors signal-to-noise ratio and atmospheric effects, i.e. the radiometric quality of the RapidEye imagery. The July 16 scene, for example, was partly influenced by haze and cirrus clouds, which could influence the TOC reflectances despite the conducted sensor calibrations and atmospheric corrections. On the other hand, unexpected canopy occurrences such as dense predominantly erectophile, blooming, or freshly mown canopies and their associated reflectances are challenging. It can hence be concluded that these influences on the RS spectra are relatively larger than the influence of the regularization techniques, and that sound RS data preprocessing is crucial for successful LAI estimation. Alternatively, a coupled soil-leaf-canopy-atmosphere model such as the one used in Laurent et al. (2011) might improve the data quality. Applying any necessary topographic and geometric correction on the resulting LAI map only might also reduce these problems.

The EFAST analysis indicated the high relevance of other PROSAIL parameters in addition to LAI, namely the LIDF, C_{ab}, and soil *bf* parameters. This is why in this thesis another emphasis was on the analysis and validation of these physically derived vegetation parameters, and on radiation transfer modeling uncertainty measures, which are only seldom assessed in the literature. Several indicators for impaired physical LAI estimation have been presented, such as high RMSE and LAI variances within the multiple solution sample, or improbable low LIDF and C_{ab} estimates. The mapping of these measures indicated an increased modeling uncertainty for extremely high and low LAI values, most probably due to an insufficiently wide model parameterization. Further, it was shown that canopy

Table 7-1: Overview of error ranges associated to regularization techniques (top), LAI modeling (middle), and the match between modeled and measured spectra (bottom).

	Range of RMSEs
Use of different no. solution samples	0.50*
Use of mean or median	0.03*
Use of additional VIs	0.29*
Use of noise	0.02*
Estimation error for individual scenes using the same model settings	0.48
Overall match of simulated and measured spectra for each scene	0.01

* mean over all tested scenes

occurrences which deviate strongly from model assumptions, e.g. blooming, canopy gaps, and large amounts of litter on the meadows are problematic for LAI modeling of grasslands. Thus, parameterization of the RTM with regard to the phenological phase constitutes an important but very sensitive procedure when working on grassland.

3) Which of the empirical-statistical and physical LAI modeling approaches is more appropriate for grassland LAI derivation?

After adapting both approaches to the sensor and to the canopy and terrain conditions of the area, the results of the inverted PROSAIL model are compared against the best performing regression models. Table 5-2 and Table 6-4 show the R^2, RMSE, and rRMSE values of the six LAI maps for which contemporaneous validation data were available using statistical and physical models. For nearly all scenes, the statistical models based on *in situ* measurements perform better than the physical approach. However, the differences between these result varies among the different scenes. For the May 9, July 16, and September 6 scenes the differences in rRMSE are below 4 %, which indicates the high potential of the physical LAI derivation approach for all vegetation states during the phenological cycle. For the May 25 and August 13 scenes the PROSAIL approach achieves 10.4 % and 17.1 % less accuracy than the statistical approach. As was outlined above, LAI derivation in the May 25 scene was confronted with two specific problems, namely freshly mown meadows as well as dense and blooming meadows. Both effects, overestimation and underestimation of LAI, were less pronounced for the statistically derived LAI of this scene, as here the time specific regression captures these systematic offsets better. The signal degradation due to blooming and a high amount or erected grasses was obviously not that influential as in the inverted RTM, probably as the most strongly affected green band is not used in the applied VI. Very low LAI values could also be well reproduced using a quadratic polynomial model. The RTM results of the August 13 scene show a strong negative bias, which might be caused by an unfitting model parameterization for this point in time. The accuracy of the statistically derived LAI from the April 25 scene is more than 40 % higher than the RTM result. Obviously, the modeling of such early vegetation stages is challenging, while empirical regression models can better adapt to the exceptional vegetation signals resulting from large shares of senescent leaf material and freshly sprouting grasses. Thus, overall a higher LAI prediction accuracy can be reported for the empirical-statistical approach, which decreases to only little above 50 %, however, if no contemporaneous field data are available and a model trained on another data set has to be used.

With regard to the resulting LAI maps, the same subset as used in chapters 5 and 6 is used here to illustrate differences in spatial distribution of estimated LAI for the September 6, 2011 scene (see Figure 7-1). The pattern of low and high LAI values is consistent in both maps, but the empirical-statistically derived LAI is lower overall and shows much more nuances. In the RTM based LAI map, all densely vegetated fields seem to have a similar LAI value, but only few medium LAI areas occur. In the statistically derived map, fields of medium high LAI dominate in the middle and southern parts, while only few very high LAI areas occur, e.g. in the south-western part of the map. These are the same areas which were identified as affected by saturation in the RTM map (see Figure 6-16, bottom left plot). Thus, while the regression model scatter plots (Figure 5-1) indicated signal saturation in the summer scenes, it becomes clear in this comparison that the “artificial” saturation effect (see chapter 6.6.1) introduced by RTM modeling even outranges such reduced sensitivities. Hence, it can be concluded that, apart from the overall accuracy of the derived LAI maps, the

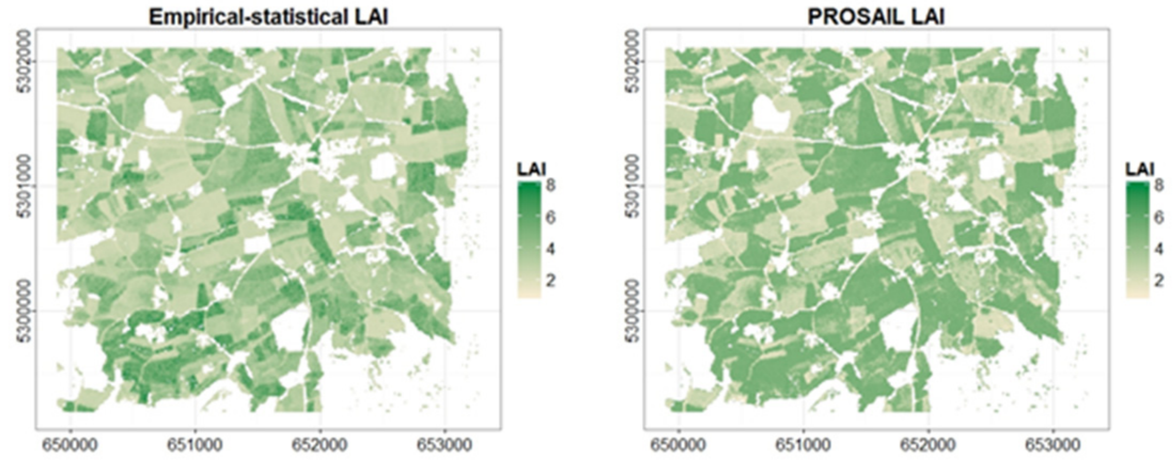

Figure 7-1: Maps of the statistically (left) and physically (right) derived LAI, showing a subset of the September 6 scene.

regression modeling approach better capture gradual LAI variability and better reproduce extreme values.

Only few studies exist in which these two approaches, their LAI derivation accuracies and the derived maps, are systematically compared, and none have been performed for grasslands. Only Vuolo et al. (2010) briefly present LAI derivation results for crops at one point in time, which achieve higher accuracies with an LUT inversion approach compared to empirical relationships. As this is a very sparse reference data base, the representativeness of this comparison is difficult to assess, and further studies would be desirable. However, apart from the absolute accuracy and plausibility of the derived LAI, the two modeling approaches can be compared based on a range of other aspects (see Table 7-2). With regard to computational effort and time expenditure, the statistical approach performs much better, as it is computationally less demanding, whilst running the PROSAIL model as well as its inversion cannot be conducted in near real-time for this spatial resolution and topographic conditions (see below). Conversely, the RTM approach is superior to the statistical approach with regard to the delivery of more than one useful biophysical variable. Further, for the RTM based LAI maps pixel-wise uncertainty measures could be derived, while for the statistically derived LAI only one global model coefficient is available.

Table 7-2: Quantitative and qualitative comparison of the two LAI derivation methods.

	Empirical-statistical	PROSAIL
Average accuracy		
With date specific field data	80 %	-
Without date specific field data	51 %	70 %
Computing time	Minutes	Weeks
Derivation of other plant canopy properties except LAI	No	Yes
Generation of pixel-wise uncertainty measures	No	Yes

The selection of one of the two LAI derivation approaches ultimately depends on the purpose of the derived grassland LAI information. To assess the spatial variability of LAI at a single point in time, a statistical regression model optimized with regard to the used mathematical model and VI would be the choice. If the aim is automated LAI derivation, especially if an assimilation of the data in a land surface process model is aspired, the independence from field data and the associated quality flag might compensate for approximately 10 % lower prediction accuracy.

7.2. Potential and limitations of high resolution data for grassland LAI derivation

4) Does the use of high spatial resolution remote sensing data for LAI derivation involve specific advantages and limitations?

In this thesis, with RapidEye high spatial resolution multispectral RS data were used to derive LAI of spatially and temporally very variable grasslands over a medium size catchment and topographically demanding area. In this context, the high spatial resolution of the RapidEye data enabled a reliable land cover classification with a low number of spectrally mixed pixels in each class, and thus a reduced LAI mapping error due to misclassifications or pixel impurity (Dorigo et al., 2009). The high spatial resolution SRTM DEM also provided valuable information necessary for the calculation of the local system geometries in the partly mountainous landscape and thus reduced errors introduced by the use of wrong local system geometries. However, in case of missing system geometry information, e.g. when using topographically uncorrected RS data in the empirical-statistical approach, or also in case of pixel impurity due to canopy gaps, shadows or foreign objects, such high spatial resolution data potentially show strong deviations in reflectance values. These high contrasts in local reflectances, which are not balanced by the surrounding surface reflectances, can lead to unexpected behavior of the LAI derivation algorithm.

With regard to RTM inversion, it has been reported in the literature that coarse spatial resolution can introduce a bias on LAI estimation due to the invalid assumption of spatially homogeneous pixels, and thus high spatial resolution data should be preferred (Garrigues et al., 2006; González-Sanpedro et al.; Duveiller et al., 2011a). Indeed, the use of RapidEye pixels being smaller than individual fields enabled RTM inversion over homogeneous canopies in most cases, besides the above mentioned disturbances. Widlowski et al. (2005), however, argue that turbid medium models are rather suitable for coarse resolution data especially in the face of clumped canopies or canopy gaps. In these cases, boundary effects would reduce the accuracy of low LAI estimates, as it was shown in this thesis for intensively grazed pastures. This overestimation error due to canopy gaps, for example, is reduced when using data with a spatial resolution of 20 or 30 m (Asam et al., in press). Thus, the optimal spatial resolution with regard to modeling accuracy depends on the landscape structure and the canopy homogeneity, and would need to be systematically analyzed over areas of different levels of heterogeneity. For the study site analyzed in this thesis, the preliminary analysis (Asam et al., in press) indicated that LAI estimation did not deteriorate significantly with a reduced pixel size of 20 - 50 m. Instead, the LAI estimation accuracy was stable around an RMSE of 0.9 averaged over four different scenes, as long as individual fields with a homogeneous structure could still be identified. The proposed model regularization techniques could also be applied regardless of a specific data type or spatial resolution. This reduced spatial resolution further enabled a considerable acceleration of the LAI map derivation. The computing time thus plays an important role for the evaluation of a suitable spatial resolution. This time constraint might also be the restraining factor for the use of very high spatial resolution imagery such as from the IKONOS or Quickbird sensors for LAI derivation on a landscape scale, next to the reduced spectral resolution, i.e. a missing red edge band, of some of these sensors.

7.3. Outlook

RTMs are nowadays used to produce spatially and temporally continuous fields of LAI for environmental monitoring or to be integrated into process models, as this information cannot be provided routinely based on empirical-statistical methods with the required high accuracy. To develop routines based on RTMs, a robust and automated LAI deviation has been a prominent objective in the RS community for decades (Baret and Buis, 2008; Verrelst et al., 2014). However, the large scale mapping of other biophysical leaf and canopy parameters such as chlorophyll, water content, dry matter content, biomass, and fPAR using RTMs also developed during the last few years for purposes such as yield estimation, pest control, or forest fire risk assessment (Jacquemoud et al., 2009). Apart from these classical applications in vegetation monitoring, RTMs are also increasingly used for other purposes such as radiometric accuracy assessments (Vermote et al., 2014) or crop classification (Klug et al., 2014), so that their use and importance will probably increase over the next few years.

Nevertheless, with regard to LAI derivation, and especially with regard to grassland LAI derivation, the aspired target accuracy of 10 % required by GCOS (2006) has not yet been met with the exception of a few local studies on crop LAI mapping. Hence, efforts will be continuously directed towards this parameter, and should increasingly focus on natural and semi-natural ecosystems. In this context, it is of practical relevance that the LUT algorithm proposed in this thesis is not defined to specific RS data and can be easily extended to other sensors.

The Landsat 8 and the upcoming Sentinel-2 sensors will constitute a valuable basis for the development of algorithms, due to their improved temporal and spatial resolutions, which qualifies these sensors for an improved ecosystem monitoring (Drusch et al., 2012). The topographic and BRDF correction proposed for Sentinel-2 will probably also provide a high radiometric quality and reduce the need for multiple directional simulations (Gascon and Colin, 2014). However, apart from these properties, the improved spectral resolution, namely additional bands in the red edge, NIR, and SWIR spectral domains, is also expected to improve LAI modeling (Dorigo, 2007). As can be seen from the SA performed in chapter 6.2.2, these wavelengths are especially sensitive to LAI variations, which is why their use might increase the stability of RTM inversions.

Apart from the data type used in this thesis, several other RS data are already being used in the radiation transfer modeling context and might contribute to LAI derivation in the future. Due to the anisotropic behavior of vegetation canopies, which is largely influenced by its structure (see chapter 2.2.1), multi-angular RS data are able to capture such structural information. The use of multi-angular observations increases the dimensionality of the inversion problem (Martonchik et al., 2000; Kimes et al., 2002; Dorigo, 2007; Lavergne et al., 2007; Verhoef, 2007; Wang et al., 2013). Furthermore, laser scanning, radar detection, and microwave RS contribute to enhanced estimation of canopy structure elements (Hyyppä et al., 2000; Koetz et al., 2007b). As mentioned above, hyperspectral data also raise the dimensionality of the inversion problem, and have been increasingly used as an input to RTM inversion (Jacquemoud et al., 2000; Fernandes et al., 2004; Kötz et al., 2004; Meroni et al., 2004; Zarco-Tejada et al., 2004; Schlerf and Atzberger, 2006; Verhoef, 2007; Ustin et al., 2009). However, these studies aim rather at the identification of optimal spectral resolution settings than at automated LAI derivation.

The combined use of different data sets and data types is hence a promising approach to LAI estimation (Dorigo, 2007; Liang, 2008). This could either be achieved by automatically using additional RS data for restricting the LUT (e.g. deriving information on structural parameters from radar or LIDAR data), or by building a spectral data base that contains spectra simulated under several system geometries which is then inverted against contemporaneous mono- as well as multi-angular data. These approaches of integrating independent information sources are also the only means to overcome the saturation problem inherent in solar-reflective RS. Finally, the automated derivation of spatially and temporally continuous LAI might even be based on ensembles of LAI algorithms and RS input data (Baret et al., 2013).

References

Abuelgasim, A.A., Gopal, S., & Strahler, A.H. (1998): Forward and inverse modelling of canopy directional reflectance using a neural network. *International Journal of Remote Sensing 19* (3), 453–471.

Ahmad, S.P., & Deering, D.W. (1992): A simple analytical function for bidirectional reflectance. *Journal of Geophysical Research 97* (D17), 18867–18886.

Allen, M.T., Prusinkiewicz, P., & DeJong, T.M. (2005): Using L-systems for modeling source-sink interactions, architecture and physiology of growing trees: the L-PEACH model. *New Phytologist 166* (3), 869–880.

Allen, R.G., Pereira, L.S., Raes, D., & Smith, M. (2000): *Crop evapotranspiration. Guidelines for computing crop water requirements.* FAO irrigation and drainage paper *56*. Rome. FAO.

Allen, W.A., Gayle, T.V., & Richardson, A.J. (1970): Plant-canopy irradiance specified by the Duntley equations. *Journal of the Optical Society of America 60* (3), 372–376.

Allen, W.A., & Richardson, A.J. (1968): Interaction of light with a plant canopy *58* (8), 1023–1028.

Andrieu, B. (1997): Evaluation of an improved version of SAIL model for simulating bidirectional reflectance of sugar beet canopies. *Remote Sensing of Environment 60* (3), 247–257.

Asam, S., Fabritius, H., Klein, D., Conrad, C., & Dech, S. (2013): Derivation of leaf area index for grassland within alpine upland using multi-temporal RapidEye data. *International Journal of Remote Sensing 34* (23), 8628–8652.

Asam, S., Pasolli, L., Notarnicola, C., & Klein, D. (in press): Comparison of leaf area indices for grasslands within the alpine uplands based on multi-scale satellite data time series and radiation transfer modeling. In *7th International Workshop on the Analysis of Multi-Temporal Remote Sensing Images (MultiTemp), 2013*.

Asner, G.P. (1998): Biophysical and biochemical sources of variability in canopy reflectance. *Remote Sensing of Environment 64* (3), 234–253.

Asner, G.P., Wessman, C.A., Bateson, C., & Privette, J.L. (2000): Impact of tissue, canopy, and landscape factors on the hyperspectral reflectance variability of arid ecosystems. *Remote Sensing of Environment 74* (1), 69–84.

Asrar, G. (Ed.) (1989): Theory and applications of optical remote sensing. New York. Wiley.

Asrar, G., Kanemasu, E., Miller, G., & Weiser, R. (1986): Light interception and leaf area estimates from measurements of grass canopy reflectance. *IEEE Transactions on Geoscience and Remote Sensing 24* (1), 76–82.

Atzberger, C. (2000): Development of an invertible forest reflectance model: The INFOR-Model. In M.F. Buchroithner (Ed.), *A decade of trans-European remote sensing cooperation. Proceedings of the 20th EARSeL Symposium* (pp. 39–44).

Atzberger, C. (2004): Object-based retrieval of biophysical canopy variables using artificial neural nets and radiative transfer models. *Remote Sensing of Environment 93* (1-2), 53–67.

Atzberger, C. (2010): Inverting the PROSAIL canopy reflectance model using neural nets trained on streamlined databases. *Journal of Spectral Imaging 1* (1), 1–13.

Atzberger, C. (2013): Advances in remote sensing of agriculture: Context description, existing operational monitoring systems and major information needs. *Remote Sensing 5* (2), 949–981.

Atzberger, C., Guérif, M., Baret, F., & Werner, W. (2010): Comparative analysis of three chemometric techniques for the spectroradiometric assessment of canopy chlorophyll content in winter wheat. *Computers and Electronics in Agriculture 73* (2), 165–173.

Atzberger, C., Jarmer, T., Kötz, B., Schlerf, M., & Werner, W. (2003a): Spectroradiometric determination of wheat bio-physical variables. Comparison of different empirical-statistical approaches. In R. Goossens (Ed.), *Remote sensing in transition. Proceedings of the 23rd Symposium of the European Association of Remote Sensing Laboratories, Ghent, Belgium, June 2 - 5*. Rotterdam. Millpress.

Atzberger, C., Jarmer, T., Schlerf, M., Koetz, B., & Werner, W. (2003b): Retrieval of wheat biophysical attributes from hyperspectral data and SAILH+PROSPECT radiative transfer model. In *Proceedings of the 3rd EARSeL Workshop on imaging spectroscopy* (pp. 473–482).

Atzberger, C., & Richter, K. (2012): Spatially constrained inversion of radiative transfer models for improved LAI mapping from future Sentinel-2 imagery. *Remote Sensing of Environment 120,* 208–218.

Bacour, C. (2002): Design and analysis of numerical experiments to compare four canopy reflectance models. *Remote Sensing of Environment 79* (1), 72–83.

Bacour, C., Baret, F., Béal, D., Weiss, M., & Pavageau, K. (2006): Neural network estimation of LAI, fAPAR, fCover and LAI×Cab, from top of canopy MERIS reflectance data: Principles and validation. *Remote Sensing of Environment 105* (4), 313–325.

Bacour, C., Baret, F., & Jacquemoud, S. (2002a): Information content of HyMap hyperspectral imagery. In *Proceedings of the 1st International Symposium on Recent Advances in Quantitative Remote Sensing* (pp. 503–508).

Bacour, C., Jacquemoud, S., Leroy, M., Hautecoeur, O., Weiss, M., Prévot, L., Bruguier, N., & Chauki, H. (2002b): Reliability of the estimation of vegetation characteristics by inversion of three canopy reflectance models on airborne POLDER data. *Agronomie 22* (6), 555–565.

Bacour, C., Jacquemoud, S., Vogt, P., Hosgood, B., Andreoli, G., & Frangi, J.P. (2001): Optimal sampling configurations for the estimation of canopy properties from BRDF data acquired with the EGO/JRC. In *Proc. 8th International Symposium Physical Measurements & Signatures in Remote Sensing* (pp. 481–486).

Balthasar, K., Geissler, P., Heissbauer, H., Jungk, G., Müller, M., Pinsl, L., & Teichmüller, M. (1975): *Die oberbayerische Pechkohle*. Geologica Bavarica *73*. München.

Baranoski, G.V., & Rokne, J.G. (1997): An algorithmic reflectance and transmittance model for plant tissue. *Computer Graphics Forum 16* (3), 141–150.

Barclay, H., & Trofymow, J. (2000): Relationship of readings from the LI-COR canopy analyzer to total one-sided leaf area index and stand structure in immature Douglas-fir. *Forest Ecology and Management 132* (2-3), 121–126.

Barclay, H., Trofymow, J., & Leach, R. (2000): Assessing bias from boles in calculating leaf area index in immature Douglas-fir with the LI-COR canopy analyzer. *Agricultural and Forest Meteorology 100* (2-3), 255–260.

Baret, F. (2010): Biophysical vegetation variables retrieval from remote sensing observations. *Proc. SPIE 7824,* 17–19.

Baret, F., Bacour, C., Béal, D., Weiss, M., Berthelot, B., & Regner, P. (2006): Algorithm theoretical basis document for MERIS top of canopy land products (TOC_VEG). Online available at: http://www.brockmann-consult.de/beam/software/repositories/4.6/beam-meris-veg-2.0.1/docs/MERIS_ATBD_TOA_VEG_03_06.pdf.

Baret, F., & Buis, S. (2008): Estimating canopy characteristics from remote sensing observations. Review of methods and associated problems. In S. Liang (Ed.), *Advances in Land Remote Sensing: System, Modeling, Inversion and Application*. Springer.

Baret, F., Clevers, J., & Steven, M. (1995): The robustness of canopy gap fraction estimates from red and near-infrared reflectances: A comparison of approaches. *Remote Sensing of*

Environment 54 (2), 141–151.

Baret, F., & Fourty, T. (1997): Estimation of leaf water content and specific leaf weight from reflectance and transmittance measurements. *Agronomie 17* (9-10), 455–464.

Baret, F., & Guyot, G. (1991): Potentials and limits of vegetation indices for LAI and APAR assessment. *Remote Sensing of Environment 35* (2-3), 161–173.

Baret, F., Guyot, G., & Major, D. (1989): TSAVI: A vegetation index which minimizes soil brightness effects on LAI and APAR estimation. In *12th Canadian Symposium on Remote Sensing Geoscience and Remote Sensing Symposium* (pp. 1355–1358). New York. IEEE.

Baret, F., Hagolle, O., Geiger, B., Bicheron, P., Miras, B., Huc, M., Berthelot, B., Niño, F., Weiss, M., Samain, O., Roujean, J.L., & Leroy, M. (2007): LAI, fAPAR and fCover CYCLOPES global products derived from VEGETATION. *Remote Sensing of Environment 110* (3), 275–286.

Baret, F., Jacquemoud, S., Guyot, G., & Leprieur, C. (1992): Modeled analysis of the biophysical nature of spectral shifts and comparison with information content of broad bands. *Remote Sensing of Environment 41* (2-3), 133–142.

Baret, F., Makhmara, H., Lacaze, R., & Smets, B. (2010a): BioPar product user manual. LAI, FAPAR, FCover, NDVI Version 1 from SPOT/VEGETATION data. Online available at: http://web.vgt.vito.be/documents/BioPar/g2-BP-RP-BP053-ProductUserManual-LAIFAPARFCoverNDVIV1.pdf.

Baret, F., Solan, B. de, Lopez-Lozano, R., Ma, K., & Weiss, M. (2010b): GAI estimates of row crops from downward looking digital photos taken perpendicular to rows at 57.5° zenith angle: Theoretical considerations based on 3D architecture models and application to wheat crops. *Agricultural and Forest Meteorology 150* (11), 1393–1401.

Baret, F., Weiss, M., Allard, D., Garrigues, S., Leroy, M., Jeanjean, H., Fernandes, R., Myneni, R., Privette, J., Morisette, J., Bohbot, H., Bosseno, R., Dedieu, G., Bella, C., Duchemin, B., Espana, M., Gond, V., Gu, X.F., Guyon, D., Lelong, C., Maisongrande, P., Mougin, E., Nilson, T., Veroustraete, F., & Vintilla, R. (2003): VALERI: a network of sites and a methodology for the validation of medium spatial resolution land satellite products. Online available at: http://www.avignon.inra.fr/valeri/.

Baret, F., Weiss, M., Lacaze, R., Camacho-de Coca, F., Makhmara, H., Pacholcyzk, P., & Smets, B. (2013): GEOV1: LAI and FAPAR essential climate variables and FCOVER global time series capitalizing over existing products. Part1: Principles of development and production. *Remote Sensing of Environment 137,* 299–309.

Bauer, D.F. (1972): Constructing confidence sets using rank statistics. *Journal of the American Statistical Association 67* (339), 687–690.

Bayerisches Landesamt für Statistik und Datenverarbeitung (2013a): Statistik kommunal 2012. Eine Auswahl wichtiger statistischer Daten für den Landkreis Weilheim-Schongau. Online available at: https://www.statistik.bayern.de/.

Bayerisches Landesamt für Statistik und Datenverarbeitung (2013b): Statistik kommunal 2012. Eine Auswahl wichtiger statistischer Daten für den Landkreis Garmisch-Partenkirchen. Online available at: https://www.statistik.bayern.de/.

Bayerisches Landesamt für Statistik und Datenverarbeitung (2013c): Statistik kommunal 2012. Eine Auswahl wichtiger statistischer Daten Bayern. Bayerisches Landesamt für Statistik und Datenverarbeitung. Online available at: https://www.statistik.bayern.de/.

Bayerisches Staatsministerium für Wirtschaft und Medien Energie und Technologie (2013): Bayerns Wirtschaft in Zahlen 2013. Online available at: http://www.stmwi.bayern.de/fileadmin/user_upload/stmwivt/Publikationen/2013/BayernsWirtschaft_in_Zahlen_2013_deutsch.pdf.

Beale, R., & Jackson, T. (1998): *Neural computing. An introduction.* Bristol. Inst. of Physics Publ.

Becker, A., Körner, C., Brun, J.-J., Guisan, A., & Tappeiner, U. (2007): Ecological and land use studies along elevational gradients. *Mountain Research and Development 27* (1), 58–65.

Bégué, A. (1992): Modeling hemispherical and directional radiative fluxes in regular-clumped canopies. *Remote Sensing of Environment 40* (3), 219–230.

Béland, M., Widlowski, J.-L., Fournier, R.A., Côté, J.-F., & Verstraete, M.M. (2011): Estimating leaf area distribution in savanna trees from terrestrial LiDAR measurements. *Agricultural and Forest Meteorology 151* (9), 1252–1266.

Bengsch, L., & Neumann, A. (2013): Wirtschaftsfaktor Tourismus im Landkreis Garmisch-Partenkirchen (Zugspitz-Region) 2012. München. Online available at: http://www.kreisentwicklungsgesellschaft.de/media/files/tourismus/Wirtschaftsfaktor_Tourismus_Zugspitz-Region_Garmisch-Partenkirchen_2012.pdf.

Beniston, M. (2005): Mountain climates and climatic change: An overview of processes focusing on the European Alps. *Pure and Applied Geophysics 162* (8-9), 1587–1606.

Berk, A., Anderson, G.P., Acharya, P.K., & Shettle, E. (2008): MODTRAN 5.2.0.0 User's Manual. Spectral Sciences Inc., Burlington MA, Air Force Research Laboratory. Hanscom MA.

Berterretche, M., Hudak, A.T., Cohen, W.B., Maiersperger, T.K., Gower, S.T., & Dungan, J. (2005): Comparison of regression and geostatistical methods for mapping Leaf Area Index (LAI) with Landsat ETM+ data over a boreal forest. *Remote Sensing of Environment 96* (1), 49–61.

BfN (2014): The High Nature Value farmland indicator in Germany. Online available at: http://www.bfn.de/0315_hnv+M52087573ab0.html.

Bicheron, P., & Leroy, M. (1999): A method of biophysical parameter retrieval at global scale by inversion of a vegetation reflectance model. *Remote Sensing of Environment 67* (3), 251–266.

Bittner, S., Gayler, S., Biernath, C., Winkler, J.B., Seifert, S., Pretzsch, H., & Priesack, E. (2012): Evaluation of a ray-tracing canopy light model based on terrestrial laser scans. *Canadian Journal of Remote Sensing 38* (5), 619–628.

Black, T.A., Chen, J.M., Lee, X., & Sagar, R.M. (1991): Characteristics of shortwave and longwave irradiances under a Douglas-fir forest stand. *Canadian Journal of Forest Research 21* (7), 1020–1028.

BlackBridge (2012): Spectral response curves of the RapidEye sensor. BlackBridge. Online available at: http://blackbridge.com/rapideye/upload/Spectral_Response_Curves.pdf.

Bogena, H., Puetz, T., Vereecken, H., Kruger, E., Zacharias, S., Dietrich, P., Wollschlager, U., Kunstmann, H., Papen, H., Schmid, H.P., Munch, J.C., Priesack, E., Schwank, M., Bens, O., Brauer, A., Borg, E., & Hajnsek, I. (2012): TERENO - Long-term monitoring network for terrestrial environmental research. *Hydrologie und Wasserbewirtschaftung 56* (3), 138–143.

Bolstad, P.V., & Gower, S.T. (1990): Estimation of leaf area index in fourteen southern Wisconsin forest stands using a portable radiometer. *Tree Physiology 7* (1-4), 115–124.

Bonan, G.B. (1993): Importance of leaf area index and forest type when estimating photosynthesis in boreal forests. *Remote Sensing of Environment 43* (3), 303–314.

Bonan, G.B. (1995): Land-atmosphere CO 2 exchange simulated by a land surface process model coupled to an atmospheric general circulation model. *Journal of Geophysical Research 100* (D2), 2817–2831.

Bonan, G.B. (1997): Effects of land use on the climate of the United States. *Climatic Change 37* (3), 449–486.

Borel, C.C., Gerstl, S.A., & Powers, B.J. (1991): The radiosity method in optical remote sensing of structured 3-D surfaces. *Remote Sensing of Environment 36* (1), 13–44.

Borra, S., & Di Ciaccio, A. (2010): Measuring the prediction error. A comparison of cross-validation, bootstrap and covariance penalty methods. *Computational Statistics & Data*

Analysis 54 (12), 2976–2989.

Bousquet, L., Lachérade, S., Jacquemoud, S., & Moya, I. (2005): Leaf BRDF measurements and model for specular and diffuse components differentiation. *Remote Sensing of Environment 98* (2-3), 201–211.

Bowyer, P., & Danson, F. (2004): Sensitivity of spectral reflectance to variation in live fuel moisture content at leaf and canopy level. *Remote Sensing of Environment 92* (3), 297–308.

Brantley, S.T., Zinnert, J.C., & Young, D.R. (2011): Application of hyperspectral vegetation indices to detect variations in high leaf area index temperate shrub thicket canopies. *Remote Sensing of Environment 115* (2), 514–523.

Bréda, N. (2003): Ground-based measurements of leaf area index: a review of methods, instruments and current controversies. *Journal of Experimental Botany 54* (392), 2403–2417.

Breiman, L. (1996): Bagging predictors. *Machine Learning 24* (2), 123–140.

Breiman, L. (1998): *Classification and regression trees* (3rd ed.). Boca Raton u.a. Chapman & Hall CRC.

Breiman, L. (2001): Random forests. *Machine Learning 45* (1), 5–32.

Brenner, A.J., Cueto Romero, M., Garcia Haro, J., Gilabert, M.A., Incoll, L.D., Martinez Fernandez, J., Porter, E., Pugnaire, F.I., & Younis, M.T. (1995): A comparison of direct and indirect methods for measuring leaf and surface areas of individual bushes. *Plant, Cell and Environment 18* (11), 1332–1340.

Breusch, T.S., & Pagan, A.R. (1979): A simple test for heteroscedasticity and random coefficient variation. *Econometrica 47* (5), 1287–1294.

Broge, N., & Leblanc, E. (2001): Comparing prediction power and stability of broadband and hyperspectral vegetation indices for estimation of green leaf area index and canopy chlorophyll density. *Remote Sensing of Environment 76* (2), 156–172.

Broge, N., & Mortensen, J. (2002): Deriving green crop area index and canopy chlorophyll density of winter wheat from spectral reflectance data. *Remote Sensing of Environment 81* (1), 45–57.

Brown, G.H. (1979): An optimization criterion for linear inverse estimation. *Technometrics 21* (4), 575–579.

Brown, L., Chen, J.M., Leblanc, S.G., & J. Cihlar (2000): A shortwave infrared modification to the simple ratio for LAI retrieval in boreal forests. An image and model analysis. *Remote Sensing of Environment 71* (1), 16–25.

Brown, S. (2002): Measuring carbon in forests: current status and future challenges. *Environmental Pollution 116* (3), 363–372.

Buermann, W. (2002): Analysis of a multiyear global vegetation leaf area index data set. *Journal of Geophysical Research 107* (D22), ACL 14-1–ACL 14-16.

Bundesamt für Naturschutz (2013): Steckbriefe der Natura 2000 Gebiete. 8431-371 Ammergebirge (FFH-Gebiet). Online available at: http://www.bfn.de/0316_steckbriefe.html?&tx_n2gebiete_pi1[detail]=ffh&tx_n2gebiete_pi1[gebnameffh]=Ammer&tx_n2gebiete_pi1[searchffh]=Suche%20starten&tx_n2gebiete_pi1[sitecode]=DE8431371&tx_n2gebiete_pi1[spid]=4624.

Burt, J.E., Barber, G.M., & Rigby, D.L. (2009): *Elementary statistics for geographers* (3rd ed.). New York. Guilford Press.

Butson, C.R., & Fernandes, R.A. (2004): A consistency analysis of surface reflectance and leaf area index retrieval from overlapping clear-sky Landsat ETM+ imagery. *Remote Sensing of Environment 89* (3), 369–380.

Caldwell, M.M., Harris, G.W., & Dzurec, R.S. (1983): A fiber optic point quadrat system for improved accuracy in vegetation sampling. *Oecologia 59* (2-3), 417–418.

Camacho-de Coca, F., Cernicharo, J., Lacaze, R., Baret, F., & Weiss, M. (2013): GEOV1: LAI, FAPAR essential climate variables and FCOVER global time series capitalizing over existing products. Part 2: Validation and intercomparison with reference products. *Remote Sensing of Environment 137,* 310–329.

Campbell, G. (1986): Extinction coefficients for radiation in plant canopies calculated using an ellipsoidal inclination angle distribution. *Agricultural and Forest Meteorology 36* (4), 317–321.

Campbell, G. (1990): Derivation of an angle density function for canopies with ellipsoidal leaf angle distributions. *Agricultural and Forest Meteorology 49* (3), 173–176.

Camps-Valls, G., Gomez-Chova, L., Richter, K., & Calpe-Maravilla, J. (2009): Biophysical parameter estimation with a semisupervised support vector machine. *IEEE Geoscience and Remote Sensing Letters 6* (2), 248–252.

Casa, R., & Jones, H.G. (2004): Retrieval of crop canopy properties: a comparison between model inversion from hyperspectral data and image classification. *International Journal of Remote Sensing 25* (6), 1119–1130.

Cayrol, P., Kergoat, L., Moulin, S., Dedieu, G., & Chehbouni, A. (2000): Calibrating a coupled SVAT–vegetation growth model with remotely sensed reflectance and surface temperature. A case study for the HAPEX-Sahel grassland sites. *Journal of Applied Meteorology 39* (12), 2452–2472.

Ceccato, P., Flasse, S., Tarantola, S., Jacquemoud, S., & Grégoire, J.-M. (2001): Detecting vegetation leaf water content using reflectance in the optical domain. *Remote Sensing of Environment 77* (1), 22–33.

Ceccato, P., Gobron, N., Flasse, S., Pinty, B., & Tarantola, S. (2002): Designing a spectral index to estimate vegetation water content from remote sensing data: Part 1. *Remote Sensing of Environment 82* (2-3), 188–197.

Cescatti, A. (1997): Modelling the radiative transfer in discontinuous canopies of asymmetric crowns. I. Model structure and algorithms. *Ecological Modelling 101* (2-3), 263–274.

Champeaux, J.-L., Masson, V., & Chauvin, F. (2005): ECOCLIMAP: a global database of land surface parameters at 1 km resolution. *Meteorological Applications 12* (1), 29–32.

Chan, J.C.-W., & Paelinckx, D. (2008): Evaluation of random forest and adaboost tree-based ensemble classification and spectral band selection for ecotope mapping using airborne hyperspectral imagery. *Remote Sensing of Environment 112* (6), 2999–3011.

Chason, J.W., Baldocchi, D.D., & Huston, M.A. (1991): A comparison of direct and indirect methods for estimating forest canopy leaf area. *Agricultural and Forest Meteorology 57* (1-3), 107–128.

Chaurasia, S., & Dadhwal, V.K. (2004): Comparison of principal component inversion with VI-empirical approach for LAI estimation using simulated reflectance data. *International Journal of Remote Sensing 25* (14), 2881–2887.

Chelle, M. (1997): Développement d'un modèle de radiosité mixte pour simuler la distribution du rayonnement dans les couverts vegetaux. Dissertation. Rennes.

Chelle, M., & Andrieu, B. (1998): The nested radiosity model for the distribution of light within plant canopies. *Ecological Modelling 111* (1), 75–91.

Chen, J.M. (1996): Evaluation of vegetation indices and a modified simple ratio for boreal applications. *Canadian Journal of Remote Sensing 22* (3), 229–242.

Chen, J.M., & Black, T.A. (1991): Measuring leaf area index of plant canopies with branch architecture. *Agricultural and Forest Meteorology 57* (1-3), 1–12.

Chen, J.M., & Black, T.A. (1992): Defining leaf area index for non-flat leaves. *Plant, Cell and Environment 15* (4), 421–429.

Chen, J.M., Black, T.A., & Adams, R. (1991): Evaluation of hemispherical photography for determining plant area index and geometry of a forest stand. *Agricultural and Forest Meteorology 56* (1-2), 129–143.

Chen, J.M., & Cihlar, J. (1995): Plant canopy gap-size analysis theory for improving optical measurements of leaf-area index. *Applied Optics 34* (27), 6211–6222.

Chen, J.M., & Cihlar, J. (1996): Retrieving leaf area index of boreal conifer forests using Landsat TM images. *Remote Sensing of Environment 55* (2), 153–162.

Chen, J.M., Govind, A., Sonnentag, O., Zhang, Y., Barr, A., & Amiro, B. (2006): Leaf area index measurements at Fluxnet-Canada forest sites. *Agricultural and Forest Meteorology 140* (1-4), 257–268.

Chen, J.M., & Leblanc, S. (1997): A four-scale bidirectional reflectance model based on canopy architecture. *IEEE Transactions on Geoscience and Remote Sensing 35* (5), 1316–1337.

Chen, J.M., Li, X., Nilson, T., & Strahler, A. (2000): Recent advances in geometrical optical modelling and its applications. *Remote Sensing Reviews 18* (2-4), 227–262.

Chen, J.M., Liu, J., Leblanc, S.G., Lacaze, R., & Roujean, J.-L. (2003): Multi-angular optical remote sensing for assessing vegetation structure and carbon absorption. *Remote Sensing of Environment 84* (4), 516–525.

Chen, J.M., Pavlic, G., Brown, L., Cihlar, J., Leblanc, S., White, H., Hall, R., Peddle, D., King, D., Trofymow, J., Swift, E., van der Sanden, J., & Pellikka, P. (2002a): Derivation and validation of Canada-wide coarse-resolution leaf area index maps using high-resolution satellite imagery and ground measurements. *Remote Sensing of Environment 80* (1), 165–184.

Chen, J.M., Pavlic, G., Brown, L., Cihlar, J., White, H., Hall, R., Peddle, D., King, D., Trofymow, J.S.E., van der Sanden, J., & Pellikka, P. (2002b): Derivation and validation of Canada-wide coarse-resolution leaf area index maps using high-resolution satellite imagery and ground measurements. *Remote Sensing of Environment* (80), 165–184.

Chen, J.M., Rich, P.M., Gower, S.T., Norman, J.M., & Plummer, S. (1997): Leaf area index of boreal forests: Theory, techniques, and measurements. *Journal of Geophysical Research 102* (D24), 29429–29443.

Cho, M.A., Skidmore, A., Corsi, F., van Wieren, S.E., & Sobhan, I. (2007): Estimation of green grass/herb biomass from airborne hyperspectral imagery using spectral indices and partial least squares regression. *International Journal of Applied Earth Observation and Geoinformation 9* (4), 414–424.

Chopping, M. (2003): Canopy attributes of desert grassland and transition communities derived from multiangular airborne imagery. *Remote Sensing of Environment 85* (3), 339–354.

Cierniewski, J., & Verbrugghe, M. (1997): Influence of soil surface roughness on soil bidirectional reflectance. *International Journal of Remote Sensing 18* (6), 1277–1288.

Clevers, J. (1989): Application of a weighted infrared-red vegetation index for estimating leaf area index by correcting for soil moisture. *Remote Sensing of Environment 29* (1), 25–37.

Cohen, W., Maiersperger, T., Turner, D., Ritts, W., Pflugmacher, D., Kennedy, R., Kirschbaum, A., Running, S., Costa, M., & Gower, S. (2006): MODIS land cover and LAI collection 4 product quality across nine sites in the western hemisphere. *IEEE Transactions on Geoscience and Remote Sensing 44* (7), 1843–1857.

Cohen, W.B., Maiersperger, T.K., Gower, S.T., & Turner, D.P. (2003a): An improved strategy for regression of biophysical variables and Landsat ETM+ data. *Remote Sensing of Environment 84* (4), 561–571.

Cohen, W.B., Maiersperger, T.K., Yang, Z., Gower, S.T., Turner, D.P., Ritts, W.D., Berterretche, M., & Running, S.W. (2003b): Comparisons of land cover and LAI estimates derived from ETM+ and MODIS for four sites in North America: a quality assessment of 2000/2001 provisional MODIS products. *Remote Sensing of Environment 88* (3), 233–255.

Colombo, R., Bellingerib, D., Fasolinic, D., & Marino, C.M. (2003): Retrieval of leaf area index in different vegetation types using high resolution satellite data. *Remote Sensing of*

Environment 86 (1), 120–131.

Colombo, R., Meroni, M., MARCHESI, A., Busetto, L., ROSSINI, M., GIARDINO, C., & Panigada, C. (2008): Estimation of leaf and canopy water content in poplar plantations by means of hyperspectral indices and inverse modeling. *Remote Sensing of Environment 112* (4), 1820–1834.

Comar, A., Baret, F., Obein, G., Simonot, L., Meneveaux, D., Viénot, F., & Solan, B. de (2014): ACT: A leaf BRDF model taking into account the azimuthal anisotropy of monocotyledonous leaf surface. *Remote Sensing of Environment 143,* 112–121.

Combal, B., Baret, F., & Weiss, M. (2002a): Improving canopy variables estimation from remote sensing data by exploiting ancillary information. Case study on sugar beet canopies. *Agronomie 22* (2), 205–215.

Combal, B., Baret, F., Weiss, M., Trubuil, A., Macé, D., Pragnère, A., Myneni, R., Knyazikhin, Y., & Wang, L. (2002b): Retrieval of canopy biophysical variables from bidirectional reflectance using prior information to solve the ill-posed inverse problem. *Remote Sensing of Environment 84* (1), 1–15.

Combal, B., Ochshepkov, S.L., Sinyuk, A., & Isaka, H. (2000): Statistical framework of the inverse problem in the retrieval of vegetation parameters. *Agronomie 20* (1), 65–77.

Combes, D., Bousquet, L., Jacquemoud, S., Sinoquet, H., Varlet-Grancher, C., & Moya, I. (2007): A new spectrogoniophotometer to measure leaf spectral and directional optical properties. *Remote Sensing of Environment 109* (1), 107–117.

Comeau, P.G., Gendron, F., & Letchford, T. (1998): A comparison of several methods for estimating light under a paper birch mixedwood stand. *Canadian Journal of Forest Research 28* (12), 1843–1850.

Conrad, C., Fritsch, S., Lex, S., Löw, F., Rücker, G., Schorcht, G., Sultanov, M., & Lamers, J. (2012): Potenziale des ‘Red Edge’ Kanals von RapidEye zur Unterscheidung und zum Monitoring landwirtschaftlicher Anbaufrüchte am Beispiel des usbekischen Bewässerungssystems Khorezm. In E. Borg, H. Daedelow, & R. Johnson (Eds.), *RapidEye science archive (RESA). Vom Algorithmus zum Produkt* (pp. 203–217). GITO.

Cukier, R., Fortuin, C., Schuler, K., Petschek, A., & Schaibly, J. (1973): Study of the sensitivity of coupled reaction systems to uncertainties in rate coefficients. I Theory. *The Journal of Chemical Physics 59* (8), 3873–3878.

Curran, P.J., Dungan, J.L., & Peterson, D.L. (2001): Estimating the foliar biochemical concentration of leaves with reflectance spectrometry. *Remote Sensing of Environment 76* (3), 349–359.

Curran, P.J., & Hay, A. (1986): The importance of measurement error for certain procedures in remote sensing at optical wavelengths. *Photogrammetric Engineering and Remote Sensing 52* (2), 229–241.

Cutini, A., Matteucci, G., & Mugnozza, G.S. (1998): Estimation of leaf area index with the Li-Cor LAI 2000 in deciduous forests. *Forest Ecology and Management 105* (1-3), 55–65.

Da Silva, D., Boudon, F., Godin, C., & Sinoquet, H. (2008): Multiscale framework for modeling and analyzing light interception by trees. *Multiscale Modeling & Simulation 7* (2), 910–933.

Danson, F.M., & Aldakheel, Y.Y. (2000): Diurnal water stress in sugar beet: Spectral reflectance measurements and modelling. *Agronomie 20* (1), 31–39.

Darvishzadeh, R., Matkan, A.A., & Dashti Ahangar, A. (2012): Inversion of a radiative transfer model for estimation of rice canopy chlorophyll content using a Lookup-Table approach. *IEEE Journal of Selected Topics in Applied Earth Observations and Remote Sensing 5* (4), 1222–1230.

Darvishzadeh, R., Skidmore, A., Atzberger, C., & van Wieren, S. (2008a): Estimation of vegetation LAI from hyperspectral reflectance data: Effects of soil type and plant architecture. *International Journal of Applied Earth Observation and Geoinformation*

10 (3), 358–373.

Darvishzadeh, R., Skidmore, A., Schlerf, M., & Atzberger, C. (2008b): Inversion of a radiative transfer model for estimating vegetation LAI and chlorophyll in a heterogeneous grassland. *Remote Sensing of Environment 112* (5), 2592–2604.

Darvishzadeh, R., Skidmore, A., Schlerf, M., Atzberger, C., Corsi, F., & Cho, M. (2008c): LAI and chlorophyll estimation for a heterogeneous grassland using hyperspectral measurements. *ISPRS Journal of Photogrammetry and Remote Sensing 63* (4), 409–426.

Daughtry, C. (2000): Estimating corn leaf chlorophyll concentration from leaf and canopy reflectance. *Remote Sensing of Environment 74* (2), 229–239.

De Jong, S.M., Pebesma, E.J., & Lacaze, B. (2003): Above-ground biomass assessment of Mediterranean forests using airborne imaging spectrometry: The DAIS Peyne experiment. *International Journal of Remote Sensing 24* (7), 1505–1520.

Decagon Devices (2013): AccuPAR PAR/LAI ceptometer. Model LP-80. Operator's Manual.

Demarez, V., Duthoit, S., Baret, F., Weiss, M., & Dedieu, G. (2008): Estimation of leaf area and clumping indexes of crops with hemispherical photographs. *Agricultural and Forest Meteorology 148* (4), 644–655.

Deng, F., Chen, J.M., Plummer, S., Chen, M., & Pisek, J. (2006): Algorithm for global leaf area index retrieval using satellite imagery. *IEEE Transactions on Geoscience and Remote Sensing 44* (8), 2219–2229.

Dente, L., Satalino, G., Mattia, F., & Rinaldi, M. (2008): Assimilation of leaf area index derived from ASAR and MERIS data into CERES-Wheat model to map wheat yield. *Remote Sensing of Environment 112* (4), 1395–1407.

DigitalGlobe (2010): The benefits of the 8 spectral bands of WorldView-2. Online available at: http://www.digitalglobe.com/sites/default/files/DG-8SPECTRAL-WP_0.pdf.

Dirnböck, T., Essl, F., & Rabitsch, W. (2011): Disproportional risk for habitat loss of high-altitude endemic species under climate change. *Global Change Biology 17* (2), 990–996.

Disney, M., Lewis, P., & North, P. (2000): Monte Carlo ray tracing in optical canopy reflectance modelling. *Remote Sensing Reviews 18* (2-4), 163–196.

Disney, M., Lewis, P., & Saich, P. (2006): 3D modelling of forest canopy structure for remote sensing simulations in the optical and microwave domains. *Remote Sensing of Environment 100* (1), 114–132.

Dongus, H. (1993): *Die naturräumlichen Einheiten auf Blatt 188/194 Kaufbeuren-Mittenwald.* Geographische Landesaufnahme 1:200000 / Naturräumliche Gliederung Deutschlands *188/194.* Bonn-Bad Godesberg. Bundesforschungsanstalt für Landeskunde und Raumordnung.

Doraiswamy, P., Hatfield, J., Jackson, T., Akhmedov, B., Prueger, J., & Stern, A. (2004): Crop condition and yield simulations using Landsat and MODIS. *Remote Sensing of Environment 92* (4), 548–559.

Dorigo, W. (2007): Retrieving canopy variables by radiative transfer model inversion. A regional approach for imaging spectrometer data. Dissertation. Department für Ökologie und Ökosystemmanagement. München.

Dorigo, W., Richter, R., Baret, F., Bamler, R., & Wagner, W. (2009): Enhanced automated canopy characterization from hyperspectral data by a novel two step radiative transfer model inversion approach. *Remote Sensing 1* (4), 1139–1170.

Dorigo, W., Zurita-Milla, R., De Wit, A.J.W., Brazile, J., Singh, R., & Schaepman, M. (2007): A review on reflective remote sensing and data assimilation techniques for enhanced agroecosystem modeling. *International Journal of Applied Earth Observation and Geoinformation 9* (2), 165–193.

Drusch, M., Del Bello, U., Carlier, S., Colin, O., Fernandez, V., Gascon, F., Hoersch, B., Isola, C., Laberinti, P., Martimort, P., Meygret, A., Spoto, F., Sy, O., Marchese, F., & Bargellini,

P. (2012): Sentinel-2: ESA's optical high-resolution mission for GMES operational services. *Remote Sensing of Environment 120,* 25–36.

Drusch, M., Gascon, F., & Berger, M. (2010): Sentinel-2 mission requirements document 2010. Online available at: http://esamultimedia.esa.int/docs/GMES/Sentinel-2_MRD.pdf.

Dufrêne, E., & Bréda, N. (1995): Estimation of deciduous forest leaf area index using direct and indirect methods. *Oecologia 104* (2), 156–162.

Durbha, S.S., King, R.L., & Younan, N.H. (2007): Support vector machines regression for retrieval of leaf area index from multiangle imaging spectroradiometer. *Remote Sensing of Environment 107* (1-2), 348–361.

Durbin, J., & Watson, G.S. (1971): Testing for serial correlation in least squares regression. III. *Biometrika 58* (1), 1–19.

Duveiller, G., Baret, F., & Defourny, P. (2011a): Crop specific green area index retrieval from MODIS data at regional scale by controlling pixel-target adequacy. *Remote Sensing of Environment 115* (10), 2686–2701.

Duveiller, G., & Defourny, P. (2010): A conceptual framework to define the spatial resolution requirements for agricultural monitoring using remote sensing. *Remote Sensing of Environment 114* (11), 2637–2650.

Duveiller, G., Weiss, M., Baret, F., & Defourny, P. (2011b): Retrieving wheat green area index during the growing season from optical time series measurements based on neural network radiative transfer inversion. *Remote Sensing of Environment 115* (3), 887–896.

Ehammer, A., Fritsch, S., Conrad, C., Lamers, J., & Dech, S. (2010): Statistical derivation of fPAR and LAI for irrigated cotton and rice in arid Uzbekistan by combining multi-temporal RapidEye data and ground measurements. In C.M.U. Neale, & A. Maltese (Eds.), *SPIE Proceedings 7824* (pp. 1–10).

Eitel, J.U., Vierling, L.A., Litvak, M.E., Long, D.S., Schulthess, U., Ager, A.A., Krofcheck, D.J., & Stoscheck, L. (2011): Broadband, red-edge information from satellites improves early stress detection in a New Mexico conifer woodland. *Remote Sensing of Environment 115* (12), 3640–3646.

Ellenberg, H., & Leuschner, C. (2010): *Vegetation Mitteleuropas mit den Alpen in ökologischer, dynamischer und historischer Sicht* (6th ed.). UTB für Wissenschaft *8104*. Stuttgart. Ulmer.

Englund, S.R., O'Brien, J.J., & Clark, D.B. (2000): Evaluation of digital and film hemispherical photography and spherical densiometry for measuring forest light environments. *Canadian Journal of Forest Research 30* (12), 1999–2005.

Eriksson, H., Eklundh, L., Hall, K., & Lindroth, A. (2005): Estimating LAI in deciduous forest stands. *Agricultural and Forest Meteorology 129* (1-2), 27–37.

Faivre, R., Leenhardt, D., Voltz, M., Benoît, M., Papy, F., Dedieu, G., & Wallach, D. (2004): Spatializing crop models. *Agronomie 24* (4), 205–217.

Fan, L., Gao, Y., Brück, H., & Bernhofer, C. (2009): Investigating the relationship between NDVI and LAI in semi-arid grassland in Inner Mongolia using in-situ measurements. *Theoretical and Applied Climatology 95* (1-2), 151–156.

Fang, H. (2003): Retrieving leaf area index using a genetic algorithm with a canopy radiative transfer model. *Remote Sensing of Environment 85* (3), 257–270.

Fang, H., & Liang, S. (2005): A hybrid inversion method for mapping leaf area index from MODIS data: experiments and application to broadleaf and needleleaf canopies. *Remote Sensing of Environment 94* (3), 405–424.

Fang, H., Wei, S., & Liang, S. (2012): Validation of MODIS and CYCLOPES LAI products using global field measurement data. *Remote Sensing of Environment 119,* 43–54.

FAO (2013): *FAO Statistical Yearbook 2013.* Food & Agriculture Organization of the United Nation.

Farr, T.G., Rosen, P.A., Caro, E., Crippen, R., Duren, R., Hensley, S., Kobrick, M., Paller, M., Rodriguez, E., Roth, L., Seal, D., Shaffer, S., Shimada, J., Umland, J., Werner, M., Oskin, M., Burbank, D., & Alsdorf, D. (2007): The shuttle radar topography mission. *Reviews of Geophysics 45* (2), 1–33.

Farys, M. (2003): Influence of soil salinity on soil bidirectional reflectance in optical domain. In *IEEE Workshop on advances in techniques for analysis of remotely sensed data* (pp. 187–192).

Fassnacht, K.S., Gower, S.T., MacKenzie, M.D., Nordheim, E.V., & Lillesand, T.M. (1997): Estimating the leaf area index of North Central Wisconsin forests using the Landsat Thematic Mapper. *Remote Sensing of Environment 61* (2), 229–245.

Fassnacht, K.S., Gower, S.T., Norman, J., & McMurtic, R. (1994): A comparison of optical and direct methods for estimating foliage surface area index in forests. *Agricultural and Forest Meteorology 71* (1-2), 183–207.

Féret, J.-B., François, C., Asner, G.P., Gitelson, A.A., Martin, R.E., Bidel, L.P., Ustin, S.L., Le Maire, G., & Jacquemoud, S. (2008): PROSPECT-4 and 5: Advances in the leaf optical properties model separating photosynthetic pigments. *Remote Sensing of Environment 112* (6), 3030–3043.

Féret, J.-B., François, C., Gitelson, A., Asner, G.P., Barry, K.M., Panigada, C., Richardson, A.D., & Jacquemoud, S. (2011): Optimizing spectral indices and chemometric analysis of leaf chemical properties using radiative transfer modeling. *Remote Sensing of Environment 115* (10), 2742–2750.

Fernandes, R., Butson, C., Leblanc, S.G., & Latifovic, R. (2003): Landsat-5 TM and Landsat-7 ETM+ based accuracy assessment of leaf area index products for Canada derived from SPOT-4 VEGETATION data. *Canadian Journal of Remote Sensing 29* (2), 241–258.

Fernandes, R., & G. Leblanc, S. (2005): Parametric (modified least squares) and non-parametric (Theil–Sen) linear regressions for predicting biophysical parameters in the presence of measurement errors. *Remote Sensing of Environment 95* (3), 303–316.

Fernandes, R.A., Miller, J.R., Chen, J.M., & Rubinstein, I.G. (2004): Evaluating image-based estimates of leaf area index in boreal conifer stands over a range of scales using high-resolution CASI imagery. *Remote Sensing of Environment 89* (2), 200–216.

Ferrier, P., Crebassol, P., Dedieu, G., Hagolle, O., Meygret, A., Tinto, F., Yaniv, Y., & Herscovitz, J. (2010): VENµS (Vegetation and environment monitoring on a new micro satellite). In *IEEE International Geoscience and Remote Sensing Symposium (IGARSS), 25 - 30 July 2010, Honolulu, Hawaii, USA.* (pp. 3736–3739). Piscataway, NJ.

Field, A.P., Miles, J., & Field, Z. (2012): *Discovering statistics using R* (1st ed.). Los Angeles. SAGE.

Fischer, K. (2002): Deutschlands Alpenanteil. In H. Liedtke, & J. Marcinek (Eds.), *Physische Geographie Deutschlands. 84 Tabellen* (pp. 477–501). Gotha. Klett-Perthes.

Flerchinger, G.N., Kustas, W.P., & Weltz, M.A. (1998): Simulating surface energy fluxes and radiometric surface temperatures for two arid vegetation communities using the SHAW model. *Journal of Applied Meteorology 37* (5), 449–460.

Foley, J.A., Levis, S., Costa, M.H., Cramer, W., & Pollard, D. (2000): Incorporating dynamic vegetation cover within global climate models. *Ecological Applications 10* (6), 1620–1632.

Fournier, R.A., Rich, P.M., & Landry, R. (1997): Hierarchical characterization of canopy architecture for boreal forest. *Journal of Geophysical Research 102* (D24), 29445–29454.

Fourty, T., & Baret, F. (1997): Vegetation water and dry matter contents estimated from top-of-the-atmosphere reflectance data: A simulation study. *Remote Sensing of Environment 61* (1), 34–45.

Fourty, T., Baret, F., Jacquemoud, S., Schmuck, G., & Verdebout, J. (1996): Leaf optical properties with explicit description of its biochemical composition: Direct and inverse problems. *Remote Sensing of Environment 56* (2), 104–117.

François, C., Ottlé, C., Olioso, A., Prévot, L., Bruguier, N., & Ducros, Y. (2002): Conversion of 400-1100 nm vegetation albedo measurements into total shortwave broadband albedo using a canopy radiative transfer model. *Agronomie 22* (6), 611–618.

Frank, A., & Karn, J. (2003): Vegetation indices, CO2 flux, and biomass for Northern Plains grasslands. *Journal of Range Management Archives 56* (4), 382–387.

Frank, H. (1979): Glazial übertiefte Täler im Bereich des Isar-Loisach-Gletschers: Neue Erkenntnisse über Aufbau und Mächtigkeit des Quartärs in den alpinen Tälern, im Gebiet des „Murnauer Schotters“ und im „Tölzer Lobus“. *E&G – Quaternary Science Journal 29* (1), 77–99.

Franklin, S., & Wulder, M. (2002): Remote sensing methods in medium spatial resolution satellite data land cover classification of large areas. *Progress in Physical Geography 26* (2), 173–205.

Frazer, G.W., Trofymow, J.A., & Lertzman, K.P. (1997): *A method for estimating canopy openness, effective leaf area index, and photosynthetically active photon flux density using hemispherical photography and computerized image analysis techniques*. Information Report *373*. Victoria, B.C. Canadian Forest Service Pacific Forestry Centre.

Freudenberger, W., & Schwerd, K. (1996): *Erläuterungen zur Geologischen Karte von Bayern 1:500000* (4th ed.). Bayerisches Geologisches Landesamt.

Friedl, M.A., Schimel, D.S., Michaelsen, J., Davis, F.W., & Walker, H. (1994): Estimating grassland biomass and leaf area index using ground and satellite data. *International Journal of Remote Sensing 15* (7), 1401–1420.

Friese, M., Frank, T., Hank, T., Bach, H., & Mauser, W. (2011): RapidSAR - Integrative Nutzung von RapidEye und TerraSAR-X durch Datenassimilation in landwirtschaftliche Produktionsmodelle. In E. Borg, & H. Daedelow (Eds.), *RapidEye science archive. Erste Ergebnisse*. 3. RESA Workshop 2011 (pp. 147–164). Neustrelitz. GITO.

Ganapol, B., & Myneni, R. (1992): The Fn method for the one-angle radiative transfer equation applied to plant canopies. *Remote Sensing of Environment 39* (3), 213–231.

Ganapol, B.D., Johnson, L.F., Hammer, P.D., Hlavka, C.A., & Peterson, D.L. (1998): LEAFMOD: A new within-leaf radiative transfer model. *Remote Sensing of Environment 63* (2), 182–193.

Ganguly, S., Nemani, R.R., Zhang, G., Hashimoto, H., Milesi, C., Michaelis, A., Wang, W., Votava, P., Samanta, A., Melton, F., Dungan, J.L., Vermote, E., Gao, F., Knyazikhin, Y., & Myneni, R.B. (2012): Generating global leaf area index from Landsat: Algorithm formulation and demonstration. *Remote Sensing of Environment 122,* 185–202.

Gao, B.-C., Montes, M.J., Davis, C.O., & Goetz, A.F. (2009): Atmospheric correction algorithms for hyperspectral remote sensing data of land and ocean. *Remote Sensing of Environment 113,* S17-S24.

Garrigues, S., Allard, D., Baret, F., & Weiss, M. (2006): Quantifying spatial heterogeneity at the landscape scale using variogram models. *Remote Sensing of Environment 103* (1), 81–96.

Garrigues, S., Allard, D., Weiss, M., & Baret, F. (2002): Comparing VALERI sampling schemes to better represent high spatial resolution satellite pixel from ground measurements: How to characterize an ESU. Online available at: http://w3.avignon.inra.fr/valeri/methodology/samplingschemes.pdf.

Garrigues, S., Lacaze, R., Baret, F., Morisette, J.T., Weiss, M., Nickeson, J.E., Fernandes, R., Plummer, S., Shabanov, N.V., Myneni, R.B., Knyazikhin, Y., & Yang, W. (2008a): Validation and intercomparison of global leaf area index products derived from remote sensing data. *Journal of Geophysical Research 113* (G2),

Garrigues, S., Shabanov, N., Swanson, K., Morisette, J., Baret, F., & Myneni, R. (2008b): Intercomparison and sensitivity analysis of leaf area index retrievals from LAI-2000, AccuPAR, and digital hemispherical photography over croplands. *Agricultural and Forest Meteorology 148* (8-9), 1193–1209.

Gascon, F., & Colin, O. (2014): S-2 products. In ESA (Ed.), *Sentinel-2 for Science Workshop* (p. 3–3).

Gastellu-Etchegorry, J., Gascon, F., & Estève, P. (2003): An interpolation procedure for generalizing a look-up table inversion method. *Remote Sensing of Environment 87* (1), 55–71.

Gastellu-Etchegorry, J., Guillevic, P., Zagolski, F., Demarez, V., Trichon, V., Deering, D.W., & Leroy, M. (1999): Modeling BRF and radiation regime of boreal and tropical forests. *Remote Sensing of Environment 68* (3), 281–316.

Gastellu-Etchegorry, J.P., Martin, E., & Gascon, F. (2004): DART: a 3D model for simulating satellite images and studying surface radiation budget. *International Journal of Remote Sensing 25* (1), 73–96.

Gastellu-Etchegorry, J.-P., Demarez, V., Pinel, V., & Zagolski, F. (1996): Modeling radiative transfer in heterogeneous 3-D vegetation canopies. *Remote Sensing of Environment 58* (2), 131–156.

Gausman, H., Allen, W.A., & Cardenas, R. (1969): Reflectance of cotton leaves and their structure. *Remote Sensing of Environment 1* (1), 19–22.

GCOS (2006): Systematic observation requirements for satellite-based products for climate. Supplemental details to the satellite-based component of the “Implementation Plan for the Global Observing System for Climate in Support of the UNFCCC”. World Meteorological Organization.

Gemmell, F. (2000): Testing the utility of multi-angle spectral data for reducing the effects of background spectral variations in forest reflectance model inversion. *Remote Sensing of Environment 72* (1), 46–63.

Gislason, P.O., Benediktsson, J.A., & Sveinsson, J.R. (2006): Random forests for land cover classification. *Pattern Recognition Letters 27* (4), 294–300.

Gitelson, A., & Merzlyak, M.N. (1994): Spectral reflectance changes associated with autumn senescence of Aesculus hippocastanum L. and Acer platanoides L. leaves. Spectral features and relation to chlorophyll estimation. *Journal of Plant Physiology 143* (3), 286–292.

Glenn, E.P., Huete, A.R., Nagler, P.L., & Nelson, S.G. (2008): Relationship between remotely-sensed vegetation indices, canopy attributes and plant physiological processes: What vegetation indices can and cannot tell us about the landscape. *Sensors 8* (4), 2136–2160.

Gobron, N., Pinty, B., & Verstraete, M.M. (1997a): Theoretical limits to the estimation of the leaf area index on the basis of visible and near-infrared remote sensing data. *IEEE Transactions on Geoscience and Remote Sensing 35* (6), 1438–1445.

Gobron, N., Pinty, B., Verstraete, M.M., & Govaerts, Y. (1997b): A semidiscrete model for the scattering of light by vegetation. *Journal of Geophysical Research 102* (D8), 9431–9446.

Goel, N. (1989): Inversion of canopy reflectance models for estimation of biophysical parameters from reflectance data. In G. Asrar (Ed.), *Theory and applications of optical remote sensing* (pp. 205–250). New York. Wiley.

Goel, N.S. (1988): Models of vegetation canopy reflectance and their use in estimation of biophysical parameters from reflectance data. *Remote Sensing Reviews 4* (1), 1–212.

Goel, N.S., & Grier, T. (1988): Estimation of canopy parameters for inhomogeneous vegetation canopies from reflectance data: III. Trim: A model for radiative transfer in heterogeneous three-dimensional canopies. *Remote Sensing of Environment 25* (3), 255–293.

Goel, N.S., & Norman, J.M. (1990): Remote sensing and biophysical measurements of soils and vegetation. *Remote Sensing Reviews 5* (1), 1–12.

Goel, N.S., Rozehnal, I., & Thompson, R.L. (1991): A computer graphics based model for scattering from objects of arbitrary shapes in the optical region. *Remote Sensing of Environment 36* (2), 73–104.

Goel, N.S., & Strebel, D. (1983): Inversion of vegetation canopy reflectance models for estimating agronomic variables. I. Problem definition and initial results using the suits model. *Remote Sensing of Environment 13* (6), 487–507.

Goel, N.S., & Strebel, D.E. (1984): Simple beta distribution representation of leaf orientation in vegetation canopies. *Agronomy Journal 76* (5), 800–802.

Goel, N.S., & Thompson, R.L. (1984a): Inversion of vegetation canopy reflectance models for estimating agronomic variables. III. Estimation using only canopy reflectance data as illustrated by the suits model. *Remote Sensing of Environment 15* (3), 223–236.

Goel, N.S., & Thompson, R.L. (1984b): Inversion of vegetation canopy reflectance models for estimating agronomic variables. V. Estimation of leaf area index and average leaf angle using measured canopy reflectances. *Remote Sensing of Environment 16* (1), 69–85.

Goel, N.S., & Thompson, R.L. (2000): A snapshot of canopy reflectance models and a universal model for the radiation regime. *Remote Sensing Reviews 18* (2-4), 197–225.

Gong, P. (1999): Inverting a canopy reflectance model using a neural network. *International Journal of Remote Sensing 20* (1), 111–122.

Gonsamo Gosa, A., Schaepman–Strub, G., Kooistra, L., & Schaepman, M. (2007): Estimation of leaf area index using optical field instruments and imaging spectroscopy. In *Proceedings of the 5th EARSeL Workshop on Imaging Spectroscopy* (pp. 1–12).

González-Sanpedro, M., Le Toan, T., Moreno, J., Kergoat, L., & Rubio, E. (2008): Seasonal variations of leaf area index of agricultural fields retrieved from Landsat data. *Remote Sensing of Environment 112* (3), 810–824.

Govaerts, Y.M., Jacquemoud, S., Verstraete, M.M., & Ustin, S.L. (1996): Three-dimensional radiation transfer modeling in a dicotyledon leaf. *Applied Optics 35* (33), 6585–6598.

Gower, S.T., Kucharik, C.J., & Norman, J.M. (1999): Direct and indirect estimation of leaf area index, fAPAR, and net primary production of terrestrial ecosystems. *Remote Sensing of Environment 70* (1), 29–51.

Gower, S.T., & Norman, J.M. (1991): Rapid estimation of leaf area index in conifer and broad-leaf plantations. *Ecology 72* (5), 1896–1900.

Grau, E., & Gastellu-Etchegorry, J.-P. (2013): Radiative transfer modeling in the earth–atmosphere system with DART model. *Remote Sensing of Environment 139,* 149–170.

Guimaraes, T.G., Fontes, P.C.R., Pereira, P.R.G., Alvarez V., V.H., & Monnerat, P.H. (1999): Teores de clorofila determinados por medidor portátil e sua relação com formas de nitrogênio em folhas de tomateiro cultivados em dois tipos de solo. *Bragantia 58* (1), 209–216.

Haboudane, D. (2004): Hyperspectral vegetation indices and novel algorithms for predicting green LAI of crop canopies: Modeling and validation in the context of precision agriculture. *Remote Sensing of Environment 90* (3), 337–352.

Haboudane, D., Miller, J.R., Tremblay, N., Zarco-Tejada, P.J., & Dextraze, L. (2002): Integrated narrow-band vegetation indices for prediction of crop chlorophyll content for application to precision agriculture. *Remote Sensing of Environment 81* (2-3), 416–426.

Hadamard, J. (1902): Sur les problèmes aux dérivées partielles et leur signification physique. In *Princeton University Bulletin* (pp. 49–52).

Hammersley, J.M., & Handscomb, D.C. (1964): *Monte Carlo Methods.* New York. Wiley & Sons.

Hansen, P., & Schjoerring, J. (2003): Reflectance measurement of canopy biomass and nitrogen status in wheat crops using normalized difference vegetation indices and partial least squares regression. *Remote Sensing of Environment 86* (4), 542–553.

Hapke, B. (1981): Bidirectional reflectance spectroscopy: 1. Theory. *Journal of Geophysical*

Research 86 (B4), 3039–3054.

Hartwich, R., Behrens, J., Eckelmann, W., Haase, G., Richter, A., Roeschmann, G., & Schmidt, R. (1998): *Bodenübersichtskarte der Bundesrepublik Deutschland. im Maßstab 1:1000000 (BÜK 1000).* Hannover. Bundesanstalt für Geowissenschaften und Rohstoffe.

Hastie, T., Tibshirani, R., & Friedman, J.H. (2009): *The elements of statistical learning. Data mining, inference, and prediction* (2nd ed.). Springer series in statistics. New York. Springer.

He, J.-S., Wang, X., Schmid, B., Flynn, D.F.B., Li, X., Reich, P.B., & Fang, J. (2010): Taxonomic identity, phylogeny, climate and soil fertility as drivers of leaf traits across Chinese grassland biomes. *Journal of Plant Research 123* (4), 551–561.

He, W., & Yang, H. (2013): Winter wheat leaf area index retrieval with multi-angle and multi-spectral Terra/Aqua MODIS data. *Transactions of the Chinese Society of Agricultural Engineering 29* (4), 204–212.

He, Y., Guo, X., & Wilmshurst, J. (2006): Studying mixed grassland ecosystems I: suitable hyperspectral vegetation indices. *Canadian Journal of Remote Sensing 32,* 96–107.

Hedley, J., Roelfsema, C., & Phinn, S.R. (2009): Efficient radiative transfer model inversion for remote sensing applications. *Remote Sensing of Environment 113* (11), 2527–2532.

Heiskanen, J. (2006): Estimating aboveground tree biomass and leaf area index in a mountain birch forest using ASTER satellite data. *International Journal of Remote Sensing 27* (6), 1135–1158.

Heiskanen, J., Rautiainen, M., Stenberg, P., Mõttus, M., Vesanto, V.-H., Korhonen, L., & Majasalmi, T. (2012): Seasonal variation in MODIS LAI for a boreal forest area in Finland. *Remote Sensing of Environment 126,* 104–115.

Ho, T.K. (1998): The random subspace method for constructing decision forests. *IEEE Transactions on Pattern Analysis and Machine Intelligence 20* (8), 832–844.

Hopkins, A., & Holz, B. (2006): Grassland for agriculture and nature conservation: Production, quality and multi-functionality. *Agronomy Research 4* (1), 3–20.

Hosoi, F., Nakai, Y., & Omasa, K. (2009): Estimating the leaf inclination angle distribution of the wheat canopy using a portable scanning lidar. *Journal of Agricultural Meteorology 65* (3), 297–302.

Houborg, R., Anderson, M., & Daughtry, C. (2009): Utility of an image-based canopy reflectance modeling tool for remote estimation of LAI and leaf chlorophyll content at the field scale. *Remote Sensing of Environment 113* (1), 259–274.

Hu, J., Su, Y., Tan, B., Huang, D., Yang, W., Schull, M., Bull, M.A., Martonchik, J.V., Diner, D.J., Knyazikhin, Y., & Myneni, R.B. (2007): Analysis of the MISR LAI/FPAR product for spatial and temporal coverage, accuracy and consistency. *Remote Sensing of Environment 107* (1-2), 334–347.

Hu, J., Tan, B., Shabanov, N., Crean, K.A., Martonchik, J.V., Diner, D.J., Knyazikhin, Y., & Myneni, R.B. (2003): Performance of the MISR LAI and FPAR algorithm: A case study in Africa. *Remote Sensing of Environment 88* (3), 324–340.

Huang, Z., Turner, B.J., Dury, S.J., Wallis, I.R., & Foley, W.J. (2004): Estimating foliage nitrogen concentration from HyMap data using continuum removal analysis. *Remote Sensing of Environment 93* (1-2), 18–29.

Huemmrich, K. (2001): The GeoSail model: a simple addition to the SAIL model to describe discontinuous canopy reflectance. *Remote Sensing of Environment 75* (3), 423–431.

Huete, A. (1988): A soil-adjusted vegetation index (SAVI). *Remote Sensing of Environment 25* (3), 295–309.

Huete, A. (1989): Soil influences in remotely sensed vegetation canopy spectra. In G. Asrar (Ed.), *Theory and applications of optical remote sensing* (pp. 107–141). New York. Wiley.

Huete, A. (1997): A comparison of vegetation indices over a global set of TM images for EOS-MODIS. *Remote Sensing of Environment 59* (3), 440–451.

Huete, A., Didan, K., Miura, T., Rodriguez, E., Gao, X., & Ferreira, L. (2002): Overview of the radiometric and biophysical performance of the MODIS vegetation indices. *Remote Sensing of Environment 83* (1-2), 195–213.

Huete, A., & Liu, H. (1994): An error and sensitivity analysis of the atmospheric- and soil-correcting variants of the NDVI for the MODIS-EOS. *IEEE Transactions on Geoscience and Remote Sensing 32* (4), 897–905.

Hüttich, C., Herold, M., Wegmann, M., Cord, A., Strohbach, B., Schmullius, C., & Dech, S. (2011): Assessing effects of temporal compositing and varying observation periods for large-area land-cover mapping in semi-arid ecosystems: Implications for global monitoring. *Remote Sensing of Environment 115* (10), 2445–2459.

Hyer, E.J., & Goetz, S.J. (2004): Comparison and sensitivity analysis of instruments and radiometric methods for LAI estimation: assessments from a boreal forest site. *Agricultural and Forest Meteorology 122* (3-4), 157–174.

Hyyppä, J., Pyysalo, U., Hyyppä, H., & Samberg, A. (2000): Elevation accuracy of laser scanning-derived digital terrain and target models in forest environment. In *Proceedings of EARSeL-SIG-Workshop LIDAR* (pp. 139–147).

Iaquinta, J., & Pinty, B. (1997): Adaptation of a bidirectional reflectance model including the hot-spot to an optically thin canopy. *Remote Sensing Reviews 15* (1-4), 195–222.

Iaquinta, J., Pinty, B., & Privette, J. (1997): Inversion of a physically based bidirectional reflectance model of vegetation. *IEEE Transactions on Geoscience and Remote Sensing 35* (3), 687–698.

Irons, J.R., Dwyer, J.L., & Barsi, J.A. (2012): The next Landsat satellite: The Landsat data continuity mission. *Remote Sensing of Environment 122,* 11–21.

Jacquemoud, S. (1993): Inversion of the PROSPECT + SAIL canopy reflectance model from AVIRIS equivalent spectra: Theoretical study. *Remote Sensing of Environment 44* (2-3), 281–292.

Jacquemoud, S., Bacour, C., Poilvé, H., & Frangi, J.-P. (2000): Comparison of four radiative transfer models to simulate plant canopies reflectance direct and inverse mode. *Remote Sensing of Environment 74* (3), 471–481.

Jacquemoud, S., & Baret, F. (1990): PROSPECT: A model of leaf optical properties spectra. *Remote Sensing of Environment 34* (2), 75–91.

Jacquemoud, S., & Baret, F. (1993): Estimating vegetation biophysical parameters by inversion of a reflectance model on high spectral resolution data. In C. Varlet-Grancher, R. Bonhomme, & H. Sinoquet (Eds.), *Crop structure and light microclimate. Characterization and applications* (pp. 339–350). Paris. INRA.

Jacquemoud, S., Baret, F., Andrieu, B., Danson, F., & Jaggard, K. (1995a): Extraction of vegetation biophysical parameters by inversion of the PROSPECT + SAIL models on sugar beet canopy reflectance data. Application to TM and AVIRIS sensors. *Remote Sensing of Environment 52* (3), 163–172.

Jacquemoud, S., Baret, F., & Hanocq, J. (1992): Modeling spectral and bidirectional soil reflectance. *Remote Sensing of Environment 41* (2-3), 123–132.

Jacquemoud, S., Flasse, S., Verdebout, J., & Schmuck, G. (1994): Comparison of several optimization methods to extract canopy biophysical parameters. In *Proc. 6th International Symposium on Physical Measurements and Signatures in Remote Sensing* (pp. 291–298).

Jacquemoud, S., Ustin, S., Verdebout, J., Schmuck, G., Andreoli, G., & Hosgood, B. (1996): Estimating leaf biochemistry using the PROSPECT leaf optical properties model. *Remote Sensing of Environment 56* (3), 194–202.

Jacquemoud, S., & Ustin, S.L. (2001): Leaf optical properties: A state of the art. In *8th International Symposium of Physical Measurements & Signatures in Remote Sensing* (pp. 223–332).

Jacquemoud, S., Verdebout, J., Schmuck, G., Andreoli, G., & Hosgood, B. (1995b): Investigation of leaf biochemistry by statistics. *Remote Sensing of Environment 54* (3), 180–188.

Jacquemoud, S., Verhoef, W., Baret, F., Bacour, C., Zarco-Tejada, P.J., Asner, G.P., François, C., & Ustin, S.L. (2009): PROSPECT+SAIL models: A review of use for vegetation characterization. *Remote Sensing of Environment 113,* S56-S66.

Jacquemoud, S., Verhoef, W., Baret, F., Zarco-Tejada, P., Asner, G.P., François, C., & Ustin, S. (2006): PROSPECT+SAIL: 15 years of use for land surface characterization. In *IEEE International Symposium on Geoscience and Remote Sensing* (pp. 1992–1995).

Jensen, J.R. (2000): *Remote sensing of the environment. An earth resource perspective.* Prentice Hall series in geographic information science. Upper Saddle River, NJ. Prentice Hall.

Johnson, L., Roczen, D., Youkhana, S., Nemani, R., & Bosch, D. (2003): Mapping vineyard leaf area with multispectral satellite imagery. *Computers and Electronics in Agriculture 38* (1), 33–44.

Jonckheere, I., Fleck, S., Nackaerts, K., Muys, B., Coppin, P., Weiss, M., & Baret, F. (2004): Review of methods for in situ leaf area index determination. Part I. Theories, sensors and hemispherical photography. *Agricultural and Forest Meteorology 121* (1-2), 19–35.

Jonckheere, I., Muys, B., & Coppin, P. (2005): Derivative analysis for in situ high dynamic range hemispherical photography and its application in forest stands. *IEEE Geoscience and Remote Sensing Letters 2* (3), 296–300.

Jones, H.G., & Vaughan, R.A. (2010): *Remote sensing of vegetation. Principles, techniques, and applications* (1st ed.). Oxford. Oxford Univ. Press.

Jordan, C.F. (1969): Derivation of leaf-area index from quality of light on the forest floor. *Ecology 50* (4), 663–666.

Jupp, D., Walker, J., & Penridge, L. (1986): Interpretation of vegetation structure in Landsat MSS imagery: a case study in disturbed semi-arid eucalypt woodlands, Part 2: Model-based analysis. *Journal of Environmental Management 23,* 35–57.

Justice, C., & Townshend, J. (1982): A comparison of unsupervised classification procedures on Landsat MSS data for an area of complex surface conditions in Basilicata, Southern Italy. *Remote Sensing of Environment 12* (5), 407–420.

Kalácska, M., Sánchez-Azofeifa, G., Rivard, B., Calvo-Alvarado, J., Journet, A., & Arroyo-Mora, J. (2004): Leaf area index measurements in a tropical moist forest: A case study from Costa Rica. *Remote Sensing of Environment 91* (2), 134–152.

Kanemasu, E., Niblett, C., Manges, H., Lenhert, D., & Newman, M. (1974): Wheat: its growth and disease severity as deduced from ERTS-1. *Remote Sensing of Environment 3* (4), 255–260.

Karnieli, A., Kaufman, Y.J., Remer, L., & Wald, A. (2001): AFRI — aerosol free vegetation index. *Remote Sensing of Environment 77* (1), 10–21.

Kaufman, Y., & Tanre, D. (1992): Atmospherically resistant vegetation index (ARVI) for EOS-MODIS. *IEEE Transactions on Geoscience and Remote Sensing 30* (2), 261–270.

Kaufman, Y., Wald, A., Remer, L., Bo-Cai Gao, Rong-Rong Li, & Flynn, L. (1997): The MODIS 2.1-µm channel-correlation with visible reflectance for use in remote sensing of aerosol. *IEEE Transactions on Geoscience and Remote Sensing 35* (5), 1286–1298.

Kauth, R.J., & Thomas, G.S. (1976): The Tasselled Cap - A graphic description of the spectral-temporal development of agricultural crops as seen by Landsat. In *LARS Symposia. Paper 159* (pp. 41–51).

Kimes, D., Gastellu-Etchegorry, J., & Estève, P. (2002): Recovery of forest canopy characteristics through inversion of a complex 3D model. *Remote Sensing of Environment 79* (2-3), 320–328.

Kimes, D.S. (1983): Dynamics of directional reflectance factor distributions for vegetation canopies. *Applied Optics 22* (9), 1364–1372.

Kimes, D.S., Knyazikhin, Y., Privette, J., Abuelgasim, A.A., & Gao, F. (2000): Inversion methods for physically-based models. *Remote Sensing Reviews 18* (2-4), 381–439.

Kimes, D.S., Nelson, R.F., Manry, M.T., & Fung, A.K. (1998): Review article: Attributes of neural networks for extracting continuous vegetation variables from optical and radar measurements. *International Journal of Remote Sensing 19* (14), 2639–2663.

Klapp, E. (1971): *Wiesen und Weiden. Eine Grünlandlehre*. Blackwell Wissenschafts-Verlag.

Klug, P., Schlenz, F:, Hank, T.B., Migdall, S., Bach, H., & Mauser, W. (2014): Generation of continuous agricultural information products using multi-temporal high resolution optical da-ta in a model framework – The M4Land project. In ESA (Ed.), *Sentinel-2 for Science Workshop* (p. 14–14).

Knyazikhin, Y., Martonchik, J.V., Myneni, R.B., Diner, D.J., & Running, S.W. (1998): Synergistic algorithm for estimating vegetation canopy leaf area index and fraction of absorbed photosynthetically active radiation from MODIS and MISR data. *Journal of Geophysical Research 103* (D24), 32257–32275.

Knyazikhin, Y.V., Marshak, A.L., & Myneni, R.B. (1992): Interaction of photons in a canopy of finite-dimensional leaves. *Remote Sensing of Environment 39* (1), 61–74.

Kobayashi, H., & Iwabuchi, H. (2008): A coupled 1-D atmosphere and 3-D canopy radiative transfer model for canopy reflectance, light environment, and photosynthesis simulation in a heterogeneous landscape. *Remote Sensing of Environment 112* (1), 173–185.

Koetz, B., Baret, F., Poilvé, H., & Hill, J. (2005a): Use of coupled canopy structure dynamic and radiative transfer models to estimate biophysical canopy characteristics. *Remote Sensing of Environment 95* (1), 115–124.

Koetz, B., Kneubuehler M., Huber S., Schopfer J., & Baret, F. (2007a): LAI estimation based on multi-temporal CHRIS/PROBA data and radiative transfer modeling. In *Proc. Envisat Symposium 2007* (pp. 1–6).

Koetz, B., Kneubühler, M., Widlowski, J.-L., Morsdorf, F., Schaepman, M., & Itten, K. (2005b): Assessment of canopy structure and heterogeneity from multi-angular CHRIS-PROBA data. In *Proceedings of the 9th International Symposium on Physical Measurements and Signatures in Remote Sensing (ISPMSRS)* (pp. 73–78).

Koetz, B., Sun, G., Morsdorf, F., Ranson, K.J., Kneubühler, M., Itten, K., & Allgöwer, B. (2007b): Fusion of imaging spectrometer and LIDAR data over combined radiative transfer models for forest canopy characterization. *Remote Sensing of Environment 106* (4), 449–459.

Kohavi, R. (1995): A study of cross-validation and bootstrap for accuracy estimation and model selection. In *IJCAI'95 Proceedings of the 14th international joint conference on Artificial intelligence* (pp. 1137–1143).

Köhl, M., Lister, A., Scott, C.T., Baldauf, T., & Plugge, D. (2011): Implications of sampling design and sample size for national carbon accounting systems. *Carbon Balance and Management 6* (10), 1–20.

Konica Minolta: Chlorophyll meter SPAD-502Plus. Online available at: http://www.konicaminolta.eu/fileadmin/content/eu/Measuring_Instruments/2_Products/1_Colour_Measurement/6_Chlorophyll_Meter/PDF/Spad502plus_EN.pdf.

Kötz, B., Schaepman, M., Morsdorf, F., Bowyer, P., Itten, K., & Allgöwer, B. (2004): Radiative transfer modeling within a heterogeneous canopy for estimation of forest fire fuel properties. *Remote Sensing of Environment 92* (3), 332–344.

Kraus, T. (2008): Ground-based validation of the MODIS leaf area index product for east African rain forest ecosystems. Dissertation. Erlangen-Nürnberg.

Kubelka, P., & Munk, F. (1931): Ein Beitrag zur Optik der Farbanstriche. *Zeitschrift für technische Physik 12,* 593–601.

Kucharik, C.J., Norman, J.M., Murdock, L.M., & Gower, S.T. (1997): Characterizing canopy nonrandomness with a multiband vegetation imager (MVI). *Journal of Geophysical Research 102* (D24), 29455–29473.

Kunstmann, H. (2008): Effective SVAT-model parameters through inverse stochastic modelling and second-order first moment propagation. *Journal of Hydrology 348* (1-2), 13–26.

Kunstmann, H., Schneider, K., Forkel, R., & Knoche, R. (2004): Impact analysis of climate change for an Alpine catchment using high resolution dynamic downscaling of ECHAM4 time slices. *Hydrology and Earth System Sciences 8* (6), 1031–1045.

Küßner, R., & Mosandl, R. (2000): Comparison of direct and indirect estimation of leaf area index in mature Norway spruce stands of eastern Germany. *Canadian Journal of Forest Research 30* (3), 440–447.

Kuusk, A. (1985): The hot spot effect of a uniform vegetation cover. *Soviet Journal of Remote Sensing 3* (4), 645–658.

Kuusk, A. (1991): The hot spot effect in plant canopy reflectance. In R.B. Myneni, & J. Ross (Eds.), *Photon-Vegetation Interactions* (pp. 139–159). Berlin, Heidelberg. Springer Berlin Heidelberg.

Kuusk, A. (1995a): A fast, invertible canopy reflectance model. *Remote Sensing of Environment 51* (3), 342–350.

Kuusk, A. (1995b): A Markov chain model of canopy reflectance. *Agricultural and Forest Meteorology 76* (3-4), 221–236.

Kuusk, A. (2000): A directional multispectral forest reflectance model. *Remote Sensing of Environment 72* (2), 244–252.

Lacaze, R. (2005): POLDER-2 land surface level-3 products. User manual algorithm description & product validation. Issue 1.40. MEDIAS-France.

Lamanda, N., Dauzat, J., Jourdan, C., Martin, P., & Malézieux, E. (2007): Using 3D architectural models to assess light availability and root bulkiness in coconut agroforestry systems. *Agroforestry Systems 72* (1), 63–74.

Landsberg, J.J., & Gower, S.T. (1997): *Applications of physiological ecology to forest management*. San Diego. Acad. Press.

Lang, A. (1987): Simplified estimate of leaf area index from transmittance of the sun's beam. *Agricultural and Forest Meteorology 41* (3-4), 179–186.

Lang, A., McMurtrie, R., & Benson, M. (1991): Validity of surface area indices of Pinus radiata estimated from transmittance of the sun's beam. *Agricultural and Forest Meteorology 57* (1-3), 157–170.

Lang, A., & Xiang, Y. (1986): Estimation of leaf area index from transmission of direct sunlight in discontinuous canopies. *Agricultural and Forest Meteorology 37* (3), 229–243.

Lang, A., Yueqin, X., & Norman, J. (1985): Crop structure and the penetration of direct sunlight. *Agricultural and Forest Meteorology 35* (1-4), 83–101.

Lang, A.R. (1986): Leaf-area and average leaf angle from transmission of direct sunlight. *Australian Journal of Botany 34* (3), 349–355.

Larsson, H. (1993): Linear regressions for canopy cover estimation in Acacia woodlands using Landsat-TM, -MSS and SPOT HRV XS data. *International Journal of Remote Sensing 14* (11), 2129–2136.

Launay, M., & Guerif, M. (2005): Assimilating remote sensing data into a crop model to improve predictive performance for spatial applications. *Agriculture, Ecosystems & Environment 111* (1-4), 321–339.

Laurent, V.C., Schaepman, M.E., Verhoef, W., Weyermann, J., & Chávez, R.O. (2014): Bayesian object-based estimation of LAI and chlorophyll from a simulated Sentinel-2 top-of-atmosphere radiance image. *Remote Sensing of Environment 140,* 318–329.

Laurent, V.C., Verhoef, W., Clevers, J.G., & Schaepman, M.E. (2011): Estimating forest variables from top-of-atmosphere radiance satellite measurements using coupled radiative transfer models. *Remote Sensing of Environment 115* (4), 1043–1052.

Laurent, V.C., Verhoef, W., Damm, A., Schaepman, M.E., & Clevers, J.G. (2013): A Bayesian object-based approach for estimating vegetation biophysical and biochemical variables from APEX at-sensor radiance data. *Remote Sensing of Environment 139,* 6–17.

Lauvernet, C., Baret, F., Hascoët, L., Buis, S., & Le Dimet, F.-X. (2008): Multitemporal-patch ensemble inversion of coupled surface–atmosphere radiative transfer models for land surface characterization. *Remote Sensing of Environment 112* (3), 851–861.

Lavergne, T., Kaminski, T., Pinty, B., Taberner, M., Gobron, N., Verstraete, M.M., Vossbeck, M., Widlowski, J.-L., & Giering, R. (2007): Application to MISR land products of an RPV model inversion package using adjoint and Hessian codes. *Remote Sensing of Environment 107* (1-2), 362–375.

Le Dantec, V., Dufrêne, E., & Saugier, B. (2000): Interannual and spatial variation in maximum leaf area index of temperate deciduous stands. *Forest Ecology and Management 134* (1-3), 71–81.

Le Maire, G., François, C., & Dufrêne, E. (2004): Towards universal broad leaf chlorophyll indices using PROSPECT simulated database and hyperspectral reflectance measurements. *Remote Sensing of Environment 89* (1), 1–28.

Le Maire, G., François, C., Soudani, K., Berveiller, D., Pontailler, J.-Y., Bréda, N., Genet, H., Davi, H., & Dufrêne, E. (2008): Calibration and validation of hyperspectral indices for the estimation of broadleaved forest leaf chlorophyll content, leaf mass per area, leaf area index and leaf canopy biomass. *Remote Sensing of Environment 112* (10), 3846–3864.

Le Maire, G., Marsden, C., Nouvellon, Y., Grinand, C., Hakamada, R., Stape, J.-L., & Laclau, J.-P. (2011): MODIS NDVI time-series allow the monitoring of Eucalyptus plantation biomass. *Remote Sensing of Environment 115* (10), 2613–2625.

Leblanc, S.G. (2002): Correction to the plant canopy gap-size analysis theory used by the tracing radiation and architecture of canopies instrument. *Applied Optics 41* (36), 7667–7670.

Leblanc, S.G. (2004): Digital hemispherical photography manual. Version 1.0. Canada Centre for Remote Sensing, Natural. Ottawa.

Leblanc, S.G., & Chen, J.M. (2001): A practical scheme for correcting multiple scattering effects on optical LAI measurements. *Agricultural and Forest Meteorology 110* (2), 125–139.

Leblanc, S.G., Chen, J.M., Fernandes, R., Deering, D.W., & Conley, A. (2005): Methodology comparison for canopy structure parameters extraction from digital hemispherical photography in boreal forests. *Agricultural and Forest Meteorology 129* (3-4), 187–207.

Lee, K.-S., Cohen, W.B., Kennedy, R.E., Maiersperger, T.K., & Gower, S.T. (2004): Hyperspectral versus multispectral data for estimating leaf area index in four different biomes. *Remote Sensing of Environment 91* (3-4), 508–520.

Lefsky, M.A., Cohen, W.B., Parker, G.G., & Harding, D.J. (2002): Lidar remote sensing for ecosystem studies. *BioScience 52* (1), 19–30.

Leonenko, G., Los, S., & North, P. (2013a): Retrieval of leaf area index from MODIS surface reflectance by model inversion using different minimization criteria. *Remote Sensing of Environment 139,* 257–270.

Leonenko, G., Los, S., & North, P. (2013b): Statistical distances and their applications to biophysical parameter estimation: Information measures, M-estimates, and minimum contrast methods. *Remote Sensing 5* (3), 1355–1388.

Levy, P., & Jarvis, P. (1999): Direct and indirect measurements of LAI in millet and fallow vegetation in HAPEX-Sahel. *Agricultural and Forest Meteorology 97* (3), 199–212.

Lex, S., Conrad, C., & Schorcht, G. (2013): Analyzing the seasonal relations between in situ fpar / LAI of cotton and spectral information of RapidEye. In E. Borg, H. Daedelow, & R.

Johnson (Eds.), *From the basics to the service : proceedings of the 5th RESA-Workshop* (pp. 143–156). Berlin. GITO.

Li, X., & Strahler, A. (1985): Geometric-optical modeling of a conifer forest canopy. *IEEE Transactions on Geoscience and Remote Sensing 23* (5), 705–721.

Li, X., & Strahler, A. (1986): Geometric-optical bidirectional reflectance modeling of a conifer forest canopy. *IEEE Transactions on Geoscience and Remote Sensing 24* (6), 906–919.

Li, X., & Strahler, A. (1992): Geometric-optical bidirectional reflectance modeling of the discrete crown vegetation canopy: effect of crown shape and mutual shadowing. *IEEE Transactions on Geoscience and Remote Sensing 30* (2), 276–292.

Liang, S. (Ed.) (2004): Quantitative remote sensing of land surfaces. Hoboken, N.J. Wiley-Interscience.

Liang, S. (Ed.) (2008): Advances in Land Remote Sensing: System, Modeling, Inversion and Application. Springer.

Liang, S., Fallah-Adl, H., Kalluri, S., JáJá, J., Kaufman, Y.J., & Townshend, J.R.G. (1997): An operational atmospheric correction algorithm for Landsat Thematic Mapper imagery over the land. *Journal of Geophysical Research 102* (D14), 17173–17186.

Liang, S., Fang, H., & Chen, M. (2001): Atmospheric correction of Landsat ETM+ land surface imagery. Part I: Methods. *IEEE Transactions on Geoscience and Remote Sensing 39* (11), 2490–2498.

Liang, S., & Strahler, A. (1993): An analytic BRDF model of canopy radiative transfer and its inversion. *IEEE Transactions on Geoscience and Remote Sensing 31* (5), 1081–1092.

Liang, S., & Strahler, A. (1994): Retrieval of surface BRDF from multiangle remotely sensed data. *Remote Sensing of Environment 50* (1), 18–30.

Liang, S., & Strahler, A. (2000): Land surface bi-directional reflectance distribution function (BRDF): Recent advances and future prospects. *Remote Sensing Reviews 18,* 83–511.

Liaw, A., & Wiener, M. (2002): Classification and regression by randomForest. *R News 2* (3), 18–22.

LI-COR (2009): LAI-2200 Plant Canopy Analyzer. Instruction Manual. LI-COR Inc. Lincoln.

Lillesand, T.M., & Kiefer, R.W. (2000): *Remote sensing and image interpretation* (4th ed.). New York. Wiley.

Löw, F., Michel, U., Dech, S., & Conrad, C. (2013): Impact of feature selection on the accuracy and spatial uncertainty of per-field crop classification using support vector machines. *ISPRS Journal of Photogrammetry and Remote Sensing 85,* 102–119.

Löw, F., Schorcht, G., Michel, U., Dech, S., & Conrad, C. (2012): Per-field crop classification in irrigated agricultural regions in middle Asia using random forest and support vector machine ensemble. In S. Habib, D. Messinger, A. Maltese, U. Michel, D.L. Civco, M. Ehlers, K. Schulz, & K.G. Nikolakopoulos (Eds.), *SPIE Proceedings 8538*.

Lucht, W., Schaaf, C., & Strahler, A. (2000): An algorithm for the retrieval of albedo from space using semiempirical BRDF models. *IEEE Transactions on Geoscience and Remote Sensing 38* (2), 977–998.

Ludwig, R. (2000): *Die flächenverteilte Modellierung von Wasserhaushalt und Abflussbildung im Einzugsgebiet der Ammer*. Münchner Geographische Abhandlungen *32*. München, Germany.

Macfarlane, C., Coote, M., White, D.A., & Adams, M.A. (2000): Photographic exposure affects indirect estimation of leaf area in plantations of Eucalyptus globulus Labill. *Agricultural and Forest Meteorology 100* (2-3), 155–168.

Macfarlane, C., Hoffman, M., Eamus, D., Kerp, N., Higginson, S., McMurtrie, R., & Adams, M.A. (2007): Estimation of leaf area index in eucalypt forest using digital photography. *Agricultural and Forest Meteorology 143* (3-4), 176–188.

Madeira, A., Gillespie, T., & Duke, C. (2001): Effect of wetness on turfgrass canopy reflectance. *Agricultural and Forest Meteorology 107* (2), 117–130.

Maier, S. (2000): Modeling the radiative transfer in leaves in the 300nm to 2.5µm wavelength region taking into consideration chlorophyll fluorescence - The leaf model SLOPE. Dissertation. Munich.

Major, D., Schaalje, G., Wiegand, C., & Blad, B. (1992): Accuracy and sensitivity analyses of SAIL model-predicted reflectance of maize. *Remote Sensing of Environment 41* (1), 61–70.

Mannschatz, T., & Dietrich, P. (2013): Uncertainties of LAI estimation from satellite images due to atmospheric correction. In E. Borg, H. Daedelow, & R. Johnson (Eds.), *From the basics to the service : proceedings of the 5th RESA-Workshop* (pp. 273–289). Berlin. GITO.

Markwell, J., Osterman, J.C., & Mitchell, J.L. (1995): Calibration of the Minolta SPAD-502 leaf chlorophyll meter. *Photosynthesis Research 46* (3), 467–472.

Martonchik, J.V., Bruegge, C.J., & Strahler, A.H. (2000): A review of reflectance nomenclature used in remote sensing. *Remote Sensing Reviews 19* (1-4), 9–20.

Masson, V., Champeaux, J.-L., Chauvin, F., Meriguet, C., & Lacaze, R. (2003): A global database of land surface parameters at 1-km resolution in meteorological and climate models. *Journal of Climate 16* (9), 1261–1282.

Matsushita, B., & Tamura, M. (2002): Integrating remotely sensed data with an ecosystem model to estimate net primary productivity in East Asia. *Remote Sensing of Environment 81* (1), 58–66.

McCoy, R.M. (2005): *Field methods in remote sensing*. New York. Guilford Press.

Medhurst, J.L., & Beadle, C.L. (2001): Crown structure and leaf area index development in thinned and unthinned Eucalyptus nitens plantations. *Tree physiology 21* (12-13), 989–999.

Meroni, M., Colombo, R., & Panigada, C. (2004): Inversion of a radiative transfer model with hyperspectral observations for LAI mapping in poplar plantations. *Remote Sensing of Environment 92* (2), 195–206.

Meyer, R.K.F., & Schmidt-Kaler, H. (1997): *Wanderungen in die Erdgeschichte – Band 8: Auf den Spuren der Eiszeit südlich von München - östlicher Teil* (2nd ed.). Pfeil Verlag.

Miller, J. (1967): A formula for average foliage density. *Australian Journal of Botany 15,* 141–144.

Miller, J., Berger, M., Goulas, Y., Jacquemoud, S., Louis, J., Moise, N., Mohammed, G., Moreno, J., Moya, I., Pedrós, R., Verhoef, W., & Zarco-Tejada, P. (2005): Development of a Vegetation Fluorescence Canopy Model. ESTEC Contract No. 16365/02/NL/FF, Final Report.

Monsi, M., & Saeki, T. (1953): Über den Lichtfaktor in den Pflanzengesellschaften und seine Bedeutung für die Stoffproduktion. *Japanese Journal of Botany 14,* 22–52.

Morisette, J., Baret, F., Privette, J., Myneni, R., Nickeson, J., Garrigues, S., Shabanov, N., Weiss, M., Fernandes, R., Leblanc, S., Kalacska, M., Sanchez-Azofeifa, G., Chubey, M., Rivard, B., Stenberg, P., Rautiainen, M., Voipio, P., Manninen, T., Pilant, A., Lewis, T., Iiames, J., Colombo, R., Meroni, M., Busetto, L., Cohen, W., Turner, D., Warner, E., Petersen, G., Seufert, G., & Cook, R. (2006): Validation of global moderate-resolution LAI products: a framework proposed within the CEOS land product validation subgroup. *IEEE Transactions on Geoscience and Remote Sensing 44* (7), 1804–1817.

Moulin, S., Bondeau, A., & Delecolle, R. (1998): Combining agricultural crop models and satellite observations: From field to regional scales. *International Journal of Remote Sensing 19* (6), 1021–1036.

Mu, X., Yan, G., & Li, Z. (2008): Uncertainty and sensitivity ratio of parameters in estimating and promoting retrieval accuracy. *International Journal of Remote Sensing 29* (17-18), 4891–4905.

Mueller, E.N., Güntner, A., Francke, T., & Mamede, G. (2008): Modelling water availability, sediment export and reservoir sedimentation in drylands with the WASA-SED Model. *Geoscientific Model Development Discussions 1* (1), 285–314.

Mutanga, O., Skidmore, A., & Prins, H. (2004): Predicting in situ pasture quality in the Kruger National Park, South Africa, using continuum-removed absorption features. *Remote Sensing of Environment 89* (3), 393–408.

Myneni, R., Hoffman, S., Knyazikhin, Y., Privette, J., Glassy, J., Tian, Y., Wang, Y., Song, X., Zhang, Y., Smith, G., Lotsch, A., Friedl, M., Morisette, J., Votava, P., Nemani, R., & Running, S. (2002): Global products of vegetation leaf area and fraction absorbed PAR from year one of MODIS data. *Remote Sensing of Environment 83* (1-2), 214–231.

Myneni, R., Ramakrishna, R., Nemani, R., & Running, S. (1997): Estimation of global leaf area index and absorbed par using radiative transfer models. *IEEE Transactions on Geoscience and Remote Sensing 35* (6), 1380–1393.

Myneni, R.B., Asrar, G., & Gerstl, S.A. (1990): Radiative transfer in three dimensional leaf canopies. *Transport Theory and Statistical Physics 19* (3-5), 205–250.

Myneni, R.B., & Ross, J. (Eds.) (1991): Photon-Vegetation Interactions. Berlin, Heidelberg. Springer Berlin Heidelberg.

Nackaerts, K., Coppin, P., Muys, B., & Hermy, M. (2000): Sampling methodology for LAI measurements with LAI-2000 in small forest stands. *Agricultural and Forest Meteorology 101* (4), 247–250.

Nagy, L., Grabherr, G., Körner, C., & Thompson, D.B.A. (Eds.) (2003): Alpine Biodiversity in Europe. Berlin, Heidelberg. Springer.

Navulur, K. (2006): *Multispectral Image Analysis Using the Object-Oriented Paradigm.* CRC Press.

Nemani, R., Pierce, L., Running, S., & Band, L. (1993): Forest ecosystem processes at the watershed scale: sensitivity to remotely-sensed leaf area index estimates. *International Journal of Remote Sensing 14* (13), 2519–2534.

Neumann, H., Den Hartog, G., & Shaw, R. (1989): Leaf area measurements based on hemispheric photographs and leaf-litter collection in a deciduous forest during autumn leaf-fall. *Agricultural and Forest Meteorology 45* (3-4), 325–345.

Nieke, J., Solbrig, M., & Neumann, A. (1999): Noise contributions for imaging spectrometers. *Applied Optics 38* (24), 5191–5194.

Nilson, T. (1971): A theoretical analysis of the frequency of gaps in plant stands. *Agricultural Meteorology 8,* 25–38.

Nilson, T., & Kuusk, A. (1989): A reflectance model for the homogeneous plant canopy and its inversion. *Remote Sensing of Environment 27* (2), 157–167.

Nilson, T., & Peterson, U. (1991): A forest canopy reflectance model and a test case. *Remote Sensing of Environment 37* (2), 131–142.

Norman, J.M., & Campbell, G. (1989): Canopy structure. In R. Pearcy, J. Ehleringer, H. Mooney, & P. Rundel (Eds.), *Plant physiological ecology: Field methods and instrumentation* (pp. 301–325). London. Chapman and Hall.

North, P. (1996): Three-dimensional forest light interaction model using a Monte Carlo method. *IEEE Transactions on Geoscience and Remote Sensing 34* (4), 946–956.

North, P.R. (2002): Estimation of fAPAR, LAI, and vegetation fractional cover from ATSR-2 imagery. *Remote Sensing of Environment 80* (1), 114–121.

Oehmichen, G. (2004): Auf Satellitendaten basierende Ableitungen von Parametern zur Beschreibung Terrestrischer Ökosysteme. Methodische Untersuchung zur Ableitung der Chlorophyll(a+b)-Konzentration und des Blattflächenindexes aus Fernerkundungsdaten. Dissertation. Berlin.

O'Hara, K.L., & Valappil, N.I. (1995): Sapwood–leaf area prediction equations for multi-aged ponderosa pine stands in western Montana and central Oregon. *Canadian Journal of Forest Research 25* (9), 1553–1557.

Olioso, A., Inoue, Y., Ortega-FARIAS, S., Demarty, J., Wigneron, J.-P., Braud, I., Jacob, F., Lecharpentier, P., Ottlé, C., Calvet, J.-C., & Brisson, N. (2005): Future directions for advanced evapotranspiration modeling: Assimilation of remote sensing data into crop simulation models and SVAT models. *Irrigation and Drainage Systems 19* (3-4), 377–412.

Pal, M. (2005): Random forest classifier for remote sensing classification. *International Journal of Remote Sensing 26* (1), 217–222.

Pasolli, L. (2012): Advanced methods for the retrieval of geo-/bio-physical variables from remote sensing imagery. Dissertation. University of Trento.

Pasolli, L., Notarnicola, C., Bruzzone, L., & Zebisch, M. (2011): Spatial and temporal mapping of leaf area index in Alpine pastures and meadows with satellite MODIS imagery. In L. Bruzzone (Ed.), *6th international workshop on the analysis of multi-temporal remote sensing images (MultiTemp), 2011* (pp. 109–112).

Pauli, H., Gottfried, M., Dirnböck, T., Dullinger, S., & Grabherr, G. (2003a): Assessing the long-term dynamics of endemic plants at summit habitats. In L. Nagy, G. Grabherr, C. Körner, & D.B.A. Thompson (Eds.), *Alpine Biodiversity in Europe* (pp. 195–207). Berlin, Heidelberg. Springer.

Pauli, H., Gottfried, M., & Grabherr, G. (2003b): Effects of climate change on the alpine and nival vegetation of the Alps. *Journal of Mountain Ecology 7* (suppl.), 9–12.

Pearson, R.L., & Miller, L.D. (1972): *Remote mapping of standing crop biomass for estimation of the productivity of the short-grass Prairie, Pawnee National Grasslands, Colorado*. Fort Collins, Colorado. Colorado State University.

Peterson, D.L., Spanner, M.A., Running, S.W., & Teuber, K.B. (1987): Relationship of thematic mapper simulator data to leaf area index of temperate coniferous forests. *Remote Sensing of Environment 22* (3), 323–341.

Pinty, B., Gobron, N., Widlowski, J.-L., Gerstl, S.A.W., Verstraete, M.M., Antunes, M., Bacour, C., Gascon, F., Gastellu, J.-P., Goel, N., Jacquemoud, S., North, P., Qin, W., & Thompson, R. (2001): Radiation transfer model intercomparison (RAMI) exercise. *Journal of Geophysical Research: Atmospheres 106* (D11), 11937–11956.

Pinty, B., & Verstraete, M.M. (1991): Extracting information on surface properties from bidirectional reflectance measurements. *Journal of Geophysical Research 96* (D2), 2865–2874.

Pinty, B., Verstraete, M.M., & Dickinson, R.E. (1990): A physical model of the bidirectional reflectance of vegetation canopies: 2. Inversion and validation. *Journal of Geophysical Research 95* (D8), 11767–11775.

Pinty, B.W.J.-L., Taberner, M., Gobron, N., Verstraete, M.M., Disney, M., Gascon, F., Gastellu, J.-P., Jiang, L., Kuusk, A., Lewis, P., Li, X., Ni-Meister, W., Nilson, T., North, P., Qin, W., Su, L., Tang, S., Thompson, R., Verhoef, W., Wang, H., Wang, J., Yan, G., & Zang, H. (2004): Radiation transfer model intercomparison (RAMI) exercise: Results from the second phase. *Journal of Geophysical Research 109* (D6), 1–19.

Planchais, I., & Pontailler, J.-Y. (1999): Validity of leaf areas and angles estimated in a beech forest from analysis of gap frequencies, using hemispherical photographs and a plant canopy analyzer. *Annals of Forest Science 56* (1), 1–10.

Plummer, S., Arino, O., Simon, M., & Steffen, W. (2006): Establishing a earth observation product service for the terrestrial carbon community: The Globcarbon initiative. *Mitigation and Adaptation Strategies for Global Change 11* (1), 97–111.

Poilvé, H. (2012): BioPar Product User Manual MERIS FR Biophysical Products. g2-BP-RP-BP053. Astrium GeoInformation Services. Online available at: http://web.vgt.vito.be/documents/BioPar/g2-BP-RP-BP053-ProductUserManual-MERISFR-I1.50.pdf.

Poorter, H., Niinemets, Ü., Poorter, L., Wright, I.J., & Villar, R. (2009): Causes and consequences of variation in leaf mass per area (LMA): A meta-analysis. *New Phytologist 182* (3), 565–588.

Potithep, S., Nagai, S., Nasahara, K.N., Muraoka, H., & Suzuki, R. (2013): Two separate periods of the LAI–VIs relationships using in situ measurements in a deciduous broadleaf forest. *Agricultural and Forest Meteorology 169,* 148–155.

Potter, C., Li, S., Huang, S., & Crabtree, R.L. (2012): Analysis of sapling density regeneration in Yellowstone National Park with hyperspectral remote sensing data. *Remote Sensing of Environment 121,* 61–68.

Powell, S.L., Cohen, W.B., Healey, S.P., Kennedy, R.E., Moisen, G.G., Pierce, K.B., & Ohmann, J.L. (2010): Quantification of live aboveground forest biomass dynamics with Landsat time-series and field inventory data: A comparison of empirical modeling approaches. *Remote Sensing of Environment 114* (5), 1053–1068.

Privette, J., Myneni, R., Emery, W., & Hall, F. (1996): Optimal sampling conditions for estimating grassland parameters via reflectance. *IEEE Transactions on Geoscience and Remote Sensing 34* (1), 272–284.

Privette, J., Myneni, R., Tucker, C., & Emery, W. (1994): Invertibility of a 1-D discrete ordinates canopy reflectance model. *Remote Sensing of Environment 48* (1), 89–105.

Privette, J.L., Eck, T.F., & Deering, D.W. (1997): Estimating spectral albedo and nadir reflectance through inversion of simple BRDF models with AVHRR/MODIS-like data. *Journal of Geophysical Research 102* (D24), 29529–29542.

Pujol, G., Iooss, B., & Janon, A. (2013): *Sensitivity v1.7. Sensitivity Analysis*. R Package.

Qi, J., Chehbouni, A., Huete, A., Kerr, Y., & Sorooshian, S. (1994): A modified soil adjusted vegetation index. *Remote Sensing of Environment 48,* 119–207.

Qin, W., & Gerstl, S.A. (2000): 3-D scene modeling of semidesert vegetation cover and its radiation regime. *Remote Sensing of Environment 74* (1), 145–162.

Qiu, J., Gao, W., & Lesht, B.M. (1998): Inverting optical reflectance to estimate surface properties of vegetation canopies. *International Journal of Remote Sensing 19* (4), 641–656.

Quaife, T., Lewis, P., Dekauwe, M., Williams, M., Law, B., Disney, M., & Bowyer, P. (2008): Assimilating canopy reflectance data into an ecosystem model with an Ensemble Kalman Filter. *Remote Sensing of Environment 112* (4), 1347–1364.

R Development Core Team (2008): *R: A language and environment for statistical computing*. Vienna, Austria.

Rabus, B., Eineder, M., Roth, A., & Bamler, R. (2003): The shuttle radar topography mission—a new class of digital elevation models acquired by spaceborne radar. *ISPRS Journal of Photogrammetry and Remote Sensing 57* (4), 241–262.

Rammig, A., Jonas, T., Zimmermann, N.E., & Rixen, C. (2010): Changes in alpine plant growth under future climate conditions. *Biogeosciences 7* (6), 2013–2024.

RapidEye (2011): Satellite Imagery Product Specifications. Version 3.2. RapidEye AG.

Reid, W.V. (2005): *Ecosystems and human well-being. Synthesis.* A report of the Millennium Ecosystems Assessment. Washington, DC. Island Press.

Reulke, R., & Weichelt, H. (2012): SNR evaluation of the RapidEye space-borne cameras. *Photogrammetrie - Fernerkundung - Geoinformation 2012* (1), 29–38.

Rich, P.M. (1990): Characterizing plant canopies with hemispherical photographs. *Remote Sensing Reviews 5* (1), 13–29.

Richards, J.A., & Jia, X. (2006): *Remote sensing digital image analysis. An introduction* (4th ed.). Berlin. Springer.

Richardson, A.J., & Wiegand, C.L. (1977): Distinguishing vegetation from soil background information. *Photogrammetric Engineering and Remote Sensing 43* (12), 1541–1552.

Richter, K., Atzberger, C., Hank, T.B., & Mauser, W. (2012a): Derivation of biophysical variables from Earth observation data: validation and statistical measures. *Journal of*

Applied Remote Sensing 6 (1), 63557.

Richter, K., Atzberger, C., Vuolo, F., & D'Urso, G. (2011): Evaluation of Sentinel-2 spectral sampling for radiative transfer model based LAI estimation of wheat, sugar beet, and maize. *IEEE Journal of Selected Topics in Applied Earth Observations and Remote Sensing 4* (2), 458–464.

Richter, K., Atzberger, C., Vuolo, F., Weihs, P., & D'Urso, G. (2009): Experimental assessment of the Sentinel-2 band setting for RTM-based LAI retrieval of sugar beet and maize. *Canadian Journal of Remote Sensing 35* (3), 230–247.

Richter, K., Hank, T.B., Vuolo, F., Mauser, W., & D'Urso, G. (2012b): Optimal exploitation of the Sentinel-2 spectral capabilities for crop leaf area index mapping. *Remote Sensing 4* (12), 561–582.

Richter, R., & Schläpfer, D. (2012): Atmospheric / Topographic correction for satellite imagery. ATCOR-2/3 User Guide, Version 8.2 BETA. DLR - German Aerospace Center, Remote Sensing Data Center.

Richter, T., & Fukshansky, L. (1996): Optics of a bifacial leaf: 1. A novel combined procedure for deriving the optical parameters. *Photochemistry and Photobiology 63* (4), 507–516.

Rinaldi, M., Ruggieri, S., Garofalo, P., Vonella, A.V., Satalino, G., & Soldo, P. (2010): Leaf area index retrieval using high resolution remote sensing data. *Italian Journal of Agronomy 5,* 155–166.

Rippl, C.F. (2011): Thermische Entwicklung des Ammersees als regionale Auswirkung des Globalen Wandels. Dissertation. Fakultät für Geowissenschaften. München.

Rivera, J., Verrelst, J., Leonenko, G., & Moreno, J. (2013): Multiple cost functions and regularization options for improved retrieval of leaf chlorophyll content and LAI through inversion of the PROSAIL model. *Remote Sensing 5* (7), 3280–3304.

Rochdi, N., & Fernandes, R. (2010): Systematic mapping of leaf area index across Canada using 250-meter MODIS data. *Remote Sensing of Environment 114* (5), 1130–1135.

Rogers, R., & Hinckley, T.M. (1979): Foliar weight and area related to current sapwood area in oak. *Forest Science 25* (2), 298–303.

Rondeaux, G., Steven, M., & Baret, F. (1996): Optimization of soil-adjusted vegetation indices. *Remote Sensing of Environment 55* (2), 95–107.

Rosema, A., Verhoef, W., Noorbergen, H., & Borgesius, J. (1992): A new forest light interaction model in support of forest monitoring. *Remote Sensing of Environment 42* (1), 23–41.

Rosema, A., Verhoef, W., Schroote, J., & SNEL, J. (1991): Simulating fluorescence light-canopy interaction in support of laser-induced fluorescence measurements. *Remote Sensing of Environment 37* (2), 117–130.

Rosenqvist, Å., Milne, A., Lucas, R., Imhoff, M., & Dobson, C. (2003): A review of remote sensing technology in support of the Kyoto Protocol. *Environmental Science & Policy 6* (5), 441–455.

Ross, J. (1981): *The radiation regime and architecture of plant stands.* Tasks for vegetation sciences 3 *3*. Dordrecht. Springer.

Roujean, J.-L. (2002): Global mapping of vegetation parameters from POLDER multiangular measurements for studies of surface-atmosphere interactions: A pragmatic method and its validation. *Journal of Geophysical Research 107* (D12), ACL 6-1–ACL 6-14.

Roujean, J.-L., & Bréon, F.M. (1995): Estimating PAR absorbed by vegetation from bidirectional reflectance measurements. *Remote Sensing of Environment 51* (3), 375–384.

Roupsard, O., Dauzat, J., Nouvellon, Y., Deveau, A., Feintrenie, L., Saint-André, L., Mialet-Serra, I., Braconnier, S., Bonnefond, J.-M., Berbigier, P., Epron, D., Jourdan, C., Navarro, M., & Bouillet, J.-P. (2008): Cross-validating Sun-shade and 3D models of light absorption by a tree-crop canopy. *Agricultural and Forest Meteorology 148* (4), 549–

564.

Rouse, J., Haas, R., Schell, J., & Deering, J. (1974): Monitoring vegetation systems in the Great Plains with ERTS. In S.C. Freden, E.P. Mercanti, & M.A. Becker (Eds.), *NASA SP-351: Proceedings of the Third Symposium on Significant Results Obtained with ERTS-1* (pp. 309–317).

Rowland, C., Danson, F., North, P., & Plummer, S. (2001): Comparison of neural network and LUT inversion techniques for retrieving forest LAI. In M. Leroy (Ed.), *Physical measurements and signatures in remote sensing* (pp. 499–504). The Netherlands. Balkema Publishers.

Royston, J.P. (1982): Algorithm AS 181: The W test for normality. *Applied Statistics 31* (2), 176.

Ruecker, G.R., Dorigo, W.A., Lamers, J., Ibragimov, N., Kienzler, K., Strunz, G., & Mueller, A. (2006): Regional estimation of leaf chlorophyll in cotton in Uzbekistan by upscaling a vegetation index from plant scale to Proba-1/CHRIS hyperspectral satellite data. In *Proceedings of the 4th Proba-1/CHRIS-Workshop* (pp. 1–8).

Rumelhart, D.E., Hinton, G.E., & Williams, R.J. (1986): Learning representations by back-propagating errors. *Nature 323* (6088), 533–536.

Running, S.W., & Coughlan, J.C. (1988): A general model of forest ecosystem processes for regional applications I. Hydrologic balance, canopy gas exchange and primary production processes. *Ecological Modelling 42* (2), 125–154.

Running, S.W., Nemani, R.R., Peterson, D.L., Band, L.E., Potts, D.F., Pierce, L.L., & Spanner, M.A. (1989): Mapping regional forest evapotranspiration and photosynthesis by coupling satellite data with ecosystem simulation. *Ecology 70* (4), 1090–1101.

Ryu, Y., Nilson, T., Kobayashi, H., Sonnentag, O., Law, B.E., & Baldocchi, D.D. (2010): On the correct estimation of effective leaf area index: Does it reveal information on clumping effects? *Agricultural and Forest Meteorology 150* (3), 463–472.

Saeki, T. (1975): Distribution of radiant energy and CO2 in terrestrial communities. In J.P. Cooper (Ed.), *Photosynthesis and productivity in different environments*. Cambridge, New York. Cambridge University Press.

Saltelli, A. (1999): Sensitivity analysis: Could better methods be used? *Journal of Geophysical Research 104* (D3), 3789–3793.

Saltelli, A. (2000): *Sensitivity analysis*. Chichester. Wiley.

Saltelli, A. (2008): *Global sensitivity analysis. The primer*. Chichester. Wiley.

Saltelli, A., Tarantola, S., & Chan, K.P.-S. (1999): A quantitative model-independent method for global sensitivity analysis of model output. *Technometrics 41* (1), 39–56.

Sandmeier, S., & Deering, D.W. (1999): Structure analysis and classification of boreal forests using airborne hyperspectral BRDF data from ASAS. *Remote Sensing of Environment 69* (3), 281–295.

Sandmeier, S., & Itten, K. (1999): A field goniometer system (FIGOS) for acquisition of hyperspectral BRDF data. *IEEE Transactions on Geoscience and Remote Sensing 37* (2), 978–986.

Sandmeier, S., Müller, C., Hosgood, B., & Andreoli, G. (1998): Physical mechanisms in hyperspectral BRDF data of grass and watercress. *Remote Sensing of Environment 66* (2), 222–233.

Schaepman-Strub, G., Schaepman, M., Painter, T., Dangel, S., & Martonchik, J. (2006): Reflectance quantities in optical remote sensing—definitions and case studies. *Remote Sensing of Environment 103* (1), 27–42.

Schlerf, M., & Atzberger, C. (2006): Inversion of a forest reflectance model to estimate structural canopy variables from hyperspectral remote sensing data. *Remote Sensing of Environment 100* (3), 281–294.

Schlerf, M., Atzberger, C., & Hill, J. (2005): Remote sensing of forest biophysical variables using HyMap imaging spectrometer data. *Remote Sensing of Environment 95* (2), 177–194.

Schlerf, M., Verhoef, W., Buddenbaum, H., Hill, K., Atzberger, C., & Skidmore, A. (2007): Comparing three canopy reflectance models with hyperspectral multi-angular satellite data. In *Proceedings of the 10th International Symposium on Physical Measurements and Spectral Signatures in Remote Sensing* (pp. 404–407).

Sellers, P.J. (1997): Modeling the exchanges of energy, water, and carbon between continents and the atmosphere. *Science 275* (5299), 502–509.

Sellers, P.J., Tucker, C.J., Collatz, G.J., Los, S.O., Justice, C.O., Dazlich, D.A., & Randall, D.A. (1996): A revised land surface parameterization (SiB2) for atmospheric GCMS. Part II: The generation of global fields of terrestrial biophysical parameters from satellite data. *Journal of Climate 9* (4), 706–737.

Seni, G., & Elder, J.F. (2010): Ensemble methods in data mining: Improving accuracy through combining predictions. *Synthesis Lectures on Data Mining and Knowledge Discovery 2* (1), 1–126.

Shabanov, N.V., Knyazikhin, Y., Baret, F., & Myneni, R.B. (2000): Stochastic modeling of radiation regime in discontinuous vegetation canopies. *Remote Sensing of Environment 74* (1), 125–144.

Si, Y., Schlerf, M., Zurita-Milla, R., Skidmore, A., & Wang, T. (2012): Mapping spatio-temporal variation of grassland quantity and quality using MERIS data and the PROSAIL model. *Remote Sensing of Environment 121,* 415–425.

Silva, J.P. (2008): *LIFE and Europe's grasslands. Restoring a forgotten habitat*. Europäische Kommission / Generaldirektion Umwelt. Luxembourg. Office for Official Publications of the European Communities.

Sims, D.A., & Gamon, J.A. (2002): Relationships between leaf pigment content and spectral reflectance across a wide range of species, leaf structures and developmental stages. *Remote Sensing of Environment 81* (2-3), 337–354.

Smiatek, G., Kunstmann, H., & Werhahn, J. (2012): Implementation and performance analysis of a high resolution coupled numerical weather and river runoff prediction model system for an Alpine catchment. *Environmental Modelling & Software 38,* 231–243.

Smit, H., Metzger, M., & Ewert, F. (2008): Spatial distribution of grassland productivity and land use in Europe. *Agricultural Systems 98* (3), 208–219.

Smith, N.J. (1991): Predicting radiation attenuation in stands of Douglas-Fir. *Forest Science 37* (5), pp. 1213-1223.

Smith, N.J. (1993): Estimating leaf area index and light extinction coefficients in stands of Douglas-fir (Pseudotsugamenziesii). *Canadian Journal of Forest Research 23* (2), 317–321.

Soenen, S., Peddle, D., Coburn, C., Hall, R., & Hall, F. (2009): Canopy reflectance model inversion in multiple forward mode: Forest structural information retrieval from solution set distributions. *Photogrammetric Engineering & Remote Sensing 75* (4), 361–374.

Song, C., Woodcock, C.E., Seto, K.C., Lenney, M.P., & Macomber, S.A. (2001): Classification and change detection using Landsat TM data: When and how to correct atmospheric effects? *Remote Sensing of Environment 75* (2), 230–244.

Soudani, K., François, C., Le Maire, G., Le Dantec, V., & Dufrêne, E. (2006): Comparative analysis of IKONOS, SPOT, and ETM+ data for leaf area index estimation in temperate coniferous and deciduous forest stands. *Remote Sensing of Environment 102* (1-2), 161–175.

Spearman, C. (1907): Demonstration of formulae for true measurement of correlation. *The American Journal of Psychology 18* (2), 161–169.

Sprintsin, M., Karnieli, A., Berliner, P., Rotenberg, E., Yakir, D., & Cohen, S. (2009): Evaluating the performance of the MODIS Leaf Area Index (LAI) product over a

Mediterranean dryland planted forest. *International Journal of Remote Sensing 30* (19), 5061–5069.

Stenberg, P., Linder, S., Smolander, H., & Flower-Ellis, J. (1994): Performance of the LAI-2000 plant canopy analyzer in estimating leaf area index of some Scots pine stands. *Tree Physiology 14* (7-8-9), 981–995.

Stöckli, R., Rutishauser, T., Dragoni, D., O'Keefe, J., Thornton, P.E., Jolly, M., Lu, L., & Denning, A.S. (2008): Remote sensing data assimilation for a prognostic phenology model. *Journal of Geophysical Research 113* (G4), G04021.

Stolz, R. (1998): *Die Verwendung der Fuzzy-Logic-Theorie zur wissensbasierten Klassifikation von Fernerkundungsdaten. Ein methodischer Ansatz zur Verbesserung von Landnutzungsklassifikationen in mesoskaligen heterogenen Räumen, dargestellt am Einzugsgebiet der Ammer.* Münchener geographische Abhandlungen *26*. München. Geobuch-Verlag.

Strahler, A.H., & Jupp, D.L. (1990): Modeling bidirectional reflectance of forests and woodlands using boolean models and geometric optics. *Remote Sensing of Environment 34* (3), 153–166.

Suits, G. (1972): The calculation of the directional reflectance of a vegetative canopy. *Remote Sensing of Environment 2,* 117–125.

Suttie, J.M., Reynolds, S.G., & Batello, C. (Eds.) (2005): Grasslands of the world. Rome. FAO.

Tang, H., Brolly, M., Zhao, F., Strahler, A.H., Schaaf, C.L., Ganguly, S., Zhang, G., & Dubayah, R. (2014): Deriving and validating Leaf Area Index (LAI) at multiple spatial scales through lidar remote sensing: A case study in Sierra National Forest, CA. *Remote Sensing of Environment 143,* 131–141.

Tarantola, A. (2005): *Inverse problem theory and methods for model parameter estimation.* Philadelphia, PA. Siam.

Tewolde, H., Sistani, K.R., Rowe, D.E., Adeli, A., & Tsegaye, T. (2005): Estimating cotton leaf area index nondestructively with a light sensor. *Agronomy Journal 97* (4), 1158–1163.

Tillack, A., Clasen, A., Kleinschmit, B., & Förster, M. (2014): Estimation of the seasonal leaf area index in an alluvial forest using high-resolution satellite-based vegetation indices. *Remote Sensing of Environment 141,* 52–63.

Turner, D.P., Cohen, W.B., Kennedy, R.E., Fassnacht, K.S., & Briggs, J.M. (1999): Relationships between leaf area index and Landsat TM spectral vegetation indices across three temperate zone sites. *Remote Sensing of Environment 70* (1), 52–68.

Turner, D.P., Ollinger, S.V., & Kimball, J.S. (2004): Integrating remote sensing and ecosystem process models for landscape- to regional-scale analysis of the carbon cycle. *BioScience 54* (6), 573–584.

Tyc, G., Tulip, J., Schulten, D., Krischke, M., & Oxfort, M. (2005): The RapidEye mission design. *Acta Astronautica 56* (1-2), 213–219.

Ustin, S.L., Gitelson, A., Jacquemoud, S., Schaepman, M., Asner, G.P., Gamon, J.A., & Zarco-Tejada, P. (2009): Retrieval of foliar information about plant pigment systems from high resolution spectroscopy. *Remote Sensing of Environment 113,* S67-S77.

van Gardingen, P., Jackson, G., Hernandez-Daumas, S., Russell, G., & Sharp, L. (1999): Leaf area index estimates obtained for clumped canopies using hemispherical photography. *Agricultural and Forest Meteorology 94* (3-4), 243–257.

van Gorsel, E., Kljun, N., Leuning, R., Berni, J., Cabello-Leblic, A., Held, A., Haverd, V., Hopkinson, C., Chasmer. L., & Youngentob, K. (2011): Use of High Resolution Lidar and Hyperspectral Data to Evaluate the Sensitivity of Net Ecosystem Exchange to Stand Structural and Plant Chemical Properties. In *34th International Symposium on Remote Sensing of Environment (ISRSE)* (pp. 1–4).

Vanderbilt, V., Bauer, M., & Silva, L. (1979): Prediction of solar irradiance distribution in a wheat canopy using a laser technique. *Agricultural Meteorology 20* (2), 147–160.

Vapnik, V.N. (1999): *The nature of statistical learning theory* (2nd ed.). Statistics for engineering and information science. New York. Springer.

Verger, A., Baret, F., & Camacho-de Coca, F. (2011a): Optimal modalities for radiative transfer-neural network estimation of canopy biophysical characteristics: Evaluation over an agricultural area with CHRIS/PROBA observations. *Remote Sensing of Environment 115* (2), 415–426.

Verger, A., Baret, F., & Weiss, M. (2008): Performances of neural networks for deriving LAI estimates from existing CYCLOPES and MODIS products. *Remote Sensing of Environment 112* (6), 2789–2803.

Verger, A., Baret, F., & Weiss, M. (2011b): A multisensor fusion approach to improve LAI time series. *Remote Sensing of Environment 115* (10), 2460–2470.

Verhoef, W. (1984): Light scattering by leaf layers with application to canopy reflectance modeling: The SAIL model. *Remote Sensing of Environment 16* (2), 125–141.

Verhoef, W. (1985): Earth observation modeling based on layer scattering matrices. *Remote Sensing of Environment 17* (2), 165–178.

Verhoef, W. (1998): Theory of radiative transfer models applied in optical remote sensing of vegetation canopies. Dissertation. Wageningen.

Verhoef, W. (2002): Improved modelling of multiple scattering in leaf canopies: The model SAIL++. In J.A. Sobrino (Ed.), *Proceedings of the First International Symposium on Recent Advances in Quantitative Remote Sensing, Auditori de Torrent, Spain, 16-20 September 2002* (pp. 11–20). Valencia, Spain. Publicacions de la Universitat de Valencia.

Verhoef, W. (2007): A Bayesian optimisation approach for model inversion of hyperspectral-multidirectional observations: the balance with a priori information. In M. Schaepman, S. Liang, N. Groot, & M. Kneubühler (Eds.), *Proceedings of the 10th International Symposium on Physical Measurements and Spectral Signatures in Remote Sensing (ISPMSRS'07)*. Vol. XXXVI, part 7/C50 (pp. 208–213).

Verhoef, W., & Bach, H. (2003): Simulation of hyperspectral and directional radiance images using coupled biophysical and atmospheric radiative transfer models. *Remote Sensing of Environment 87* (1), 23–41.

Verhoef, W., & Bach, H. (2007): Coupled soil–leaf-canopy and atmosphere radiative transfer modeling to simulate hyperspectral multi-angular surface reflectance and TOA radiance data. *Remote Sensing of Environment 109* (2), 166–182.

Verhoef, W., Jia, L., Xiao, Q., & Su, Z. (2007): Unified optical-thermal four-stream radiative transfer theory for homogeneous vegetation canopies. *IEEE Transactions on Geoscience and Remote Sensing 45* (6), 1808–1822.

Vermote, E., Claverie, M., Masek, J., Becker-Reshef, I., & Justice, C. (2014): A merged surface reflectance product from the Landsat and Sentinel-2 missions. In ESA (Ed.), *Sentinel-2 for Science Workshop* (p. 6–6).

Verrelst, J., Muñoz, J., Alonso, L., Delegido, J., Rivera, J.P., Camps-Valls, G., & Moreno, J. (2012a): Machine learning regression algorithms for biophysical parameter retrieval: Opportunities for Sentinel-2 and -3. *Remote Sensing of Environment 118,* 127–139.

Verrelst, J., Rivera, J.P., Alonso, L., & Moreno, J. (2011): ARTMO: An automated radiative transfer models operator toolbox for automated retrieval of biophysical parameters through model inversion. In *Proceeding of the EARSeL 7th SIG-Imaging Spectroscopy Workshop*.

Verrelst, J., Rivera, J.P., Leonenko, G., Alonso, L., & Moreno, J. (2014): Optimizing LUT-based RTM inversion for semiautomatic mapping of crop biophysical parameters from Sentinel-2 and -3 data: Role of cost functions. *IEEE Transactions on Geoscience and Remote Sensing 52* (1), 257–269.

Verrelst, J., Romijn, E., & Kooistra, L. (2012b): Mapping vegetation density in a heterogeneous river floodplain ecosystem using pointable CHRIS/PROBA data. *Remote*

Sensing 4 (12), 2866–2889.

Verstraete, M., Pinty, B., & Myneni, R. (1996): Potential and limitations of information extraction on the terrestrial biosphere from satellite remote sensing. *Remote Sensing of Environment 58* (2), 201–214.

Verstraete, M.M., Pinty, B., & Dickinson, R.E. (1990): A physical model of the bidirectional reflectance of vegetation canopies: 1. Theory. *Journal of Geophysical Research 95* (D8), 11755–11765.

Vertessy, R.A., Benyon, R.G., O'Sullivan, S.K., & Gribben, P.R. (1995): Relationships between stem diameter, sapwood area, leaf area and transpiration in a young mountain ash forest. *Tree physiology 15* (9), 559–567.

Vescovo, L., & Gianelle, D. (2008): Using the MIR bands in vegetation indices for the estimation of grassland biophysical parameters from satellite remote sensing in the Alps region of Trentino (Italy). *Advances in Space Research 41* (11), 1764–1772.

Viña, A., & Gitelson, A. (2005): New developments in the remote estimation of the fraction of absorbed photosynthetically active radiation in crops. *Geophysical Research Letters 32* (17), L17403.

Vohland, M., & Jarmer, T. (2008): Estimating structural and biochemical parameters for grassland from spectroradiometer data by radiative transfer modelling (PROSPECT+SAIL). *International Journal of Remote Sensing 29* (1), 191–209.

Vohland, M., Mader, S., & Dorigo, W. (2010): Applying different inversion techniques to retrieve stand variables of summer barley with PROSPECT+SAIL. *International Journal of Applied Earth Observation and Geoinformation 12* (2), 71–80.

Vuolo, F., Atzberger, C., Richter, K., D'Urso, G., & Dash, J. (2010): Retrieval of biophysical vegetation products from RapidEye imagery. In W. Wagner, & Székely B. (Eds.), *Proceedings of the ISPRS Technical Commission VII Symposium - 100 Years ISPRS - Advancing Remote Sensing Science*.

Vuolo, F., Dash, J., Curran, P.J., Lajas, D., & Kwiatkowska, E. (2012): Methodologies and uncertainties in the use of the terrestrial chlorophyll index for the Sentinel-3 mission. *Remote Sensing 4* (12), 1112–1133.

Vuolo, F., Dini, L., & D'Urso, G. (2008): Retrieval of leaf area index from CHRIS/PROBA data: an analysis of the directional and spectral information content. *International Journal of Remote Sensing 29* (17-18), 5063–5072.

Vuolo, F., Neugebauer, N., Bolognesi, S., Atzberger, C., & D'Urso, G. (2013): Estimation of leaf area index using DEIMOS-1 data: Application and transferability of a semi-empirical relationship between two agricultural areas. *Remote Sensing 5* (3), 1274–1291.

Wagner, S., & Hagemeier, M. (2006): Method of segmentation affects leaf inclination angle estimation in hemispherical photography. *Agricultural and Forest Meteorology 139* (1-2), 12–24.

Wagner, W. (2013): Tourismus in Bayern. München.

WallisDeVries, M.F., Poschlod, P., & Willems, J.H. (2002): Challenges for the conservation of calcareous grasslands in northwestern Europe: integrating the requirements of flora and fauna. *Biological Conservation 104* (3), 265–273.

Wang, L., Dong, T., Zhang, G., & Niu, Z. (2013): LAI retrieval using PROSAIL model and optimal angle combination of multi-angular data in wheat. *IEEE Journal of Selected Topics in Applied Earth Observations and Remote Sensing 6* (3), 1730–1736.

Wang, Q., Adiku, S., Tenhunen, J., & Granier, A. (2005): On the relationship of NDVI with leaf area index in a deciduous forest site. *Remote Sensing of Environment 94* (2), 244–255.

Wang, W.-M., Li, Z.-L., & Su, H.-B. (2007): Comparison of leaf angle distribution functions: Effects on extinction coefficient and fraction of sunlit foliage. *Agricultural and Forest Meteorology 143* (1-2), 106–122.

Watson, D. (1947): Comparative physiological studies on the growth of field crops. I. Variation in net assimilation rate and leaf area between species and varieties, and within and between years. *Annals of Botany 11* (41), 41–76.

Watts, J.D., & Lawrence, R.L. (2008): Merging random forest classification with an object-oriented approach for analysis of agricultural lands. In *The International Archives of the Photogrammetry, Remote Sensing and Spatial Information Sciences Vol. XXXVII* (pp. 579–582).

Weiss, M., & Baret, F. (2010): CAN-EYE V6.1 User Manual. INRA.

Weiss, M., Baret, F., Garrigues, S., & Lacaze, R. (2007): LAI and fAPAR CYCLOPES global products derived from VEGETATION. Part 2: validation and comparison with MODIS collection 4 products. *Remote Sensing of Environment 110* (3), 317–331.

Weiss, M., Baret, F., Leroy, M., Hautecoeur, O., Bacour, C., Prévot, L., & Bruguier, N. (2002): Validation of neural net techniques to estimate canopy biophysical variables from remote sensing data. *Agronomie 22* (6), 547–553.

Weiss, M., Baret, F., Myneni, R.B., Pragnère, A., & Knyazikhin, Y. (2000): Investigation of a model inversion technique to estimate canopy biophysical variables from spectral and directional reflectance data. *Agronomie 20* (1), 3–22.

Weiss, M., Baret, F., Smith, G., Jonckheere, I., & Coppin, P. (2004): Review of methods for in situ leaf area index (LAI) determination. *Agricultural and Forest Meteorology 121* (1-2), 37–53.

Weiss, M., Troufleau, D., Baret, F., Chauki, H., Prévot, L., Olioso, A., Bruguier, N., & Brisson, N. (2001): Coupling canopy functioning and radiative transfer models for remote sensing data assimilation. *Agricultural and Forest Meteorology 108* (2), 113–128.

Wellburn, A.R. (1994): The spectral determination of chlorophylls a and b, as well as total carotenoids, using various solvents with spectrophotometers of different resolution. *Journal of Plant Physiology 144* (3), 307–313.

Welles, J.M. (1990): Some indirect methods of estimating canopy structure. *Remote Sensing Reviews 5* (1), 31–43.

Welles, J.M., & Norman, J.M. (1991): Instrument for indirect measurement of canopy architecture. *Agronomy Journal 83* (5), 818–825.

Welles, J.M., & Norman, J.M. (1991): Photon transport in discontinuous canopies: A weighted random approach. In R.B. Myneni, & J. Ross (Eds.), *Photon-Vegetation Interactions* (pp. 389–414). Berlin, Heidelberg. Springer Berlin Heidelberg.

White, J.D., Running, S.W., Nemani, R., Keane, R.E., & Ryan, K.C. (1997): Measurement and remote sensing of LAI in Rocky Mountain montane ecosystems. *Canadian Journal of Forest Research 27* (11), 1714–1727.

White, M.A., Asner, G.P., Nemani, R.R., Privette, J.L., & Running, S.W. (2000): Measuring fractional cover and leaf area index in arid ecosystems: Digital camera, radiation transmittance, and laser altimetry methods. *Remote Sensing of Environment 74* (1), 45–57.

Widlowski, J.-L., Côté, J.-F., & Béland, M. (2014): Abstract tree crowns in 3D radiative transfer models: Impact on simulated open-canopy reflectances. *Remote Sensing of Environment 142,* 155–175.

Widlowski, J.-L., Lavergne, T., Pinty, B., Verstraete, M., & Gobron, N. (2006a): Rayspread: A virtual laboratory for rapid BRF simulations over 3-D plant canopies. In F. Graziani (Ed.), *Computational methods in transport* (pp. 211–231). Berlin/Heidelberg. Springer-Verlag.

Widlowski, J.-L., Pinty, B., Gobron, N., Verstraete, M.M., Diner, D.J., & Davis, A.B. (2004): Canopy structure parameters derived from multi-angular remote sensing data for terrestrial carbon studies. *Climatic Change 67* (2-3), 403–415.

Widlowski, J.-L., Pinty, B., Lavergne, T., Verstraete, M., & Gobron, N. (2005): Using 1-D models to interpret the reflectance anisotropy of 3-D canopy targets: issues and caveats.

IEEE Transactions on Geoscience and Remote Sensing 43 (9), 2008–2017.

Widlowski, J.-L., Pinty, B., Lavergne, T., Verstraete, M.M., & Gobron, N. (2006b): Horizontal radiation transport in 3-D forest canopies at multiple spatial resolutions: Simulated impact on canopy absorption. *Remote Sensing of Environment 103* (4), 379–397.

Widlowski, J.-L., Pinty, B., Lopatka, M., Atzberger, C., Buzica, D., Chelle, M., Disney, M., Gastellu-Etchegorry, J.-P., Gerboles, M., Gobron, N., Grau, E., Huang, H., Kallel, A., Kobayashi, H., Lewis, P.E., Qin, W., Schlerf, M., Stuckens, J., & Xie, D. (2013): The fourth radiation transfer model intercomparison (RAMI-IV): Proficiency testing of canopy reflectance models with ISO-13528. *Journal of Geophysical Research: Atmospheres 118* (13), 6869–6890.

Widlowski, J.-L., Taberner, M., Pinty, B., Bruniquel-Pinel, V., Disney, M., Fernandes, R., Gastellu-Etchegorry, J.-P., Gobron, N., Kuusk, A., Lavergne, T., Leblanc, S., Lewis, P.E., Martin, E., Mõttus, M., North, P.R.J., Qin, W., Robustelli, M., Rochdi, N., Ruiloba, R., Soler, C., Thompson, R., Verhoef, W., Verstraete, M.M., & Xie, D. (2007): Third radiation transfer model intercomparison (RAMI) exercise: Documenting progress in canopy reflectance models. *Journal of Geophysical Research 112* (D9), D09111.

Wiegand, C., Maas, S., Aase, J., Hatfield, J., Pinter, P., Jackson, R., Kanemasu, E., & Lapitan, R. (1992): Multisite analyses of spectral-biophysical data for wheat. *Remote Sensing of Environment 42* (1), 1–21.

Wigmosta, M.S., Vail, L.W., & Lettenmaier, D.P. (1994): A distributed hydrology-vegetation model for complex terrain. *Water Resources Research 30* (6), 1665–1679.

Wilhelm, W., Ruwe, K., & Schlemmer, M.R. (2000): Comparison of three leaf area index meters in a corn canopy. *Crop Science 40,* 1179–1183.

Wilson, W.J. (1959): Analysis of the spatial distribution of foliage by two-dimensional point quadrats. *New Phytologist 58* (1), 92–99.

Wilson, W.J. (1960): Inclined point quadrats. *New Phytologist 59* (1), 1–7.

Wirth, R., Weber, B., & Ryel, R.J. (2001): Spatial and temporal variability of canopy structure in a tropical moist forest. *Acta Oecologica 22* (5-6), 235–244.

Wit, C. de (1965): Photosynthesis of leaf canopies. Agricultural research reports 663. Wageningen University.

Wohlfahrt, G., & Cernusca, A. (2002): Momentum transfer by a mountain meadow canopy: A simulation analysis based on Massman's (1997) model. *Boundary-Layer Meteorology 103* (3), 391–407.

Wohlfahrt, G., Sapinsky, S., Tappeiner, U., & Cernusca, A. (2001): Estimation of plant area index of grasslands from measurements of canopy radiation profiles. *Agricultural and Forest Meteorology 109* (1), 1–12.

Xiong, Z., & Zhang, Y. (2009): A generic method for RPC refinement using ground control information. *Photogrammetric Engineering & Remote Sensing 75* (9), 1083–1092.

Xu, D., Guo, X., Li, Z., Yang, X., & Yin, H. (2014): Measuring the dead component of mixed grassland with Landsat imagery. *Remote Sensing of Environment 142,* 33–43.

Yang, P., Shibasaki, R., Wenbin Wu, Qingbo Zhou, Zhongxin Chen, Yan Zha, Yun Shi, & Huajun Tang (2007): Evaluation of MODIS land cover and LAI products in cropland of North China plain using in situ measurements and Landsat TM images. *IEEE Transactions on Geoscience and Remote Sensing 45* (10), 3087–3097.

Yang, W., Shabanov, N., Huang, D., Wang, W., Dickinson, R., Nemani, R., Knyazikhin, Y., & Myneni, R. (2006): Analysis of leaf area index products from combination of MODIS Terra and Aqua data. *Remote Sensing of Environment 104* (3), 297–312.

Yang, X., Huang, J., Wu, Y., Wang, J., Wang, P., Wang, X., & Huete, A.R. (2011): Estimating biophysical parameters of rice with remote sensing data using support vector machines. *Science China Life Sciences 54* (3), 272–281.

Zarco-Tejada, P., Miller, J., Morales, A., Berjón, A., & Agüera, J. (2004): Hyperspectral indices and model simulation for chlorophyll estimation in open-canopy tree crops. *Remote Sensing of Environment 90* (4), 463–476.

Zarco-Tejada, P., Rueda, C., & Ustin, S. (2003): Water content estimation in vegetation with MODIS reflectance data and model inversion methods. *Remote Sensing of Environment 85* (1), 109–124.

Zhang, Q., Xiao, X., Braswell, B., Linder, E., Baret, F., & Mooretti, B. (2005a): Estimating light absorption by chlorophyll, leaf and canopy in a deciduous broadleaf forest using MODIS data and a radiative transfer model. *Remote Sensing of Environment 99* (3), 357–371.

Zhang, Y., Chen, J.M., & Miller, J.R. (2005b): Determining digital hemispherical photograph exposure for leaf area index estimation. *Agricultural and Forest Meteorology 133* (1-4), 166–181.

Zhang, Y., Shabanov, N., Knyazikhin, Y., & Myneni, R. (2002): Assessing the information content of multiangle satellite data for mapping biomes. *Remote Sensing of Environment 80* (3), 435–446.

Appendix

Table A-1: Overview of global and regional operationally available LAI products. This table contains selected information and does not claim to be complete.

Product/Program	Sensor	Platform	Model	Inversion	Spatial resolution	Temporal resolution	Region	Reference
Global products								
MODIS c5	MODIS	Terra + Aqua	3D RTM	LUT	1km	4- to 8-day composites		Myneni et al., 2002 Yang et al., 2006
MISR Level 3 LAI	MISR	Terra	3D RTM	LUT	1.1 km	Monthly		Knyazikhin et al., 1998a Knyazikhin et al., 1998b Hu et al., 2007
CYCLOPES V3,1 LAI	VEGETATION	SPOT	PROSPECT + SAIL	ANN	1 km	10 days		Baret et al., 2007 Weiss et al., 2007
GEOV1	VEGETATION	SPOT	-	ANN	1 km	10 days		Baret et al., 2013
GLOBCARBON LAI	VEGETATION ATSR -2 MERIS	SPOT ENVISAT	4-scale GORT	parametric	1 km	Monthly		Deng et al., 2006 Plummer et al., 2006
ECOCLIMAP	AVHRR	NOAA	-	parametric	1 km	Monthly		Champeaux et al., 2005 Masson et al., 2003
-	AVHRR	NOAA	3D RTM	parametric	8 km	Monthly		Myneni et al., 1997 Buermann, 2002
POLDER LAI	POLDER	ADEOS	PROSPECT + Kuusk	ANN	6 km	Monthly		Roujean, 2002 Lacaze, 2005
Landsat LAI	TM + ETM+	Landsat 5 + 7	3D RTM	LUT	30 m	-		Ganguly et al., 2012
Regional products							**Region**	
Geoland2 Biopar LAI	MERIS	ENVISAT	PROSPECT + SAIL	ANN	300 m	10 days	Europe	Bacour et al., 2006
CCRS LAI	VEGETATION AVHRR	SPOT NOAA	-	parametric	1 km	10 days	Canada	Chen et al., 2002
	MODIS	Terra + Aqua	-	parametric	250 km	10 days	Canada	Rochdi & Fernandes,2010

Table A-2: Overview of the acquisition conditions of the RapidEye scenes used in this study.

Acquisition Date	Local Time	Platform	Position of Scene Center	Cloud Cover	Satellite Zenith Angle	Satellite Azimuth Angle	Sun Zenith Angle	Sun Azimuth Angle	Relative Azimuth Angle
2011									
08.04.	12:07	RE-1	47.750 N 10.940 E	5 %	14.6	280.6	40.4	176.3	104.3
17.04.	12:04	RE-5	47.695 N 11.615 E	10 %	6.9	102.3	37.1	180.6	78.3
20.04.	12:16	RE-3	47.764 N 10.599 E	2 %	3.3	102.1	36.1	180.1	78.1
05.05.	12:03	RE-4	47.764 N 10.422 E	0 %	7.4	281.1	31.4	178.2	102.9
09.05.	12:14	RE-3	47.738 N 11.045 E	1 %	3.4	102.1	30.2	181.4	79.3
25.05.	12:12	RE-5	47.758 N 10.790 E	1 %	4.0	281.3	26.6	179.3	102.1
16.07.	12:04	RE-5	47.728 N 11.224 E	3 %	15.1	281.5	26.4	171.4	110.1
21.08.	12:21	RE-2	47.742 N 10.929 E	3 %	6.9	102.5	35.4	180.8	78.3
06.09.	12:14	RE-4	47.747 N 10.886 E	2 %	0.4	281.8	41.1	179.8	102.0
26.09.	12:14	RE-5	47.711 N 11.387 E	5 %	3.3	102.1	48.8	183.0	80.9
2012									
22.03.	12:12	RE-2	47.735 N 11.154 E	17 %	10.2	279.6	46.7	176.7	102.9
25.04.	12:24	RE-2	47.760 N 10.555 E	17 %	6.9	102.5	34.2	183.9	81.4
14.05.	12:23	RE-2	47.745 N 10.879 E	10 %	6.9	102.5	28.9	185.1	82.7
26.05.	12:13	RE-5	47.740 N 11.019 E	11 %	3.8	281.4	26.3	180.3	101.1
16.06.	12:17	RE-2	47.713 N 11.390 E	8 %	0.5	281.7	24.2	181.1	100.6
18.07.	12:09	RE-1	47.710 N 11.526 E	6 %	14.6	280.3	26.7	174.3	106.1
23.07.	12:13	RE-1	47.752 N 10.850 E	11 %	11.0	280.7	27.7	175.3	105.4
13.08.	12:11	RE-3	47.740 N 11.022 E	22 %	7.5	281.0	33.1	175.8	105.2
20.08.	12:19	RE-5	47.684 N 11.543 E	2 %	10.2	105.0	35.3	180.8	75.9
29.08.	12:08	RE-5	47.753 N 10.840 E	2 %	14.9	280.2	38.5	176.3	103.9

Table A-3: Overview of the automatically derived scene visibilities [km] used in ATCOR for atmospheric corrections of the individual RapidEye scenes and elevation classes.

Scene	**Elevation class 1** (average ground elevation: 760 m)	**Elevation class 2** (average ground elevation: 1290 m)	**Elevation class 3** (average ground elevation: 1680 m)	**Haze Removal**
April 8, 2011	22.0	18.1	15.1	No
April 17, 2011	49.5	39.4	33.5	No
April 20, 2011	40.8	33.5	29.9	No
May 5, 2011	88.9	65.7	54.0	No
May 9, 2011	95.4	73.4	59.3	No
May 25, 2011	42.3	32.6	27.0	No
July 16, 2011	62.3	47.5	36.8	No
August 21, 2011	22.9	19.9	18.1	Yes
September 6, 2011	69.4	65.7	43.9	No
September 26, 2011	73.4	69.4	45.6	No
March 22, 2012	56.5	36.8	25.1	No
April 25, 2012	24.5	21.5	19.1	Yes
May 14, 2012	35.7	30.8	26.3	No
May 26, 2012	27.6	22.9	19.9	No
June 16, 2012	33.5	25.7	22.0	No
July 18, 2012	42.3	33.5	33.5	No
July 23, 2012	33.5	26.3	22.0	No
August 13, 2012	32.6	25.7	21.1	No
August 20, 2012	73.4	65.7	65.7	No
August 29, 2012	65.7	51.6	42.3	Yes

Table A-4: Confusion matrix for the land cover classification based on two RapidEye scenes (May 9, 2011, and July 16, 2011). The test set error rate is 6.4 %.

	Rock / Concrete	Forest	Grassland	Moorland	Rape	Maize	Wheat	N° validation pixels	Class Error [%]
Rock / Concrete	2675	2	14	6	0	0	1	2698	0.85
Forest	0	2976	24	0	0	0	0	3000	0.80
Grassland	237	22	2672	40	0	0	29	3000	10.93
Moorland	144	0	198	2346	0	59	0	2747	14.60
Rape	4	0	6	0	1630	0	5	1645	0.91
Maize	19	0	0	372	0	2428	0	2819	13.87
Wheat	0	0	22	0	0	0	2978	3000	0.73

Table A-5: Confusion matrix for the land cover classification based on one RapidEye scene (May 9, 2011). The test set error rate is 8.8 %.

	Rock / Concrete	Forest	Grassland	Moorland	Rape	Maize	Wheat	N° validation pixels	Class Error [%]
Rock / Concrete	2770	2	59	103	0	65	1	3000	7.67
Forest	0	2693	205	0	0	0	102	3000	10.23
Grassland	34	38	2719	152	14	10	33	3000	9.37
Moorland	97	0	112	2481	0	107	0	2797	11.30
Rape	0	0	5	0	1948	0	0	1953	0.26
Maize	60	0	0	95	0	2708	0	2863	5.41
Wheat	0	21	402	0	0	0	2577	3000	14.10

Table A-6: Overview of VIs used for the establishment of transfer functions.

Vegetation Index	**Equation**	**Reference**
	Ratio Indices	
Simple Ratio	$SR = \frac{\rho\mathrm{NIR}}{\rho\mathrm{Red}}$	(Jordan, 1969) (Pearson and Miller, 1972)
Normalized Difference Vegetation Index	$\mathrm{NDVI} = \frac{\rho\mathrm{NIR} - \rho\ \mathrm{Red}}{\rho\mathrm{NIR} + \rho\mathrm{Red}}$	(Rouse et al., 1974)
Renormalized Difference Vegetation Index	$\mathrm{RDVI} = \frac{\rho\mathrm{NIR} - \rho\mathrm{Red}}{\sqrt{\rho\mathrm{NIR} + \rho\mathrm{Red}}}$	(Roujean and Bréon, 1995)
Atmospherically Resistant Vegetation Index	$ARVI = \frac{\rho\mathrm{NIR} - (\rho\mathrm{Red} - (\rho\mathrm{Blue} - \rho\mathrm{Red}))}{\rho\mathrm{NIR} + (\rho\mathrm{Red} - (\rho\mathrm{Blue} - \rho\mathrm{Red}))}$	(Kaufman and Tanre, 1992)
Modified SR 1	$MSR1 = \frac{\frac{\rho\mathrm{NIR}}{\rho\mathrm{Red}} - 1}{\sqrt{\frac{\rho\mathrm{NIR}}{\rho\mathrm{Red}}} + 1}$	(Chen, 1996)
Modified SR 2	$MSR2 = \frac{\rho\mathrm{NIR} - \rho\ \mathrm{Blue}}{\rho\mathrm{Red} - \rho\ \mathrm{Blue}}$	(Sims and Gamon, 2002)
	Orthogonal Indices	
Difference Vegetation Index	$DVI = \rho\mathrm{NIR} - \rho\mathrm{Red}$	(Jordan, 1969)
Perpendicular Vegetation Index	$PVI = \frac{\rho\mathrm{NIR} - a * \rho\mathrm{Red} - \mathrm{b}}{\sqrt{a^2 + 1}}$	(Richardson and Wiegand, 1977)
	Hybrid Indices	
Soil Adjusted Vegetation Index	$\mathrm{SAVI} = \frac{(1 + \mathrm{L}) * (\rho\mathrm{NIR} - \rho\mathrm{Red})}{(\rho\mathrm{NIR} + \rho\mathrm{Red} + \mathrm{L})}$	(Huete, 1988)
Optimized SAVI	$OSAVI = (1 + 0.16) * \frac{\rho\mathrm{NIR} - \rho\mathrm{Red}}{\rho\mathrm{NIR} + \rho\mathrm{Red} + 0.16}$	(Rondeaux et al., 1996)
Modified SAVI	$MSAVI = 0.5\left[(2\rho\mathrm{NIR} + 1 - \sqrt{(2\rho\mathrm{NIR} + 1)^2 - 8(\rho\mathrm{NIR} - \rho\mathrm{Red})}\right]$	(Qi et al., 1994)
Transformed SAVI	$TSAVI = a * \frac{\rho\mathrm{NIR} - \mathrm{a} * \rho\mathrm{Red} - \mathrm{b}}{a * \rho\mathrm{NIR} + \rho\mathrm{Red} - \mathrm{ab}}$	(Baret et al., 1989)
Soil and Atmosphere Resistant Vegetation Index	$SARVI = (1 + L)\frac{\rho\mathrm{NIR} - (\rho\mathrm{Red} - (\rho\mathrm{Blue} - \rho\mathrm{Red}))}{\rho\mathrm{NIR} + (\rho\mathrm{Red} - (\rho\mathrm{Blue} - \rho\mathrm{Red})) + L}$	(Kaufman and Tanre, 1992)
Enhanced Vegetation Index	$EVI = 2.5\frac{\rho\mathrm{NIR} - \rho\mathrm{Red}}{1 + \rho\mathrm{NIR} + C_1 * \rho\mathrm{Red} - C_2 * \rho\mathrm{Blue}}$	(Huete et al., 2002)
	Rededge Indices	
Modified Red Edge SR	$MSR_{re} = \frac{\rho\mathrm{NIR} - \rho\ \mathrm{Blue}}{\rho\mathrm{RE} - \rho\ \mathrm{Blue}}$	(Sims and Gamon, 2002)
NDVI RedEdge	$\mathrm{NDVI}_{\mathrm{rededge}} = \frac{\rho\mathrm{NIR} - \rho\mathrm{RE}}{\rho\mathrm{NIR} + \rho\mathrm{RE}}$	(Gitelson and Merzlyak, 1994)
Red edge Ratio Index 1	$\mathrm{RRI1} = \frac{\rho\mathrm{NIR}}{\rho\mathrm{RE}}$	(Ehammer et al., 2010)

(continued)

Vegetation Index	**Equation**	**Reference**
Red edge Ratio Index 2	$\mathrm{RRI2} = \frac{\rho\mathrm{RE}}{\rho\mathrm{Red}}$	(Ehammer et al., 2010)
Curvature	$\mathrm{Curvature} = \frac{\left(\frac{\rho NIR\ -\ \rho RE}{\lambda NIR\ -\lambda RE}\right) - \left(\frac{\rho RE\ -\ \rho Red}{\lambda RE\ -\lambda Red}\right)}{\lambda NIR\ -\lambda Red}$	(Conrad et al., 2012)
Length	$Length = \sqrt{(\rho NIR\ -\ \rho RE)^2 + (\lambda NIR\ -\lambda RE)^2} + \sqrt{(\rho RE\ -\ \rho Red)^2 + (\lambda RE\ -\lambda Red)^2}$	(Conrad et al., 2012)
Relative Length	$rLength = \frac{Length}{\sqrt{(\rho NIR\ -\ \rho Red)^2 + (\lambda NIR\ -\lambda Red)^2}}$	(Conrad et al., 2012)
	Modified Chlorophyll Indices	
Modified CARI	$MCARI = [(\rho RE - \rho Red) - 0.2(\rho RE - \rho Green)]\frac{\rho RE}{\rho Red}$	(Daughtry, 2000)
MCARI1	$\mathrm{MCARI1} = 1.2[2.5(\rho NIR - \rho Red) - 1.3(\rho NIR - \rho\mathrm{Green})]$	(Haboudane, 2004)
MCARI2	$MCARI2 = \frac{1.5[2.5(\rho NIR - \rho Red) - 1.3(\rho NIR - \rho Green)]}{\sqrt{(2\rho NIR + 1)^2 - \left(6\rho NIR - 5\sqrt{\rho Red}\right) - 0.5}}$	(Haboudane, 2004)
Modified Triangular Vegetation Index	$\mathrm{MTVI}=1.2[1.2(\rho NIR - \rho Green) - 2.5(\rho Red - \rho Green)]$	(Haboudane, 2004)

Note: ρ = reflectance, λ = wavelength, a= 1.0 – 1.6 (scene dependent), b= 0.002 – 0.1 (scene dependent), L = 0.5 (Baret and Guyot, 1991), C1= 6, C2= 7.5.

Table A-7: Empirical-statistical modeling results: Adjusted regression coefficients R^2_{adj} and according significance levels α of polynomial, exponential, power and linear model fits for all tested VIs and each field campaign data set.

	April 25 (n = 10)								May 9 (n = 13)								May 25 (n = 18)							
	linear		power		exponential		cubic		linear		power		exponential		cubic		linear		power		exponential		cubic	
	R^2_{adj}	α	R^2_{adj}	α	R^2_{adj}	α	R^2_{adj}	α	R^2_{adj}	α	R^2_{adj}	α	R^2_{adj}	α	R^2_{adj}	α	R^2_{adj}	α	R^2_{adj}	α	R^2_{adj}	α	R^2_{adj}	α
SR	0.629	**	0.665	**	0.589	**	0.742	**			0.336	*	0.332	*	0.267	.	0.374	**	0.379	**	0.406	**	0.366	*
MSR1	0.671	**	0.677	**	0.634	**	0.745	**			0.336	*	0.335	*	0.269	.	0.342	**	0.367	*	0.392	**	0.360	*
MSR2	0.647	**	0.688	**	0.587	**	**0.813**	**			0.280	*	0.205	.	0.257	.								
NDVI	**0.741**	***	**0.724**	**	**0.716**	**	0.739	**	0.335	*	0.335	*	0.333	*			0.258	*	0.328	*	0.346	*	0.340	*
RDVI	0.704	**	0.694	**	0.684	**	0.689	**	0.531	**	0.522	**	0.509	**	0.490	*	0.227	*	0.249	*	0.264	*	0.224	.
ARVI	**0.760**	***	**0.745**	***	**0.732**	**	0.757	**	0.336	*	0.335	*	0.332	*			0.278	*	0.334	*	0.359	*	0.348	*
DVI	0.644	**	0.639	**	0.623	**	0.636	*	0.592	**	0.582	**	0.551	**	0.569	**	0.200	*	0.205	.	0.219	*	0.169	.
PVI	0.652	**	0.650	**	0.631	**	0.644	*	0.592	**	0.588	**	0.551	**	0.569	**	0.200	*	0.198	.	0.219	*	0.170	.
SAVI	0.704	**	0.695	**	0.684	**	0.688	**	0.533	**	0.525	**	0.513	**	0.491	*	0.224	*	0.244	*	0.260	*	0.220	.
	0.711	**	0.704	**	0.690	**	0.702	**	0.518	**	0.512	**	0.499	**	0.475	*	0.238	*	0.253	*	0.273	*	0.232	.
OSAVI	**0.739**	***	**0.727**	**	**0.719**	**	0.724	**	0.462	**	0.457	*	0.451	*	0.409	*	0.241	*	0.280	*	0.297	*	0.269	*
TSAVI	**0.746**	***	**0.731**	**	**0.723**	**	0.739	**	0.368	*	0.366	*	0.364	*			0.236	*	0.288	*	0.318	*	0.311	*
SARVI	**0.734**	***	**0.726**	**	**0.713**	**	0.720	**	0.490	**	0.485	**	0.473	**	0.444	*	0.251	*	0.272	*	0.298	*	0.263	*
EVI	0.707	**	0.700	**	0.687	**	0.692	**	0.534	**	0.525	**	0.505	**	0.498	*	0.242	*	0.257	*	0.274	*	0.232	.
MSR_{re}	**0.732**	***	**0.718**	**	**0.701**	**	0.756	**					0.168	.			**0.606**	***	**0.701**	***	**0.730**	***	**0.738**	***
$NDVI_{re}$	**0.741**	***	**0.728**	**	**0.715**	**	0.748	**			0.161	.	0.181	.	0.347	*	0.452	**	0.622	***	0.661	***	0.691	***
RRI1	0.717	**	0.706	**	0.686	**	0.744	**			0.192	.	0.211	.			0.567	***	**0.679**	***	**0.713**	***	**0.726**	***
RRI2	0.589	**	0.606	**	0.544	**	0.723	**	0.439	**	0.436	*	0.413	*	0.416	*								
Curv	0.697	**	**0.731**	**	0.662	**	0.724	**					0.168	.	0.344	*	0.559	***	0.600	***	0.667	***	0.694	***
Length	0.643	**	0.637	**	0.622	**	0.637	*	0.587	**	0.572	**	0.544	**	0.568	**	0.211	*	0.220	*	0.232	*	0.183	.
rLength	0.540	**	0.493	*			0.747	**									0.534	***	0.547	***			0.522	**
MCARI	0.580	**	0.608	**	0.541	**			**0.659**	***	**0.660**	**	**0.627**	**	**0.629**	**								
MCARI1	0.631	**	0.628	**	0.612	**	0.616	*	0.605	**	0.597	**	0.567	**	0.578	**	0.165	.	0.167	.	0.176	.		
MCARI2	0.678	**	0.675	**	0.658	**	0.667	**	0.554	**	0.549	**	0.529	**	0.517	*	0.194	*	0.199	.	0.213	.		
MTVI1	0.631	**	0.628	**	0.612	**	0.616	*	0.605	**	0.597	**	0.567	**	0.578	**	0.165	.	0.167	.	0.176	.		

(continued)

	July 16 (n = 25)								August 13 (n = 22)								September 6 (n = 33)							
	linear		power		exponential		cubic		linear		power		exponential		cubic		linear		power		exponential		cubic	
	R2	a	R2	a	R2	a	R2	a	R2	a	R2	a	R2	a	R2	a	R2	a	R2	a	R2	a	R2	a
SR	0.513	***	0.514	***	0.493	***	0.495	***	0.620	***	0.626	***	0.574	***	0.609	***	**0.833**	***	**0.820**	***	**0.861**	***	**0.859**	***
MSR1	0.512	***	0.514	***	0.509	***	0.491	***	0.622	***	0.624	***	0.614	***	0.606	***	0.783	***	**0.797**	***	**0.844**	***	**0.857**	***
MSR2	0.350	**	0.367	**	0.318	**	0.352	**	0.557	***	0.584	***	0.482	***	0.595	***			0.736	***	0.682	***	0.744	***
NDVI	0.476	***	0.504	***	0.511	***	0.519	***	0.530	***	0.588	**	0.605	***	0.609	***	0.617	***	0.709	***	0.739	***	0.781	***
RDVI	0.242	**	0.253	**	0.275	**	0.318	**	0.661	***	**0.703**	***	**0.714**	***	**0.702**	***	0.681	***	0.749	***	0.794	***	0.810	***
ARVI	0.428	***	0.451	***	0.463	***	0.468	***	0.538	***	0.580	**	0.606	***	0.606	***	0.605	***	0.668	***	0.716	***	0.758	***
DVI	0.165	*	0.159	*	0.187	*	0.216	*	0.710	***	**0.725**	***	**0.723**	***	**0.713**	***	0.723	***	0.751	***	0.805	***	0.813	***
PVI	0.193	*	0.178	*	0.218	*	0.245	*	0.707	***	**0.718**	***	**0.722**	***	**0.712**	***	0.734	***	0.746	***	0.810	***	**0.819**	***
SAVI	0.232	**	0.241	**	0.266	**	0.327	**	0.654	***	**0.698**	***	**0.711**	***	**0.700**	***	0.662	***	0.737	***	0.787	***	0.804	***
MSAVI	0.253	**	0.257	**	0.289	**	0.352	**	0.647	***	0.678	***	**0.693**	***	0.679	***	0.694	***	0.741	***	0.803	***	**0.819**	***
OSAVI	0.314	**	0.336	**	0.354	**	0.404	**	0.604	***	0.662	***	0.680	***	0.675	***	0.627	***	0.726	***	0.769	***	0.790	***
TSAVI	0.422	***	0.450	***	0.466	***	0.495	***	0.525	***	0.580	**	0.607	***	0.614	***	0.603	***	0.688	***	0.729	***	0.771	***
SARVI	0.260	**	0.265	**	0.290	**	0.320	**	0.636	***	0.673	***	**0.697**	***	0.686	***	0.669	***	0.715	***	0.780	***	0.801	***
EVI	0.192	*	0.192	*	0.215	*	0.237	*	0.670	***	**0.699**	***	**0.709**	***	0.695	***	0.687	***	0.731	***	0.788	***	0.803	***
MSRre	**0.607**	***			**0.608**	***			0.705	***	**0.724**	***	**0.720**	***	**0.710**	***	0.760	***			0.798	***	0.795	***
NDVI$_{re}$	**0.615**	***	**0.626**	***			**0.614**	***	0.642	***	**0.696**	***	**0.714**	***	**0.708**	***	0.723	***					0.812	***
RRI1	**0.626**	***			**0.619**	***	**0.609**	***	0.702	***	**0.720**	***	**0.714**	***	**0.706**	***	0.790	***			**0.826**	***	**0.824**	***
RRI2	0.408	***	0.408	***	0.402	***	0.381	**	0.541	***	0.539	***	0.487	**	0.537	***	0.770	***	**0.795**	***	**0.830**	***	**0.845**	***
Curv	**0.611**	***	0.517	***			0.598	***	**0.748**	***	0.637	***			**0.736**	***	**0.813**	***			**0.832**	***	**0.827**	***
Length	0.173	*	0.173	*	0.194	*	0.217	*	**0.715**	***	**0.728**	***	**0.721**	***	**0.714**	***	0.747	***	**0.779**	***	0.812	***	**0.817**	***
rLength	**0.619**	***					**0.641**	***	0.676	***	0.635	***			0.661	***	0.602	***	0.610	***			0.597	***
MCARI	0.141	*	0.122	.	0.153	*	0.136	.	0.536	***	0.545	***	0.478	**	0.541	***	0.711	***	0.698	***	0.749	***	0.749	***
MCARI1	0.141	*	0.134	*	0.158	*	0.176	*	0.688	***	**0.706**	***	**0.710**	***	0.698	***	0.710	***	0.737	***	0.796	***	0.805	***
MCARI2	0.208	*	0.204	*	0.235	*	0.274	*	0.654	***	0.676	***	**0.690**	***	0.674	***	0.706	***	0.734	***	0.801	***	0.815	***
MTVI1	0.141	*	0.134	*	0.158	*	0.176	*	0.688	***	**0.706**	***	**0.710**	***	0.698	***	0.710	***	0.737	***	0.796	***	0.805	***

Note: R^2_{adj}= adjusted coefficient of determination. α = significance level: 0.1 ’.’ 0.05 ’*’ 0.01 ’**’ 0.001 ’***’0.

2011

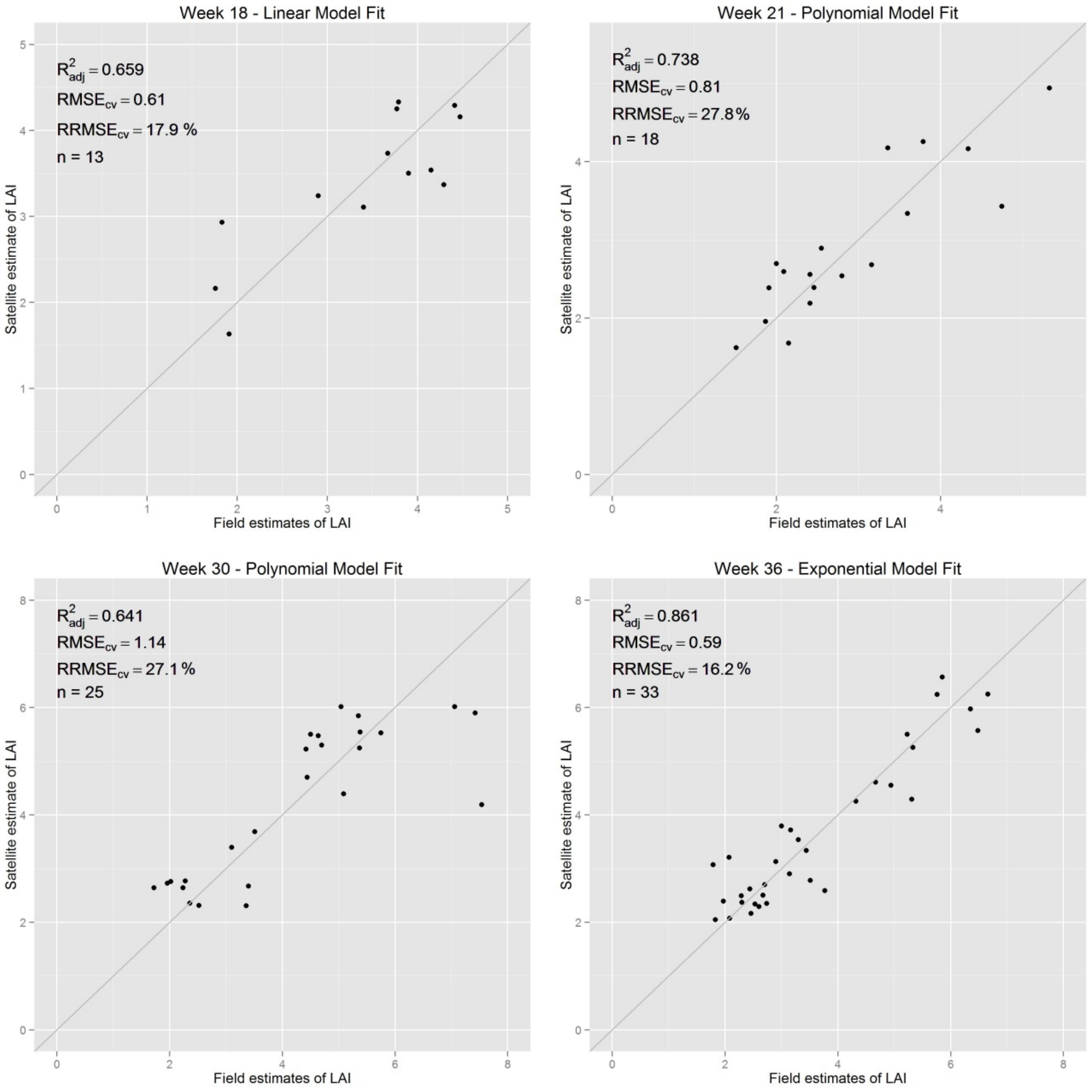

2012

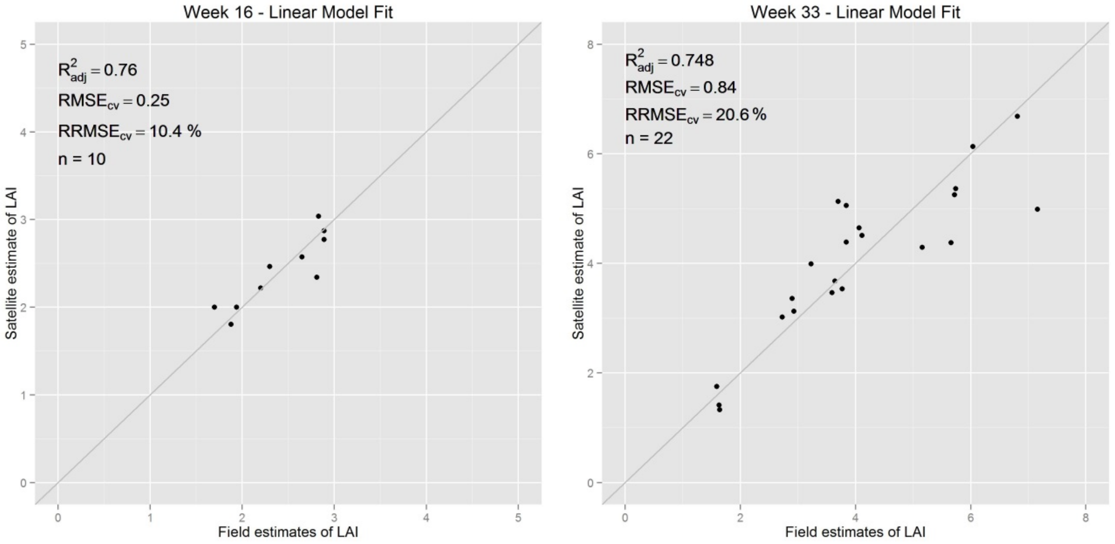

Figure A-1: Scatterplots of LAI estimation for the six different scenes. R^2_{adj} is the adjusted coefficient of determination, $RMSE_{cv}$ and $rRMSE_{cv}$ are the cross-validated absolute and relative root mean squared error.

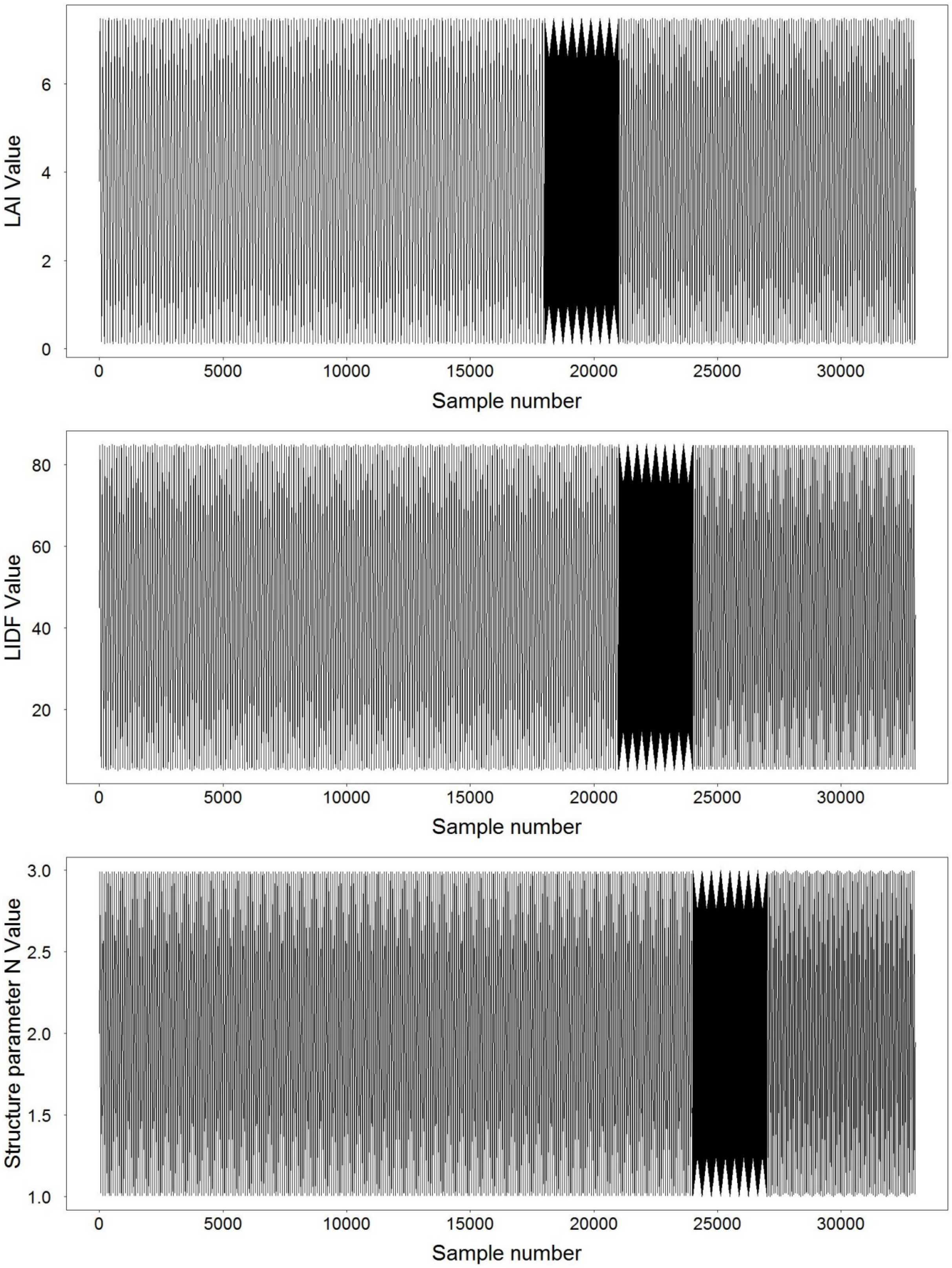

Figure A-2: Example search curves of the EFAST algorithm scanning the LAI (above), LIDF (middle), and N (below) parameter spaces using the altering frequencies ω_{LAI}= {26, 374, 31}, ω_{LIDF}= {31, 374, 36}, and ω_{N}={36, 374,41}, respectively. The phase-shifts are depicted as black areas.

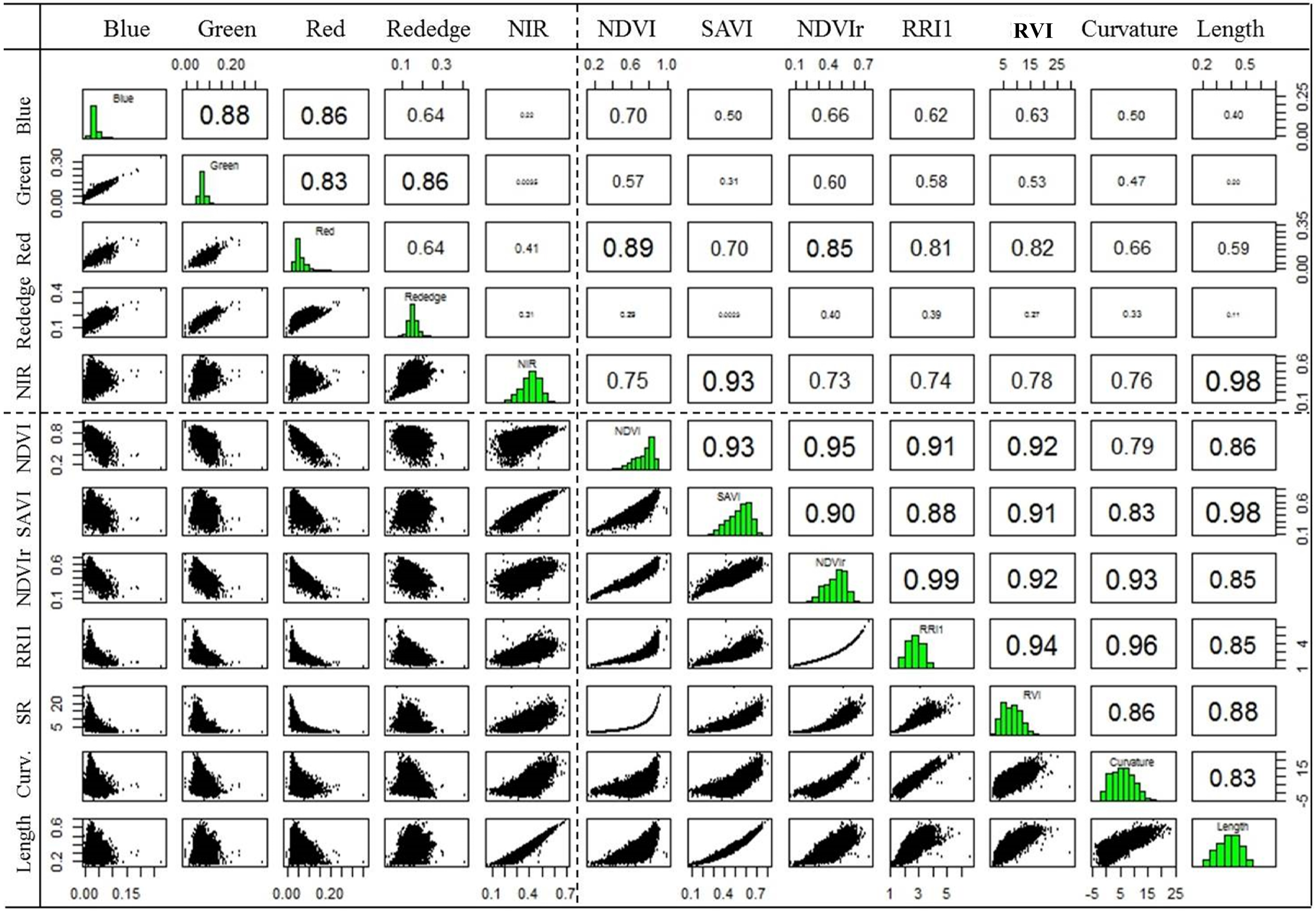

Figure A-3: Scatter plot matrix of the RapidEye band reflectances and of selected VIs used in the EFAST SA. In the diagonal, the histograms of each band are shown, while in the off-diagonal the correlation coefficients and the scatterplots are given. The scatter plots are based on the grassland reflectance data of the May 25, 2011 RapidEye scene.

Table A-8: Review on PROSAIL parameterizations for crop and grassland canopies. A “-“ indicates that the value was either not indicated in the study, or that the parameter was not set in the respective model version. This table contains selected information and does not claim to be complete.

	Parameters	N	C_{ab}	C_{ar}	C_w	C_m	Cbp	LAI	LIDF	*hs*	Soil *bf*	SKYL
	Units	-	µg*cm^{-2}	µg*cm^{-2}	cm	g*cm^{-2}	-	m^2*m^{-2}	°	m*m^{-1}	-	-
Studies	Biome											
(Verrelst et al., 2014)	Crops	1.3 – 2.5	5 – 75	-	0.002 – 0.05	0.001 – 0.03	-	0.1 – 7.0	40 – 70	0.05 – 0.5	0 – 1.0	0.05
(Pasolli, 2012)	Grassland	1.5 – 1.9	15 - 55	-	0.01 – 0.02	0.005 – 0.01	0 – 0.1	0.1 – 8.0	-	0.05 – 0.25	-	0.1
(Atzberger and Richter, 2012)	Alfalfa sugar beet garlic	2.0	20 - 70	-	0.02	0.004 – 0.0055	-	0.01 – 8.0	20 - 70	0.01 – 1.0	0.6 – 1.4	0.1
(Duveiller et al., 2011)	Wheat	1.2 – 1.8	20 – 70	-	-	0.003 – 0.011	0 – 0.2	0 – 8.0	30 - 80	0.1 – 0.5	0.5 – 3.5	-
(Atzberger, 2010)	Wheat	1.7 – 2.3	10 – 80	-	0.004 – 0.044	0.0008 – 0.016	-	0 - 10	67 - 73	0.08 – 0.12	0.9 – 1.1	-
(Vuolo et al., 2010)	Fruit trees Maize div. crops	1.3 – 2.0	10 - 70	-	-	0.004 – 0.007	-	0 – 6.0	35 - 70	0.01 – 1.0	0.6 – 1.4	-
(Darvishzadeh et al., 2008b)	Grassland	1.5 – 1.9	15 - 55	-	0.01 – 0.02	0.005 – 0.01	-	0.3 – 7.5	40 - 70	0.05 – 0.1	0.5 – 1.5	-
(Vohland and Jarmer, 2008)	Grassland	1.6	1 - 100	-	0.001 – 0.04	0.001 – 0.016	-	0.01 – 8.0	20 - 70	0.1	-	0.01
(Koetz et al., 2005a)	Maize	1.2 – 1.8	20 – 80	-	0.01 – 0.03	-	-	0 – 7.0	55 – 65	0.01 – 0.2	0.7 – 1.3	-
(Haboudane, 2004)	Crops	1.41	5 - 100	-	0.0015	0.0035	-	0.1 – 12	-	-	-	1.0
(Atzberger, 2004)	Crops	1.0 – 2.8	20 - 80	-	0.004 – 0.034	0.002 – 0.018	-	0 – 3.0	20 - 70	0.01 – 0.09	-	0.1
(Weiss et al., 2000)	Maize	1.0 – 2.5	20 - 100	-	0.005 – 0.025	0.0013 – 0.006	-	0 – 8.0	20 - 75	0.05 – 1.0	0.5 – 1.5	-

Table A-9: PROSAIL parameter settings and size of LUT for each RapidEye scene. For each parameter, the value range ('rng.') and sampling interval ('int.') is given. For fixed values, just the selected level is indicated. The sun and sensor zenith angles vary over the scenes due to the local topography, so only the number of viewing angles combinations is indicated.

2011											
Parameters		Units	April 8	April 20	May 5	May 9	May 25	July 16	August 21	September 6	September 26
PROSPECT variables			Rng / Int	Rng / Int	Rng / Int	Rng / Int	Rng / Int	Rng / Int	Rng / Int	Rng / Int	Rng / Int
N	Structure	-	1.3 – 1.9/0.3	1.3 – 1.9/0.3	1.3 – 1.9/0.3	1.3 – 1.9/0.3	1.3 – 1.9/0.3	1.3 – 1.9/0.3	1.3 – 1.9/0.3	1.3 – 1.9/0.3	1.3 – 1.9/0.3
C_{ab}	Chlorophyll	$\mu g*cm^{-2}$	10-40/10	10-50/10	10-60/10	10-60/10	10-70/10	20-80/10	20-80/10	20-80/10	20-70
C^{ar}	Carotenoid	$\mu g*cm^{-2}$	4	7	7	7	10	12	12	12	10
C_w	water	cm	0.02	0.02	0.02	0.02	0.02	0.02	0.02	0.02	0.02
C_m	Dry matter	$g*cm^{-2}$	.005 – .015 /.005	.005 – .015 /.005	.004 – .012 /.004	.004 – .012 /.004	.004 – .012 /.004	.004 – .012 /.004	.004 – .012 /.004	.004 – .012 /.004	.004 – .012 /.004
C_{bp}	Brown pig.	-	0.4	0.4	0.4	0.4	0.4	0.4	0.4	0.4	0.4
SAIL variables											
LAI	Leaf area	m^2*m^{-2}	0.2 – 3.8 / 0.2	0.2 – 4.0 / 0.2	0.2 – 4.4/ 0.2	0.2 – 4.4 / 0.2	0.2 – 5.0 / 0.2	0.2 – 7.0 / 0.2	0.2 – 6.8 / 0.2	0.2 – 6.2 / 0.2	0.2 – 5.2 / 0.2
LIDF	Leaf angle	°	36 – 78 / 6	36 – 78 / 6	36 – 78 / 6	36 – 78 / 6	30 – 78 / 6	30 – 78 / 6	30 - 78 / 6	30 – 78 / 6	30-72/6
hs	Hot spot	$m*m^{-1}$	0.10	0.10	0.10	0.10	0.11	0.10	0.12	0.14	0.12
soil *bf*	ρ_{soil}	-	0.1 – 0.7 / 0.1	0.0 – 0.7 / 0.1	0.1 – 0.7 / 0.1	0.1 – 0.7 / 0.1	0.1 – 0.8 / 0.1	0.0 – 0.9 / 0.1	0.0 – 0.8 / 0.1	0.0 – 1 / 0.1	0.0 – 0.6 / 0.1
SKYL	Diffuse light	-	0.13	0.12	0.13	0.10	0.14	0.18	0.13	0.10	0.13
θ_s	Solar zenith	°	150 combs.	135 combs.	125 combs.	112 combs.	104 combs.	130 combs.	135 combs.	120 combs.	120 combs.
θ_o	Obs. zenith	°									
φ_r	Rel.azimuth	°	104.26	78.16	102.92	79.33	102.08	110.10	78.32	102.00	80.87
Number of LUT entries			33516	57600	66528	66528	113400	198450	173502	140616	78624

(continued)

2012

Parameters		Units	March 22	April 25	May 14	May 26	June 16	July 18	July 23	August 13	August 20	August 29
PROSPECT variables			Rng / Int	Rng / Int	Rng / Int	Rng / Int	Rng / Int	Rng / Int	Rng / Int	Rng / Int	Rng / Int	Rng / Int
N	Structure	-	1.3 – 1.9/0.3	1.3 – 1.9/0.3	1.3 – 1.9/0.3	1.3 – 1.9/0.3	1.3 – 1.9/0.3	1.3 – 1.9/0.3	1.3 – 1.9/0.3	1.3 – 1.9/0.3	1.3 – 1.9/0.3	1.3 – 1.9/0.3
C_{ab}	Chlorophyll	µg*cm^{-2}	10-40/10	10-50/10	10-60/10	10-70/10	20-80/10	20-80/10	20-80/10	20-80/10	20-80/10	20-80/10
C_{ar}	Carotenoid	µg*cm^{-2}	4	7	7	10	12	12	12	12	12	12
C_w	water	cm	0.02	0.02	0.02	0.02	0.02	0.02	0.02	0.02	0.02	0.02
C_m	Dry matter	g *cm^{-2}	.004 – .012/.004	.004 – .012/.004	.004 – .012/.004	.004 – .012/.004	.004 – .012/.004	.004 – .012/.004	.004 – .012/.004	.004 – .012/.004	.004 – .012/.004	.004 – .012/.004
C_{bp}	Brown pig.	-	0.4	0.4	0.4	0.4	0.4	0.4	0.4	0.4	0.4	0.4
SAIL variables												
LAI	Leaf area	m^2*m^{-2}	0.2 – 3.6 / 0.2	0.2 – 4.0 / 0.2	0.2 – 4.6 / 0.2	0.2 – 5.0 / 0.2	0.2 – 6.0 / 0.2	0.2 – 7.0 / 0.2	0.2 – 7.0 / 0.2	0.2 – 6.8 / 0.2	0.2 – 6.8 / 0.2	0.2 – 6.6 / 0.2
LIDF	Leaf angle	°	36 – 78 / 6	36 – 78 / 6	36 – 78 / 6	30 – 78 / 6	30 – 78 / 6	30 – 78 / 6	30 – 78 / 6	30 – 78 / 6	30 – 78 / 6	30 – 78 / 6
hs	Hot spot	m*m^{-1}	0.10	0.10	0.10	0.10	0.10	0.10	0.10	0.10	0.10	0.10
soil *bf*	ρ_{soil}	-	0.0 – 0.8 / 0.1	0.0 – 0.6 / 0.1	0.0 – 0.6 / 0.1	0.1 – 0.8 / 0.1	0.1 – 1.0 / 0.1	0.0 – 0.9 / 0.1	0.0 – 0.9 / 0.1	0.0 – 0.8 / 0.1	0.1 – 0.8 / 0.1	0.1 – 0.7 / 0.1
SKYL	Diffuse light	-	0.14	0.12	0.12	0.12	0.10	0.12	0.14	0.11	0.11	0.09
θ_s	Solar zenith	°	135 combs.	135 combs.	126 combs.	104 combs.	104 combs.	130 combs.	122 combs.	135 combs.	150 combs.	157 combs.
θ_o	Obs. zenith	°										
φ_r	Rel.azimuth	°	102.93	81.35	82.66	101.13	100.57	106.06	105.37	105.20	75.88	103.89
Number of LUT entries			33516	57600	66528	66528	113400	198450	198450	173502	154224	130977

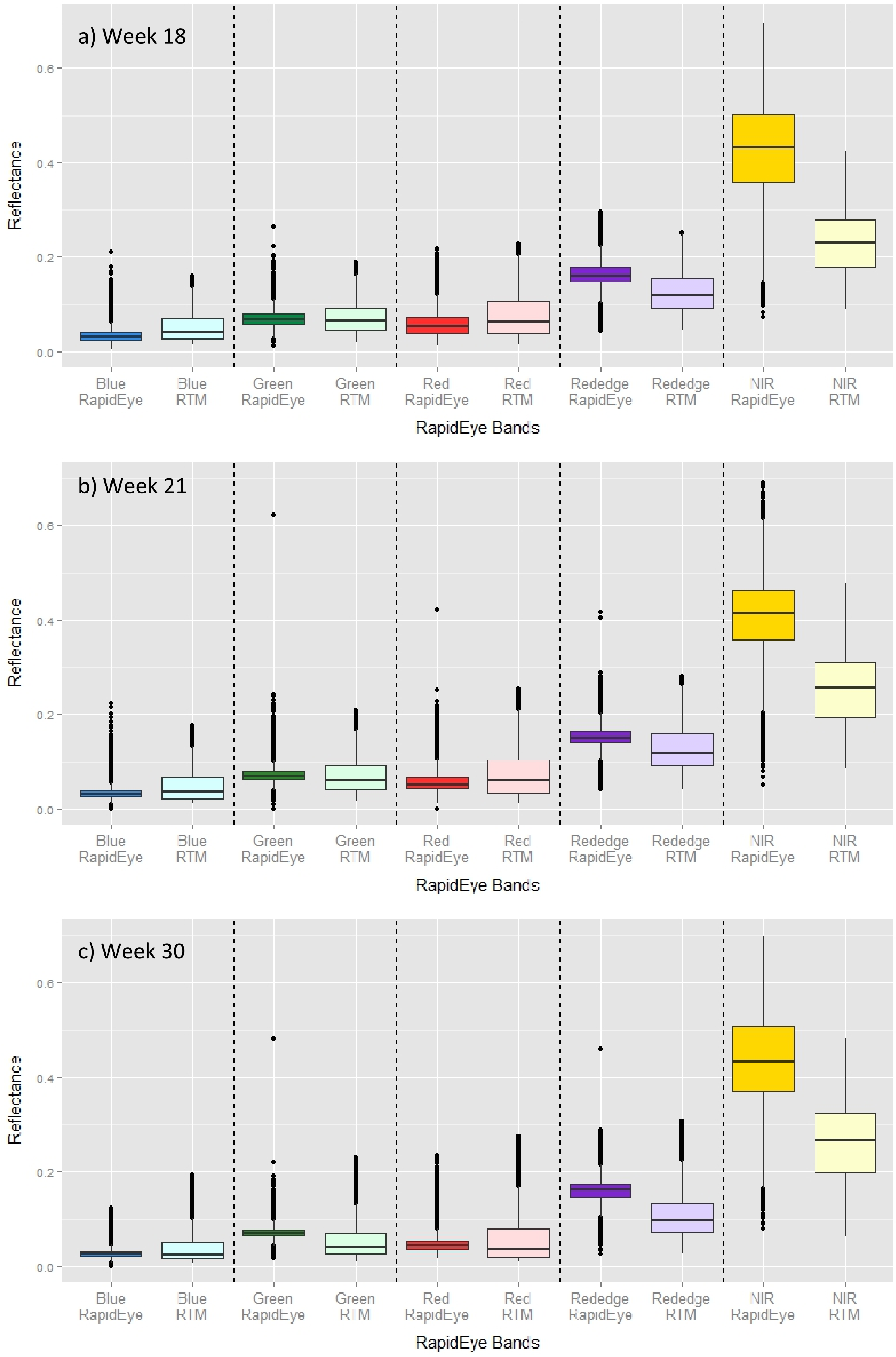

Figure A-4: Distributions of measured and simulated grassland reflectances for six RapidEye scenes. In each figure, the boxplots of the reflectances sampled from the grassland areas in the RapidEye scenes and from the LUTs are shown for each band side by side. The number of pixel reflectances sampled equals the number of the LUT entries for each scene.

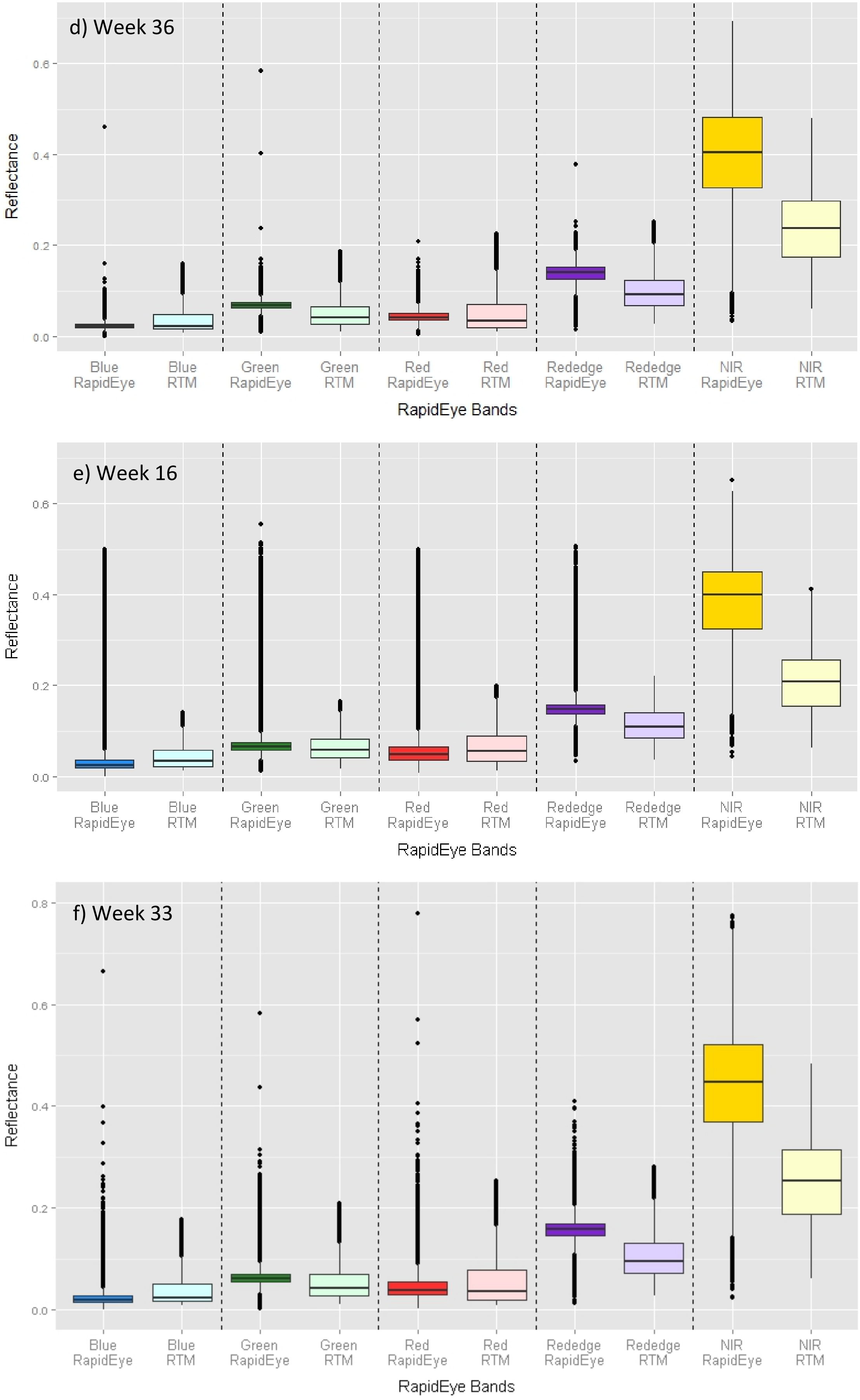

Figure A-4 *(continued)*

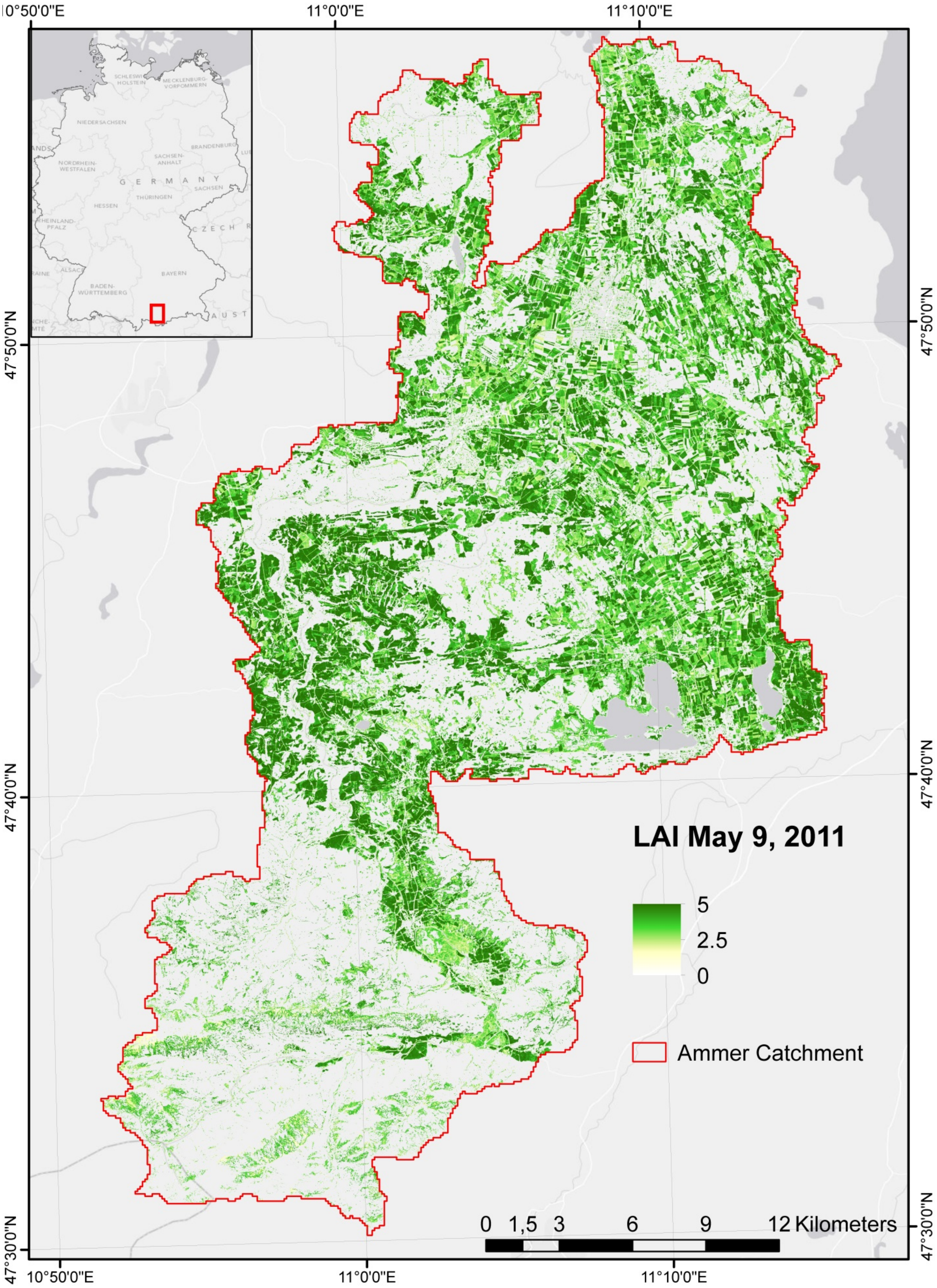

Figure A-5: Physically modeled grassland LAI map of the Ammer catchment for May 9, 2011.

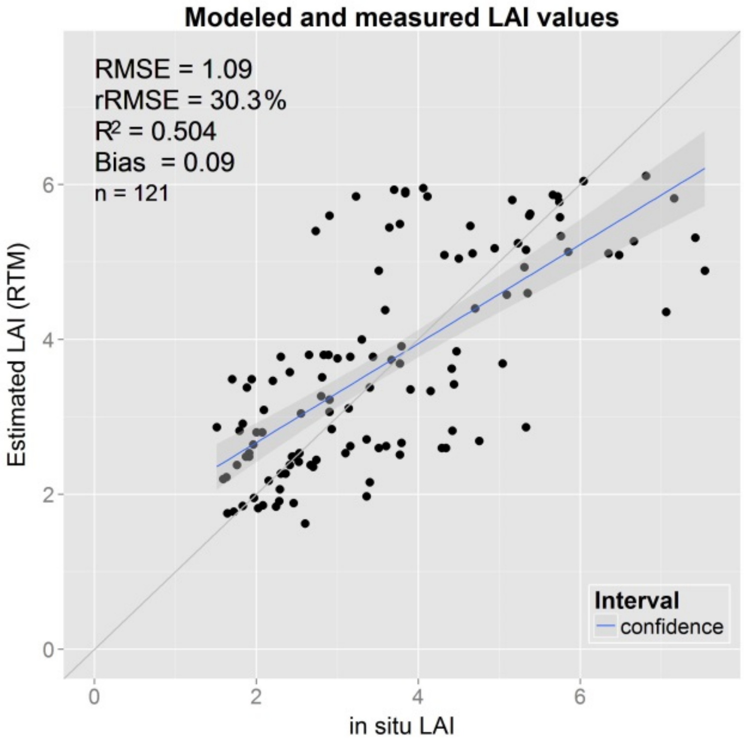

Figure A-6: Scatter plot of all *in situ* LAI measurements vs. PROSAIL LAI estimates.

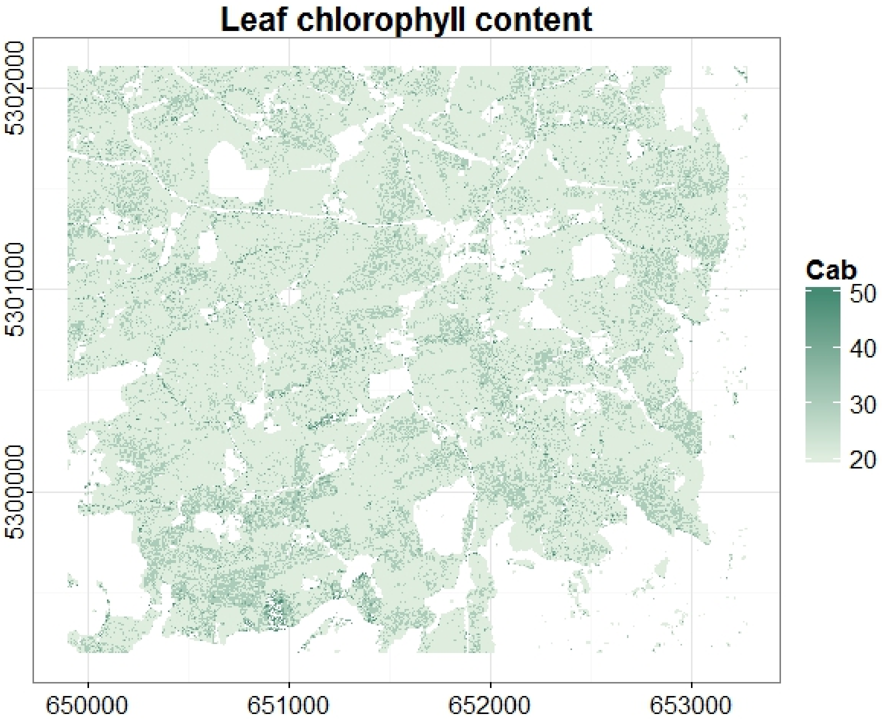

Figure A-7: Leaf chlorophyll content for a subset of the September 6, 2011 scene

2011

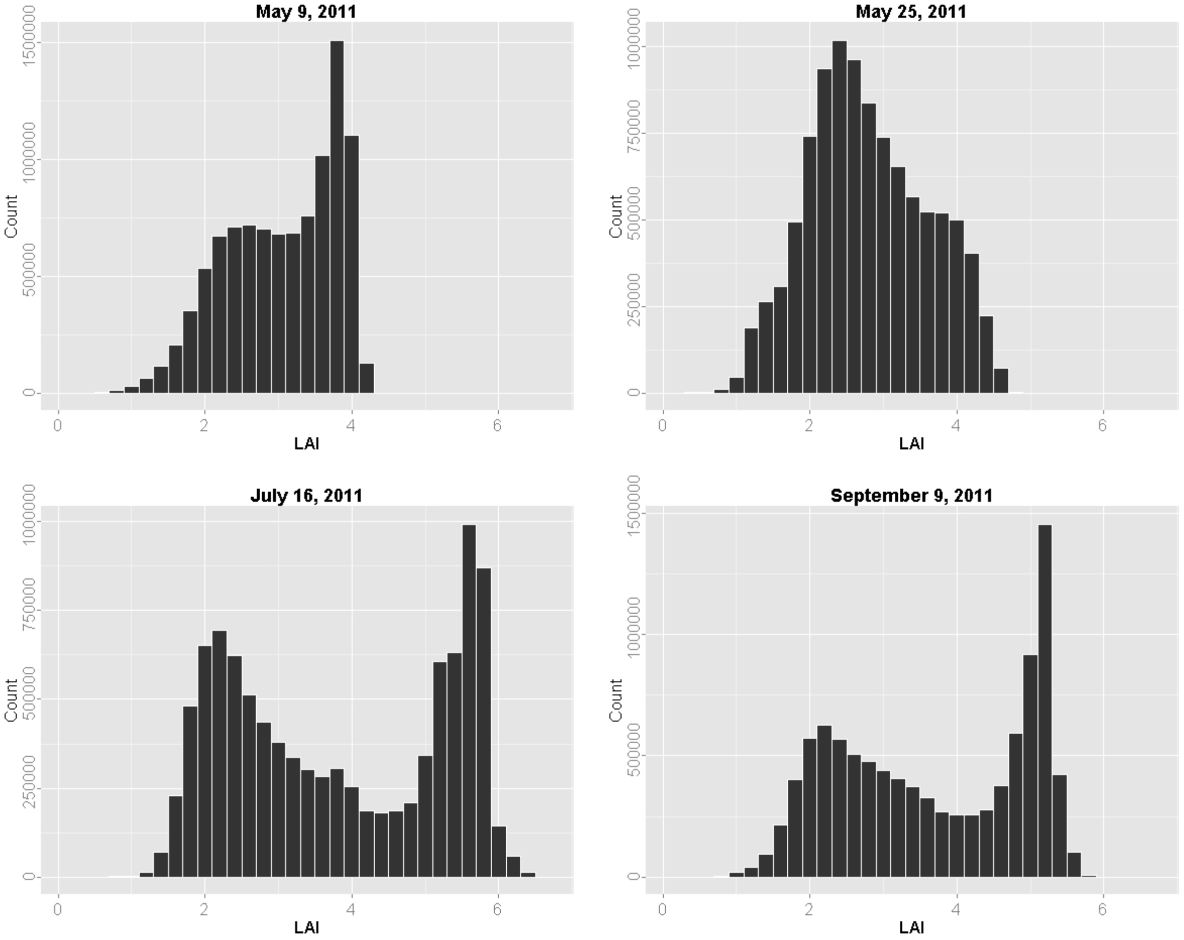

2012

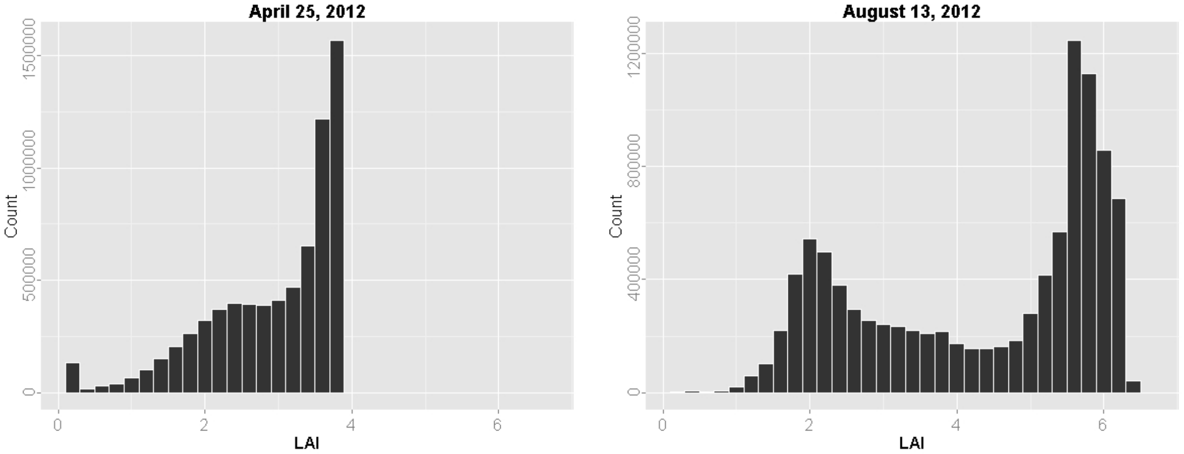

Figure A-8: Parameter distributions of the physically modeled LAI maps for the six points in time for which contemporaneous *in situ* data were available. For the generation of the graphs, subsets of 10 million pixels were drawn from the grassland areas within each scene.

Acknowledgements

The completion of this thesis would never have been possible without the support of many people. First and foremost, I would like to thank my supervisor Prof. Dr. Stefan Dech for providing me with the opportunity to conduct a PhD at the Department of Remote Sensing at the University of Würzburg. I would like to thank him for his scientific guidance and fruitful feedback, his support, and for his confidence in letting me develop my own ideas and research focus. Secondly, I would like to thank Prof. Dr. Harald Kunstmann (Karlsruhe Institute of Technology (KIT)/IMK-IFU, University of Augsburg) for accepting to be the second advisor of my thesis, also within the framework of my MICMoR 'Thesis Advisory Committee'. I am grateful to him for providing me with access to the infrastructure of the KIT Campus Alpin in Garmisch-Partenkirchen, and for his valuable suggestions regarding some statistical and modeling aspects of my thesis. Further, I owe special thanks to my mentor Dr. Doris Klein (DLR) for her unfailing encouragement and guidance during all stages of my thesis, her willingness to deal with real and imaginary problems at any time, and the great times we had together in Kyrgyzstan, Italy, Canada, and in the Ammer catchment. I personally profited a lot from her comments and constructive criticism and would like to thank her for her commitment during all these years.

During my time at the Department of Remote Sensing in Würzburg, I learned a lot, and I am grateful to my past and present colleagues for creating a unique working atmosphere and for being kind and helpful whenever I had a doubt or a favor to ask. I also would like to thank them for letting me occupy large parts of the computing capacity of the department during the last month of this thesis. Therefore, I want to extend my appreciation to Christian Bäuerlein, Christopher Conrad, Anna Cord, Gerald Forkuor, Sebastian Fritsch, Ursula Geßner, Vitus Himmler, Christian Hüttich, Patrick Knöfel, Carina Kübert, Tobias Landmann, Hooman Latifi, Benjamin Leutner, Sylvia Lex, Fabian Löw, Miriam Machwitz, Noellie Rüth, Gunther Schorcht, Martin Schmidt, Matthias Schramm, Simon Sebold, Michael Thiel, Yvonne Walz, Martin Wegmann, and Julian Zeidler. Special thanks to Doris Klein, Ursula Gessner, Carina Kübert, Fabian Löw, Sebastian Fritsch, and Benjamin Leutner for proof-reading and their valuable suggestions which greatly improved this manuscript. A special word of thanks goes to Julian Zeidler and Benjamin Leutner for their technical support regarding all sorts of hardware, software, and programming problems, as well as for the valuable discussions on many mathematical-statistical maneuvers. Moreover, I am grateful to my office colleagues Anna Cord and Carina Kübert, and later Sebastian Fritsch, Partick Knöfel, and Fabian Löw for the many chats, sometimes with, mostly without meaningful content, and fun moments in the office. I further would like to thank Andrea Ehammer and Heiko Fabritius for their patient and reliable help during the field measurements, as well as for enduring many uncomfortable weather conditions and wildlife encounters.

During this PhD, I greatly benefited from the cooperation with the Institute for Applied Remote Sensing at the European Academy (EURAC) of Bolzano/Italy under the guidance of Dr. Marc Zebisch, and I want to express my thanks to Dr. Luca Pasolli for sharing his knowledge on radiation transfer modeling with me, as to Dr. Marc Zebisch, Dr. Claudia Notarnicola, and all members of the working group for welcoming me at EURAC during two very fruitful visits. Grazie!

Being a fellow in the MICMoR (Mechanisms and Interactions of Climate Change in Mountain Regions) Helmholtz Research School provided me with opportunities to get insights in other environmental research disciplines and to think out of the box, with the chance to actively participate in the development of a sophisticated PhD program, as well as with financial support for conference attendances and research stays abroad. I would like to thank the MICMoR Core Team as well as Dr. Elija Bleher and Petra Gruppenberger of the Coordination Office for their support, for the perfect organization of all events, and for their help with many administrative tasks. I also would like to thank my fellow MICMoR students for the great times and fruitful discussions during the courses and retreats.

I would like to thank the RapidEye Science Archive (RESA), which is hosted by the German Aerospace Agency (DLR), for providing the RapidEye data this thesis is based on. The *in situ* data measurements and analysis conducted in this thesis relied on a wide range of instruments, software, and shared personal experiences. I would like to thank the DLR for providing the LAI-2000 PCA instrument. The KIT IMK-IFU also supported me strongly in this regard. I would like to thank Carsten Jahn for installing and maintaining the hemispherical cameras on the TERENO sites, Dr. Rainer Gasche for his unbureaucratic support in letting me use the lab, the precision scales and the drying cabinet, and Katja Heidbach for providing me with the TERENO irradiance data. Further, I received manifold assistance and advice from the scientific community during meetings or via email, and hence I also would like to thank Dr. Roberto Colombo (Università Milano Bicocca) for his ideas and suggestions on the field campaign design, Dr. Jean-Baptiste Féret (Carnegie Institution for Science) for his help with taming the PROSAIL model, Dr. Rolf Richter (DLR) for valuable suggestions regarding the data preprocessing, Dr. Marie Weiss (INRA, EMMAH) for her support with the CAN-EYE program, Annika Müller (LI-COR) for sorting out some statistical details with the LAI PCA instrument, Florian Marshall (University of Augsburg) for his assistance with mathematics and the MATLAB software, Prof. Dr. Georg Wohlfahrt (University of Innsbruck) for letting me use the leaf scanner, and Dr. Markus Burghardt (Biozentrum, University of Würzburg) for allowing me to use his lab for the chlorophyll measurement.

I am also very grateful to my family for their unconditional support and their understanding during the last few years. Many thanks also to my friends who took my mind of science and back to the things that matter from time to time. Special thanks go to Lena Odell for linguistic proof-reading under these ‘circumstances’! Finally, I would like to express my profound gratefulness to Tim for his patience, humor, and encouragement whenever I needed it. Thank you!

Sarah Asam